UNIVERSITAT DE BARCELONA

Theories of gravitation confronted with cosmological observations

Carlos García García

Doctoral thesis

Theories of gravitation confronted with cosmological observations

Carlos García García

Supervised by:

Pilar Ruiz Lapuente
Miguel Zumalacárregui

UNIVERSITAT DE BARCELONA

Theories of gravitation confronted with cosmological observations

Memòria presentada per optar al grau de doctor per la Universitat de Barcelona

Programa de doctorat en Física

Autor:
Carlos García García

Directors:
Pilar Ruiz-Lapuente
Miguel Zumalacárregui

Tutor:
Domènec Espriu Climent

UNIVERSITAT DE BARCELONA

Statement

The following work is based on a series of articles written in collaboration with other researchers [1–5]. In particular, Chapter 6 is based on my two articles Refs. [1, 2]; Chapter 7 is based on Ref. [4], Chapter 8 is based on Ref. [3] and Chapter 9 is based on Ref. [5]. The Conclusions in Chapter 10 will summarize the findings of my PhD thesis. Finally, I will note that content in Part II is meant to be an introduction to my work and is based on other author's work. In particular, Chapter 2, a brief summary of the Standard Model, is mainly based on Refs. [6–10] and references therein. Chapter 3, a quick summary of the present status of cosmological observations, is based on Refs. [6, 7, 9, 10] and references therein. In particular, Sections 3.1 and 3.3 mainly follow Ref. [10], while Section 3.2 follows Ref. [9]. Finally, Chapter 4 introduces Modify Gravity and is mainly based on Refs. [11–13] and references therein. In Chapter 5 some of the forthcoming next-generation surveys that have been more related to my work will be described following their scientific or white papers. I claim no authorship of the content of these Chapters.

Carlos García García
Madrid, April 2020

1. **Dark energy from α-attractors: phenomenology and observational constraints**, C. García-García, E. V. Linder, P. Ruíz-Lapuente and M. Zumalacárregui, *JCAP* **1808** (2018) 022 [1803.00661].

2. **α-attractor dark energy in view of next-generation cosmological surveys**, C. García-García, P. Ruíz-Lapuente, D. Alonso and M. Zumalacárregui, *JCAP* **1907** (2019) 025 [1905.03753].

3. **Disconnected pseudo-C_l covariances for projected large-scale structure data**, C. García-García, D. Alonso and E. Bellini, *JCAP* **2019** (2019) 043 [1906.11765].

4. **Theoretical priors in scalar-tensor cosmologies: thawing quintessence**, C. García-García, P. G. Ferreira, E. Bellini, D. Traykova and M. Zumalacárregui, *Phys. Rev.* **D101** (2020) 063508 [1911.02868].

5. **S_8 time evolution in view of KiDS-450, DES-Y1 and Planck CMB data**, C. García-García, D. Alonso, E. Bellini, P. G. Ferreira, E.-M. Mueller, P. Ruiz-Lapuente, *In preparation.*

Contents

Preface

I present here my last three years' work. During this time I have been able to explore branches of cosmology that I only knew remotely. Coming from a heavy theoretical background, I had never worked too close to observations and data analysis. I had, however, analyzed the phenomenology of a particular viable solution of Bigravity/Massive gravity and naively imposed observational constraints.

My first work in my PhD was, consequently, the analysis of the phenomenology of a particular kind of Dark Energy that could be also linked to Inflation. We then made a full comparison of the theoretical predictions with the most recent Cosmic Microwave Background (CMB), Baryon Acoustic Oscillations and Type Ia supernovae data. Furthermore, we predicted what would be the impact on the constraints with next-generation surveys measurements. We learnt that this model could address correctly the observations by its ability to mimic the Standard Cosmological Model predictions and that forthcoming data might be able to distinguish both of them.

From the idea of having different models having similar impact on the observations, we started our next project. We wanted to identify what was the common framework that different models share to impact similarly on the observables. We wanted to dissect these models and find a unified way of describing them, taking into account only their effect on what we can actually measure. Despite several problems, from code, statistical techniques, etc. we managed to find an accurate framework for a specific, although quite common, case: quintessence. In fact, we showed that the usual CPL parametrization could be good enough to describe the observables up to recombination.

In all these projects, we had to make use of observational likelihoods (i.e. the probability density functions that tell you the probability of seeing what have been measured with a set of given parameters) from different surveys, in order to explore the parameter space of our models and find the observationally preferred regions. Having accurate likelihoods is, then, mandatory if one wants to test Modified Gravity models. However, the exact computation might be really inefficient (if even possible) for some next-generation surveys.

This is the case of Large Scale Structure surveys, that will reach such resolution that the full computation of the likelihood might be intractable. In fact, it scales as the sixth power of the maximum angular moment ($O(\ell^6_{\rm max})$) of the survey. We showed, however, that it is possible to reduce it to $O(\ell^3_{\rm max})$ doing some approximations while accurately recovering the posterior distribution of the cosmological parameters (i.e. the observationally preferred region).

This approximation will be used in a on-going project of reconstructing the growth history of the Universe using early (CMB) and local measurements (galaxies distribution and shapes), which might give us a hint about the current tension that the KiDS survey shows with Planck's CMB results.

These projects constitute the main scientific contribution I have made during these three years. Some projects died after the incredible and unexpected measurement of the gravitational wave speed that has had incredible consequences for the Modified Gravity community, *probably*

ruling out many theories. This can be seen as an opportunity as Modified Gravity has never been so restricted as now, letting us focus on those models that might have more chances of being true. Other projects, however, are still ongoing or planned for the future. For instance, an improvement on our LSS likelihood estimate that made it work for shear-B modes would be relevant as their non-trivial detection would kill General Relativity.

This is an interesting moment to work on cosmology, Modified Gravity and observations. We have reached unprecedented precision on cosmological measurements and cosmological parameter estimation. We have, furthermore, *probably* killed all Modified Gravity models that modify the gravitational waves speed. But, however, there are still fundamental questions that arise from the Standard Cosmological model and, perhaps more importantly, there seems to be some discrepancy between theory and data, which might be the whisper of forthcoming data announcing the end of the Standard Cosmological Model. Next-generation data might well be the starting shot of a new quest: the quest for the establishment of the new Standard Cosmological Model. If this is the case, we are, fortunately, full of ideas.

Acknowledgments: During these three years I have had the opportunity of working and meeting a lot of incredible people. First my advisors, Miguel and Pilar, for their support and advise and for giving me the opportunity and encourage me to travel abroad to work with very renown people and groups. In addition, I must specially thank Miguel for one of the most useful lessons I have ever received, one that goes beyond academic life: the techniques for an effective communication (written or oral) of my work. I also thank Pilar for always being at hand when I needed her. Thanks to my advisors' encouragement for travelling I had the opportunity of expending three months in UC Berkeley and LBNL, as well as uncountable times in Oxford (also thanks to Pedro G. Ferreira for this). I have to thank Pedro G. Ferreira his willingness for constantly inviting me to the Department of Astrophysics of Oxford. This gave me the opportunity to meet and work with the incredible people that form the group, as well as enjoy all the talks, seminars and activities that they organize. Of course, I have an special word for all those I met in Oxford: Chris, Emilio, Eva, Darsh, David, Dina, Giulia, Max, Becca, Shahab,... And, in particular, I must say that it has been and continues being a pleasure to work with my collaborators: Pedro, Emilio, David and Dina. From Berkeley I must mention Chang (thanks for the bike!), Emanuele, Emmanuel, Eric, Simone,... and Mateo and Roy, my housemates that were incredible hosts and tourist guides. Finally, of course, I cannot forget these people from Madrid, both UAM and UCM, Antonio, Clara, Héctor, José María, José Cembranos, José Manuel, Luis, Miguel, Prado,... This work is also work of all the people I met and worked with in my visits, schools and conferences but it is also of those I have discussed, trained, drunk and partied with (and that have coped with me) during these three years; i.e. my family, friends (IFF colleges includes) and, of course, Liss.

Resumen

En la era de la Cosmología de Precisión, en que tenemos un buen entendimiento de gran parte de los eventos astrofísicos y de la evolución del cosmos desde sus primeros momentos hasta hoy, el Universo sigue siendo un gran desconocido en cuanto a su composición. Sólo el 5% de la energía del Universo puede describirse dentro del modelo estándar de partículas y el resto, cerca del 95%, no parece estar compuesto por ninguna partícula conocida y solo se lo conoce por sus efectos gravitatorios; tanto a pequeña escala (e.g. galaxias), como a gran escala (e.g. expansión del Universo).

Del 5%, la mayoría se corresponde con materia bariónica y sólo cerca del 0.01% lo forman partículas moviéndose a velocidades relativistas (fotones y neutrinos), que llamamos radiación. Del 95% restante, al igual, podemos distinguir dos componentes diferentes: una atractiva, que llamamos materia oscura (DM), que sigue la distribución de materia del Universo, y otra repulsiva, que recibe el nombre de energía oscura (DE) y que llena todo el espacio-tiempo homogéneamente (o eso creemos a día de hoy). Su proporción es también desigual. Mientras que sólo cerca del 25% de la energía corresponde a la materia oscura, el 70% se debe a la energía oscura.

Los nombres no son casuales. La materia oscura se llama así por tener una dinámica igual que la materia conocida, excepto por no interactuar, que se conozca, más que gravitatoriamente. Se cree que está compuesta de partículas ligeras, que solo interaccionan débilmente y que se mueven a bajas velocidades. De ahí que normalmente se la llame materia oscura fría (CDM). En cambio, la energía oscura es una completa desconocida. Solo se sabe de ella que produce la expansión acelerada del espacio-tiempo y se cree que la produce una especie de energía del vacío, cuya densidad ha permanecido constante durante toda la historia del Universo. A este nuevo componente se lo conoce como Constante Cosmológica (Λ).

La unión de todos estos componentes, junto con la Relatividad General, simetría a gran escala (homogeneidad e isotropía) y ciertas condiciones iniciales (adiabáticas y espectro invariante de escala), forman el Modelo Cosmológico Estándar, ΛCDM. Este modelo ha demostrado ser el que mejor describe nuestro Universo, según las observaciones más recientes que tenemos. No obstante, algunas de ellas parecen estar apuntando en otra dirección.

Las estimaciones del ritmo actual de expansión del Universo, H_0, obtenidas con supernovas de tipo Ia (SNe Ia) por el equipo de Riess et al, calibrando sus distancias con la "escalera de distancias", parecen superar por 4.4σ el valor dado por mediciones del Fondo Cósmico de Microondas (CMB) y de las Oscilaciones Acústicas de Bariones (BAO). Además, las mediciones de la distribución de materia usando el efecto de lente débil de la misión KiDS-450, dan valores 3.2σ más bajos del parámetro S_8, que mide la granularidad de la materia en el Universo. No obstante, estas tensiones están siendo estudiadas en la actualidad y tienen sus detractores. Métodos alternativos que emplean la punta de la rama de las gigantes rojas (TRGB) reducen el valor de H_0 y son compatibles con los de Planck y Riess et al. Igualmente, otras misiones que han utilizado el efecto de lente débil para estimar la distribución de materia del Universo, como DES, dan valores de S_8 compatibles con Planck.

En cualquier caso, la existencia o no de tensiones entre el Modelo Cosmológico Estándar y las observaciones del Universo se verá clara con la nueva generación de misiones cosmológicas. Éstas, que incluyen LSST, DESI, WFIRST, Euclid, SKA, etc. van a alcanzar una precisión nunca antes obtenida en los parámetros cosmológicos ($\sim 1\%$), gracias tanto a la mejora de los equipos como al tamaño de las muestras. Serán capaces de observar la distribución de galaxias, el efecto de lente débil y SNe Ia, llegando incluso hasta redshift $z \gtrsim 6$ (con LSST) en el caso de galaxias y $z \sim 1.7$ en el caso de SNe Ia (con WFIRST). En el caso de que las discrepancias entre modelo y observaciones sean reales, éstas serán evidentes con los nuevos datos. Entonces, habrá que buscar un modelo alternativo capaz de reproducir la historia del Universo. Pero no sólo será necesaria esta investigación si el Modelo Cosmológico Estándar deja de describir lo que vemos. En caso contrario, será necesario dar respuesta a una serie de problemas fundamentales que tiene en su seno.

Estos problemas son: el problema de la coincidencia y el de la constante cosmológica. El primero tiene que ver con la necesidad de ajustar con precisión las condiciones iniciales del Universo para dar lugar al Universo que vemos. En otras palabras, para el Modelo Cosmológico Estándar, nuestra realidad es muy improbable. El segundo problema tiene que ver con dar una explicación al origen de la energía oscura. Si es una constante cosmológica se esperaría que fuera producida por la energía del vacío del Universo. En cambio, el valor de Λ y el de la energía del vacío divergen 120 órdenes de magnitud. Es necesario entender esta diferencia.

Algunas soluciones pasan por aplicar el principio antrópico, que se ocuparía del problema de la coincidencia, o tratar de describir ΛCDM como una teoría efectiva a baja energía, que pueda explicar por qué la densidad de energía de la Constante Cosmológica es tan pequeña. A esto se le llama *degravitation*. No obstante, explorar modelos alternativos que puedan reproducir igual o mejor que ΛCDM las observaciones es necesario. No sólo para ver si se ajustan mejor a la realidad, sino también para encontrar una teoría más fundamentada en primeros principios.

De esta manera, esta tesis explora extensiones de ΛCDM, en el contexto de la energía oscura y la Gravedad Modificada. El primer capítulo que presentamos en la parte III, Capítulo 6, muestra un modelo de energía oscura que enlaza el proceso de inflación, el cual sería el responsable de la rápida y acelerada expansión del Universo en sus primeros instantes de vida, y el de expansión acelerada de la época actual. La conexión la realiza un campo escalar, que habría sobrevivido a la inflación y cuya densidad de energía vuelve a ser hoy no despreciable. De esta forma, la energía oscura estaría formada por este campo.

La dinámica del campo escalar está definida por su potencial de energía, que se englobaría dentro de la clase de modelos de inflación α-attractors. Éstos están favorecidos por las observaciones del CMB de Planck, por sus predicciones del ratio tensor-escalar, r, e índice espectral, n_s. Además, tienen relación con teorías más fundamentales de altas energías.

Después de estudiar su fenomenología como modelo de energía oscura, comparamos sus predicciones con los datos actuales de CMB (Planck 2015), BAO (BOSS DR12) y SNe Ia (Pantheon) y vemos que el modelo es capaz de reproducirlos. Esto se debe a que la energía oscura de α-attractors tiene una región (infinita) del espacio de parámetros en que se recupera (o se está muy cerca de) una constante cosmológica. Además, estudiamos si sería posible distinguir este modelo de ΛCDM con los datos de las misiones futuras. El resultado es que, dependiendo de la región del potencial en que se ubique el campo inicialmente, un análisis conjunto de S4CMB, LSST y SNe Ia de WFIRST podría detectar una desviación respecto a ΛCDM de 3σ.

No obstante, el alcance de este estudio es limitado. Hay tantos modelos cosmológicos propuestos, que adoptar un nuevo modelo cosmológico estándar pasaría por probar un gran número de ellos, si no todos. Esto es inviable, especialmente teniendo en cuenta el volumen de datos que tendremos la próxima década. Para evitar este problema, es usual parametrizar las funciones básicas que definen los modelos (e.g. la ecuación de estado, w) y encontrar los valores de los

parámetros compatibles con las observaciones. De esta forma, se logra reconstruir la evolución temporal que mejor describe las observaciones actuales.

Esta aproximación tiene un problema y es que estas funciones se encuentran fácilmente desde la definición del Lagrangiano, pero éste no se recupera trivialmente desde las funciones. Esto se debe a la degeneración en el espacio de parámetros de las teorías y, entre diferentes teorías, en la fenomenología. Como consecuencia, es probable que los datos apunten a funciones básicas que no están relacionadas con un Lagrangiano físico; es decir, con una teoría de altas energías bien establecida.

La solución que proponemos en esta Tesis (Capítulo 7) es encontrar el espacio de parámetros de la parametrización que da lugar a evoluciones estables y observacionalmente diferentes. En el Capítulo 7 hemos estudiado la clase de modelos de quintaesencia llamada *thawing* y encontrado las distribuciones de probabilidad (PDF) asociadas a diferentes clases de modelos. Hemos visto que los parámetros necesarios para describir los observables hasta recombinación son los usuales w_0 y w_a. Imponiendo las PDF's a las cotas observacionales comprobamos que una gran parte queda excluida. Es decir, nos permite centrarnos en la región que proviene de una teoría fundamental.

Éste es un primer paso para hacer lo mismo con modelos más generales y, en última instancia, con Horndeski. El objetivo de generalizar a Horndeski es que es la teoría más general, con un campo escalar, métrica, localidad e invarianza Lorentz que da lugar a ecuaciones de segundo orden del movimiento (requisito suficiente para evitar la inestabilidad de Ostrogradsky). Es decir, incluye muchas de las teorías más conocidas y estudiadas: quintaesencia, $f(R)$, galileons, Brans-Dicke, etc.

No obstante, no sólo es importante tener una buena descripción teórica de los modelos de energía oscura o Gravedad Modificada que se quieren probar. Para poner cotas a los parámetros cosmológicos, es crucial tener una estimación correcta de la *likelihood* de las observaciones; es decir, de la probabilidad de haber obtenido las mediciones hechas, dado un conjunto de parámetros cosmológicos.

Ésto no es trivial. En el Capítulo 8 tratamos el caso de observaciones de la Estructura a Gran Escala (LSS, del inglés) del Universo. En este caso, la *likelihood* recibe tres contribuciones: una gausiana, de las escalas no causalmente conectadas; otra no gausiana, de las escalas causalmente conectadas; y otra llamada Super Sample Covariance (SSC), que induce correlaciones entre diferentes escalas, por las perturbaciones de densidad a escalas mayores que la escala del volumen observado. Nosotros nos centramos en la parte gausiana, que es la contribución principal a la *likelihood*. Ésta se puede obtener exactamente de manera analítica. No obstante, este cómputo escala con la escala angular mínima accesible, $\ell_{\rm max}$, como $O(\ell_{\rm max}^6)$, lo que lo hace inviable para las observaciones futuras, que llegarán a resolver escalas muy pequeñas ($\ell_{\rm max} \gg 1$). Nuestra solución es la *Narrow Kernel Approximation* (NKA), que escala como $O(\ell_{\rm max}^3)$. La NKA reproduce la matriz de covarianza con gran precisión (menos para el modo-B del campo de *shear* del efecto de lente débil) y permite recuperar con exactitud la distribución de probabilidad de los parámetros cosmológicos.

Por su utilidad, implementamos la NKA en `NaMaster`, un código desarrollado por la Colaboración Científica para la energía oscura (DESC) de LSST para trabajar con las observaciones de LSS, y ha sido ya utilizada por la colaboración. Nosotros estamos utilizando la NKA en nuestro estudio de la tensión en el parámetro S_8, recogido en el Capítulo 9. En él presentamos cómo reconstruimos la evolución temporal del parámetro S_8 con observaciones del CMB de Planck y de la distribución de galaxias y del efecto de lente débil de DES y, en el futuro, de KiDS. Mostramos el modelo cosmológico teórico que hemos utilizado para estimar la parte Gaussiana de la *likelihood* con la NKA, que utilizaomos para obtener la evolución de $S_8(z)$ compatible con las observaciones. Para explorar evoluciones diferentes a las de ΛCDM, estudiamos los resul-

tados de ΛCDM y de un modelo con el ratio de crecimiento de las perturbaciones modificado linealmente, encontrando que ambas evoluciones de $S_8(z)$ son compatibles. Una vez incluyamos las partes no gausianas de la *likelihood*, repetiremos el análisis y añadiremos los datos de KiDS. De la comparación de los resultados con DES y KiDS, esperamos poder entender el origen (y evolución) de la tensión en el parámetro S_8.

En resumen, en esta tesis hemos tratado uno de los problemas fundamentales de la Cosmología Moderna: el origen de la energía oscura. Esto lo hemos hecho desde diferentes puntos de vista. Por un lado, hemos tratado modelos y parametrizaciones convenientes para usar con los datos futuros. Por otro, hemos desarrollado una aproximación de la *likelihood* de LSS, igualmente necesaria en los estudios de la compatibilidad observacional de los modelos de energía oscura, tanto para los datos actuales como futuros de LSS. En particular, nosotros la estamos utilizando en nuestro estudio de la tensión en S_8.

El modelo de energía oscura estudiado es la energía oscura de los α-attractors, compatible con las observaciones actuales e inspirado en los modelos de mismo nombre de Inflación. Este modelo relacionaría Inflación y energía oscura y podría ser distinguido del Modelo Cosmológico Estándar con las observaciones futuras. Además, dado el volumen de datos que habrá la próxima década y su precisión, hemos propuesto un método para validar grandes clases de modelos de una forma eficaz. Para ello, hemos mostrado, pormenorizadamente, el caso de modelos de quintaesencia de tipo *thawing*, donde la parametrización usual, w_0-w_a, permite reproducir los observables hasta recombinación (si se eligen inteligentemente). Con asunciones mínimas, hemos construido su distribución de probabilidad y mostrado su poder al aplicarla a las cotas observacionales. De esta forma, gran parte del espacio de parámetros queda excluido, centrándonos en la región de interés fundamental.

Con la misma idea de aprovechar al máximo los datos futuros, hemos trabajado en uno de los grandes retos: la correcta estimación de la *likelihood* para poder obtener cotas fiables sobre los parámetros cosmológicos. En este terreno, para observaciones de LSS, hemos desarrollado e implementado la NKA, que permite reducir el coste computacional de la estimación de la contribución principal de $O(\ell_{\rm max}^6)$ (inviable dadas las escalas a las que accederán las próximas misiones) a $O(\ell_{\rm max}^3)$, sin afectar a las cotas en los parámetros cosmológicos. Como consecuencia, el DESC de LSST ha empezado a utilizarla y a nosotros nos está permitiendo estudiar la evolución del crecimiento de estructura, parametrizada con $S_8(z)$. Con ello pretendemos entender el origen de la tensión advertida por KiDS en el parámetro S_8, cuando su valor es obtenido con observaciones locales (con el efecto de lente débil) o lejanas (con el CMB).

Para finalizar, es importante recordar la necesidad de explorar modelos alternativos de gravedad y energía oscura. Por un lado, parece que los datos actuales quieren indicar que las predicciones del Modelo Cosmológico Estándar a tiempos tempranos (CMB) y tardíos (LSS y SNe Ia) están en tensión. Aunque es pronto para saberlo, esto podría ser el anticipo de lo que los futuros datos traerán consigo. No obstante, también podría pasar que, una vez más, el modelo ΛCDM saliera victorioso. Incluso en este caso, la necesidad de explorar más allá sigue estando ahí para entender cómo el Modelo Cosmológico Estándar, que padece de una serie de problemas fundamentales, es capaz de describir tan bien nuestro Universo.

Es con este objetivo de intentar dar luz a estos interrogantes, que el trabajo recogido en esta tesis, aquí se presenta.

Part I

Introduction

Chapter 1

Introduction

This thesis is focused on one of the main topics of Modern Cosmology: dark energy. In this work, dark energy has been studied from a wide variety points of view, ranging from observational tests of particular dark energy models, to general frameworks to study large classes of models with future and current data in an efficient way. It also gets closer to data and develops and implements accurate approximations of the Large Scale Structure (LSS) likelihood, that will allow us to study the S_8 tension [14].

Few years ago, Cosmology entered the precision era thanks to WMAP [15] (and Planck [16]) measurements of the Cosmic Microwave Background (CMB). However, this will be superseded by the next generation of surveys that will bring unprecedented precise data during the next decade. They will collect a huge amount of information of many cosmological observables, such as galaxy clustering or supernovae (SNe), that will allow to reduce the uncertainty on the cosmological parameters to the order of 1% [17–19].

The Standard Cosmological Model, ΛCDM, has been proved to be extremely successful on explaining our observations of the Universe. However, recent studies have shown increasing tensions between parameters estimated using Cosmic Microwave Background (CMB) measurements of Planck, which assume as fiducial cosmology ΛCDM, and local Universe observations. In particular, the Kilo Degree Survey (KiDS-450) collaboration have shown a 3.2σ discrepancy on the S_8 parameter [14], related to the granularity of matter in the Universe; while Riess et al., using distance-ladder calibrated SNe Ia, have reported a 4.4σ higher value of the current value of the Hubble parameter, H_0 [20]. Nevertheless, these tensions are being currently studied and discussed (e.g. Refs. [21–24] or see Section 3.3.1) and could just be statistical fluctuations or the result of underestimated systematics. For instance, alternative measurements of H_0 using stars of the Tip of the Red Giant Branch (TRGB) give results compatible with both Planck and Riess et al. [23]. Furthermore, in the S_8 case, the Dark Energy Survey reported no tension on S_8 using independent measurements of galaxy clustering and tomographic weak lensing [21, 22]. In any case, their discrepancy or agreement will be clear with next-generation data.

In this context of possible tensions between ΛCDM and observations the study of alternative cosmological models might be more compelling. However, one must bear in mind that, even if ΛCDM perfectly agreed with data, one would have to give answer to two fundamental problems: the coincidence problem and the size of the cosmological constant. The first is related to the fact that our existence is unlikely; i.e. unnatural, in the ΛCDM model. This is unappealing. The second problem comes from the discrepancy between our theoretical expectation of the size of the cosmological constant: observations point to a value 120 orders of magnitude lower than that theoretically expected one. Possible solutions invoke the so-called anthropic principle [25] or *degravitation* theories, in which ΛCDM is an effective low energy theory of some more fundamental higher energy theory (e.g. [26, 27]). In this context, the study of alternative

models of dark energy or Gravity could also be found helpful, shedding some light to these fundamental problems of ΛCDM. Nevertheless, independently of ΛCDM, it is always possible that other models different from the Standard Cosmological Model could better fit current or future observations.

In the following Sections we will briefly review the outline of this Thesis (Section 1.1) as well as the objectives and methodology (Section 1.2) followed. As it will be seen, Modern Cosmology is a multidisciplinary science where observations, phenomenology and theory must be used together in order to unravel one of the still mysterious components of the Universe: dark energy.

1.1 Outline

Part II will cover the basics of Modern Cosmology that will be later used in Part III. Chapter 2 (main Refs. [6–10]) will briefly review the theory behind the Standard Cosmological Model and its main equations. Chapter 3 (main Refs. [6, 7, 9, 10]) will show the current status of cosmological observations and how they are done and used. Finally, Chapter 4 (main Refs. [11–13, 28]) will first show the Laboratory and Solar System constraints that any theory of Gravity must satisfy. Then, it will focus on one of the most general cases, the Horndeski theory [29]. This includes many well known scalar field models and, in particular, quintesssence that will be studied more in detail in Part III. Finally, we include a brief summary of some of the most important next-generation surveys and their prospects in Chapter 5.

Part III is the core of the thesis where the actual original work and results are shown. It covers three different Sections devoted to different published articles [1–4] (Chapters 6 - 8) and an ongoing unpublished project on the S_8 tension [5] (Chapter 9). Chapter 6 studies the phenomenology and the observational constraints of the α-attractors dark energy model [1]. Furthermore, it shows the expected constraints with next-generation surveys, which could distinguish it from ΛCDM [2]. Chapter 7 can be thought as a generalization of previous Chapter 6. Using thawing quintessence as example, Chapter 7 shows an efficient and accurate framework to be used with next-generation data to test large classes of models. Using the common w_0-w_a parametrization it is possible to build theoretical priors that can be used to reduce the observational constraints to the theoretically motivated area [4]. Chapter 8 develops an accurate approximation of the Gaussian (not causally connected) part of the LSS likelihood that is able to reduce the computational expense from $O(\ell^6_{\rm max})$ (inviable with next-generation data) to $O(\ell^3_{\rm max})$, making it possible to use future data in cosmological studies [3]. Finally, in Chapter 9, we analyze the evolution of structure growth with Planck and DES observations, and explore a general modification of ΛCDM.

We will conclude in Part IV.

1.2 Objectives and methodology

This thesis had two goals:

- Primary: The study of alternative cosmological models, including its phenomenology and observational viability.
- Secondary: The study of relevant cosmological probes such as SNe Ia, BAO, CMB, etc.

We have worked on these broad objectives, having four published articles and an ongoing project on these subjects that will be reviewed throughout this Thesis. Chapters 6 and 7 are focused on alternative cosmological models. In particular, Chapter 6 thoroughly review the phenomenology

of the α-attractors dark energy model and test its observational viability and the tightness of the future constraints with next-generation data. On the other hand, Chapter 7 has a more general approach and develops a framework to classify wide classes of models and make the study of their observational constraints straightforward. Chapter 8 is focused on LSS observations and presents a accurate approximation of their likelihood to be used with current and future data (secondary goal). Finally, Chapter 9, presents our ongoing study of the S_8 tension, that includes data from DES and KiDS. This study could shed light on the origin of this tension, which could strengthen the argument in favor of alternative cosmological models and better understand the phenomenological requirements of alternative models.

The different projects have required different approaches and methodologies, which are explained in their corresponding Chapters. Nevertheless, we can extract some common features. These are:

- Phenomenology. Given a set of cosmological parameters and initial conditions we integrate the cosmological equations and find the evolution of different parameters of interest. These can be observables like the luminous distance, $D_{\rm L}$, or the power spectra of the matter linear perturbations. The main three programs used for this are:
  - the Boltzmann-code `Cosmic Linear Anisotropy Solving System` (`CLASS`)[1] [30] and its generalization to Horndeski [29], the `Horndeski in the Cosmic Linear Anisotropy Solving System` (`hi_class`)[2] [31, 32]. These are codes that solve the cosmological equations and can compute the cosmology up to linear perturbation level given a set of parameters.
  - the `Core Cosmology Library` (`CCL`)[3] [33]. It is a standardized library to compute different observables important for cosmology. It has been developed by the Large Synoptic Survey Telescope (LSST) Dark Energy Science Collaboration (DESC) [17, 34] and will be the standard analysis package used by LSST.
  - `NaMaster`[4] [35]. A LSST DESC code to work with the pseudo-C_ℓ formalism (see e.g. Ref. [35].
- Sampling. In order to study the statistical properties of the cosmological models, their observational constraints or the goodness of our approximation of the LSS likelihood, we need to run many simulations varying the cosmological parameters and/or their initial conditions. This is done in a Markov Chain Monte Carlo (MCMC) with `MontePython`[5] [36, 37] (an MCMC sampler specially developed to interface with `CLASS/hi_class` and easily generalizable to `CCL`). The two sampling algorithms that we have used are the Metropolis-Hasting [38, 39] and Goodman-Weare [40] affine invariant sampler algorithms.
- Cosmological parameters constraints. We study the theoretical and observational viability of the parameter space through Bayesian inference, introducing the appropriate likelihood and prior distributions in the MCMC sampling algorithm.
- Forecast. Apart from the current observational constraints, we have used the Fisher formalism to predict how these will tighten with future surveys. We have used and modified `GoFish`[6]. This code is specially useful for predictions for S4CMB and photometric LSS

[1] `https://github.com/lesgourg/class_public`

[2] `https://github.com/miguelzuma/hi_class_public`

[3] `https://github.com/LSSTDESC/CCL`

[4] `https://github.com/LSSTDESC/NaMaster`

[5] `https://github.com/brinckmann/montepython_public`

[6] `https://gitlab.com/carlosggarcia/GoFish_aatt-forecast/tree/aatt`, a modified version of `https://github.com/damonge/GoFish` (the master branch of the former repository)

surveys, such as LSST, as it can take into account the power spectra auto- and cross-correlations between different redshift bins and surveys.

- Software development. All projects have involved a substantial amount of coding. We have implemented new models in `hi_class` and `GoFish` and new likelihoods in `MontePython` and `NaMaster`. Furthermore, we have contributed to these programs by fixing bugs. For instance, we fixed the CosmoHammer [41, 42] (Goodman-Weare sampler) implementation in `MontePython` and memory leakages on `MontePython` and `hi_class`. My software repositories are `https://github.com/carlosggarcia` and `https://gitlab.com/carlosggarcia`.

Part II

Foundations

Chapter 2

The Standard Cosmological Model

The Standard Cosmological Model, ΛCDM, is the most successful theory that describes the evolution of our Universe and reproduces current cosmological observations. It describes an Universe that started in an infinitesimal portion of space-time from quantum fluctuations, that grew exponentially, evolved from a hot bath of particles and cooled down to form the first atoms, being nowadays (almost perfectly) homogeneous and isotropic at large scales. The ingredients of this universe are of four kinds: radiation (photons and neutrinos), baryonic matter, cold dark mater (CDM) and dark energy (DE). Therefore, the ΛCDM model, although is able to address correctly current observations, introduces two unknown fluids: cold dark matter and dark energy. Cold dark matter is supposed to be formed of weakly interacting particles and can only be detected by its gravitational effects, equivalent to those of regular matter. Dark energy, instead, has antigravitational properties, which produce the accelerated expansion of the Universe when dominates. These two fluids constitute the 95.1% of the energy content of the universe [43], leaving just the 4.9% to those components we actually know: baryonic matter (4.9%) and radiation (10^{-2}%) [44].

By the time inflation ended, the Universe had expanded, typically, around $50 \lesssim N \lesssim 60$ e-folds; i.e. e^N times, erasing (almost) any existing anisotropy[1]. At that time, the Universe ended up filled by fast moving particles with such a high temperature that not even atoms could form: it was a "soup" of (mainly) hot photons, electrons and protons, colliding one with another. As time passed and the Universe continued slowly expanding, the temperature dropped. When it dropped enough that photons could not break hydrogen atoms, electrons and protons bounded together and photons started traveling freely. While the hydrogen atoms sourced the formation of cosmological structures, allowing for the formation of galaxies and stars; the photons continued traveling, loosing energy as the Universe expanded. These photons reached us and fill the Universe in an almost perfectly homogeneous way. They constitute what we call the Cosmic Microwave Background (CMB) and provides us with the earliest image of the Universe we have so far.

This early epoch of radiation domination gave way to the next cosmological stage: the matter domination era. Free of the pressure that radiation exerted, matter gravitational attraction pushed the accretion of matter, giving birth to the first stars and galaxies. It is now, in the present, when a new era has come to start. This epoch is characterized by the accelerated expansion of the Universe and, if ΛCDM is true, it will be the last cosmological era. Dark energy, that is now as important as the matter content, will end up overcoming it. As a consequence, in the future, matter, as radiation now, will negligibly contribute to the total energy of the Universe and the observable universe will shrink as galaxy groups are put apart

[1]Fortunately, this process was not perfect and some anisotropies remained, allowing for matter accretion at much later times, seeding the first stars and galaxies.

from each other.

In the following Sections, we will briefly review the mathematical formulation of modern cosmology and present the most relevant equations for this Thesis. In particular, we will review the background evolution in Section 2.1. In Section 2.1.1 we will summarize the main equations and findings on linear perturbation evolution as well as discuss some particular cases as the definition of power spectrum and weak lensing. Next, in Section 2.2, the basics of inflationary theory will be shown. We will conclude this Chapter by enumerating the fundamental and observational challenges of ΛCDM today in Section 2.3.

2.1 General relativity and Cosmology

Based on observations of CMB [15, 43, 45–48] and Large Scale Structure (e.g. Ref. [49]), i.e. local measurements of galaxies distribution and shapes, we know that the Universe is homogeneous and isotropic at large scales. Mathematically, the geometry of such space is described by the Friedman-Lemaître-Robertson-Walker (FLRW) metric ($g_{\mu\nu}$),

$$\mathrm{d}s^2 = g_{\mu\nu}\mathrm{d}x^\mu \mathrm{d}x^\nu = -\mathrm{d}t^2 + a(t)^2\left(\frac{\mathrm{d}r^2}{1-kr^2} + r^2\mathrm{d}\theta^2 + r^2\sin^2\theta\,\mathrm{d}\phi^2\right). \tag{2.1}$$

Here, t is the proper time, a the scale factor, k the curvature of the Universe and r, θ and ϕ, the usual spherical coordinates. From the CMB and Baryon Acoustic Oscillations (BAO) joint analysis, we know the curvature of our Universe is compatible with a flat universe ($\Omega_k = -kc^2/H_0^2 = 0.001 \pm 0.002$) [43] and, therefore, we will restrict ourselves to the particular case with $k = 0$. Here, H_0 is the value of the Hubble parameter,

$$H \equiv \frac{\dot{a}}{a}, \tag{2.2}$$

today and c, the speed of light. In the previous expression, $\dot{a} \equiv \mathrm{d}a/\mathrm{d}t$. It is sometimes convenient to factorize the scale factor in Eq. 2.1. In that case, one would define the conformal time, τ, so that $\mathrm{d}\tau \equiv \mathrm{d}t/a$.

We can derive the Einstein equations from a variational principle varying the Einstein-Hilbert action,

$$S_{\mathrm{EH}} = \int \mathrm{d}^4x\sqrt{-g}\frac{R}{16\pi G} + S_{\mathrm{m}}[g_{\mu\nu}], \tag{2.3}$$

where g represents the determinant of the metric tensor $g_{\mu\nu}$, G the gravitational constant, R the Ricci scalar and S_{m} the material content action, minimally coupled to gravity through the metric $g_{\mu\nu}$. In what follows, we will work in natural units ($c = 1$, $\hbar = 1$, $M_{\mathrm{P}}^2 = \hbar c/8\pi G = 1$). Varying the action with respect to the metric, one reaches the Einstein equations:

$$G_{\mu\nu} \equiv R_{\mu\nu} - \frac{1}{2}g_{\mu\nu}R = 8\pi G T_{\mu\nu}, \tag{2.4}$$

with $G_{\mu\nu}$ the Einstein tensor, $R_{\mu\nu}$ the Ricci tensor and $T_{\mu\nu} \equiv -2\delta S_{\mathrm{m}}/\delta g_{\mu\nu}$ the energy-momentum tensor, which, for perfect isotropic and homogeneous fluids, is diagonal and given by $T_{\mu\mu} = (-\rho(t),\, p(t),\, p(t),\, p(t))$. In this idealized case, the pressure, p, is related to the energy density, ρ, by the equation of state: $p = w\rho$. The energy-momentum tensor is conserved; i.e.

$$\nabla_\mu T^{\mu\nu} = 0 \rightarrow \rho_{,t} + 3H\rho(1+w) = 0. \tag{2.5}$$

Here, ∇_μ is the covariant derivative and we have defined $\rho_{,t} \equiv \partial\rho/\partial t$. Taking into account that matter has $w = 0$ and radiation $w = 1/3$,

$$\rho_{\mathrm{m}} \propto a^{-3} \qquad \text{and} \qquad \rho_{\mathrm{r}} \propto a^{-4}, \tag{2.6}$$

respectively.

Using Equation 2.4, we can deduce the Friedmann equations. The 00 component yields the first Friedmann equation,

$$H^2 = \sum_i \frac{\rho_i}{3} \qquad \text{or, equivalently,} \qquad 1 = \sum_i \Omega_i \equiv \sum_i \frac{\rho_i}{3H^2} \tag{2.7}$$

where we have introduced the density parameter $\Omega_i \equiv \rho_i/3H^2$ for convenience. From the ii components we obtain the second Friedmann equation,

$$\frac{\ddot{a}}{a} = -\frac{1}{3}(\rho + 3p)\,. \tag{2.8}$$

From this equation, an obvious solution to the accelerated expansion of the Universe is the existence of an additional fluid with $w < -1/3$. The best candidate at this moment is the cosmological constant, Λ, whose equation of state is $w = -1$. Its addition modifies the Einstein-Hilbert action (Equation 2.3) to

$$S_{\text{EH}+\Lambda} = \int \mathrm{d}^4x\sqrt{-g}\frac{1}{2}(R - 2\Lambda) + S_{\text{m}}[g_{\mu\nu}]\,, \tag{2.9}$$

and the Einstein equations,

$$G_{\mu\nu} \equiv R_{\mu\nu} - \frac{1}{2}g_{\mu\nu}R + g_{\mu\nu}\Lambda = 8\pi G T_{\mu\nu}\,. \tag{2.10}$$

Of course, it could have been also added to S_{m}.

An important concept that will be used along this Thesis is that of *redshift*, z. As a consequence of the expanding universe, all light emitted is affected by a frequency shift,

$$1 + z = \frac{\lambda_0}{\lambda_i} = \frac{a_0}{a_i}\,, \tag{2.11}$$

where λ is the wavelength, and 0 and i stand for today and initial, respectively. If, as customary, we take $a_0 = 1$, the redshift is related to the scale factor by $1 + z = 1/a$, being equivalent to talk about *redshift* and scale factor.

Furthermore, redshift is also equivalent to distance and time. For a photon, the comoving distance, χ, that travels since emission is given by

$$\int_{r(a)}^{r_0} \frac{\mathrm{d}r'}{\sqrt{1 - kr'^2}} \equiv \chi = \int_{t(a)}^{t_0} \frac{\mathrm{d}t'}{a(t')} = \int_a^1 \frac{\mathrm{d}a'}{a'^2 H(a')}\,, \tag{2.12}$$

where we used the fact that photons travel along null geodesics ($\mathrm{d}s^2 = 0$). In this case ($k = 0$), $\chi = r$, but, in general, $\mathrm{d}\chi = \mathrm{d}r/\sqrt{1 - kr^2}$. We keep this notation for generality. This quantity is related with measurable cosmological distances. In particular, the angular diameter distance, i.e. the distance computed from the subtended angle, Θ, of a source of known length, l, can be measured (along with H) in Type Ia supernovae (SNe Ia) and BAO observations and is given by

$$D_{\text{A}} \simeq \frac{l}{\Theta} = \frac{\chi}{1 + z}\,, \tag{2.13}$$

assuming that the subtended angle (Θ) is small. Alternatively, one can use the emitted and received light from an object, whose flux scales with distance as d^{-2}. This distance is called luminosity distance and is given by

$$D_{\text{L}} = (1 + z)\chi = (1 + z)^2 D_{\text{A}}\,. \tag{2.14}$$

This expression is obtained taking into account that the observed flux in an expanding universe is related to the source luminosity, L, by $F = La^2/4\pi\chi^2$, accounting for the fact that flux is reduced by the photon energy loss and the decrease of the reception rate by a factor a, respectively.

We have presented here the most relevant equations for this Thesis at background level; i.e. the perfectly homogeneous and isotropic case. In the following subsections, we will address the fact that the Universe is not perfectly smooth but has some anisotropies. We will study how these small perturbations around the homogeneous case grew.

2.1.1 Perturbations

We have shown the main expressions that govern the background cosmology, i.e. the perfectly homogeneous and isotropic approximation. There are, however, inhomogeneities at smaller scales that we need to take into account to extract the most from the CMB and Large Scale Structure (LSS) observations. Important quantities in these cases are the power spectra or the 2-point correlation function of different quantities such as the temperature fluctuations and photon's polarization in the CMB and the galaxy overdensity and shear modes for LSS. In this Section we will review the theoretical predictions for those quantities in the framework of ΛCDM, which can be then compared with the observations.

We will follow Ref. [9] in this analysis. First, we will start perturbing the FLRW metric (Equation 2.1). In the Newtonian gauge, it is given by

$$\mathrm{d}s^2 = -(1+2\Psi)\mathrm{d}t^2 + (1+2\Phi)a(t)^2\delta_{ij}\mathrm{d}x^i\mathrm{d}x^j\,. \tag{2.15}$$

This gauge is also known as the longitudinal or shear-free guage, as the only metric perturbation left are diagonal. In general, however, the perturbed metric also contains vector and tensor perturbations.

As we saw, the Einstein equations relate the Universe geometry and the matter content. Now, introducing the first order perturbations of the Einstein and energy-momentum tensors, $G_{\mu\nu} = G^{(0)}_{\mu\nu} + \delta G_{\mu\nu}$ and $T_{\mu\nu} = T^{(0)}_{\mu\nu} + \delta T_{\mu\nu}$, respectively, the Einstein equations become

$$G^{(0)}_{\mu\nu} = T^{(0)}_{\mu\nu}\,, \qquad G_{\mu\nu} = \delta T_{\mu\nu}\,, \tag{2.16}$$

which give the evolution equations at background and first perturbation level, respectively. The former was already studied in the previous Section (Equation 2.4).

Assuming that the approximation of perfect fluids remains valid at this level[2]

$$\delta T_{\mu\nu} = \rho[\delta(1+c_\mathrm{s}^2)u_\nu u^\mu + (1+w)(\delta u_\nu u^\mu + u_\nu \delta u^\mu) + c_\mathrm{s}^2\delta\delta^\mu_\nu]\,. \tag{2.18}$$

where $\delta = \delta\rho/\rho \equiv (\rho(\mathbf{x}) - \bar{\rho})/\bar{\rho}$ is the density contrast (with $\bar{\rho}$ the density mean value), u_ν is the four-velocity and the sound speed,

$$c_\mathrm{s}^2 = \frac{\delta p}{\delta\rho}\,. \tag{2.19}$$

[2]The general energy-momentum tensor of a fluid is given by

$$T_{\mu\nu} = (\rho + p)u_\mu u_\nu + p g_{\mu\nu} + [q_\mu u\nu + q_\nu u_\mu + \pi_{\mu\nu}]\,, \tag{2.17}$$

where u_ν is the field four-velocity and q_μ and $\pi_{\mu\nu}$ are the heat flux vector and the viscous shear tensor, respectively. These two, q_μ and $\pi_{\mu\nu}$, are zero for perfect fluids.

If we computed the perturbed Einstein tensor, we would see that the Einstein equations for the **single fluid** case are given by

$$3\mathcal{H}(\mathcal{H}\Psi - \Phi') + \nabla^2\Phi = -a^2\delta\rho/2\,, \tag{2.20}$$
$$\nabla^2(\Phi' - \mathcal{H}\Psi) = a^2(1+w)\rho\theta\,, \tag{2.21}$$
$$\Psi = -\Phi\,, \tag{2.22}$$
$$\Phi'' + 2\mathcal{H}\Phi' - \mathcal{H}\Psi' - (\mathcal{H}^2 + 2\mathcal{H}')\Psi = -a^2c_{\rm s}^2\delta\rho/2\,, \tag{2.23}$$

where $\mathcal{H} \equiv aH$, $\theta \equiv \nabla_i v^i$ is the velocity divergence and the primes are derivatives of conformal time, τ.

Furthermore, the covariant divergence of the energy-momentum tensor yields the continuity and Euler equations,

$$\delta' + 3\mathcal{H}(c_{\rm s}^2 - w)\delta = -(1+w)(\theta + 3\Phi')\,, \tag{2.24}$$
$$\theta' + \left[\mathcal{H}(1-3w) + \frac{w'}{1+w}\right]\theta = -\nabla^2\left(\frac{c_{\rm s}^2}{1+w}\delta + \Psi\right)\,, \tag{2.25}$$

which for non-relativistic matter; i.e. for matter after recombination, become

$$\delta' = -\theta - 3\Phi'\,, \tag{2.26}$$
$$\theta' + \mathcal{H}\theta = -\nabla^2(c_{\rm s}^2\delta + \Psi)\,. \tag{2.27}$$

The continuity equation shows that matter perturbations will grow at points where there is an accretion of matter (matter flows towards that point). The Euler equation shows that the peculiar acceleration depends on the gradient of the potential and pressure.

Their Fourier transformed counterparts are

$$k^2\Phi + 3\mathcal{H}(\Phi' - \mathcal{H}\Psi) = a^2\rho\delta/2\,, \tag{2.28}$$
$$k^2(\Phi' - \mathcal{H}\Psi) = a^2(1+w)\rho\theta/2\,, \tag{2.29}$$
$$\Psi = -\Phi\,, \tag{2.30}$$
$$\Phi'' + 2\mathcal{H}\Phi' - \mathcal{H}\Psi' - (\mathcal{H}^2 + 2\mathcal{H}')\Psi = -a^2c_{\rm s}^2\delta\rho/2\,, \tag{2.31}$$
$$\delta' + 3\mathcal{H}(c_{\rm s}^2 - w)\delta = -(1+w)(\theta + 3\Phi')\,, \tag{2.32}$$
$$\theta' + \left[\mathcal{H}(1-3w) + \frac{w'}{1+w}\right]\theta = -k^2\left(\frac{c_{\rm s}^2}{1+w}\delta + \Psi\right)\,, \tag{2.33}$$

where we have omitted the subindex $\mathbf{k}$ and $\theta \equiv \theta_{\mathbf{k}} = ik_jv^j$. Combining them we can obtain the Poisson equation,

$$k^2\Phi = a^2\rho\delta^*/2\,, \tag{2.34}$$

with $\delta^* \equiv \delta + 3\mathcal{H}(w+1)\theta/k^2$, the *total-matter* variable. Using Equations 2.28, 2.30 and 2.31,

$$\Phi'' + 3\mathcal{H}(1+c_{\rm s}^2)\Phi' + (c_{\rm s}^2k^2 + 3\mathcal{H}^2c_{\rm s}^2 + 2\mathcal{H}' + \mathcal{H}^2)\Phi = 0\,, \tag{2.35}$$

and, with Poisson equation, one gets the evolution equation for δ^*,

$$(\delta^*)'' + \mathcal{H}(1 + 3c_{\rm s}^2 - 6w)(\delta^*)' - \left[\frac{3}{2}\mathcal{H}^2(1 - 6c_{\rm s}^2 - 3w^2 + 3w) - c_{\rm s}^2k^2\right]\delta^* = 0\,. \tag{2.36}$$

One can easily see that, for scales (well) outside the horizon ($k \ll \mathcal{H}$), in matter or radiation domination (and, in general, for fluids with $c_{\rm s}^2 = w =$ constant), Equation 2.28 gives (recall we are in the single fluid case)

$$\delta = 2\Phi = \text{constant}\,, \tag{2.37}$$

where the last equality comes from the dominant solution of Equation 2.35. This means that modes outside of the horizon will freeze until they re-enter it.

On the contrary, for scales (deep) inside the horizon ($k \gg \mathcal{H}$),

$$\delta'' + \mathcal{H}(1-3w)\delta' + \left(k^2 c_{\rm s}^2 - (1+w)\frac{3}{2}\mathcal{H}^2\right)\delta = 0\,, \tag{2.38}$$

where we had assumed that $w =$ constant. When ($c_{\rm s}k \gg \mathcal{H}$) one obtains the wave equation of a fluid with sound speed $c_{\rm s}$, $\delta'' + c_{\rm s}^2 k^2 \delta = 0$. We can define the Jeans length for a general fluid with equation of state w[3],

$$\lambda_{\rm J} = c_{\rm s}\sqrt{\frac{\pi}{G(1+w)\rho}}\,, \tag{2.39}$$

where $\lambda_{\rm J}$ is a physical length; i.e. given by $2\pi a/k$. Perturbations modes smaller than the Jeans length will undergo damped oscillations, produced by the balance between pressure and gravitational attraction. These oscillations will be found in the CMB and LSS observations and are a key probe of the accelerated expansion of the Universe, called Baryon Acoustic Oscillations for its origin during radiation era, when the Universe was filled by a photon-baryon plasma. On the contrary, larger scales ($c_{\rm s}k \ll \mathcal{H}$) will be governed by

$$\delta'' + \mathcal{H}(1-3w)\delta' - (1+w)\frac{3}{2}\mathcal{H}^2\delta = 0\,, \tag{2.40}$$

with two solutions of the kind $\delta = Aa^{\lambda(w)}$, with A a constant and

$$\lambda(w) = \frac{1}{4}(\pm\sqrt{81w^2 - 42w + 25} + 9w - 1)\,. \tag{2.41}$$

For cold dark matter ($w = 0$), $\lambda = 1, -3/2$, while for radiation ($w = 1/3$), $\lambda = (1 \pm \sqrt{5})/2$. This means that at super-horizon scales, the perturbations will *indefinitely* grow as pressure will not be strong enough to compensate gravity.

This is, however, valid just for a single fluid. If we had **multiple perfect fluids**, the Einstein equations will depend on the total effective fluid while the continuity equation $\delta T^{\mu}_{\nu;\mu} = 0$ will give two differential equations for each of them. Therefore, the evolution equations will be

$$\Psi = -\Phi\,, \tag{2.42}$$

$$k^2(\Phi' - \mathcal{H}\Psi) = a^2(1+w_{\rm eff})\rho_{\rm t}\theta_{\rm t}/2\,, \tag{2.43}$$

$$k^2\Phi + 3\mathcal{H}(\Phi' - \mathcal{H}\Psi) = a^2\rho_{\rm t}\delta_{\rm t}/2\,, \tag{2.44}$$

$$\delta_i' + 3\mathcal{H}((c_{\rm s}^2)_i - w_i)\delta_i = -(1+w_i)(\theta_i + 3\Phi')\,, \tag{2.45}$$

$$\theta_i' + \left[\mathcal{H}(1-3w_i) + \frac{w_i'}{1+w_i}\right]\theta_i = -k^2\left(\frac{(c_{\rm s}^2)_i}{1+w_i}\delta_i + \Psi\right)\,, \tag{2.46}$$

where the subindex i stands for each fluid and

$$\rho_{\rm t} = \sum_i \rho_i\,, \tag{2.47}$$

$$\delta_{\rm t} = \sum_i \Omega_i\delta_i\,, \tag{2.48}$$

$$w_{\rm eff} = \sum_i \Omega_i w_i = -1 - \frac{2}{3}\frac{\dot{H}}{H^2}\,, \tag{2.49}$$

$$\theta_{\rm t} = \frac{\sum_i (1+w_i)\Omega_i\theta_i}{1+w_{\rm eff}}\,. \tag{2.50}$$

[3]Normally, it is defined in the context of pressureless fluids as cold dark matter; i.e. for $w = 0$

In radiation era, at sub-horizon scales, the perturbation evolution equations (neglecting baryons) are

$$\delta_{\rm m}'' + \mathcal{H}\delta_{\rm m}' - \frac{3}{2}\mathcal{H}^2(\Omega_{\rm m}\delta_{\rm m} + \Omega_{\rm r}\delta_{\rm r}) = 0\,, \tag{2.51}$$

$$\delta_{\rm r}'' + \frac{k^2}{3}\delta_{\rm r} = 0\,, \tag{2.52}$$

which show that $\delta_{\rm r}$ (and the baryons coupled to radiation) will oscillate, imprinting in the CMB the BAO as we saw before. Because its average $\langle\delta_{\rm r}\rangle \sim 0$, we can approximate $\Omega_{\rm m}\delta_{\rm m} + \Omega_{\rm r}\delta_{\rm r} \sim 0$, and obtain

$$\delta_{\rm m} = C_1 + C_2\int\frac{{\rm d}\tau}{a} \propto \log(a)\,. \tag{2.53}$$

The matter overdensities will mildly grow during radiation era and will only really grow when matter dominates, with $\delta \propto a$, as we saw before.

Similarly, in matter domination we will have the following equations for cold dark matter ($\delta_{\rm c}$) and baryons ($\delta_{\rm b}$),

$$\delta_{\rm c}'' + \mathcal{H}\delta_{\rm c}' - \frac{3}{2}\mathcal{H}^2(\Omega_{\rm c}\delta_{\rm c} + \Omega_{\rm b}\delta_{\rm b}) = \delta_{\rm c}'' + \mathcal{H}\delta_{\rm c}' - \frac{3}{2}\mathcal{H}^2(\Omega_{\rm c}\delta_{\rm c}) \simeq 0\,, \tag{2.54}$$

$$\delta_{\rm b}'' + \mathcal{H}\delta_{\rm b}' - \frac{3}{2}\mathcal{H}^2(\Omega_{\rm c}\delta_{\rm c} + \Omega_{\rm b}\delta_{\rm b}) = \delta_{\rm b}'' + \mathcal{H}\delta_{\rm b}' - \frac{3}{2}\mathcal{H}^2(\Omega_{\rm c}\delta_{\rm c}) \simeq 0\,, \tag{2.55}$$

where we have taken into account that baryons constitute a small fraction of the total matter content ($|\Omega_{\rm b}\delta_{\rm b}| \ll |\Omega_{\rm c}\delta_{\rm c}|$). Consequently, baryons will have a negligible impact on cold dark matter and cold dark matter perturbations will grow independently of baryons. However, baryons, instead, will be dragged by cold dark matter.

One needs, however, a more detailed computation in order to compare the theoretical predictions with CMB observations. For such cases, one cannot neglect the non-diagonal terms of the energy-momentum tensor. In fact, one needs to account for the interactions between baryons and photons and, therefore, needs to work with the **full distribution function** $f(\mathbf{P}, \mathbf{x}, t)$; where $\mathbf{P}$ is the four-momentum vector. In this case,

$$T^{\mu}_{\ \nu}(\mathbf{x}, t) = \frac{g_i}{(2\pi)^3}\int {\rm d}^3\mathbf{x}\sqrt{-g}\frac{P^\mu P_\nu}{P^0}f(\mathbf{P}, \mathbf{x}, t)\,, \tag{2.56}$$

where $P^0 \equiv {\rm d}t/{\rm d}\lambda_s$, $P^i = {\rm d}x^i/{\rm d}\lambda_s$, with λ_s the particle path parameter and g_i, the number of internal degrees of freedom. Recall that $P^2 = -m^2$ for a particle of mass m and can be seen that $\mathbf{P} = ([1-\Psi]p, [1-\Phi]/a\, p\hat{p}^i)$, with $p = \sqrt{P_i P^i}$ and $\hat{p}^i \equiv P^i/|P|$. The energy density is then given by $-T^0_{\ 0}$, the pressure by $T^i_{\ i}/3$ and the shear,

$$T^i_{\ j} \propto \frac{P^i P_j}{(P^0)^2} = \frac{{\rm d}x^i {\rm d}x_j}{{\rm d}t^2} = v^i v_j\,. \tag{2.57}$$

For massive non-relativistic particles it contributes at second order of perturbation. However, for relativistic or massless particles, this term is present at linear order, meaning that neutrinos and photons will contribute to the shear term.

The full set of equations in this case is

$$\Theta' = -\Phi' - ik\mu(\Theta + \Psi) - \tau_{\rm op}'(\Theta_0 - \Theta + \mu v_{\rm b})\,, \tag{2.58}$$

$$\delta_{\rm b}' = -ikv_{\rm b} - 3\Phi'\,, \tag{2.59}$$

$$v_{\rm b}' = -\mathcal{H}v_{\rm b} - ik\Psi + \frac{\tau_{\rm op}'}{R_s}(3i\Theta_1 + v_{\rm b})\,, \tag{2.60}$$

$$\delta_{\rm c}' = -ikv_{\rm c} - 3\Phi'\,, \tag{2.61}$$

$$v_{\rm c}' = -\mathcal{H}v_{\rm c} - ik\Psi\,, \tag{2.62}$$

where

$$\Theta \equiv \int \mathrm{d}^3\mathbf{x} e^{-i\mathbf{k}\mathbf{x}} \frac{\delta T}{T}(t, \mathbf{x}, \hat{p}^i)\,, \tag{2.63}$$

$$\tau_{\rm op} \equiv \int_{\eta}^{\eta_0} \mathrm{d}\tilde{\eta}\, a\, n_e \sigma_{\rm T}\,, \tag{2.64}$$

$$v_{\rm b} = -i\theta_b/k\,, \tag{2.65}$$

$$R_s \equiv \frac{3}{4}\rho_{\rm b}\rho_\gamma\,. \tag{2.66}$$

Here, $\tau_{\rm op}$ is the optical depth and the integration is over the conformal time that we called η (instead of τ to avoid confusion), with n_e the free electron density and $\sigma_{\rm T}$ the Thomson cross-section. The variables Θ_0 and Θ_1 in Equations 2.58 and 2.60 are the monopole and dipole of the temperature fluctuation,

$$\Theta_\ell \equiv \frac{1}{(-i)^\ell} \int_{-1}^{1} \frac{\mathrm{d}\mu}{2} \mathcal{P}_\ell(\mu)\Theta(\mu)\,, \tag{2.67}$$

where $\mathcal{P}_\ell$ is the Legendre polynomials of order ℓ, and $\mathcal{P}_0(\mu) = 1$ and $\mathcal{P}_1(\mu) = \mu$.

In this regime, $\Phi \neq \Psi$, although it can be approximately recovered if the quadrupole is negligible. There exists, however, an analytic expression deep in radiation at sub-horizon scales:

$$\Phi = -\Psi \left(1 + \frac{2}{5} f_\nu\right)\,, \tag{2.68}$$

where f_ν is the neutrino's distribution function.

For a more detailed discussion, we refer to Refs. [6, 9].

Power spectra

We have developed the evolution equations of perturbations in ΛCDM. However, we cannot track the evolution of a single perturbation back in time from observations, specially given the limited amount of independent measurements that we can make of the same object on the sky. We can, however, study the statistical properties of matter and radiation distribution on the Universe using different techniques.

This means that the two of the most important (and used) quantities in CMB and LSS studies are the correlation function ($\xi(\mathbf{r})$) and the power spectrum ($P(\mathbf{k})$) [6],

$$\xi(\mathbf{r}) = \langle \delta(\mathbf{x})\delta(\mathbf{x}')\rangle = \frac{1}{V}\int \mathrm{d}^3\mathbf{x}\, \delta(\mathbf{x})\delta(\mathbf{x}-\mathbf{r})\,, \tag{2.69}$$

$$V\langle \delta_{\mathbf{k}}\delta_{\mathbf{k}'}\rangle = (2\pi)^3 V^{-1} P(\mathbf{k})\delta^3(\mathbf{k}-\mathbf{k}')\,, \tag{2.70}$$

where the integrations are over the volume of the survey, V, and $\mathbf{r} = \mathbf{x} - \mathbf{x}'$. Furthermore, these quantities are related by a Fourier transform,

$$P(\mathbf{k}) = \int \mathrm{d}^3\mathbf{x} e^{-i\mathbf{k}\cdot\mathbf{r}} \xi(\mathbf{r})\,. \tag{2.71}$$

Apart from these quantities, it is sometimes useful to work with the angular power spectrum, C_ℓ. This is defined as the variance of the harmonic coefficients, $a_{\ell m}$, of the projected overdensity field $\delta(\mathbf{x})$ on the sky. The projected field is defined as

$$\tilde{\delta}(\theta, \phi) = \int_0^\infty \mathrm{d}\chi w(\chi)\delta(\chi, \theta, \phi)\,, \tag{2.72}$$

where $w(\chi)$ is an unit-normalized selection function that weights our capability to measure δ at a given comoving distance χ. Now, it can be decomposed in spherical harmonics so that

$$\tilde{\delta}(\theta,\phi) = \sum_{l=0} \sum_{m=-l}^{l} a_{\ell m} Y_{\ell m}(\theta,\phi)\,, \tag{2.73}$$

where the $Y_{\ell m}(\theta,\phi)$ are the spherical harmonics. Then, the angular power spectrum is given by the variance of the $a_{\ell m}$ coefficients,

$$C_\ell = \langle a_{\ell m} a^\dagger_{\ell' m'} \rangle \delta_{\ell\ell'} \delta_{mm'}\,. \tag{2.74}$$

These are the expressions for the auto-correlation of the field $\delta(\mathbf{x})$. However, one can also compute the cross-correlation of two different field $\delta_1(\mathbf{x})$ and $\delta_2(\mathbf{x}')$; i.e. $\langle \delta_1 \delta_2 \rangle$. Note that these fields can be different observational targets (e.g. temperature fluctuations and matter overdensities) or be in different redshifts (e.g. at recombination and $z = 1$). In this case the angular power spectrum is generalized to

$$C_\ell = \langle a_{\ell m} b^\dagger_{\ell' m'} \rangle \delta_{\ell\ell'} \delta_{mm'}\,, \tag{2.75}$$

where $a_{\ell m}$ and $b_{\ell m}$ are the spherical harmonics components of the fields δ_1 and δ_2, respectively.

We will see in Chapter 3 how to use these quantities to compare our predictions with observational data.

Weak lensing

An important observable in LSS surveys is the deformation of galaxy shapes due to gravity. Photons, in their travel to us, suffer the gravitational attraction of mass concentrations, modifying the shape of the objects we see on the sky. If we define the lensing potential $\psi \equiv \Phi - \Psi$, the light displacement on the 2D sky plane ($\mathbf{x} = (x^1, x^2)$) of an object at a distance r is given by

$$\frac{\mathrm{d}^2}{dr^2}(r\theta^i) = \psi_{,i}\,, \tag{2.76}$$

where we had into account that, since the displacement is small, we can easily substitute Cartesian coordinates by angles, $x^i = r\theta^i$. Integrating,

$$\theta^i = \theta^i_0 + \int_0^r \mathrm{d}r' \left(1 - \frac{r'}{r} r'\right) \psi_{,ij}(r', r'\theta^1_0, r'\theta^2_0)\,, \tag{2.77}$$

where θ^i_0 is the measured angle on the sky.

Now, we can see how an object (e.g. a galaxy) will be deformed by weak lensing computing the evolution of the light rays that part from points separated by $\Delta\Theta_0$,

$$\Delta\theta^i = \Delta\theta^i_0 + \Delta\theta^j_0 \int_0^r \mathrm{d}r' r' \left(1 - \frac{r'}{r}\right) \psi_{,ij}(r', r'\theta^1_0, r'\theta^2_0)\,. \tag{2.78}$$

Therefore, weak lensing can be described as

$$A_{ij} \equiv \frac{\partial \theta^2_s}{\partial \theta^j_0} = \delta_{ij} + D_{ij}\,, \tag{2.79}$$

with the distortion tensor, D_{ij},

$$\int_0^r \mathrm{d}r' r' \left(1 - \frac{r'}{r}\right) \psi_{,ij}(r', r'\theta^1_0, r'\theta^2_0) = \begin{pmatrix} -\kappa - \gamma_1 & -\gamma_2 \\ -\gamma_2 & -\kappa + \gamma_1 \end{pmatrix}. \tag{2.80}$$

The parameter κ is the convergence and is related to the magnification of the source image. It is given by

$$\kappa = -\frac{1}{2}\int_0^r \mathrm{d}r' r' \left(1 - \frac{r'}{r}\right)(\psi_{,11} + \psi_{,22})\,, \tag{2.81}$$

The shear modes, γ_1 and γ_2, describe the distortion of the object and are given by

$$\gamma_1 = -\frac{1}{2}\int_0^r \mathrm{d}r' r' \left(1 - \frac{r'}{r}\right)(\psi_{,11} - \psi_{,22})\,, \tag{2.82}$$

$$\gamma_2 = -\int_0^r \mathrm{d}r' r' \left(1 - \frac{r'}{r}\right)\psi_{,12}\,. \tag{2.83}$$

The magnification parameter cannot be, at this moment, inferred from LSS cosmological observations because the intrinsic galactic luminosity vary that much that the signal is overrun by noise. However, the shear modes can be estimated looking at the galaxy deformation, being an important observable that tracks the matter distribution of the Universe.

2.2 Inflation

The Universe has been seen to be homogeneous and isotropic at large scales [45–48]. In fact, non causally connected areas of the Universe share similar statistical properties. Explaining why different patches of the sky are similar even though they did have independent evolutions is one of the most important open questions in cosmology today and poses the so-called *Horizon problem*.

Furthermore, observations of CMB also show that our Universe is compatible with being flat [46–48]. Although, in principle, it could have been open ($\Omega_K < 1$) or closed ($\Omega_K > 1$), observations point to $\Omega_K = 0.001 \pm 0.002$, which might seem unlikely if curvature could have any other value. This is known as the *flatness problem*.

Inflation was postulated to solve these *problems*. Following inflationary theory, the Universe originally was just empty spacetime with density fluctuations of elementary particles that created and annihilated. However, at some point, the Universe started to expand acceleratedly (until the Universe was e^{50} - e^{60} times larger), erasing, almost perfectly, the density fluctuations, distributing homogeneously the particles in the Universe. In this way, this mechanism allows to explain the homogeneity of the Universe and why distant causally disconnected parts are related. They are because they were causally connected before. Furthermore, such accelerated expansion stretched the spacetime that much that, independently of its previous geometry, it became flat.

The mechanism that causes the accelerated expansion is similar to that of dark energy: one needs a fluid with $w < -1/3$. It can be obtained with a scalar field, called the inflaton, as is commonly done. The action of such theory would be given by

$$S = \int \mathrm{d}^4\mathbf{x}\sqrt{-g}\frac{R}{16\pi G} + \frac{1}{2}g^{\mu\nu}\partial_\mu\partial_\nu\phi + V(\phi)\,, \tag{2.84}$$

where ϕ is the scalar field and $V(\phi)$ its potential energy. During inflation the dominant component was the scalar field and we can neglect terms involving matter and radiation.

Varying the inflationary action, one finds that the evolution of the scalar field is given by the Klein-Gordon equation,

$$\ddot{\phi} + 3H\dot{\phi} - \frac{1}{a^2}\nabla^2\phi + V'(\phi) = 0\,, \tag{2.85}$$

where V' is the derivative respect to the argument, ϕ, of the potential energy and ∇^2 is the Laplacian in comoving coordinates. The term $\nabla^2\phi = 0$ if the field is homogeneous and isotropic.

The density and pressure energy of the scalar field are given by

$$\rho = \frac{1}{2}\dot{\phi}^2 + V(\phi)\,, \qquad p = \frac{1}{2}\dot{\phi}^2 - V(\phi)\,, \tag{2.86}$$

and, therefore, its equation of state,

$$w = \frac{1/2\dot{\phi}^2 - V(\phi)}{1/2\dot{\phi}^2 + V(\phi)}\,, \tag{2.87}$$

will be $w < -1/3$ when the potential energy, $V(\phi)$, dominates over the kinetic energy, $\dot{\phi}^2/2$.

As a consequence, the shape of the potential will determine its evolution. Current CMB observations favor concave potentials and a duration of $50 - 60$ efolds [50]. The efolds measure the duration of inflation and correspond to

$$N = \int_{t_1}^{t_2} \mathrm{d}t H(t) \tag{2.88}$$

so that the Universe expanded a factor e^N. Furthermore, observations also favor the slow-roll models, i.e. models for which $\ddot{\phi} \simeq 0$ and $\dot{\phi}^2 \ll V(\phi)$ [50]. In this case, one can define the slow-roll parameters,

$$\epsilon = \frac{1}{2}M_{\mathrm{P}}^2\left(\frac{V'}{V}\right)^2 \simeq -\frac{\dot{H}}{H^2}\,, \qquad \eta = M_{\mathrm{P}}^2\left(\frac{V''}{V}\right)^2\,, \tag{2.89}$$

related by

$$\eta = 2\epsilon - \frac{\mathrm{d}\ln\epsilon}{\mathrm{d}N}\,. \tag{2.90}$$

This relation comes from the fact that the Friedmann and the field evolution equations (Equations 2.7 and 2.85), during slow-roll, can be approximated, respectively, by

$$H^2 = \frac{1}{3}V(\phi)\,, \qquad 3H\dot{\phi} = -\frac{\mathrm{d}V(\phi)}{\mathrm{d}\phi}\,. \tag{2.91}$$

During slow-roll, $\epsilon \ll 1$ and $\tau \ll 1$. Once they become of order $O(1)$, the field starts moving fast. In convex and slow-roll models, the field is moving, normally, towards a convex minimum. Once the field starts moving fast, it quickly starts oscillating around the minimum and inflation ends. One can add a friction term to the field equation (e.g. a radiative term), so that oscillations are damped.

However, the observables quantities are at perturbation level. CMB directly constrains the primordial power spectrum. If we naively perturb the field, $\phi(\mathbf{x},t) = \phi_0(t) + \delta\phi(\mathbf{x},t)$ and Fourier transform the field Equation 2.85, the perturbation evolution equation would be

$$\ddot{\phi}_{\mathbf{k}} + 3H\dot{\phi}_{\mathbf{k}} + \left(\frac{k^2}{a^2} - V''(\phi_0)\right)\phi_{\mathbf{k}} = 0\,, \tag{2.92}$$

where, for simplicity, we have called the Fourier component of the field perturbation, $\delta\phi(\mathbf{x},t)$, $\phi_{\mathbf{k}}$.

In slow-roll, $V''(\phi_0)$ can be neglected and the previous equation can be easily solved in conformal time, τ,

$$(a\phi_{\mathbf{k}})'' + \left(k^2 - \frac{z''}{z}\right)(a\phi_{\mathbf{k}}) = 0\,, \tag{2.93}$$

with $z = a\dot{\phi}/H$.

Similarly, for the tensor modes (gravitational waves) perturbations, one has

$$\ddot{h}_{\mathbf{k}} + 2H\dot{h}_{\mathbf{k}} + \frac{k^2}{a^2}h_{\mathbf{k}} = 0\,, \tag{2.94}$$

which, in conformal time becomes,

$$(ah_{\mathbf{k}})'' + \left(k^2 - \frac{a''}{a}\right)(ah_{\mathbf{k}}) = 0\,. \tag{2.95}$$

Note that these equations have been obtained without neglecting the field potential and, therefore, the tensor perturbations are not affected by it, in contrast to the scalar perturbations.

The superhorizon solutions ($aH \gg k$) of the scalar and tensor perturbations go as

$$\phi_{\mathbf{k}} = \text{constant}\,, \qquad \mathcal{H}_{\mathbf{k}} \propto k^{-3/2}\,. \tag{2.96}$$

The observable quantities will be the power spectrum of the curvature (R_k) and horizon scale (T_k) perturbations [10],

$$R_k = \frac{\delta a}{a} = \frac{H^2}{2\phi\dot{\phi}}\,, \qquad T_k = 4H\,, \tag{2.97}$$

that correspond to

$$\langle R_k^2\rangle = \frac{1}{24\pi^2}\frac{V}{\epsilon}\Big|_{k=Ha}\,, \qquad \langle T_k^2\rangle = \frac{2V}{3\pi^2}\Big|_{k=Ha}\,. \tag{2.98}$$

Note that these expressions are evaluated when the scale k exits the horizon, and define a direct measurable quantity, the tensor-to-scalar ratio:

$$r = \frac{\langle T_k^2\rangle}{\langle R_k^2\rangle} = 16\epsilon \tag{2.99}$$

Using these quantities one can define the normalized powers spectra, multiplying by $k^3/2\pi^2$ the previous expressions,

$$P_R^2(k) = \frac{k^3}{2\pi^2}\langle R_k^2\rangle = A_R\left(\frac{k}{k_{\rm p}}\right)^{n_{\rm s}(k)-1}\,, \qquad P_T^2(k) = \frac{k^3}{2\pi^2}\langle T_k^2\rangle = A_T\left(\frac{k}{k_{\rm p}}\right)^{n_{\rm t}(k)}\,, \tag{2.100}$$

where $k_{\rm p}$ is the pivot scale and is conventionally taken to be $k_{\rm p} = 0.002\,{\rm Mpc}^{-1}$ (see e.g. Planck 2018 results [50]). In a de Sitter expansion, P_R is scale independent as $\langle R_k^2\rangle \propto k^{-3}$. As we expect inflation to be closed to de Sitter, one adds -1 to the exponent, so that $n_{\rm s} \sim 1$. The tensor-to-scalar ratio can also be derived from the amplitudes A_R and A_T, with $r = A_T/A_R$.

The scale dependence of the spectral index, $n_{\rm s}$, is known as the running index and is given by

$$\alpha_{\rm s} = \frac{{\rm d}n_{\rm s}}{{\rm d}\ln k}\,. \tag{2.101}$$

Finally, together with the tensor-to-scalar ratio, these scalars, $n_{\rm s}$ and $n_{\rm t}$, are directly measurable with CMB data and can be related to the slow-roll parameters,

$$n_{\rm s}(k) - 1 = 3\eta - 6\epsilon\,, \quad n_{\rm t}(k) = -2\epsilon\,, \quad r = -8\eta\,, \tag{2.102}$$

being the last expression a consistency test.

A more detailed discussion can be found in Refs. [6, 9].

2.3 Theoretical and observational challenges of ΛCDM

The Standard Cosmological Model, ΛCDM, is able to correctly describe current observations and, in fact, better than any other. However, there might be some fundamental and, lately, observational considerations that could motivate the exploration of alternative models.

Early (CMB) and late-time (local) observations seem to disagree in the expansion rate today [20], H_0, and the matter density combined with the fluctuation power spectrum amplitude [14, 51], $S_8 \equiv \sigma_8\sqrt{\Omega_{\rm m}/0.3}$. SN Ia measurements of H_0 disagree with CMB's value by 4.4σ, while S_8 does by 3.2σ [51]. Although enthusiasts can see on these tensions evidence for new physics, a 3.2σ deviation is not a strong discrepancy and could just well be a statistical fluctuation, specially when independent estimations by the Dark Energy Survey (DES) of S_8 show no discrepancy with Planck results [21]. Furthermore, the H_0 tension has some controversy and has been claimed to be product of bad calibration [52]. In fact, using stars on the Tip of Red Giant Branch to calibrate the supernovae distance yields an intermediate value that is compatible with CMB and Riess' values [23]. This will be discussed in more detail in Section 3.3. Nonetheless, although it is soon to know if there is new physics, if these tensions were true it will become clear with the forthcoming next-generation data and, in that case, a new cosmological model will be needed.

Apart from the observational considerations presented above, the ΛCDM model has some theoretical concerns that must be addressed even if observational tensions disappear. They are

- the coincidence problem. The ΛCDM model needs of fine tunning on the initial conditions of dark energy density; i.e. our Universe is an unlikely realization for ΛCDM. The initial value of the dark energy density was much lower than that of matter or radiation; in fact, $\rho_\Lambda/\rho_{\rm r} \sim a^4$ and $\rho_\Lambda/\rho_{\rm m} \sim a^{-3}$. This means that, at Big Bang Nucleosynthesis (BBN) epoch, at $z \sim 10^8$, dark energy density was 32 orders of magnitude lower than radiation energy density and 24 orders of magnitude lower than matter's.

- the cosmological constant problem. The vacuum energy of the Universe, which would contribute as a cosmological constant, diverge from the value necessary of Λ to explain the accelerated expansion by 120 orders of magnitude. While the vacuum energy is expected to be of order the Planck mass [53],

$$\rho_{\rm vacuum} \sim M_{\rm P}^4 \sim (10^{18}\,{\rm GeV})^4\,, \tag{2.103}$$

  the cosmological constant value compatible with current observations ($\Omega_\Lambda \sim 0.7$ [43]) is

$$\rho_\Lambda \sim (10^{-12}\,{\rm GeV})^4 \sim 10^{-120} M_{\rm P}^4\,. \tag{2.104}$$

A proposed solution is the *anthropic principle* [25], which considers that one has to take into account the fact of our existence. There are two different classes:

- Weak anthropic principle (WAP): Our spatial and temporal location in the Universe must be such that it is compatible with life, in order of having us as observers.

- Strong anthropic principle (SAP): Physics, both the Universe and the fundamental constants, must be such that there can be observers at some stage.

Invoking the WAP, the possible values of the cosmological constant energy density (before it was known that the Universe expanded acceleratedly) are upper-bounded by structure and astrophysical evolution; i.e. the cosmological constant cannot dominate over matter at times earlier than $z \gtrsim 1$; and lower-bounded by the requirement of $H > 0$ [54],

$$-10^{-123}G^{-2} \sim -6\times10^{-121}M_{\rm P}^4 \lesssim \rho_\Lambda \lesssim 3\times10^{-121}G^{-2} \sim 2\times10^{-118}\,. \tag{2.105}$$

As expected, the measured value $\rho_\Lambda \sim 10^{-120} M_{\rm P}^4$ is compatible with Weinberg's anthropic bounds.

An alternative approach is to *degravitate* the cosmological constant; i.e. decouple the cosmological constant from gravity. It was realized that the underlying problem is that, on the contrary to what happens with other physical laws, gravity is not shift-symmetric [26]; i.e it is not invariant under $T_{\mu\nu} \to T_{\mu\nu} + \Lambda g_{\mu\nu}$. One could think, then, that what we see is the low energy regime of a higher order theory of gravity. It is possible to construct such models with $T_{\mu\nu} \to T_{\mu\nu} + \Lambda g_{\mu\nu}$ invariance [26, 55, 56]. Another approach to *degravitate* the vacuum energy is *cascading gravity*, that has a characteristic length scale above which gravitational forces coming from sources with larger characteristic wavelengths are weaker than in GR. On the contrary, at smaller scales it recovers GR [27, 57]. In addition, one could just *forget* about the cosmological constant problem, hoping to be solved by some unknown mechanism and explore other sources of accelerated expansion, such as extra component in the Universe or modified version of Gravity. This is what we have explored in this Thesis and we briefly introduce in Chapter 4.

For a more detailed discussion on these topics, we refer to e.g. Refs. [8, 9].

Chapter 3

The status of cosmological observations

Precision cosmology is real today. Last decade has brought a considerable amount of accurate data that allows to constrain the cosmological parameters of the Standard Model with, approximately, 10% error. This will be reduced to 1% by next-generation cosmological experiments. In the 2020's, the next-generation surveys will start collecting data with more precise equipment and larger coverage of the sky. Furthermore, they will overlap, allowing for cross-correlation analyses of overlapping independent measurements that will allow to beat the cosmic variance in some cases [58].

Cosmological measurements can be divided in four main different groups: measurements of the Cosmic Microwave Background (CMB), Large Scale Structure (LSS), Type Ia supernovae (SNe Ia) and, more recently, Gravitational Waves (GW). CMB is the remnant of the primordial universe photons that started traveling freely once the Universe temperature was cold enough to star forming hydrogen. CMB measurements are the most precise measurements in cosmology that we have today and they constitute the earliest image of the Universe we have so far. CMB temperature was measured with high precision by the Cosmic Background Explorer (COBE) mission [59], and constitute the best black body ever observed. The Wilkinson Microwave Anisotropy Probe (WMAP) [15] satellite obtained the first high resolution image of CMB, improving previous constraints on the ΛCDM parameter space by a factor 68,000 [15], allowing cosmology to enter the precision era. Finally, Planck accessed to much lower scales, improving the resolution of CMB maps and, consequently, the parameter constraints [16]. It is important to note that CMB experiments do not only measure the CMB temperature but also its polarization field. In fact, a detection of the rotational B-mode would be a strong evidence (although not proof) of inflation. Inflationary models naturally produce tensor fluctuations (see e.g. Section 2.2) that would imprint the B-modes onto the CMB photons.

The Large Scale Structure (LSS) experiments map the matter distribution using galaxies distribution and shape deformation due to weak lensing as tracers. In fact, the combination of both is able to break degeneracies with the cosmological parameters and, therefore, an accurate description of both fields at different redshift is one of the main observational targets of the next-generation LSS surveys. However, since we do not know the initial conditions of the Universe, we do not have a theoretical prediction to directly compare them with. Instead, what we can do is to analyze and compare the statistical properties of the matter and shear fields (as well as temperature and polarization in the CMB) theoretically predicted and observationally measured. Consequently, two of the most helpful quantities are the 2-point correlation function and the power spectra, which can be directly compared with our theoretical predictions. However, they also have valuable information on their own. For instance, it is possible to detect the

existence of a characteristic scale in the LSS of the Universe looking at the correlation function or power spectra of the matter distribution. This scale corresponds to the Baryonic Acoustic Oscillations (BAO). As we saw in Section 2.1.1, they are the imprint of the sound waves in the baryon-radiation fluid prior recombination, produced by the balance between the gravitational attraction and pressure repulsion. As a consequence, the BAO are also present in the CMB and can be tracked from recombination to the present. Since the BAO comoving scale is fixed, it constitutes an standard ruler and can be used to infer the expansion rate of the Universe at different epochs.

The Type Ia supernovae are probably the most famous standard candles as they were responsible of the first positive detection of the accelerated expansion of the Universe, strongly supporting the existence of dark energy [60, 61]. The SNe Ia have characteristic light patterns that can be normalized, making it possible to compare SNe at different redshifts and estimate the expansion rate of the Universe (see e.g. [62] or Section 3.3). Furthermore, if one can correctly calibrate the absolute magnitude of the SNe Ia by using lower redshift measurements (e.g. cepheids or TRGB starts) with the so-called *distance ladder* method, one can also estimate H_0 (see e.g. Refs. [20, 23] or Section 3.3.1). Furthermore, another extra advantage of using SNe Ia as standard candles is that they are quite bright and can be seen from really far.

Gravitational waves have joined the group of traditional cosmological observations. The first detection of a gravitational wave was on September 14, 2015 [63] and many others have followed them. Although it is still soon to make cosmology with gravitational waves, which will require a larger sample of detections, they (might[1]) have already imposed stringent constraints on the possible modifications of Gravity (see e.g. Refs. [28, 65–70]). Thanks to the (lucky and unlikely) simultaneous detection of the gravitational wave GW170817 and its electromagnetic counterpart GRB170817A, it was possible to measure the speed of gravitational waves to be $|c_{\rm gw}-1| \sim 10^{15}$ [71]. Furthermore, these events can also be used to estimate the value of H_0 [72], although with much larger errors than CMB, LSS and SN Ia measurements. This will change with a larger sample of simultaneous detections.

The next-generation experiments will include the Stage-4 CMB, a collaboration of different third generation experiments such as the Atacama Cosmology Telescope (ACTPol) [73], the South Pole Telescope (SPT-3G) [74], BICEP2/Keck [75] or Simons Array [76] that will cover around a 70% of the sky and will reduce the white-noise level to $\sigma_T \sim 1\,\mu{\rm K}-{\rm arcmin}$ [77]. In addition, LSS surveys such as the Large Synoptic Spectroscopic Telescope (LSST) [17], the Dark Energy Scientific Instrument (DESI) [19], the Wide Field Infrared Space Telescope (WFIRST) [78] and Euclid [79] will map the galaxy (and matter) distribution, getting the largest sample ever had with $10^9 - 10^{10}$ galaxies in it (taking into account that just LSST will measure 4×10^9 galaxies [17]) and reach $z \gtrsim 6$. In addition, WFIRST, Euclid and LSST, among others, will also detect SNe Ia, improving the sample size by 2 orders of magnitude. The largest contribution will come from LSST which will observe $\sim 10^5$ SNe Ia [34]. In addition, WFIRST and Euclid samples will be of order $\sim 2\times10^3$ [78] and $\sim 2\times10^4$ [79], respectively. They will deep as $z\sim1.2$ [79] in the case of Euclid, $z\sim1.7$ for WFIRST [78] and $z\sim1$ for LSST [17]. With this amount of supernovae, one will be able to study their statistical distribution and properties.

The other main surveys are devoted to gravitational wave detection and will allow to explore new frequency bands accessing farther and more massive events. For that, there will be three kind of strategies: ground-based observatories such as the Kamioka Gravitational Wave Detector (KAGRA) [80], that has recently joined the Laser Interferometer Gravitational-Wave

[1]It has been argued that if one considers Modified Gravity an Effective Field Theory of some higher energy theory, its cut-off would be close to the energy scale of the GW event. In that case, the measurement of the gravitational wave speed would set weak constraints as, in that regime, it is expected that $c_{\rm gw}\to1$ [64].

Observatory (LIGO) [81] and Virgo [82] GW detectors; space-based detectors such as the Laser Interferometer Space Antenna (LISA) [83] and pulsar timing arrays (PTA) such as the International Pulsar Timing Array (IPTA) [84] or the Square Kilometer Array (SKA) [85]. They will explore different frequency bands, complementing each other. Ground-base surveys detect on the $\sim 10^2$ Hz, while LISA will on the mHz and PTA on the nHz, approximately. The frequency of the gravitational waves depend on the mass of the sources so that the more massive the objects are the lower frequency the gravitational waves have. The number of events that will be detected is still unclear given the uncertainty on the physical processes that produce detectable gravitational waves.

In the following sections, we will briefly review the current status of CMB, LSS, SN Ia and GW observations and how they are undertaken. In addition, we will briefly review the prospects of next-generation experiments.

3.1 The Comic Microwave Background (CMB)

The Cosmic Microwave Background is the earliest image of the Universe that we have access to nowadays. It is formed by the photons that started traveling freely after recombination (the moment when hydrogen atoms could start forming). CMB experiments measure photon's temperature and polarization distribution on the sky. This, however, does not directly yield the true CMB values. All the data need to be first cleaned up and, in this case, one first needs to remove the contribution coming from foregrouds, i.e. dust (thermal emission and tiny spinning grains), CO emission lines at high frequencies, free-free radiation, synchrotron radiation, Cosmic Infrared Background (CIB) and the Sunyaev-Zel'dovich (SZ) secondary CMB distorsion, apart from known point sources and galaxy clusters.

Once the map has been cleaned up and reconstructed, one ends up with a pixelated 2D-image of the sky, that can be used to compute statistical quantities that can be confronted with theoretical predictions. As we saw in Section 2.1.1, the two-point correlation function or the power spectrum are two of the most used and useful quantities, as we cannot directly compare the measured fields with theory. From a theoretical point of view, we can only access the statistical properties of the density fluctuations. The computation of their actual value requires to know the initial conditions, which remain unknown. These, according to the general current belief, would be set by the quantum fluctuations during the inflationary epoch.

In comparison with Section 2.1.1, here we do not have an infinite resolution and have to work with a pixelated version of the fields. Quantitatively, this is translated to changing the space integrals by summations over the pixels. For instance, for the real-space correlation function of a field $f(\theta, \phi)$, whose value at pixel p are $f^*(\theta'_p, \phi'_p)$, we have (Equation 2.69),

$$\xi(\mathbf{\Theta}) = \langle f(\theta_p, \phi_p) f^*(\theta'_p, \phi'_p) \rangle \,, \tag{3.1}$$

where the average is over all pixels and $\mathbf{\Theta}$ is the angular separation between the pixels p and p'. On its part, the angular power spectrum, C_ℓ, (Equation 2.74) would be given by the estimator

$$\hat{C}_\ell = \frac{1}{2\ell + 1} \sum_{m=-\ell}^{m=\ell} |\hat{a}_{\ell m}|^2 \,. \tag{3.2}$$

where

$$\hat{a}_{\ell m} = \frac{4\pi}{N_{\rm pix}} \sum_{p=0}^{N_{\rm pix}-1} Y^*_{\ell m}(\theta_p, \phi_p) f(\theta_p, \phi_p) \,, \tag{3.3}$$

with p going through all the image pixels ($N_{\rm pix}$) and Y^* being the conjugated of the spherical harmonics, $Y_{\ell m}(\theta,\phi)$. Recall that a function $f(\theta,\phi)$, defined on a sphere, can be written in spherical harmonics with

$$f(\theta,\phi) = \sum_{\ell=0}^{\ell_{max}} \sum_{m=-\ell}^{\ell} a_{\ell m} Y_{\ell m}(\theta,\phi)\,, \tag{3.4}$$

where ℓ_{max} is the highest accessible angular frequency. When $\ell_{max} \to \infty$, the transformation is exact. As we saw in Section 2.1.1, one can also compute the cross-correlation of different fields, even at different redshifts, just by substituting one of the $\hat{a}_{\ell m}$ in Equation 3.2 by its corresponding spherical harmonics coefficient computed as in Equation 3.3.

The statistical studies of CMB show that the primordial universe was isotropic and homogeneous, without structure at large scales [45–48]. In fact, the data are consistent with an isotropic and homogeneous Gaussian field [48]. At large scales, however, there seems to be some "anomalies" (non-Gaussianities). Planck 2018 results [48] addressed the following "anomalies": the lack of large-angle correlations, an hemispherical power asymmetry, the preference of odd-parity modes in the angular power spectrum and an unexpected large temperature decrement in the southern hemisphere. The statistical significance of such anomalies, however, is low and they might be just statistical fluctuations. Furthermore, polarization maps show no or small evidence of such anomalies [48]. In any case, additional data and better foreground modeling is needed to give a final word about the existence of CMB "anomalies".

Although the CMB is statistically homogeneous and isotropic, it is populated of small anisotropies at all scales. As we will see, those at smaller scales will start growing at a certain moment, constituting the seeds of current cosmological structures which, otherwise, would not exist. These anisotropies are mainly originated by the balance between gravitational attraction and pressure repulsion in the photon-baryons fluid, tightly coupled by Compton scattering, which can be readily seen in the perturbation evolution equation,

$$\ddot{\delta} + 2H\dot{\delta} - 4\pi G\rho_{\rm m}\delta = 4\pi G(\rho_{\rm r} + 3p_{\rm r})s - \frac{1}{a^2}\frac{\nabla^2 p_{\rm r}}{\rho_{\rm r} + p_{\rm r} + p_{\rm m}}, \tag{3.5}$$

where $\rho_{\rm r}$ and $\rho_{\rm m}$ are the radiation and matter energy densities, respectively; $p_{\rm r}$ and $p_{\rm m}$ their pressures and $\delta = \delta\rho_{\rm m}/\rho_{\rm m} = 3/4s$, with $s = \delta\rho_{\rm r}/\rho_{\rm r}$, is the matter overdensity as $\delta\rho$ stands for a small variation of ρ. The relation between the radiation and matter fluctuations is imposed by the requirement of having a constant entropy during the compression/expansion of the fluid. As a consequence of being tightly coupled, the process is (mostly) adiabatic.

The third term on the left hand side of Equation 3.5 and the first on the right hand side are sourced by matter and radiation gravitational interaction, respectively; while the last term of Equation 3.5 is sourced by radiation pressure. This equation has a decaying and an oscillatory solution that imprints the acoustic peaks (BAO) on CMB, depending on the scale of the sound wave. In terms of the density contrast and Fourier space Equation 3.5 becomes

$$\ddot{\delta} + 2H\dot{\delta} - \left[4\pi G\left(\rho_{\rm m} + \frac{8}{3}\rho_{\rm r}\right) - k^2 c_{\rm s}^2\right]\delta = 0 \tag{3.6}$$

where $k = 2\pi/\lambda$ is the wavelength of the sound wave considered and its speed of sound,

$$c_{\rm s}^2 = \partial p_{\rm m}/\partial\rho_{\rm m} = \frac{1}{3}\frac{1}{1 + 3\rho_{\rm m}/4\rho_{\rm r}}\,. \tag{3.7}$$

The limiting wavelength, that cancels the term in brackets in Equation 3.6, is the so-called Jean's scale (see also Section 2.1.1),

$$\lambda_{\rm J} = \left(\frac{\pi c_{\rm s}^2}{G\rho_{\rm m}}\right)^{1/2}, \tag{3.8}$$

Modes well above the Jean's scale ($\lambda \gg \lambda_{\rm J}$) are slowly growing, while those well below it ($\lambda \ll \lambda_{\rm J}$) are oscillatory and responsible of the Baryon Acoustic Oscilations (BAO) imprint that we see today in the CMB.

Finally, Thomson scattering damps BAO at small scales as

$$\alpha \sim e^{-(2r_{\rm d}/\lambda)^2}, \tag{3.9}$$

where $r_{\rm d}^2 \sim (\sigma_{\rm T} n_e H)^{-1}$ is the diffusion distance at recombination, with $\sigma_{\rm T}$ the Thomson cross-section and n_e the free electron density. This effect is also known as Silk damping [86].

The angular size of the first acoustic peak is the most constrained parameter (of the usual varied ones in ΛCDM[2]) we have today in cosmology, fixed with 0.03% precision ($100\,\theta_* = 1.0411 \pm 0.0003$). This peak corresponds to the sound horizon at drag epoch ($z_{\rm d}$), shortly after recombination, when photons and baryons decouple,

$$r_{\rm d}(z) = \int_{1+z_{\rm d}}^{\infty} {\rm d}z' \frac{c_{\rm s}(z')}{H(z')}\,, \tag{3.10}$$

where $c_{\rm s}$ is the sound speed of the fluid filling the Universe at that epoch,

$$c_{\rm s}(z) = \frac{1}{\sqrt{3}} \left(1 + \frac{3\Omega_{\rm b}}{4\Omega_\gamma}\right)^{-1/2}. \tag{3.11}$$

Here, $\Omega_x = \rho_x(z)/3H(z)^2$ with $x = b, \gamma$ is the normalized density of baryons and photons, respectively. This measurement translates in a high precision measurement of the angular distance at recombination, with a relative error $\sim 0.3\%$ [87].

Apart from the BAO, there are other contributions to the CMB anisotropies. Following Ref. [10], we list some of them:

- The Doppler effect. Produced by our motion relative to the CMB photons. It contributes with
$$\frac{\Delta T}{T} = \mathbf{n} \cdot (\mathbf{v_O} - \mathbf{v_E})\,, \tag{3.12}$$
where E stands for emitter and O for observer, $\mathbf{n}$ the direction of line of sight and $\mathbf{v_E}$ and $\mathbf{v_O}$ the velocity of the emitter and the observer, respectively.

- The Sachs-Wolfe (SW) effect:
  - The recombination Sachs-Wolfe effect [88]. Produced by the Thomson scattering of photons moving across inhomogeneities of the gravitational potential (ϕ) or matter peculiar velocities, at recombination time:
  $$\frac{\Delta T}{T} = \frac{1}{3}\Delta\phi\,. \tag{3.13}$$
  A Doppler effect will also contribute if photons are not at rest with respect to the Universe expansion at recombination.
  - The integrated Sachs-Wolfe (ISW) effect. Produced by all gravitational inhomogeneities that photons find after recombination in their travel to us.

[2]It can be discussed that, in a more general case, the speed of gravitational waves is more constrained, with $|c_{\rm gw} - 1| < 10^{-15}$ [71].

Using Ref. [89] notation,

$$\left(\frac{\Delta T}{T}\right)_{\mathrm{O}}^{\mathrm{SW}} = \left(\frac{\Delta T}{T}\right)_{\mathrm{E}} + \frac{1}{3}(\phi_{\mathrm{O}} - \phi_{\mathrm{E}}) + \mathbf{n}\cdot(\mathbf{v_O} - \mathbf{v_E}) + 2\int_{\mathrm{E}}^{\mathrm{O}} \mathrm{d}t \frac{\partial \phi}{\partial t}\,. \tag{3.14}$$

The first two terms are the acoustic peaks and the recombination SW effect, the next one is the Doppler effect and finally, the third one, is the ISW effect.

- Polarization effects [90]. Produced by Thomson scattering at decoupling.
- The Rees-Sciama effect [91]. Related to the SW effect, it is caused by photon's redshift when going through large evolving structures as galaxies or super-clusters, for which the gravitational potential when the photon enters differs from the gravitational potential when the photon escapes. It vanishes at linear theory of perturbations and affects at late times.
- The Sunyaev-Zel'dovich (SZ) effect. Produced by electrons scattering CMB photons going through X-ray emitting galaxy cluster gas. It can be divided in the kinetic SZ (kSZ) effect and the thermal SZ (tSZ), depending on whether the electron's motion is due to the cluster moving respect to the CMB or not, respectively.
- The Vishniac effect. Produced by the correlation between the motion of bulk electrons and their density. It contributes approximately as

$$\frac{\Delta T}{T} \sim -\int \mathrm{d}t\, n_e \sigma_{\mathrm{T}} \mathbf{n}\cdot\mathbf{v} e^{-\tau}\,, \tag{3.15}$$

  where $\mathbf{v}$ the electrons velocity and τ is the optical depth (Equation 2.64) along the line of sight. This is a second order effect that can become dominant at small scales.
- Gravitational lensing of the CMB radiation. Produced by matter distribution between the last scattering surface and us that deflects CMB photons.

As might have been noticed, we can classify these effects into two groups, depending on the moment when they affect. For instance, effects happening during recombination are called *primary* effects, while those taking place at late time are known as *secondary* effects. Of those listed above, the Doppler, SW and polarization effects would be primary effects. While the ISW, Rees-Sciama, SZ, Vishniac and lensing effects would be secondary effects.

CMB is affected by early universe physics making it an excellent probe to constrain inflationary models. During the typical single scalar inflationary models, the scalar field and tensor perturbations would be given by Equations 2.93 and 2.95

$$(a\delta\phi_{\mathbf{k}})'' + \left(k^2 - \frac{z''}{z}\right)(a\delta\phi_{\mathbf{k}}) = 0\,, \qquad (ah_{\mathbf{k}})'' + \left(k^2 - \frac{a''}{a}\right)(ah_{\mathbf{k}}) = 0\,, \tag{3.16}$$

where $\delta\phi_{\mathbf{k}}$ and $h_{\mathbf{k}}$ are the Fourier transformed of the inflationary scalar field fluctuation and the tensor perturbation of the metric, $z = a\dot{\delta\phi}_k$ and the primes denote derivatives respect to the conformal time.

The scalar field perturbation induces a perturbation on the curvature, $R = H\delta\phi/\dot{\phi}$, whose primordial power spectrum can be observationally constrained. For that, it is typically parametrized as (Equation 2.100)

$$P_R(k) = A_{\mathrm{s}}\left(\frac{k}{k_{\mathrm{p}}}\right)^{n_{\mathrm{s}}-1}\,, \tag{3.17}$$

where $A_{\rm s}$, the scalar amplitude, and $n_{\rm s}$, the spectral index, can be theoretically predicted by inflationary models. In general, $n_{\rm s}$ can depend on the scale, k. $k_{\rm p}$ is the pivot scale (sometimes also called k_*) and can be chosen arbitrarily, being $k_{\rm p} = 0.002\,{\rm Mpc}^{-1}$ Planck's choice [50]. Similarly, tensor perturbations can be described by (Equation 2.100)

$$P_T(k) = A_T \left(\frac{k}{k_{\rm p}}\right)^{n_T} , \tag{3.18}$$

with A_T, and n_T the tensorial equivalents of $A_{\rm s}$ and $n_{\rm s}$ [3]. Current observations have ruled out the scale invariant primordial matter spectrum, measuring $n_{\rm s} = 0.9649 \pm 0.0042$ at 68% confidence level (C. L.) and show no evidence of $n_{\rm s}$ scale dependence. Furthermore, they have constrained the tensor-to-scalar ratio, $r \equiv A_T/A_{\rm s}$, to $r_{0.002} < 0.056$ [50]. The finding of tensor perturbations, predicted by many inflationary models, would greatly strengthen the idea of the existence of an inflationary epoch. However, typical models predict $N \sim 50 - 60$ e-folds during inflation and (see e.g. our work on the α-attractors in Chapter 6)

$$n_{\rm s} \simeq 1 + \frac{2}{N} , \qquad r \simeq \frac{12}{N^2} , \tag{3.19}$$

implying that $A_T \sim 10^{-3} A_{\rm s}$. Reaching such values not only needs more precise equipment but also of a better description of CMB foregrounds and contaminants.

The accurate measurements of the scalar amplitude needs of polarization data at large scales, so that the degeneracy with the reionization optical depth, τ, is broken. Doing so, $A_{\rm s}$ has been constrained to $\ln(10^{10} A_{\rm s}) = 3.044 \pm 0.014$ [50]. The reionization optical depth (τ) is the average length that is expected to travel a photon during recombination, scattered by the electrons that took a small but finite time to decouple from photons (Equation 2.64). It has been measured to be $\tau = 0.0544 \pm 0.0073$. Other quantity related to $P_{\rm m}$ is σ_8, the root mean square fluctuation in the total matter density, $\delta_{\rm m}$, in a sphere of radius $R = 8h^{-1}\,{\rm Mpc}$,

$$\sigma_8^2 = \langle \delta_{\rm m}(R, \mathbf{x})^2 W(R, r)^2 \rangle = \int \frac{{\rm d}^3\mathbf{k}}{(2\pi)^3} P_{\rm m} W(kR)^2 , \tag{3.20}$$

where W is a filter function that one applies to the δ field (i.e. $\delta \to W\delta$) in order to remove scales above R. A common one is the Top Hat filter, $W(R, r) = \Theta(R - r)$, where Θ is the Heaviside functional, whose Fourier transform is

$$W(kR) = \frac{3}{(kR)^3} [\sin(kR) - (kR)\cos(kR)] \tag{3.21}$$

CMB Planck's σ_8 value is $\sigma_8 = 0.8111 \pm 0.0060$.

Next-generation Stage-4 CMB surveys will continue increasing the cosmological parameter estimation precision (see Table 3.1). In particular, they will be able to determine r with 0.1% precision, being able to go as low as $r \sim 0.001$ [92]. This could have a huge impact on inflationary physics for which setting an upper bound $r < 0.001$ would rule out many models. In addition, it will also increase the precision to $\sim 30\%$ on the number of species and neutrino masses, when next-generation CMB and LSS data are used together. This is only an skim of the Stage-4 CMB capabilities and uses, for further reference we point to Section 5.5 and Ref. [92].

[3] The reason why $n_{\rm s}$ has a -1 as companion is because P_R is expected (and known [50]) to be almost scale invariant and, consequently, $n_{\rm s} \sim 1$

	Fiducial	Planck	S4 + Planck
$100\Omega_{\rm b}h^2$	2.22	±0.017	±0.003
$\Omega_{\rm cdm}h^2$	0.120	±0.0014	±0.0006
H_0	69.0	±0.7	±0.24
$10^9 A_{\rm s}$	2.2	±0.039	±0.021
$n_{\rm s}$	0.966	±0.004	±0.002
τ	0.06	±0.01	±0.006

Table 3.1: Stage-4 CMB cosmological parameters error estimates for ΛCDM. Taken from Table 8-1 of Ref. [92].

3.2 The Large Scale Structure (LSS)

The primordial fluctuations seen in the CMB evolved and grew on time giving us the Universe we see today. At some point, the smallest scales (i.e. $k \gtrsim 0.1h^{-1}\,\text{Mpc}$) stopped been governed by linear perturbation theory and more complex dynamics started to play a role. For instance, galaxy evolution or star formation are two completely non-linear processes and must be studied doing complex simulations. However, at large scales, the Universe is still homogeneous and isotropic and can be described with linear perturbation theory.

In contrast to CMB, that was almost instantaneous, LSS formation and evolution was a slow process, allowing for 3D maps (ϕ, θ, z). The LSS mapped quantities are the number of galaxies and the two shear modes (how the observed galaxy image is deformed by weak lensing). Finding the galaxy redshift location from its projected image is a complex process. The most accurate method is the spectroscopic analysis of the galaxy, that analyzes its spectra in the galaxy rest-frame and fits the redshift using some predefined templates (see e.g. [93]). However, this technique is very time consuming. First, it requires a long exposure time to compensate the intensity loss in the spectral decomposition. Secondly, one needs to previously know the galaxy location to set a plate with optic fiber at this specific place. This work has been done manually so far but, fortunately, DESI has automatized the process and will be able to take measures of 35 million of galaxies (including QSOs) up to $z \gtrsim 2.1$ over 5 years (2019 - 2024) [94]. On the other hand, one can relax the redshift determination. In photometric experiments, one tries to fit the spectra using just a few broad frequency channels. This makes the determination much faster (both because of the fewer points to fit, as well as for the higher light intensity in each channel), but also more redshift inacurate, allowing for larger and deeper samples than spectroscopic experiments. For instance, LSST will provide photometry for 10^{10} galaxies up to $z \gtrsim 6$ and shape measurements and six-band photometry for 4×10^9 galaxies [17].

Many other LSS surveys, such as Euclid [79] and WFIRST [78] will start collecting data during the next decade. This will result on many independent measurements of overlapping areas on the sky, which will even allow to beat the cosmic variance for some parameters by measuring the cross-correlations between different overlapping distribution maps [58].

The statistical treatment of LSS data is similar to CMB data. One has pixelated maps of galaxy number counts (or the galaxy overdensity) and the value of their shear modes, that can be used to compute statistical quantities such as the power spectrum (Equation 3.2) or the correlation function, $\xi(r)$ (Equation 3.1).

The matter distribution can be estimated using the galaxies distribution. In particular, the matter perturbations can be traced with the galaxy overdensity field. For this, the power spectrum is given by $P(\mathbf{k}) = V\delta_{\mathbf{k}}\delta^*_{\mathbf{k}}$, where $\delta_{\mathbf{k}}$ is the Fourier transform of the density contrast

field $\delta(\mathbf{x})$,

$$\delta_{\mathbf{k}} = \frac{1}{V}\int dV e^{-i\mathbf{k}\cdot\mathbf{x}}\delta(\mathbf{x})\,, \tag{3.22}$$

where V is the volume covered by the survey. However, luminous matter is just a fraction of the total matter of galaxies and, therefore, the resulting power spectrum is biased, at the linear level, by a factor $b \equiv \delta_{\rm g}/\delta_{\rm m}$,

$$P_{\rm g}(k) = b^2 P_{\rm m}(k)\,, \tag{3.23}$$

where g stands for galaxy, m for the total matter and $\delta_i \equiv \delta\rho_i/\bar{\rho}_i$ stands for the density contrast. In comparison, the weak lensing shear field is an unbiased estimator of the underlying matter distribution. The reason is that weak lensing is an effect produced by all matter between the source and us, and not only by galaxies.

For galaxy clustering measurements one must take, at least, another effect into account apart from the galaxy bias: the galaxies peculiar velocity, which will have a contribution to the total redshift. At small scales, galaxies move randomly inside galaxy clusters, resulting in the *fingers of God* effect. At large scales, however, galaxies are coupled to the density fields that push them to form larger structures. This effect shifts the real space overdensity value respect to that in redshift space by [95]

$$\delta_{{\rm s}k} = \delta_{{\rm r}k}(1+\beta\mu^2)\,, \tag{3.24}$$

where the subindices s and r stand for redshift and real space, respectively, and $\beta = f/b$ and $\mu = \cos(\widehat{\mathbf{k}\cdot\mathbf{r}})$, where $f = {\rm d}\log(\delta_{\rm m})/{\rm d}\log(a) = \dot{\delta_{\rm m}}/(H\delta_{\rm m})$ is the growth rate and $\mathbf{r}$ is the galaxy position vector. Therefore,

$$P_{\rm s}(\mathbf{k}) = P_{\rm r}(\mathbf{k})(1+\beta\mu^2)^2\,, \tag{3.25}$$

which, averaged over angles, becomes

$$P_{\rm s}(k) = P_{\rm r}(k)(1+2\beta/3+\beta/5)^2\,. \tag{3.26}$$

This boosts the power spectrum in redshift space as a result of the accretion of galaxies, making them look closer than in real space.

In addition, one has to subtract the shot noise that comes from the fact that galaxies follow a Poisson distribution and are observed on small independent patches of sky. Shot noise scales as $N^{-1/2}$, with N the number of galaxies observed and, therefore, its power spectra $P_{\rm SN} \propto N^{-1}$.

These corrections are the main contributions that must be taken into account for the overdensity power spectrum measurement. However, one also needs to assume a cosmology to obtain the actual angles and distances that go into the previous expressions. Fortunately, one can use invariant observables to relate two different cosmologies. In fact, taking into account that the subtended angle of a given feature on the sky and its comoving scale along the line of sight must be independent of the cosmology, one can see that

$$k_\perp = \frac{k_{{\rm r}\perp} d_{\rm r}}{d}\,, \qquad k_\parallel = \frac{k_{{\rm r}\parallel} H}{H_{\rm r}}\,, \tag{3.27}$$

where d stands for a distance, the subindex r for a reference cosmology, and $k_\perp$ and $k_\parallel$ are the perpendicular and parallel to the light of sight components of the vector $\mathbf{k}$. These expressions allow us to relate

$$k = Rk_{\rm r} \qquad \text{and} \qquad \mu = \frac{H\mu_{\rm r}}{H_{\rm r}R}, \tag{3.28}$$

with

$$R = \frac{\sqrt{H^2 d^2 \mu_{\rm r}^2 - H_{\rm r}^2 d_{\rm r}^2(\mu_{\rm r}^2-1)}}{H_{\rm r} d}\,. \tag{3.29}$$

Furthermore, the volume where the perturbation is measured is given by $V = \Theta^2 r^2 dr = d^2/H\mathrm{d}z$. Since $\mathrm{d}z$ is an observed quantity and, therefore, does not depend on our assumptions, VH/d^2 must be conserved and

$$V = V_r \frac{H_r d^2}{H d_r^2} \,. \tag{3.30}$$

Then, the observed power spectra is related to the true underlying one by

$$P_{\rm r}(k_{\rm r}, z) = \frac{H d_{\rm r}^2}{H_{\rm r} d^2} P(R k_{\rm r}, z) \tag{3.31}$$

which must be corrected for the observational effects previously mentioned to give

$$P_{\rm r}^{\rm obs}(k_{\rm r}, z) = P_{\rm SN}(z) + \frac{H d_{\rm r}^2}{H_{\rm r} d^2} D^2(z) b^2(z) [1 + \beta(z)^2 \mu^2]^2 P(R k_{\rm r}, z = 0) \,, \tag{3.32}$$

where $D(z) = \delta_{\rm m}(z)/\delta_{\rm m}(0)$ is the growth factor and relates the power spectra $P(k, z) = D(z)P(k, z = 0)$. This will still hold for modifications that do not vary much the sound speed so that the perturbation growth continues being scale independent.

A more detailed derivation of the previous discussion (and what follows) can be found in Ref. [9].

In the following sections, we will review some of the main features of LSS analysis of cosmological interest.

3.2.1 Baryon Acoustic Oscilations (BAO)

The overdensity 2-point correlation function and the power spectra show the imprint of the BAO, which are known to have a fixed comoving scale given by the sound horizon at drag epoch, $r_{\rm d}$ (Equation 3.10). In general, if we did not know the absolute value of the sound horizon, the best we could do would be to measure the ratios of the angular diameter distance tracking its evolution on time,

$$\frac{\Theta_1}{\Theta_2} = \frac{D_{\rm A}(z_2)(1+z_2)}{D_{\rm A}(z_1)(1+z_1)} \,, \qquad \frac{z_1}{z_2} \simeq \frac{H(z_1)}{H(z_2)} \,, \tag{3.33}$$

taking into account that the subtended angle of a given feature on the sky and its comoving scale along the line of sight are invariants.

Fortunately, $r_{\rm d}$ can be computed in a fiducial cosmology and constrain the change rates, $\alpha_\perp$ and $\alpha_\parallel$ [49, 96]:

$$\frac{D_{\rm M}(z)}{r_{\rm d}} = \alpha_\perp \frac{D_{\rm M}^{\rm fid}(z)}{r_{\rm d}^{\rm fid}} \,, \qquad \frac{D_{\rm H}(z)}{r_{\rm d}} = \alpha_\parallel \frac{D_{\rm H}^{\rm fid}(z)}{r_{\rm d}^{\rm fid}} \,, \tag{3.34}$$

where $D_{\rm H} = H^{-1}$. Alternatively, one can define the isotropically-averaged shift α and the warping factor, ϵ,

$$\alpha = \alpha_\perp^{2/3} \alpha_\parallel^{1/3} \,, \qquad \epsilon + 1 = \left(\frac{\alpha_\parallel}{\alpha_\perp} \right)^{1/3} \,, \tag{3.35}$$

and the more physical quantities, the spherical-averaged distance, $D_{\rm V}$, and the Alcock-Plaszczynski parameter, $F_{\rm AP}$,

$$D_{\rm V}(z) = \left[D_{\rm M}(z)^2 \frac{z}{H(z)} \right]^{1/3} \,, \qquad F_{\rm AP}(z) = D_{\rm M}(z) H(z) \,. \tag{3.36}$$

The physical meaning of $D_{\rm V}$ can be easily identified taking into account that BAO measurements along different redshifts track the evolution of the BAO peak in the correlation function, which

is basically the volume of a sphere of radious $r_{\rm d}$. This approximation is valid provided that one can neglect redshift distortions, which is true in luminous galaxy surveys but not for the Lyman-α Forest [96].

3.2.2 Growth function

As we saw before, the growth and the redshift distorsions are related by $\beta = f/b$. This means that once we know the bias, we can estimate f by measuring β from data. This, in turn, will allow us to search for discrepancies with ΛCDM, for which, $f = \Omega_{\rm m}^{\gamma}$, with $\gamma \sim 0.55$ [97]. In case dark energy is not the cosmological constant, this simple relation between expansion and growth does not necessarily hold. For instance, the simplest extensions would modify γ to $\gamma = \gamma(w_{\rm DE})$ [98].

In this studies, it is more common to work with the correlation function instead of the power spectrum. Fourier transforming Equation 3.25, we can obtain the correlation function in terms of β and μ [99],

$$\xi_s(r,\mu) = \xi_0(r)\mathcal{P}_0(\mu) + \xi_2(r)\mathcal{P}_2(\mu) + \xi_4(r)\mathcal{P}_4(\mu)\,, \tag{3.37}$$

where μ is the cosine of the angle formed by the line of sight and the location $\mathbf{r}$ and $\mathcal{P}_\ell(\mu)$ are Legendre polynomials whose values are $\mathcal{P}_0 = 1$, $\mathcal{P}_2 = (3\mu^2-1)/2$ and $\mathcal{P}_4 = (35\mu^4-30\mu^2+3)/8$. Finally,

$$\xi_0 = \left(1+\frac{2}{3}\beta+\frac{1}{5}\beta^2\right)\xi_r\,, \qquad \xi_2 = \left(\frac{4}{3}\beta+\frac{4}{7}\beta^2\right)[\xi_r - I_2]\,, \qquad \xi_4 = \frac{8}{35}\beta^2\left(\xi_r(r)+\frac{5}{2}I_2+\frac{7}{2}I_4\right)\,, \tag{3.38}$$

that depend on the undistorted correlation function, ξ_r, and have

$$I_2 = 3r^{-3}\int_0^r {\rm d}y y^2\xi_r(y)\,, \qquad I_4 = 5r^{-5}\int_0^r {\rm d}y y^4\xi_r(y)\,, \tag{3.39}$$

The undistorted ξ_r can be obtained from data using the Abel transform [100],

$$\xi_r(r) = -\frac{1}{\pi}\int_r^\infty {\rm d}\sigma \frac{{\rm d}\Xi(\sigma)/{\rm d}\sigma}{\sqrt{\sigma^2-r^2}}\,, \tag{3.40}$$

where $\Xi(\sigma)$ is the correlation along the transverse (to the line of sight, $\boldsymbol{\pi}$) correlation, which is not affected by the redshift distorsions,

$$\Xi(\sigma) = 2\int_0^\infty {\rm d}\pi \xi(\sigma,\pi)\,. \tag{3.41}$$

So far, we have only addressed the redshift distorsion effect that comes from the large scale velocities of galaxies draged by the gravitational potential. However, one must take also into account the *fingers of God* effect, produced by the random motion of galaxies well inside the galaxy cluster. This effect modifies the observed line-of-sight separation, π, by adding an additional term to the true separation, π_t,

$$\pi = \pi_t + \frac{v(1+z)}{H(z)}\,. \tag{3.42}$$

The peculiar velocities at small scales, v, follow an exponential distribution

$$f(v) = \frac{1}{\sqrt{2\sigma^2}}e^{-\sqrt{2}|v|/\sigma_v}\,, \tag{3.43}$$

with a velocity dispersion $\sigma_v \sim 500\,\mathrm{km\,s^{-1}}$. Therefore, the observed correlation function will be given by

$$\sigma_s(\sigma,\pi) = \int_0^\infty \mathrm{d}v f(v) \sigma_s \left[\sigma, \pi_t = \pi - \frac{v(1+z)}{H(z)}\right] . \tag{3.44}$$

In the end, one will fit $\sigma_s(\sigma,\pi;\beta,\sigma_v)$, given by the previous equation, to data and obtain β. Note, however, that all equations derived have an implicit model dependence through geometry, in particular $\mathrm{d}r = \mathrm{d}z/H$. Therefore, the estimation of β (and, consequently, f) will depend on the cosmological model assumed and one would have to repeat the study for a different set of parameters. Alternatively, one could generalized $\sigma_s(\sigma,\pi;\beta,\sigma_v)$ to explicitly include the cosmological parameters.

3.2.3 Shear

Large Scale Structure surveys, apart from counting the number of galaxies, can infer their shapes. Since light interacts with matter gravitationally, their shapes on the sky are modified versions of the source's one. Estimating their deformation is an important cosmological probe that allows to infer the weak lensing parameters κ (the convergence, that magnifies the image) and γ_1 and γ_2 (the shear modes, that stretch its shape). Furthermore, its statistical nature make it an unbiased estimator of the matter distribution.

Observationally, a galaxy is described by a luminous intensity function $I(\theta_x,\theta_y)$, centered at $\theta = (\theta_1,\theta_2) = (0,0)$. Then, one can calculate its ellipticity using the quadrupole,

$$q_{ij} = \int \mathrm{d}^2\theta I(\theta)\theta_i\theta_j \,, \tag{3.45}$$

for which the ellipticity is

$$\epsilon_1 = \frac{q_{11}-q_{22}}{q_{11}+q_{22}} \,, \qquad \epsilon_2 = \frac{2q_{12}}{q_{11}+q_{22}} \,, \tag{3.46}$$

and are related to the shear modes at first order by

$$\epsilon_1 \approx 2\gamma_1 \,, \qquad \epsilon_2 \approx 2\gamma_2 \,. \tag{3.47}$$

Apart from the gravitationally induced ellipticity, galaxies have an internal ellipticity that we take into account as shot noise. Consequently, it adds to the weak lensing power spectra

$$P_{\mathrm{int}} = \gamma_{\mathrm{int}} \frac{V}{N} \,, \tag{3.48}$$

where $\gamma_{\mathrm{int}} \equiv \langle (\gamma_i^{\mathrm{Shot}})^2 \rangle$. For instance, $\gamma_{\mathrm{int}} \simeq 0.28$ for LSST [17].

In addition, the final image distortion is the result of the gravitational effect of multiple galaxies between the source and us. In the linear level, we can simply add their contributions. This means that, for a number galaxy density, $n(r)$, the total distortion matrix is

$$D_{ij} = \int_0^\infty \mathrm{d}r' n(r') \int_0^{r'} \mathrm{d}r \left(1 - \frac{r}{r'}\right) r\psi_{,ij} = \int_0^\infty \mathrm{d}r w(r) \psi_{,ij} \,, \tag{3.49}$$

with

$$w(r) = \int_r^\infty \mathrm{d}r' \left(1 - \frac{r}{r'}\right) r n(r') \tag{3.50}$$

and $\psi \equiv \Phi - \Psi$ the lensing potential, whose gradient defines the photon's trajectory, $\mathrm{d}^2x^i/\mathrm{d}^2r = \mathrm{d}^2(r\theta^i)/\mathrm{d}^2r = \psi_{,i}$. In the previous expression, we took into account that the image displacement will be small and the approximation $x^i = r\theta^i$ holds. In redshift space,

$$D_{ij} = \int_0^\infty \frac{\mathrm{d}z}{H(z)} w(z)\psi_{,ij}[r(z), \theta_x r(z), \theta_y r(z)] \,. \tag{3.51}$$

This is a convenient expression that can be directly related with a power spectrum in 2D using the Limber equation that relates [101]:

$$F(\theta_x, \theta_y) = \int_0^\infty \mathrm{d}r w(r) f(r, \theta_x r, \theta_y) \longrightarrow P(q) = \int_0^\infty \mathrm{d}r \frac{w(r)^2}{r^2} p(q/r) \,, \tag{3.52}$$

where f is a field projected along the r-direction with a unit-normalized weight $w(r)$ and $p(k)$ is the power spectrum of f and q the modulus of $\mathbf{q} = (q_1, q_2)$.

Assuming GR and no anisotropic stress ($\Phi = -\Psi$), the Poisson equation (Equation 2.34) reads $k^2\psi_k = 3a^2H^2\Omega_\mathrm{m}\delta_\mathrm{m}$, and the convergence ($\kappa = -(D_{11} + D_{22})/2$) power spectrum is

$$P_\kappa(q) = \frac{9H_0^3}{4} \int_0^\infty \mathrm{d}z \frac{W(z)^2 E^3(z) \Omega_\mathrm{m}^2(z)}{(1+z)^4} P_{\delta_\mathrm{m}}(q/r(z)) \,, \tag{3.53}$$

where $E(z) = H(z)/H_0$ and $W(z)$ is the window function given by

$$W(z) = \int_z^\infty \frac{\mathrm{d}z'}{H(z')} \left(1 - \frac{r(z)}{r(z')}\right) n(r(z')) \,. \tag{3.54}$$

At small angles, $q = \ell/\pi$, which serves to compute the angular power spectrum.

The power spectrum of the shear modes are directly related to the convergence power spectrum and, at linear order,

$$P_{\gamma_1} = \frac{(k_x^2 - k_y^2)^2}{4k^4} P_\kappa \,, \qquad P_{\gamma_2} = \frac{(k_x^2 k_y^2)^2}{k^4} P_\kappa \,, \tag{3.55}$$

which allow to define the *electric* and *magnetic* shear components

$$E = \cos(2\phi)\gamma_1 + \sin(2\phi)\gamma_2 \tag{3.56}$$

$$B = -\sin(2\phi)\gamma_1 + \cos(2\phi)\gamma_2 \,, \tag{3.57}$$

where ϕ is the angular component of the wave vector. This yields

$$P_E = P_\kappa \,, \qquad P_B = 0. \tag{3.58}$$

For photometric surveys with galaxies in different redshift bins, there exists a correlation between different redshift bin populations [102] and can be written as

$$P_{ij}(\ell) = \frac{9H_0^3}{4} \int_0^\infty \mathrm{d}z \frac{W_i(z) W_j(z) E^3(z) \Omega_\mathrm{m}^2(z)}{(1+z)^4} P_{\delta_\mathrm{m}} \left(\frac{\ell}{\pi r(z)}\right) \,, \tag{3.59}$$

where, now, the window function W_i depends on the number density function of redshift bin i, n_i,

$$W_i(z) = \int_z^\infty \frac{\mathrm{d}z'}{H(z')} \left(1 - \frac{r(z)}{r(z')}\right) n_i(r(z')) \,. \tag{3.60}$$

If we did not assume GR, the matter overdensity power spectrum would be modified, at linear order, by

$$\Sigma \equiv q(1 - \zeta/2) \,, \tag{3.61}$$

which changes the lensing potential through

$$\frac{k^2}{a^2}\psi_k = \Sigma\rho_{\rm m}\delta_{\rm m} \tag{3.62}$$

The parameters $q = q(\ell, t)$ and $\zeta(\ell, t)$ encompass the modifications to Gravity and are defined by

$$\frac{k^2}{a^2}\Phi = 4\pi G q \delta_{\rm m}\rho_{\rm m}\,, \qquad \frac{\Phi+\Psi}{\Phi} = \zeta\,. \tag{3.63}$$

Note that ΛCDM is recovered by setting $q = 1$ and $\zeta = 0$ [4].

These expressions have been obtained in the linear regime and are valid just at large scales. In particular, the scale cut $\ell_{\rm max} \sim 500$ has been used in weak lensing studies (e.g. Ref. [103]). However, next-generation maps will have a much finer resolution and much larger $\ell_{\rm max}$. In order to be able to use the information of such scales, one needs to incorporate extra effects that we have neglected so far at the linear level and some corrections at non-linear level. For instance,

- magnification bias. Actual galaxy counts differ from randomly simulated maps by a factor given by the magnification bias. It varies with the sample [104].

- intrinsic alignments. Galaxies, depending on their kind, might tend to be oriented in the direction of the density field. It has been studied in simulations [105–110] and observations [106, 111–116] finding a dependence on the galaxy population and type. In particular, blue (spiral) galaxies intrinsic alignment measurements are compatible with 0 [112, 116]. This effect contributes less than a 5% to the lensing signal at scales above 1 arcmin but up to $\sim 50\%$ at smaller separations [110, 114].

- redshift bins overlapping. Galaxy populations in photometric surveys are distributed in width redshift bins that overlap. This overlapping introduces correlations that must be correctly addressed to accurately describe matter distribution (e.g. see LSST Science Book [17] or our work on the estimation of the Gaussian part of the covariance matrix for LSS surveys in Chapter 8).

- non-weak shear. The presence of massive halos induces a strong lensing. In particular, the shear coefficient is modified to

  $$\hat{\gamma} = \frac{\gamma}{1-\kappa}\,, \tag{3.64}$$

  which deviate about a 15% from γ at $20h^{-1}$ kpc [104]. This effect would contribute at non-linear scales.

In addition, one has to correctly model the systematic errors that introduce the observation and image processing. For an extended analysis of such processes see, for example, Ref. [117].

An important result of current weak lensing measurements is that of KiDS-450 [118] that shows a tension of $3.2\,\sigma$ with respect to Planck's CMB value of σ_8, having measured $S_8 \equiv \sigma_8\sqrt{\Omega_{\rm m}/0.3} = 0.651 \pm 0.0058$ [51] in contrast to the $S_8 = 0.832 \pm 0.013$ from Planck [43]. This tension is not present, however, in DES estimations [21]. Therefore, it will be the next-generation surveys which will allow to see if this discrepancy is physical or not. Nevertheless, it might constitute, together with the H_0 tension that we will talk about in next Section, another hint of physics beyond ΛCDM.

[4] It is also common to parametrize the presence of an anisotropic stress with $\eta \equiv \Phi/\Psi = (\zeta - 1)^{-1}$. In this case, GR is recovered with $\Sigma = \eta = q = 1$.

3.3 Type Ia supernovae (SNe Ia)

The distance measurements of Type Ia supernovae allowed the discovery of the accelerated expansion of the Universe by two independent groups: the Supernova Cosmology Project [61] and the High-Z Supernova Search Team [60]. The SNe Ia are standard candles as their light curves can be used to estimate their distance. In general, one can relate the apparent magnitude, m, of an object of known absolute magnitude, M, with the luminosity distance by

$$m = M + 5\log_{10}(D_{\rm L}) + 25\,. \tag{3.65}$$

However, in order to apply this to SN Ia light curves they need to be first calibrated. This is possible because the SNe Ia form a family that has the light curves' rate of declination correlated with the maximum luminosity, which is taken into account in the SN parametrization. For their calibration, we can remark two different numerical approaches, given their historical relevance: the *multi-colour light curve shape (MLCS)* [60, 119] and the *stretch* [120] methods. The MLCS method was used by the High-Z Supernova Search Team and consists of a linear algorithm that is able to match supernovae light curves to precomputed templates. On the other hand, the *stretch* method set the light curves in the supernova local frame by, roughly, normalizing their time delay.

In addition to color and stretch, it has been noticed a correlation of the residuals of the curve fit with the host galaxy mass. It is not yet clear its origin and there is ongoing research in order to identify what characteristic of the galaxy is causing it. However, it has been seen that a step function with $m < 10^{10} M_{\rm sun}$ in the fit can remove the correlation [121].

Once calibrated, one can test cosmological models with a modified version of previous Equation 3.65 [122],

$$m^{\rm mod} = 5\log_{10}(\mathcal{D}_{\rm L}) + \mathcal{M} - \alpha(s-1) + \beta\mathcal{C} + \delta P(M_{\rm stellar} < 10^{10} M_{\rm Sun})\,, \tag{3.66}$$

that accounts for correlations with the stretch, s, and color, $\mathcal{C}$, which are obtained fitting the light curve, and the host galaxy mass, $\delta P(M_{\rm stellar} < 10^{10} M_{\rm Sun})$. Following Ref. [122] the host galaxy mass term is added with a probability, P, to address the possible lack of information about the host galaxies mass. This was their case when using the Union2 compilation. The parameter $\mathcal{D}_{\rm L} = H_0 D_{\rm L}$ factors out the H_0 dependence, which is introduced in $\mathcal{M} = M - 5\log_{10} H_0 + 25$. $\mathcal{M}$, together with α and β, are nuisance parameters that must be fitted simultaneously with the cosmological parameters.

The parameter estimation is done minimizing the χ^2,

$$\chi^2 = \sum_{\rm sample} \frac{m^{\rm obs} - m^{\rm mod}}{\sigma^2}\,, \tag{3.67}$$

where $m^{\rm obs}$ is the observed magnitude and σ^2 the error in the measurement which can be divided on [123]: $\sigma_{\rm lc}$, that accounts for inaccuracies fitting the light curves, specially the color corrections; $\sigma_{\rm ext}$, sourced by host galaxies peculiar velocities, galaxy extinction and gravitational lensing effects; and $\sigma_{\rm sys}$ estimates the systematic errors from different samples, which are assumed to be of similar accuracy.

Once $m^{\rm mod}$ is obtained, one gets a value for the expansion rate of the Universe, $E(z) = H(z)/H_0$ (e.g. Ref [62]), at a given redshift. The relation between $m^{\rm mod}$ and the expansion rate is given by Equation 3.66 taking into account that the luminous distance is defined as

$$\mathcal{D}_{\rm L} = H_0 \int_0^z \frac{{\rm d}z'}{H(z')} = \int_0^z \frac{{\rm d}z'}{E(z')}\,. \tag{3.68}$$

Therefore, it is possible to track the evolution of the expansion rate with SN Ia measurements at different redshifts. This served to discover the accelerated expansion of the Universe and support the existence of dark energy [60, 61] and will serve to test different cosmological models.

At this moment, the most complete available sample is the Pantheon sample [124]. It includes the full set of spectroscopically confirmed SNe Ia from Pan-STARRS1 (PS1) Medium Deep Survey [125, 126], and spectroscopically confirmed SNe Ia from CfA1-4 [127–129], the Carnegie Supernova Project (CSP) [130–132], the Sloan Digital Sky Survey (SDSS) [133–135], the Supernova Legacy Survey (SNLS) [136–138], the Hubble Space Telescope (HST) Supernova surveys, the Hubble Deep Field North (HDFN) [139] survey, the Great Observatories Origins Deep Survey (GOODS) [140, 141], the Probing Acceleration Now with Supernova (PANS)[142] survey, the Cluster Supernova Search (CSS) [122] and CLASH/CANDELS[5] [62, 143, 144]. In total, Pantheon sample is formed of 1048 SNe Ia ranging $0.01 < z < 2.3$; of which, 279 SNe Ia come from PS1 ($0.03 \lesssim z \lesssim 0.68$). CfA1-4 and CSP are low redshift surveys and cover $0.01 \lesssim z \lesssim 0.1$, SDSS goes deeper with redshifts in $0.1 \lesssim z \lesssim 0.4$. The SNLS sample overlap previous ranges with supernovae in $0.3 \lesssim z \lesssim 1.1$. Finally, the HST SN samples reach to $z \sim 2.3$. Therefore, Pantheon sample is able to track the expansion rate from the dark energy dominated era to the matter dominated era, setting constraints on the change from a decelerated to an accelerated expanding Universe.

3.3.1 The "distance ladder" and the H_0 tension

While the expansion rate, $E(z)$, is inferred from the measurement of the relative magnitude, $m^{\rm mod}$, the determination of H_0 requires an accurate calibration of the absolute magnitude, M, that enters in the fitting parameter $\mathcal{M} = M - 5\log_{10} H_0 + 25$. The absolute magnitude depends on the distance to the SN, which cannot be estimated from itself. It requires to be estimated from other standard candel. The process of determining the distance of further objects using closer objects of known distance is known as the *distance ladder*. The most accepted method is the Cepheids and SNe distance ladder, which uses Cepheid stars to calibrate the distance to the SNe. One can, however, use other methods, such as those based on stars on the Tip of the Red Giant Branch (TRGB) or maser galaxies.

The Cepheids are variable stars with a periodic light cycle that can be related to their luminosity by the Leavitt Law, $L \propto P^{4/3}$, where P is the pulsational period of the star. As happened with the SNe Ia, Chepeids observations also need to take into consideration both cosmological and astrophysical effects that can produce color and luminosity intensity changes. Furthermore, they need to be tracked for a period to correctly determine its light cycle. In general, the light cycle range between $-2 < M < -6\,$mag, in a period of $2 \lesssim P \lesssim 100\,$days, which can be observationally challenging [145].

With the TRGB method, on the contrary, one just need to measure two different wavelengths (to account for interstellar extinction) at a single-epoch. This is so because stellar evolution is a well understood process and mainly determined by the mass of the star (M) and its color (related to its temperature, T), so that $L \sim M^2T^5$ [145]. However, TRGB stars are much fainter than Cepheids and cannot be used to calibrate distances as far as with them.

Using Cepheids, current estimates of H_0 disagree with Planck's by 4.4σ, having determined $H_0 = 74.03 \pm 1.42\,{\rm km\,s^{-1}Mpc^{-1}}$ [20] [6], in comparison with $H_0 = 67.4 \pm 0.5\,{\rm km\,s^{-1}Mpc^{-1}}$ [43].

[5]For their length we have omitted the full survey names in the main body of the text. CLASH stands for the Cluster Lensing And Supernova survey with Hubble and CANDELS for the Cosmic Assembly Near-infrared Deep Extragalactic Legacy Survey

[6]The H0LiCOW collaboration [146] has also estimated the value of H_0 using time-delay cosmography with quasars. It also shows a higher value of H_0 ($H_0 = 73.3^{+1.7}_{-1.8}\,{\rm km\,s^{-1}Mpc^{-1}}$) compatible with Riess et al. estimation [147]. However, one must bear in mind the complexity of this technique and the possibility of missing

However, recent estimates using the TRGB method yield an intermediate value, $H_0 = 69.8 \pm 1.9\,\mathrm{km\,s^{-1}Mpc^{-1}}$, which is 1.2σ off Planck's measurement and 1.7σ from the Cepheid-based one [23]. In addition, based on an assumption of Gaia DR2 [149] systematic error, Ref. [24] claims that previous Milky Way Cepheid calibrators and 46 Cepheids in Riess et al. scale are $\sim 12 - 15\%$ and $4.7 \pm 1.7\%$, respectively, farther than previously thought. Consequently, the Hubble parameter would be reduced to [7] $H_0 \approx 70.2 \pm 1.2\,\mathrm{km\,s^{-1}Mpc^{-1}}$, reducing the discrepancy with Planck's result to $\sim 2\sigma$ [8].

Next-generation experiments will be able to determine H_0 precisely. In fact, Gaia geometrical calibration of Cepheids and detached binaries in the Large Magellanic Cloud will make the H_0 determination be limited by the SN Ia sample size [151]. Fortunately, new samples are expected to be much larger allowing for a statistical significance increase of orders of magnitude. At low redshift ($z < 0.1$) it will grow by 5 times, due to the Zwicky Transient Facility (ZTF) [152], the Foundation Supernova Survey (FSS) [153], ATLAS [154] and the All-Sky Automated Survey for Supernovae (ASAS-SN) [155]; at mid redshift ($0.1 < z < 1$) by 2, thanks to the Dark Energy Survey (DES) [156] and by 300, thanks to LSST [34]; at high redshift ($z > 1$), the boost will be of order 1000 with WFIRST [78, 157, 158] data. Finally, provided that the SNe Ia are abundant at even higher redshifts, LSST [159] and the James Webb Space Telescope (JWST) [160] might be able to go as deep as $z \sim 5$. Therefore, if the H_0 tension is real, it will grow with new samples and will be a clear signature of physics beyond the Cosmological Standard Model pointing towards more complicated forms of dark energy.

3.4 Gravitational Waves (GW)

Gravitational wave astronomy is now a reality. The Advanced Laser Interferometer Gravitational-Wave Observatory (LIGO) [81] detected the first gravitational wave (GW150914) on September 14, 2015 [63] and, after that, many other detections have been reported [161]. The estimations on the detection rate are not yet clear as the physics/astrophysics leading to the formation of gravitational waves sources is not well understood yet (see e.g. [162]). Nonetheless, around 10^4 events might have been cataloged by 2030 [163].

Having observed the existence of gravitational waves is a remarkable milestone, probing true, once again, the predictions of GR. However, it might be equally or more important for this Thesis the measurement of the gravitational wave speed, which were seen to travel at the speed of light ($-3 \times 10^{-15} < c_{\mathrm{gw}} - 1 < 7 \times 10^{-16}$ at 95% C. L.) [71]. This was possible thanks to the detection of the gravitational wave (GW170817) and its electromagnetic counterpart (GRB170817A) on August 17, 2017 [71]. This is extremely important as having $c_{\mathrm{gw}} = c$ (might[9]) heavily restrict the possible modifications of Gravity (see e.g. Refs. [28, 65–70]).

Apart from (Advanced) LIGO, (Advanced) Virgo [82], GEO600 [164, 165] surveys have been taking measurements, covering the frequency range between the $10 - 10^4\,\mathrm{Hz}$. As we can see in Figure 3.1, these surveys just observe a limited frequency band corresponding to gravitational waves coming from compact binary inspirals [166], core collapse supernovae [167] and pulsars [168]. In the near future, it will be possible to have an accurate location ($5 - 20\,\mathrm{deg}^2$) of the source thanks to the Kamioka Gravitational Wave Detector (KAGRA) [80] which has recently started its observation period, joining the team of active gravitational waves detectors.

astrophysical sources of error (e.g. core dark matter halos [148]) in their modeling.

[7] They affirm that it would be even lower if there were a 'Local Hole'. In this case, $H_0 \approx 68.9 \pm 1.6\,\mathrm{km\,s^{-1}Mpc^{-1}}$ [24], perfectly compatible with Planck's value.

[8] Ref. [24] has been replied in Ref. [52] addressing some concerns on the method employed. However, in Ref. [150] the former team argued that either their concerns were already taken into account in Ref. [24] or did not apply.

[9] See footnote 1 on page 24

Obtaining an accurate location of the GW source requires at least three detectors with a broad frequency bandwidth and a sensitivity at most twice worse than the others [169]. Fortunately, KAGRA, LIGO and Virgo have similar sensitivity (see Figure 3.1) and will make it possible.

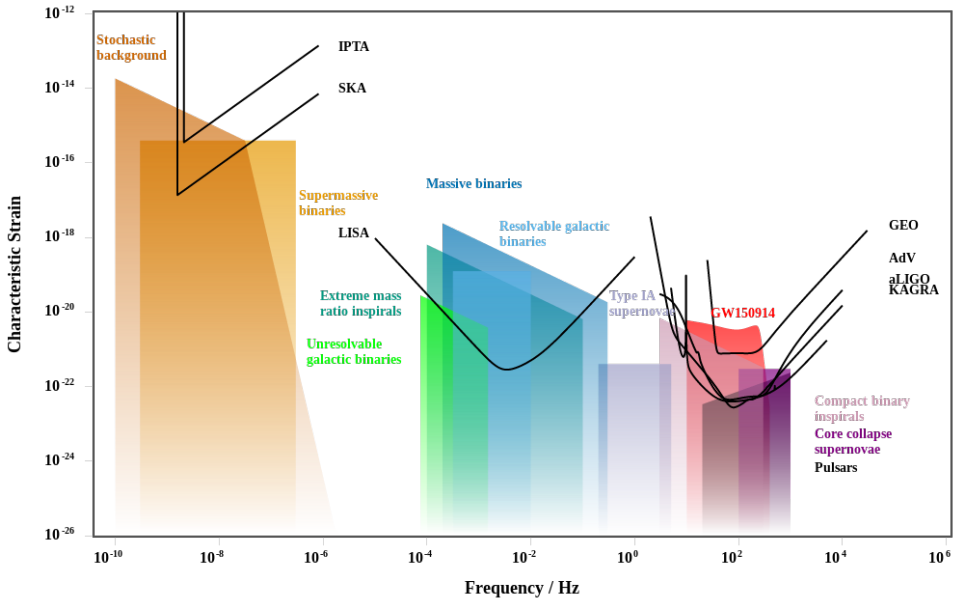

Figure 3.1: Gravitational wave detectors noise characteristic strain over gravitational waves strain depending on their origin. Figure made with `gwplotter.com` [162]

Further in time, a next-generation of gravitational waves detectors will be launched, allowing for the explorations of other gravitational wave sources. For instance, the Laser Interferometer Space Antenna (LISA) [83], the first space-based gravitational wave detector, will be sensitive to frequencies in the range $10^{-4} - 10^{-1}$ Hz, where gravitational waves from massive binaries (black holes and white dwarves) and extreme mass ratio inspirals (stellar-mass objects inspiral into a supermassive black hole) lie [162]. In addition, pulsar timing array (PTA) surveys [170], like the International Pulsar Timing Array (IPTA) [84] and the Square Kilometer Array (SKA) [85] might be able to detect the unresolved gravitational wave stochastic background produced by supermassive black-holes binaries in the frequency range $3 \times 10^{-9} - 3 \times 10^{-7}$ Hz [162].

PTA surveys might be also able to detect the cosmological stochastic gravitational wave background from inflation (see e.g Ref. [171]), first-order phase transitions (see e.g Ref. [172]) or topological defects (see e.g. [172, 173]). The characteristics of the strain and energy density boundaries depend on the frequency, the specific models and the detectors sensitivity. This is beyond the scope of this work and we refer to Ref. [174] and references therein for a more detailed analysis and list of cosmological sources.

Finally, the detection of gravitational waves and their counterparts constitute standard candles that do not require the calibration with lower redshift measurements. As such, they can be used to infer today's expansion rate. Using GW170817 and GRB170817A, the Hubble parameter has been estimated with an uncertainty of $\sim 17\%$, with $H_0 = 70^{+12.0}_{-8.0}\,\mathrm{kms}^{-1}\mathrm{Mpc}^{-1}$ at 68% C. L. [72]. This value is compatible with both early (Planck [43, 175, 176]) and late (distance ladder [20, 23, 24]) time measurements of H_0. Therefore, the rapidly growing gravitational wave samples will also be able, if electromagnetic counterparts are also found, to give an independent and precise estimate of the expansion rate of the universe, without the necessity of any form of "distance ladder".

Furthermore, the forthcoming amount of data from next-generation surveys will allow to

test GR and Modified Gravity models in a new and unexplored way [177]. Farther in time, if proposals like the arcmin space-based observatory are accepted [178], it will be possible to do precision astronomy with gravitational waves, exploring new regimes that have been hidden until now. In the end, gravitational waves discovery and detectability has open a new window of exploration that will allow to test Gravity in a way that had never been possible, looking at the very heart of GR, that is the geometrical nature of Gravity.

Chapter 4

Modified theories of Gravity and Cosmology

We have already reviewed the success of the Cosmological Standard Model addressing the cosmological observations in previous Chapters. However, in Sections 3.3.1 and 3.2.3, we also saw that current measurements seem to be discrepant at early (CMB) and late (local) times. In particular, local and CMB inferred values of Hubble rate today, H_0, and the S_8 parameter seem to differ up to 4.4σ [20] and 3.2σ [51], respectively. Furthermore, in Section 2.3 we reviewed the fundamental challenges of ΛCDM that will be needed to address even in the case it is able to explain all observations and current tensions disappear with forthcoming data. For instance, it would be of special importance to understand why the cosmological constant is 120 order of magnitude smaller than the expected value from the vacuum energy of the Universe.

In this Chapter we will study some alternative cosmological models in the context of dark energy; i.e. that try to explain the accelerated expansion of the Universe. Their study is important to identify which are plausible models and which are already ruled out. These models, in general, might or might not add a cosmological constant term but the main contribution to the accelerated expansion will come from other sources. We will investigate theories that go beyond General Relativity and, in particular, we will review the broad Horndeski theory [29]. Horndeski is one of the most common modifications of Gravity that includes many well known Modified Gravity models, such as $f(R)$, Brans-Dicke [179] or quintessence. In fact, Hondeski is one of the most general theories that adds an scalar field.

There are many different ways of modifying General Relativity (see e.g. this early review Ref. [180]). In Figure 4.1, we show a short list of them. The easiest modification consists of adding an scalar field (ϕ). This would be analog to most inflationary models, where some scalar field particle couples to gravity and produces the accelerated expansion. Its simplest form consist of allowing the cosmological constant to vary, i.e. $\Lambda \to \Lambda(\phi)$. This is called quintessence.

The Einstein equations (Equations 2.4) relate the geometry of the Universe with its content. One can, therefore, equivalently treat an additional scalar field as a contribution of some kind of particle or as a modification of the geometrical part of the equations. This is equivalent to modify the Einstein-Hilbert action (Equation 2.3). For instance, $f(R)$ theories generalize it changing the dependence on R, by considering, instead, a function $f(R)$; i.e. substituting $R \to f(R)$. As we said, these geometrical modifications can be interpreted also as new scalar field contributions to Gravity.

Quintessence and $f(R)$ are just two famous examples of Modified Gravity Models that can be described by the extra field ϕ. Among others, they belongs to Horndeski, the most general four dimensional metric theory of Gravity that preserves Lorentz invariance and incorporates an extra scalar field that yields second order equations of motion of the metric and the scalar

field [29].

The Horndeski theory was thought to be the most general theory possible with an scalar field and a metric, Lorentz-invariance and four dimensions. However, it was shown that there are models with higher order equations of motion that avoid the Ostrogradsky instability and can give cosmological viable evolutions [181–184]. These models are known as Beyond Horndeski models and have recently attracted some attention. There are now studies about the phenomenology and observational constraints of Beyond Horndeski theories [185–187].

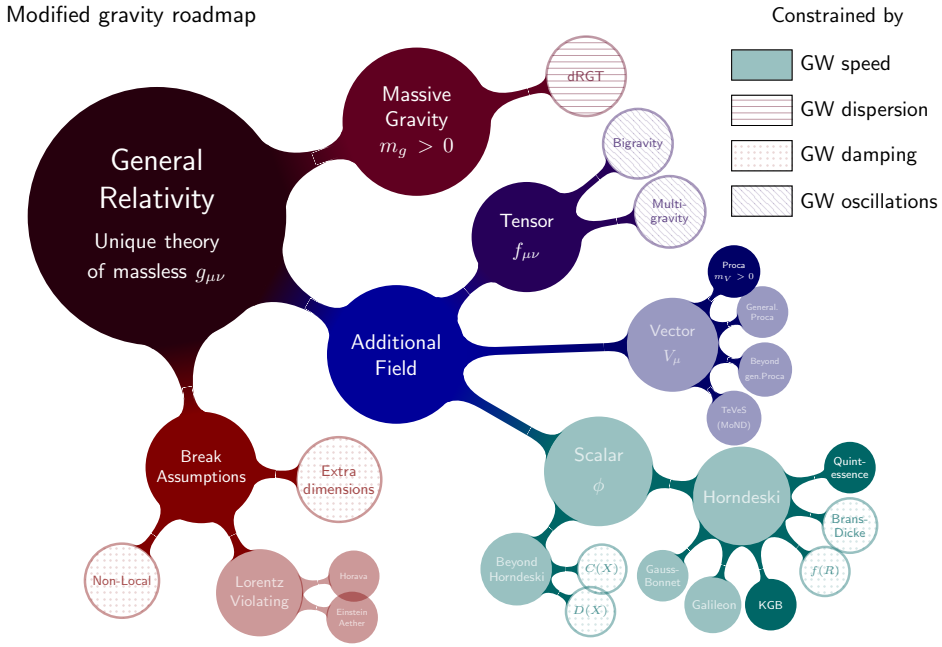

Figure 4.1: Modified gravity roadmap. Image courtesy of J.M. Ezquiaga & M. Zumalacárregui, from Ref. [28]

Although adding a scalar field is one of the simplest modifications of General Relativity, well motivated by the accelerated expansion of the Universe, it was the addition of mass to the graviton what was the first proposed Modified Gravity model. It was in 1939 by Fierz-Pauli [188]. The different models that add a mass to the graviton are called under the name of Massive Gravity. These theories need of a new non-dynamical sector that depends on a new metric tensor, $\mathcal{L}(g_{\mu\nu}, f_{\mu\nu})$. Later on, although from an independent point of view, it was realized that models with two dynamical sectors were also possible. These are the bigravity models. Although independently developed, one can think also of bigravity as a generalization of massive gravity, where the new metric is not fixed but dynamical, having $\mathcal{L}(g_{\mu\nu}, f_{\mu\nu}) + \mathcal{L}(f_{\mu\nu})$. This can be further generalized to allow for a larger number of gravitational sectors with their respective metrics. This is multigravity. These different fundamental roads followed in massive and bi/multi-gravity models are separately depicted on Figure 4.1. In particular, the later are in the path of adding extra tensor degrees of freedom.

Early models of massive gravity and bigravity were, however, plagued with instabilities and there were only particular solutions that were viable. The Boulware-Deser ghost [189] is present in most non-linear extensions of Fierz-Pauli massive gravity [188], and was thought to be unavoidable for a long time. Fortunately, it was shown that some non-linear extensions could avoid it. Among these we can highlight the Dvali-Gabadadze-Porrati (DGP) model [190], the "new massive gravity' (NMG) model [191] or the de Rham-Gabadadze-Tolley (dRGT) model [192]. The analysis of these extensions of Gravity lie outside the scope of this Thesis and we will not

pursue their analysis. A very detailed review on massive gravity is Ref. [193] and we refer to it for further information.

Vector fields, that are known to mediate weak interaction forces, could also couple to the gravitational sector and give a non-negligible contribution at cosmological scales. Models in this direction are based on the Proca action; i.e. the action that describes the interaction with a massive 1-spin field. A single vector field (with $U(1)$ gauge symmetry) would break homogeneity and isotropy, creating a preferred direction effect. This is, however, tightly constrained by CMB observations [45–48]. This can be avoided if the coupling is of three orthogonal vector fields, so that the symmetry can be realized with their spatial components. It is also possible to break the $U(1)$ symmetry and generalize Proca vector fields. These are known as generalized Proca models [194–197] and are the most general vector-tensor theories that result on second-order equations of motion [12]. They can be even further generalized allowing for higher order equations. These are the beyond generalized Proca models and are able to avoid the Ostrogradski instability [198, 199].

Finally, apart from adding extra degrees of freedom in form of scalar, vector or tensor fields, one can also relax some of the underlying assumptions of General Relativity. For instance, one can make non-local theories (e.g. Wetterich non-local gravity [200] or the recent Maggiore-Mancarella's model [201, 202]), add extra dimensions (e.g. DGP [190]) or break Lorentz invariance (e.g. Einstein-Aether [203]). These modifications lie well outside of the scope of the present work and we will not detain ourselves on them. For a review on these kind of modifications and their observational status we refer to Refs. [11, 13]. A more recent review of non-local gravity models is Ref. [204].

In what follows, we will focus only on Horndeski theory and, in particular, in quintessence. This is so because it has been the theory that has occupied the most of the work of this Thesis. However, first, in Section 4.1 we will describe the restrictions that any theory of Gravity must satisfy. We will present the Equivalence Principles and their observational status (Section 4.1.1), the Solar System constraints that must be satisfied by any viable Gravity theory (Section 4.1.2) and discuss some of the main problems underlying Modified Gravity theories (Section 4.1.3). In addition, we will shortly review Lovelock's theorem, which shows the only changes that can be done to General Relativity in order to obtain a different gravitational theory. Finally, in Section 4.2, we will briefly describe Horndeski theory and quintessence (Section 4.2.1) and show how a Modified Gravity theory could solve current observational tensions in Section 4.2.2.

4.1 Road to Modify Gravity

As we have seen in previous Chapter, cosmological observations favor ΛCDM. Furthermore, there are tight constraints on deviations from General Relativity at smaller scales. In the following section (Section 4.1.1) we will shortly review the tight constraints on any variation of the Equivalence Principles. Furthermore, in Section 4.1.2, we will also show the constraints that Solar System measurements impose. Finally, in Section 4.1.3, we will shortly review some of the most common problems of Modified Gravity models and present Lovelock's theorem that will mark the path to follow to construct any Modified Gravity theory.

4.1.1 Equivalence Principles

General Relativity lies on some fundamental principles. Constructing General Relativity with Einstein's formulation naturally results on a model of Gravity where the Weak, Einstein and Strong Equivalence Principles hold. In what follows, we will name them WEP, EEP and SEP, respectively. Einstein's formulation starts assuming a Riemannian geometry for the space-time.

In this geometry, there always exists a tangent plane at every point of the space-time, which will be Minkowski if one chooses the Lorentzian signature. This makes relativistic theories recover Minkowski locally up to tidal forces (i.e. up to second derivatives of the metric) [11]. As we will see in the definition of the different Principles, this formulation imposes the validity of the Weak Equivalence Principle (WEP) and Einstein Equivalence Principle (EEP). The Strong Equivalence Principle (SEP) will also hold. These principles state the following [11]:

- WEP: *All uncharged, freely falling test particles follow the same trajectories, once an initial position and velocity have been prescribed.*
- EEP: *The WEP is valid, and furthermore in all freely falling frames one recovers (locally, and up to tidal gravitational forces) the same laws of special relativistic physics, independent of position or velocity.*
- SEP: *The WEP is valid for massive gravitating objects as well as test particles, and in all freely falling frames one recovers (locally, and up to tidal gravitational forces) the same special relativistic physics, independent of position or velocity.*

The difference between the SEP and the EEP is that SEP generalizes EEP to objects with own gravitational forces as stars and planets [205, 206].

Laboratory and Solar System observations set tight constraints on violations of these principles. Deviations from the WEP can be constrained with great accuracy with experiments of the Eötvös kind. These experiments measure the different acceleration suffered by two different bodies of different materials attracted by the gravitational force of the Earth. The tightest constraints come from the MICROSCOPE satellite that is orbiting around the Earth. In this experiment, two different objects of same weight made of Platinum and Titanium, respectively were suspended and only attracted by Earths gravitational force. The differences on the accelerations were measured to be compatible with the WEP in a part on 10^{15}. More precisely, [207]

$$\eta_{\text{Eötvös}} \equiv \delta(\text{Ti},\text{Pt}) = 2\frac{a_{\text{Ti}} - a_{\text{Pt}}}{a_{\text{Ti}} + a_{\text{Pt}}} = [-1 \pm 9(\text{stat}) \pm 9(\text{syst})] \times 10^{-15}\,, \tag{4.1}$$

at 1σ level, with a_i the acceleration suffered by the mass i. In combination with gravitational redshift dependence experiments, one can also set tight constraints on the position dependence of physical laws [208].

There are also strong evidences for EEP being true. They come from Hughes-Drever experiments [209, 210] which looked for spatial anisotropies on the atomic emission lines. These experiments test the possibility of matter couplings to more than just one single rank-2 tensor, $g_{\mu\nu}$. If we had two, $g_{\mu\nu}$ and $h_{\mu\nu}$ [11], the Lagrangian density would be given by

$$L = \sum_I \int \mathrm{d}\lambda \left[m_I \sqrt{-g_{\mu\nu}u^\mu u^\nu} + n_I \sqrt{-h_{\mu\nu}u^\mu u^\nu} \right], \tag{4.2}$$

where m_I and n_I are the coupling of the I-field to their respective metric and $u^\mu = \mathrm{d}x^\mu/\mathrm{d}\lambda$ is the 4-velocity with respect to the parameter λ. In the case $n_I = 0$, m_I can be identified as the particle mass, the particles follow the geodesics of $g_{\mu\nu}$ and, locally, $g_{\mu\nu} = \eta_{\mu\nu} = (-1,1,1,1)$; i.e. Minkowski. This means that WEP and EEP hold. However, in the $n_I \neq 0$ case, the Euler-Lagrange equations are not geodesics equations and, consequently, the geometry cannot be Riemannian, violating EEP. In this case, the 4-momentum of a given particle, I, is given by

$$p_\mu = m\frac{g_{\mu\nu}u^\nu}{\sqrt{-g_{\alpha\beta}u^\alpha u^\beta}} + n\frac{h_{\mu\nu}u^\nu}{\sqrt{-h_{\alpha\beta}u^\alpha u^\beta}}\,, \tag{4.3}$$

which is spatially anisotropic in general. Therefore, Hughes-Drever are sensitive to different values of n_I. The most stringent constraints set the upper limit of n on [11, 211, 212]

$$n \lesssim 10^{-27} m\,. \tag{4.4}$$

Note that these constraints are not applicable to the linear decompositions of $g_{\mu\nu}$, as is the case in perturbation theory and gravitational waves where $g_{\mu\nu} \to g_{\mu\nu} + h_{\mu\nu}$, with $h \ll g$. In these cases, the Euler-Lagrange equations are geodesics and one has Riemannian geometry. Consequently, Minkowski is recovered locally and WEP and EEP hold.

From the theoretical side, EEP is also supported by Schiff's conjecture that states that *"any complete and self-consistent gravitational theory that obeys the WEP must also satisfy the EEP"* [11]. Although, it has not been proved true (nor false) yet, it has been shown that provided conservation of energy must hold, the effects of having a preferred frame or location can cause WEP violation [213]. The generalization of this result to all possible preferred frames and locations would definitely prove Schiff's conjecture [213].

4.1.2 Solar System constraints

Solar System observations set tight constraints on modifications of Gravity. In particular, we will focus on three different tests: tests of null trajectories, time-like trajectories and short-range changes of the force of Gravity.

Null trajectories are followed by massless particles such as photons. We can highlight two different type of observations: strong lensing and Shapiro time-delay [214] observations. Gravitational lensing is the name given to the deflection of light trajectory when passing by a near massive object. In General Relativity, the photon's deflection angle, θ, produced by a body of mass, M, is given by

$$\theta = \frac{2M}{d}(1 + \cos(\phi))\,, \tag{4.5}$$

where d is the impact parameter and ϕ the angle seen by the observer between the object and the photon. For a null trajectory grazing the Sun's limb, $\theta \simeq 1.75''$, which is in great agreement with current measurements [215],

$$\theta = (0.99992 \pm 0.00023) \times 1.75''\,. \tag{4.6}$$

This tight constraint is surpassed in precision by the measurements of the Shapiro time-delay effect. As well as a massless particle's trajectory is changed by the presence of matter, it does the time. The presence of a massive object, with mass M, introduces a time delay [11],

$$\Delta t = 4M \ln\left[\frac{4r_1 r_2}{d^2}\right]\,. \tag{4.7}$$

In this expression we have assumed that the distances to the observer (r_1) and photon (r_2) from the massive object are $r_1\,, r_2 \gg d$. The time delay has been measured to be, relative to the expected value of GR, $\Delta t_{\rm GR}$, [11, 216]

$$\Delta t = (1.00001 \pm 0.00001)\Delta t_{\rm GR}\,. \tag{4.8}$$

As we see, deviations from GR must be of order 10^{-5} for null trajectories.

The typical time-like trajectories tests are the measurements of the anomalous perihelium of Mercurio, the 'Nordtvedt effect' [217] and observations of gravitomagnetism [218, 219]. Relativistic theories of Gravitation introduce an effect that is not present in Newtonian theory, a precession

$$\Delta\omega = \frac{6\pi M}{p}\,, \tag{4.9}$$

in a two body system with mass M and an orbit with semi-latus rectum, p. The predicted value for Mercurio in GR is $\Delta\omega \simeq 42.98''$, compatible with the measured values within 1σ [220–222] (e.g. $\Delta\omega \simeq (42.963 \pm 0.052)''$ from Ref. [222]). These measurements also test the non-linear terms of geometry and preferred frames effects [11].

The Nordtvedt effect is the name for violations of the SEP. These do not happen in General Relativity but, in general metric theories, one can find them even though WEP and EEP hold. Therefore, finding a positive Nordtvedt effect would rule out General Relativity as a physical theory of Gravity. One can test SEP with the same kind of experiment that tested WEP; i.e. Eötvös kind of experiments, but with self-gravitating masses. The most precise measurements of the Eötvös parameter come from measurement of the separation of the Earth and the Moon. They set [223]

$$\eta_{\text{Eötvös}} = (-1.0 \pm 1.4) \times 10^{-13}\,, \tag{4.10}$$

highly constraining deviations from the SEP.

The last test that we will consider here is the observation of gravitomagnetism; i.e. the production of gravitational fields by a massive rotating object that drags space-time with it (similar to Mach's principle in hydrodynamics). In General Relativity, a gyroscope with spin $\mathbf{S}$ along its trajectory that is orbitting (free-falling) around a rotating massive body is given by [11]

$$\frac{\mathrm{d}\mathbf{S}}{\mathrm{d}\tau} = \mathbf{\Omega} \times \mathbf{S}\,, \tag{4.11}$$

with

$$\mathbf{\Omega} = \frac{3}{2}\mathbf{v} \times \nabla U - \frac{1}{2}\nabla \times \mathbf{g}\,, \tag{4.12}$$

and $\mathbf{g} = g_{0i}$, $\mathbf{v}$ the gyroscope's velocity and U the Newtonian potential at its position. The first term in $\mathbf{\Omega}$ is the geodetic precession and it is not caused by the rotation of the massive body but the time dilation caused by its presence. It is the second term, called the Lense-Thirring term, which causes the frame-dragging. This effect has recently been measured using data from the Laser Relativity Sattelite (LARES) [224] and Laser Geodynamics Sattelites (LAGEOS)-1 [225] and -2 with $2-4\%$ error to be [226]

$$\mathbf{\Omega}_{\text{L-T}} = (0.9910 \pm 0.02 \pm 0.04)\,, \tag{4.13}$$

where the errors (2% or 4%) depend on the particular analysis of the systematics. Note that the General Relativity value ($\mathbf{\Omega}_{\text{L-T}} = 1$) lies well inside the 1σ region.

Short range modifications of gravity are also predicted by different Modified Gravity theories. In particular, short range modifications can take the form of Yukawa potentials,

$$U(x) = \alpha \int \mathrm{d}^3\mathbf{x}' \frac{\rho(\mathbf{x}')e^{-|x-x'|/\lambda}}{|x-x'|}\,, \tag{4.14}$$

such as in higher order theories (e.g. Ref. [227]) or bimetric models (e.g. Ref. [228]), among others. These modifications are also highly constrained. Since they will not be explored in this Thesis, we will not continue this discussion further, but refer to some reviews on the topic such as Refs. [229, 230].

4.1.3 Ghosts, screening and the road ahead

A common problem of Modified Gravity models is the appearance of instabilities. The most famous of such are called *ghosts* and are solutions whose energy density is unbounded from below, allowing for infinite negative energy densities. Ghosts appear in theories that try to produce the

accelerated expansion of the Universe, sourced by some canonical field with antigravitational force; i.e. that satisfy $\rho + 3p < 0$; and has an equation of state $w < -1$. When these fields have even spin, their couplings to the standard fields yield negative kinetic energy terms [11]. As a consequence, the spontaneous creation of particles in ghost–no-ghost pairs is energetically favored in any Lorentz invariant theory yielding instable solutions [231].

This problem can be solved by different means. One approach would be to isolate the ghost field, so that it does not interact with non-ghost particles. Since it has to interact, at least, gravitationally to produce the accelerated expansion of the Universe [231], one can make the couplings to contribute negligibly by giving the ghost a high mass. Alternatively, one can break Lorentz invariance at some scale. However, it would have to be at low energies (the cut-off $\Lambda \lesssim 3\,\mathrm{MeV}$) to be compatible with cosmic gamma ray background observations [231]. No Lorentz-violating theory compatible with observations is known at such scales. Finally, there is an extra possibility that consists of considering the fluctuating ghost solutions as unphysical. In this sense, one can work with ghost-condensates, that are stable [232].

Another known issue of Modified Gravity models is that of *strong coupling* at low energies, breaking perturbative quantum theory. This is, however, a requirement for the Vainshtein mechanism to hold [233, 234]. The Vainshtein mechanism allows for Modified Gravity theories to satisfy the Solar System constraints [235], producing the suppression of fifth-forces at astrophysical scales. The mechanism freezes the new fields, strongly coupling them, at such scales, allowing for the appearance of effects beyond General Relativity just at cosmological scales.

Other screening mechanisms are the chameleon [236, 237] and symmetron [238] mechanisms, which introduce a dependence on the environment to suppress the extra fields at astrophysical scales. The chameleon mechanism introduces it in the effective potential, while the symmetron mechanism does it on the coupling, tending to zero at heavy sources [11].

Finally, let us state what the possible modifications of General Relativity are. These are highly determined by Lovelock's theorem that states [11]:

> *The only possible second-order Euler-Lagrange expression obtainable in a four dimensional space from a scalar density of the form $\mathcal{L} = \mathcal{L}(g_{\mu\nu})$ is*
>
> $$E_{\mu\nu} = \alpha\sqrt{-g}\left[R_{\mu\nu} - \frac{1}{2}g_{\mu\nu}R\right] + \lambda\sqrt{-g}g_{\mu\nu}\,, \tag{4.15}$$
>
> *where α and λ are constants, and $R_{\mu\nu}$ and R are the Ricci tensor and scalar curvature, respectively.*

As a consequence of Lovelock's theorem, a metric theory of Gravity with field equations different from those of General Relativity must accomplish at least one of the following changes [11]:

- Introduce extra fields apart from or instead of the metric tensor.
- Accept higher derivatives of the metric tensor in the field equations.
- Modify the number of dimensions.
- Give up either rank (2,0) tensor field equations, symmetry of the field equations under exchange of indices or divergence-free field equations. Note that in this case, the field equations could not be derived from a variational principle.
- Give up locality.

Note that, in fact, these are the different paths that we have presented at the beginning of this Chapter and depicted in Figure 4.1. In this Thesis, that is focused on Horndeski theory, we followed the path given by the first option: adding extra fields. In particular, Horndeski includes an extra scalar field, as we will see in next Section.

4.2 Horndeski theory

Among all the Modified Gravity theories, we focused on one of the most general theories: Horndeski theory. Horndeski covers many well known modifications of Gravity, such as quintessence, Brans-Dicke [179] or $f(R)$ (see Figure 4.1). It is the most general theory, with up to second order equations of motions, a metric, Lorentz invariance, locality and an extra scalar field [29].

The Lagrangian density of Horndeski is given by [29, 239, 240]

$$S[g_{\mu\nu},\phi] = \int \mathrm{d}^4x\,\sqrt{-g}\left[\sum_{i=2}^{5}\frac{1}{8\pi G_\mathrm{N}}\mathcal{L}_i[g_{\mu\nu},\phi] + \mathcal{L}_\mathrm{m}[g_{\mu\nu},\psi_M]\right], \tag{4.16}$$

where

$$\mathcal{L}_2 = G_2(\phi,\,X)\,, \tag{4.17}$$

$$\mathcal{L}_3 = -G_3(\phi,\,X)\Box\phi\,, \tag{4.18}$$

$$\mathcal{L}_4 = G_4(\phi,\,X)R + G_{4X}(\phi,\,X)\left[(\Box\phi)^2 - \phi_{;\mu\nu}\phi^{;\mu\nu}\right], \tag{4.19}$$

$$\begin{aligned}\mathcal{L}_5 = {} & G_5(\phi,\,X)G_{\mu\nu}\phi^{;\mu\nu} \\ & -\frac{1}{6}G_{5X}(\phi,\,X)\left[(\Box\phi)^3 + 2\phi_{;\mu}{}^{\nu}\phi_{;\nu}{}^{\alpha}\phi_{;\alpha}{}^{\mu} - 3\phi_{;\mu\nu}\phi^{;\mu\nu}\Box\phi\right].\end{aligned} \tag{4.20}$$

In these expressions, G_i are free functions of the scalar field, ϕ, and the kinetic term, $X = \frac{1}{2}\nabla^\mu\phi\nabla_\mu\phi$, and, for example, $G_{4X} = \partial G_4/\partial_X$. In some texts, G_2 might also be called K.

At linear perturbation level, Horndeski is fully described by 5 functions – one of background (e.g. ρ or w) and 4 at perturbation level [241]. These four functions modify different aspects of the theory and are named

- the kineticity, α_K. This is the kinetic energy of scalar perturbations coming directly from the action. Its high values suppress the sound speed of scalar perturbations. It depends on all Horndeski functions, i.e. on all G_i, and is given by

$$\begin{aligned}H^2M_*^2\alpha_\mathrm{K} \equiv {} & 2X\left(K_X + 2XK_{XX} - 2G_{3\phi} - 2XG_{3\phi X}\right) + \\ & + 12\dot\phi XH\left(G_{3X} + XG_{3XX} - 3G_{4\phi X} - 2XG_{4\phi XX}\right) + \\ & + 12XH^2\left(G_{4X} + 8XG_{4XX} + 4X^2G_{4XXX}\right) - \\ & - 12XH^2\left(G_{5\phi} + 5XG_{5\phi X} + 2X^2G_{5\phi XX}\right) + \\ & + 4\dot\phi XH^3\left(3G_{5X} + 7XG_{5XX} + 2X^2G_{5XXX}\right),\end{aligned} \tag{4.21}$$

  (4.22)

  where M_*^2 is the effective Planck mass and is given by

$$M_*^2 \equiv 2\left(G_4 - 2XG_{4X} + XG_{5\phi} - \dot\phi HXG_{5X}\right). \tag{4.23}$$

- the braiding, α_B. It mixes the kinetic terms of the scalar and metric, contributing to the former through backreaction. It introduces second order time derivatives of the metric and the scalar field in their equations of motion and causes dark energy to cluster. It receives contribution from all G_i, except G_2 (or the equivalent, $G_3(\phi)$), and is given by

$$\begin{aligned}HM_*^2\alpha_\mathrm{B} \equiv {} & 2\dot\phi\left(XG_{3X} - G_{4\phi} - 2XG_{4\phi X}\right) + \\ & + 8XH\left(G_{4X} + 2XG_{4XX} - G_{5\phi} - XG_{5\phi X}\right) + \\ & + 2\dot\phi XH^2\left(3G_{5X} + 2XG_{5XX}\right).\end{aligned} \tag{4.24}$$

  (4.25)

Model Class		$\boldsymbol{\alpha_{\rm K}}$	$\boldsymbol{\alpha_{\rm B}}$	$\boldsymbol{\alpha_{\rm M}}$	$\boldsymbol{\alpha_{\rm T}}$
$\boldsymbol{\Lambda CDM}$		**0**	**0**	**0**	**0**
quintessence	[242, 243]	$\Omega_\phi(1+w_\phi)$	0	0	0
kinetic gravity braiding	[244–246]	$m^2\big(n_m+\kappa_\phi\big)/H^2M_{\rm Pl}^2$	$m\kappa/HM_{\rm Pl}^2$	0	0
galileon cosmology	[247]	$-3/2\alpha_{\rm M}^3H^2r_{\rm c}^2e^{2\phi/M}$	$\alpha_{\rm K}/6-\alpha_{\rm M}$	$-2\dot\phi/HM$	0
BDK	[248]	$\dot\phi^2K_{,\dot\phi\dot\phi}e^{-\kappa}/H^2M^2$	$-\alpha_{\rm M}$	$\dot\kappa/H$	0
metric $f(R)$	[249, 250]	0	$-\alpha_{\rm M}$	$B\dot H/H^2$	0
f(Gauss-Bonnet)	[240, 251, 252]	0	$\frac{-2H\dot\xi}{M^2+H\dot\xi}$	$\frac{\dot H\dot\xi+H\ddot\xi}{H\left(M^2+H\dot\xi\right)}$	$\frac{\ddot\xi-H\dot\xi}{M^2+H\dot\xi}$

Table 4.1: Bellini-Sawicki functions α_i for different classes of models present in Figure 4.1. This table is based on Table 1 of Ref. [241].

- the Planck-mass run rate, $\alpha_{\rm M}$. It is the rate of evolution of the effective Planck mass, M_*, and produces an anisotropic stress on the Jordan frame. It depends on G_4 and G_5 and is defined by

$$\alpha_{\rm M} \equiv \frac{{\rm d}\ln(M_*^2)}{{\rm d}\ln(a)}\,. \tag{4.26}$$

- the tensor speed excess, $\alpha_{\rm T}$. It is the deviation of the gravitational waves speed from that of light. It produces an anisotropic stress due to changes on the matter response to the Newtonian potential Ψ even without scalar field perturbations. It receives contributions from G_4 (if $G_{4,X}\neq 0$) and G_5 and is defined by

$$\begin{aligned}\alpha_{\rm T} &\equiv 2X\left(2G_{4X}-2G_{5\phi}-\left(\ddot\phi-\dot\phi H\right)G_{5X}\right) &(4.27)\\ &\equiv 1-c_{\rm gw}^2\,. &(4.28)\end{aligned}$$

In Table 4.1 one can see the value of the Bellini-Sawicki functions for the theories shown in Figure 4.1.

The measurement of the gravitational waves speed (see Section 3.4) can be used to set tight constraints on the tensor speed excess. Taking into account the measured speed, practically the same as that of light, $\alpha_{\rm T}$ can be thought to be zero. More exactly, current constraints impose $\alpha_{\rm T}\lesssim 10^{-15}$ [28, 65–70], effectively setting $G_5=0$ and $G_4=G_4(\phi)$. This would let Horndeski with 2 free functions (G_2 and G_3) of the scalar field and its velocity and an extra function of the field (G_4). This reduction of the degrees of freedom of Horndeski can be considered as an advantage. Having excluded a large portion of Horndeski, we can now focus on the subspaces that are more likely to contain a valid candidate of dark energy.

In the definition of the Horndeski Lagrangian (Equation 4.16) all the G_i are free functions. However, not all their values are physical. Apart from the observational constraints, one must recall that Horndeski, as a Modified Gravity theory, has subspaces with ghost, gradient ($c_{\rm s}^2<0$) or tachyonic ($m_\phi^2<0$) instabilities. These can be easily excluded just looking at the definition of the sound's speed in terms of the Bellini-Sawicki parameters. This is given by

$$c_{\rm s}^2=-\frac{(2-\alpha_{\rm B})\left[\dot H-H^2(\alpha_{\rm M}-\alpha_{\rm T})-\frac{1}{2}H^2\alpha_{\rm B}(1+\alpha_{\rm T})\right]-H\dot\alpha_{\rm B}+\frac{\tilde\rho+\tilde p}{M_*^2}}{H^2\left(\alpha_{\rm K}+\frac{3}{2}\alpha_{\rm B}^2\right)}>0\,, \tag{4.29}$$

where $\tilde\rho$ and $\tilde p$ are the energy and pressure density of the Universe excluding dark energy. In addition, the conditions to avoid ghost instabilities are

$$2\alpha_{\rm K}+3\alpha_{\rm B}^2>0\,,\qquad M_*^2>0\,. \tag{4.30}$$

Tachyonic instabilities are not necessarily worrisome. In fact, there are tachyonic models that can reproduce our Universe. An example of such can be seen in Chapter 6.

In Chapter 7, we have also explored the fundamental allowed regions free of classical instabilities (ghosts and gradient instabilities) and built theoretical priors for quintessence, as a first step to do the same for Horndeski. In addition, we have also studied their constraining power and found able to highly increase the observational constraints. In this direction of finding fundamental constraints of theories, some authors are looking for the constraints that would come from thinking of Horndeski an Effective Field Theory (EFT) of a more fundamental higher energy theory.

For instance, if one understands Horndeski as an EFT theory, one must then consider its radiative stability; i.e. that loop corrections of the scalar interactions do not overrun those at leading order. This consideration can be highly restrictive if one also sets $\alpha_{\rm T} = 0$. In this case, the only viable term in the Horndeski action would be, in general, $G_4(\phi)$ or $G_3(\phi, X)$. Furthermore, the only independent Bellini-Sawicki parameter would be $\alpha_{\rm B}$ [253].

In addition, provided that Horndeski has a unitary, causal, local, Lorentz invariant UV completion, one also has to take into account the *positivity bounds* [254–259]. The simplest come from the tree-level scattering amplitude [259], $\mathcal{A}$,

$$\mathcal{A}(s,t) = c_{ss}\frac{s^2}{\Lambda_2^4} + c_{sst}\frac{s^2 t}{\Lambda_3^6} + \dots \,, \tag{4.31}$$

where s is the center of mass energy, t the momentum transfer, $\Lambda_2^2 = M_{\rm P}H_0$, $\Lambda_3^3 = M_{\rm P}H_0^2$ and the expansion coefficients are functions of G_i and obey [254, 255, 257, 258]

$$c_{ss} = c_{ss}(G_2, G_3, G_4) \geq 0\,, \qquad c_{sst} = c_{sst}(G_{3,X}, G_4, G_5) \geq -c_{ss}\Lambda_3^4/2\Lambda_2^4\,. \tag{4.32}$$

These fundamental priors have been seen to be highly restrictive in combination with current data, removing large portions of the parameter space. Even more if one also sets $\alpha_{\rm T} = 0$. In this case, they could remove the 99% of the allowed parameter space for the studied cases. Furthermore, they were also shown to be interesting in order to focus the parameter space (and its constraints) on the theoretically well based regions, which could be, otherwise, excluded by observations in favor of the unphysical regions [259].

On the contrary, thinking of Horndeski as an EFT theory might also soften observational constraints. For instance, there is an ongoing discussion about the strenght of the constraint set by the measurement of the gravitational waves speed with GW170817 and GRB170817. Thinking of Horndeski as an EFT theory of some high energy fundamental gravitational model, one would expect it to have a Lorentz invariant UV completion. Then, near the cut-off ($\Lambda_3^3 = M_{\rm P}H_0^2 \sim 100\,{\rm Hz}$) the speed of gravitational waves would be scale dependent and asymptotically luminal. Therefore, given that the scale energy of GW170817 is close to the cut-off, the constraint on the gravitational wave speed should be thought to be scale dependent, too. And, in this way, the EFT Hordenski models with $\alpha_{\rm T} \neq 0$ would remain unconstrained [64].

Let us now proceed to describe the Horndeski subclass that has occupied the most of this Thesis: quintessence.

4.2.1 Quintessence

Quintessence is the archetypical dark energy model. It was proposed as an alternative to the cosmological constant that would avoid its associated problems [242, 243] and could be found to fit better the observations. In these models, one or more scalar fields produce the accelerated expansion of the Universe, similarly to what happen in inflation. The modification to General

Relativity is straightforward as it just consists of freeing the cosmological constant to allow it to vary.

It is important to note that such a field would couple to the others fields varying the strength of the coupling constants unless a unknown symmetry removes such coupling [260]. Although these are extremely constrained by observations, there is still enough space for quintessence models to produce the accelerated expansion of the Universe (see e.g. [261, 262]).

In the formalism of Horndeski, a minimally coupled (i.e. coupled only through the metric) canonical quintessence model is given by

$$\begin{aligned} G_2 &= X - V(\phi) \\ G_3 &= 0 \\ G_4 &= \frac{1}{2} M_{\rm P}^2 \\ G_5 &= 0 \end{aligned}$$

where the $V(\phi)$ is the potential energy of the dark energy field ϕ. By analogy with perfect fluids, we can define the energy density and pressure of the quintessence field as

$$\rho_{\rm DE} = \frac{1}{2}\dot{\phi}^2 + V(\phi)\,, \qquad p_{\rm DE} = \frac{1}{2}\dot{\phi}^2 - V(\phi)\,. \tag{4.33}$$

Since we are neglecting any coupling to the matter sector, the field evolution is determined by the Klein-Gordon equation (see also equation 2.85),

$$\ddot{\phi} + 3H\dot{\phi} - \frac{1}{a^2}\nabla^2\phi + V'(\phi) = 0\,. \tag{4.34}$$

Finally, the equation of state is given by

$$w = \frac{\frac{1}{2}\dot{\phi}^2 - V(\phi)}{\frac{1}{2}\dot{\phi}^2 + V(\phi)}\,, \tag{4.35}$$

and will be $w = -1$ as long as the field kinetic energy is negligible. Furthermore, from the previous equation it can be seen that canonical quintessence models must satisfy $|w| \leq 1$.

As we can see from Table 4.1, quintessence models are fully determined by its background evolution and the only modification to General Relativity at first-order of perturbation level comes from changes on the kineticity, $\alpha_{\rm K} = \Omega_\phi(1 + w_\phi)$. Furthermore, they do not modify the sound speed, which remains $c_{\rm s}^2 = 1$ (see e.g. Ref. [263]).

Model independent approaches try to identify the evolution of the equation of state (or any other background quantity). A common parametrization, valid near the present, is the CPL parametrization [264, 265], $w = w_0 + (1 - a)w_a$ with $w_0 = w(a = 1)$ and $w_a = [{\rm d}w/{\rm d}\ln(a)]_{a=1}$. Parametrized like this, one can find two different, well distinguished regimes in the $(w_0\,, w_a)$ plane, corresponding to two different class of models: the freezing and thawing models [266, 267]. These have been represented in Figure 4.2.

Freezing and thawing models have their name given by the characteristic evolution of their equation of state. Freezing models have their equation of state $w \neq -1$ at early times and it is close to the present when it approaches $w = -1$. On the contrary, the equation of state in thawing models remains constant at $w = -1$ during the whole evolution of the Universe and only departs from $w = -1$ close to the present. This happens because thawing models have their field frozen for the whole evolution history of the Universe until near the present, when it starts moving, producing the accelerated expansion of the Universe. In contrast, in freezing models the field is moving at early times and it is close to the present when it tends to stop.

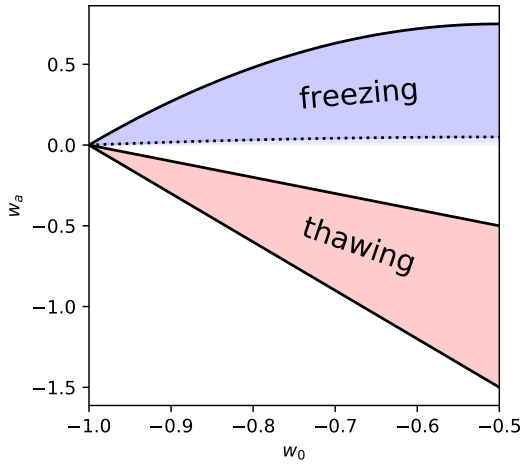

Figure 4.2: Thawing and freezing models in the CPL parameters space.

Among freezing models, one can highlight the tracker models, characterized by the behavior of the dark energy equation of state which follows that of the main component of the Universe.

In Chapter 7, we will further discuss the different kinds of quintessence, focusing on thawing models which have been seen favored by current observations [268]. Furthermore, we will explore an alternative parametrization and show that it can accurately recover the observables up to recombination and, therefore, it is suitable for use with next-generation experiments.

For very well detailed reviews on quintessence models and their physical motivations we refer to the reviews Refs. [266, 267].

4.2.2 Solving tensions between local and early universe measurements with modifications of Gravity

Finally, we want to finish this Chapter by farther motivating the study of Modified Gravity. For that, we have to recall that, as we discussed in previous Chapters, the ΛCDM model, although correctly addresses current cosmological observations, there might be in tension with current data. In particular, it seems that looking at local or early time observations the value of H_0 and the S_8 parameter diverge.

As we said in Chapter 3, this could well just be a systematic effect (as claimed for the H_0 tension in Ref. [24]) or a statistical fluctuation (as in the case of the mild tension of S_8 [118]). In any case, it will become clear when next-generation data is available and analyzed. However, it is important to note that such kind of tensions could be expected in some Modified Gravity models.

Apart from the simple solution of having a faster accelerated expansion, it has been argued that in order to explain the discrepancy between the local and CMB value of H_0, one needs to modify the sound speed at early times, around $z \sim 3000$ [269, 270]. The quartic and quintic covariant Galileon cosmology, for instance, is known to be able to solve the H_0 tension, while being compatible with other cosmological measurements [271]. Unfortunately, they were ruled out after the measurement of the gravitational waves speed as they also modify their velocity [69]. Another alternative, that even compete with ΛCDM on fitting the current cosmological observations is the Galileon ghost condensate (GCC) [272]. This model, however, still has a 2σ tension on the value of H_0 between CMB and local estimations.

The analysis of these models lay out of the scope of this Thesis and we will not discuss them further. We hope, however, that these few lines serve to emphasize the importance of studying

Modified Gravity, if it was not enough the fact that we need to keep challenging ΛCDM to make sure we have got the best of all possible theories. As we have seen, ΛCDM, although successful in explaining current observations of the Universe, has some fundamental problems (see Section 2.3) and, it seems now, might begin to have some observational challenges. If the tensions grew with next-generation data and we needed to drop ΛCDM, we, fortunately, will already know that there are some Modified Gravity models that could serve to lighten our road ahead.

Chapter 5

The next-generation surveys

During this decade several surveys will be launched and will start collecting large amounts of data. These are the so-called next-generation cosmological surveys and will be able to track the expansion and matter distribution (among other things) in the Universe with great accuracy and up to high redshift. This should allow us to identify the nature of dark energy and Gravity.

In this Chapter we will describe some of the most promising surveys. In particular, those that have played a special role in this Thesis. Among all the experiments that will be launched, we have considered the Large Spectroscopic Survey Telescope (LSST) [17], whose specifications can be found in Chapter 5.1, the Dark Energy Scientific Instrument (DESI) [19], in Chapter 5.2, Euclid [79], in Chapter 5.4 and the Stage-4 Cosmic Microwave Background (S4 CMB) [77] collaboration, that can be found in Chapter 5.5. The LSST, together with DESI, WFIRST and Euclid will be able to cover large portions of sky and map the Large Scale Structure (LSS) of the Universe with high precision and accuracy and up to high redshift. Together with these LSS surveys, the Stage-4 CMB collaboration will be collecting data, covering around the 70% of the sky. Its precise measurements will allow to set tight constraints on the early Universe physics, including inflation [77]. In addition, since these surveys will cover large areas of the sky, they will overlap. This will allow to beat the cosmic variance in some cases [58].

From those surveys that we have not considered in this Thesis, we might at least mention one of them: the Square Kilometer Array (SKA). This promising survey is planned to finish its construction phase in late 2021 [85] and will constitute the largest radio telescope. It will be formed by many individual smaller radio antennas working together, and will be able to explore the first stars and galaxies, the galaxy evolution and, more important for dark energy studies, the distribution and shape deformation of galaxies. It will be able to go up to high redshift ($z \sim 3$) and cover around $30.000\,\mathrm{deg}^2$, making possible to observe around 10^9 galaxies in the hydrogen I 21 cm band at its final stage, SKA2.

Photometric and spectroscopic surveys, such as DESI, LSST and Euclid, will be able to map other interesting stellar objects such as Type Ia supernovae (SNe Ia). Particularly important will be LSST at low redshift ($z < 1$) which will detect of order of 10^5 new SNe Ia, increasing the current sample by a factor 300 [34]. At high redshift ($z > 1$), WFIRST will multiply the sample size by 1000 [78, 157, 158]. At extremely high redshifts ($z \sim 5$), the James Webb Space Telescope (JWST) [160] and LSST [159] might be able to detect new SNe Ia, if they are abundant enough. This will allow to measure the expansion rate of the Universe from very early times at great accuracy and will allow to resolve the discussion around the H_0 tension. If it is real, it will be there.

But these classical cosmological observables are not the only ones accessible nowadays. Next decade will also bring an unprecedented amount of data on gravitational waves, which are a direct probe of Gravity. The Kamioka Gravitational Wave Detector (KAGRA) [80] has recently

Survey	Type	Area (deg^2)	$N_{\rm g}^{\rm gc}$	$N_{\rm g}^{\rm wl}$	SN Ia	FoM
LSST	GB, P	20,000	10^{10} ($z \gtrsim 6$)	4×10^9	10^5 ($z \lesssim 0.8$)	666
DESI	GB, S	14,000	3×10^7 ($z < 3.5$)	–	–	704
WFIRST	SB, PS	2,000	2×10^7 ($1.05 < z < 2.9$)	5×10^8	2700 ($z \lesssim 1.7$)	< 990
Euclid	SB, PS	15,000	5×10^7 ($0.7 < z < 2.1$)	1.5×10^9	3000 ($z \lesssim 1.2$)	1540

Table 5.1: Summary of galaxy observations prediction for the different LSS surveys considered in this Chapter. $N_{\rm g}^{\rm gc}$ and $N_{\rm g}^{\rm wl}$ stand for the number of galaxies for galaxy clustering and weak lensing, respectively. The FoM is the maximum w_0–w_a FoM that is expected to be achieved using all data available from the survey, assuming GR. Note that the galaxy clustering galaxies for spectroscopic and photospectroscopic surveys are spectroscopically measured. The FoM for WFIRST includes extra probes (see the text for more information). We could not find a estimation of the FoM with WFIRST data only.

joined the Laser Interferometer Gravitational-Wave Observatory (LIGO) [81] and VIRGO [82] gravitational wave detectors. This will allow an accurate determination of the location of the source [169]. In addition, the SKA collaboration, using pulsar clocks, can function as a pulsar timing array (PTA). These might be able to detect the unresolved gravitational wave stochastic background coming from supermassive black-holes binaries in the frequency range $3\times10^{-9}-3\times10^{-7}$ Hz [162]. Other PTA surveys will join SKA, such as the International Pulsar Timing Array (IPTA) [84].

With this prospects in mind, this Thesis has been driven by the though of being useful for next-decade analysis, anticipating plausible results and building suitable frameworks to extract the most from forthcoming data. In Part III, we will show the different projects that form this Thesis and have been carried out with idea of been helpful. In Chapter 6 we present our forecast on how the next-generation surveys will constrain specific Modified Gravity models such as the α-attractors dark energy. Furthermore, in order to use next-generation data efficiently, we build in Chapter 7 a general parametrization and theoretical priors that will allow to easily compare observational constraints with theoretical predictions, as well as restrict the studies to the fundamentally well motivated regions of the parameter space. Finally, in Chapter 8, we go closer to data and develop and implement a new efficient and accurate approximation of the main contribution of the LSS likelihood: the Guassian part. This will make possible to use forthcoming data, taking into account that the exact computation scales as $O(\ell_{\rm max}^6)$ (intractable for the expected angular resolution of next-generation surveys) while our approximation goes as $O(\ell_{\rm max}^3)$. Its utility has been already seen by the LSST DESC collaboration which has already use it in their recent pipeline test [273].

A thorough list and description of next generation surveys prospects (i.e. targets, redshifts, sample size, etc.) in the context of the different kind of cosmological probes was made in Chapter 3. In this Chapter we will describe more in depth those that have played a special role in this Thesis and that will presumably be of key importance on the understanding of the Universe in the next decade. These are: LSST (Chapter 5.1), DESI (Chapter 5.2), WFIRST (Chapter 5.3), Euclid (Chapter 5.4) and S4CMB (Chapter 5.5). A summary of the LSS (LSST, DESI, WFIRST and Euclid) surveys can be found in Table 5.1. Note that the Figure of Merit (FoM) in Table 5.1 is defined by [274]

$$\text{FoM} = \left(\det C(w_0, w_a)\right)^{-1/2}, \tag{5.1}$$

where C is the covariance matrix of the w_0-w_a parameters.

5.1 The Large Synoptic Survey Telescope

The Large Synoptic Survey Telescope (LSST) is a ground-based cosmological survey based on Cerro Pachón in Chile that will be observing the sky for ten years, starting in October, 2022. The telescope has a 8.4 m primary mirror and the largest digital camera in the world. Its effective aperture is of 6.7 m and has a field view of 9.6 $\deg^2$. It will be able to cover $20,000\,\deg^2$ of sky in six different photometric optical bands during ten years. Each patch of the sky will be imaged about 2000 times in 15 s exposures, twice per night, and each 3-4 days. In each visit, LSST will be able to detect objects as faint as $r \sim 24.5$ (5σ, point source), while using all final available images, the final survey depth will be $r \sim 27.5$ (5σ, point source). As a consequence of all this data collection, the 10-years catalog is expected to have a size of 500 PB of images and data products. This data will be publicly available for anyone to use.

With an equipment of this quality, there are many scientific goals that one can address. The Collaboration has decided that the main goals are:

- Dark matter and dark energy. LSST will be able to catalog the six-band photometry of $\sim 10^{10}$ galaxies up to $z \gtrsim 6$. From those, it will be also possible to measure the shape of 4×10^9 galaxies. This will allow to estimate the matter distribution and track the growth of structures from early times. In addition, the LSST also is expected to detect about 10^5 SNe Ia with a mean redshift of $z \sim 0.45$, going up to $z \sim 0.8$. While mainly the LSS maps can be used to constrain the amount of dark matter, as it enhances the accretion rate of matter and the growth of structures, both samples can be used to set constraints on dark energy. In fact, the w_0–w_a FoM, using only LSST data, will be FoM = 461 or 666 if one neglects the systematics that can be calibrated. Adding Stage-3 priors, FoM = 505 or 711, respectively [34].

- Solar system. LSST will also detect solar system bodies, increasing the current catalog by a factor 10 or 100, measuring their orbit, color and variations. It will detect near-Earth objects of the size of 140 m in the Main Belt of asteroids, catalog a large fraction (60 - 90%) of the population of the potentially hazardous asteroids larger than 140 m and take measurements of trans-Neptunian Objects.

- Changing sky. LSST will observe the same patch of sky twice per night and every 3-4 days. This will allow to track the evolution of sky changing phenomena, such as variable stars or cosmic explosions. It might also lead to the discovery of new transient phenomena. LSST can make a public alert in 60 s, allowing for people to observe the interesting event.

- Milky Way. LSST will map the stellar number density of $\sim 10^{10}$ main sequence stars and the metallicity of $\sim 2 \times 10^6$ stars near the turn-off main sequence (F/G) as far as 100 kpc over its full sky coverage. It will also detect luminous stars at the virial radius of the Milky Way (~ 400 kpc). Finally, LSST will construct a map of the tangential velocity field at $\gtrsim 10$ kpc with $10\,\mathrm{km\,s^{-1}}$ precision and at $\gtrsim 25$ kpc with $60\,\mathrm{km\,s^{-1}}$ precision. This amount of data supposes two orders of magnitude more than current data and will allow, among other things, to infer the matter distribution in the Milky Way and, together with the kinematic information, it may be able to break the disk/halo degeneracy present in current models.

This is just a skim of all the science one can do with LSST data. All this information and more can be found in Refs. [17, 34].

5.2 The Dark Energy Spectroscopic Instrument

The Dark Energy Spectroscopic Instrument (DESI) is a five-years (2019 - 2024) ground-based survey that aims to elucidate the nature of dark energy. For that, they will use the 4-m Mayall telescope in Kitt Peak, Arizona, with a automatized spectrograph, capable of measuring simultaneously 5000 spectra in the range of $360 - 980\,\mathrm{nm}$. DESI will cover $14,000\,\mathrm{deg}^2$, detect objects with $r \gtrsim 19.5$ and observe more than 3×10^7 galaxies and quasars, obtaining precise measurement of their redshift. The data will be publicly available.

In particular, luminous red galaxies (LRGs) will be observed up to $z = 1$; bright [OII] emission line galaxies (ELGs) up to $z = 1.7$; and quasars between $2.1 < z < 3.5$. Quasars will be used as tracers of the matter distribution and for the Ly-α forest absorption properties, that can be used to trace neutral hydrogen. In addition, there will be a magnitude-limited bright galaxy survey running the nights with bright moonlight. This will observe 10^7 galaxies at median $z \sim 0.2$. In parallel, given that low-redshift galaxies are too clustered and in order to use all available channels in the DESI instrument, the stars of the Milky Way will also be measured. These trace the dark matter halo, and would allow for small-scale tests of cosmological models.

DESI will improve at least an order of magnitude the number of galaxies observed and the comoving volume covered by BOSS. And, just with BAO measurements, the FoM of w_0–w_a improves more than 3 times (to 133) current BAO based FoM. Furthermore, using all data available from DESI, the FoM grows to 704. In addition, they will also allow to constrain the sum of the neutrino masses with an error of $0.020\,\mathrm{eV}$ at scales $k < 0.2h\,\mathrm{Mpc}^{-1}$.

It is important to note that DESI and LSST will have overlapping areas. In this sense, DESI will work as a pathfinder instrument for such kind of surveys.

This information can be found and extend in Ref. [19].

5.3 The Wide Field Infrared Survey Telescope

The Wide Field Infrared Survey Telescope (WFIRST) is a space-based spectrophotometric survey that will work on unveiling the nature of dark energy and dark matter, as well as on exploring exoplanets and infrarred astrophysics. It will start in the mid-2020 and have a duration of 5 years, with a possible 5-years extension. The WFIRST telescope has a 2.4-m primary mirror, the same size that the precursor Hubble telescope (HST), but with a Wide Field Instrument that allows to observe 100 times the HST area. In addition, thanks to the Coronagraph instrument it will be possible to observe and do spectroscopy of faint exoplanets.

For the dark energy and dark matter task, WFIRST is expected to improve current constraints on the equation of state by an order of magnitude, which would translate on a w_0–w_a FoM ~ 990, assuming GR and adding the following uncorrelated probes (Planck CBM, RSD ($z < 0.7$), BOSS BAO and ground base data for the photometric redshifts of the lensing galaxies). This is accomplished by precise measurements of galaxy redshifts, shapes and SNe Ia over a total of $2000\,\mathrm{deg}^2$ of sky. WFIRST has divided these in three different surveys: the High Latitude Spectroscopic and Imaging Surveys and the Type Ia Supernovae Survey.

The High Latitude Image Survey will take measurements of about 5×10^8 galaxy shapes and 4×10^4 massive clusters. On the other hand, the Spectroscopic survey will map the distribution of emission line galaxies between $1.05 < z < 2$ (Hα galaxies) and $1.7 < z < 2.9$ (strong emission [OIII] galaxies). It is estimated that $\sim 2 \times 10^7$ Hα galaxies and $\sim 2 \times 10^6$ [OIII] galaxies will be detected. Finally, the Type Ia Supernovae Survey is expected to discover and monitor about 2700 spectroscopically confirmed SNe Ia at redshifts $z \lesssim 1.7$.

As we said, another scientific goal of WFIRST is to improve our understanding on exoplanets. WFIRST will be able to detect around 3000 bound planets in the cold, outer regions of the

planetary systems, ranging between $0.1 - 10^4$ Earth masses, and also observe orphan planets. WFIRST will be able to detect them using microlensing, apart from direct imaging.

The third goal is to provide a useful catalog of general astrophysics. This will constitute the largest amount of observing time during the 5 years extension.

This information has been gathered from Ref. [78], where we point at for further details.

5.4 Euclid

Euclid is a 6-years space-based survey with main goals understanding dark energy, cold dark matter and the primordial structure of the Universe. It will be divided in a wide survey which will map $15,000 - 20,000\,\mathrm{deg}^2$ of extragalactic sky and a deep survey reaching 2 magnitudes deeper that will map $40\,\mathrm{deg}^2$. The satellite will be equipped with a 1.2 m-diameter primary mirror, capable of observing celestial objects by visual imaging, in the wavelength range $550 - 900\,\mathrm{nm}$, three band NIR photometry and NIR spectroscopy. The visual imaging will be able to detect 10σ extended sources with $m \sim 24.5$, while the photometry will reach 5σ point sources with $m \sim 24$. This will result on 10^{10} observed sources, from which it will be possible to have shape measurements of 1.5×10^9 galaxies and spectroscopic redshifts of 5×10^7 galaxies between $0.7 < z < 2.1$. In addition, there will be a total of ~ 3000 SNe Ia observed by Euclid to $z \sim 1.2$ with NIR light-curves and colors and 6000 more with a single detection. It will also single-detect $\sim 10^4$ core-collapsed SNe.

With this amount of data, Euclid will be able to map the matter distribution of the Universe (with weak lensing) and the BAO scale. This will set tight constraints on the possible cosmological models. In fact, the w_0–w_a FoM will improve by more than a factor 300 (to 1540 with only Euclid data and to 4020 adding Planck's data), while constraints on deviations of the growth parameter γ, the sum of neutrino masses and the initial conditions, f_{NL}, will grow by more than an order of magnitude.

In addition to the primary scientific goal of Euclid, it will be also able to make interesting astrophysical observations of objects and processes such as exoplanets, galaxy evolution or strong lensing. Additional information, and all we have discussed, can be found in Ref. [79].

5.5 Stage 4 CMB

The CMB-S4 is a ground-based survey that combines large and small telescopes at the South Pole and Cerro Toco in the Chilean Andes. These places, high and dry, were chosen because they have an open window at the microwave frequency. It is now in the pre-conceptual desing and will be fully operative, in 2029, with partial initial operations from 2026.

CMB-S4 will be able to map around the 70% [1] of the sky in the millimetric band. It will produce deep observations in a 3% of the sky with noise levels $\sigma_T < 1\,\mu$K-arcmin and have high-resolution measurements ($\leq 1.5\,$arcmin) with $\sigma_T \sim 1\,\mu$K-arcmin in the wide 70% sky coverage. This design have been chosen to meet the scientific goals:

- Primordial gravitational waves and inflation. The detection of primordial gravitational waves would strongly support the theory of inflation and would also give evidence for the quantization of gravity. S4-CMB will produce polarization maps and constrain $r < 0.001$ at 95% C. L. if no B-mode is detected and a 5σ detection if $r \geq 0.004$ (0.003) with a 4 (8) years survey.

[1] This value has been updated in the more recent *The CMB-S4 Science Case, Reference Designs and Project Plan* [77]. The previous 2017 CDT report estimation was 40% of the sky.

- Dark universe. S4-CMB will look for deviations on the thermal history from that predicted by the standard model of particles. Parametrizing the new species as $\Delta N_{\rm eff}$, they will be constrained to $\Delta N_{\rm eff} \leq 0.06$ at 95% C. L. In addition, it will improve the bounds on the decoupling temperature of scalar and spin $s > 0$ particles, by a few factors and $\sim 10^2$, respectively.

- Map the matter distribution in the Universe. S4-CMB will be able to map the matter distribution with lensing measurements and, separately, the baryonic matter with ionized gas thanks to Compton scattering, producing the tSZ and kSZ effects. These maps will be split in redshift-bins up to $z \sim 5$.

- The time-variable millimeter-wave sky. It would be one of the first surveys in the mm-band observing the variable sky. In this frequency channel one can observe transient events, Solar System objects and variable AGNs, specially blazars. This will be possible thanks to 1-2 days periodic exploration of a large fraction of sky and a ultra-deep daily survey in a small patch of it.

The two first points are the primary goals of the S4-CMB collaboration. The others, however, are secondary goals that will bring important observations to the broader cosmological and astrophysical community.

All this information and more can be found in Ref. [77].

Part III

Unveiling Dark Energy

Chapter 6

Dark energy as a remnant of inflation

As we saw in Chapter 2, the Standard Model of Cosmology relies on two epochs of accelerated expansion. A first inflationary phase in the very early universe leading to a very homogeneous, isotropic and spatially flat with a near scale invariant spectrum of curvature perturbations [50, 275]. The second acceleration era, when dark energy (DE) dominates the energy density in the late universe, is necessary to explain observations of Type Ia supernovae (SNe Ia) (e.g. Refs. [60, 61, 276]), the Cosmic Microwave Background (CMB) (e.g. Refs. [15, 43]) and the Large Scale Structure (LSS) in the matter distribution of the Universe (e.g. Ref. [49]). As we saw in Chapter 5, an ambitious observational program aims at elucidating the physics behind inflation and dark energy.

In this context, the dark-energy α-attractor model [277] is one of the models that try to describe both accelerated expansions in a common framework. These models typically have a scalar field in a potential with two plateaus that allow for a slow roll at early times, which produces inflation, and a freezing behavior at late times, that yields a cosmological constant-like expansion [278–281]. In addition, there are models that would produce dark energy from a symmetry breaking mechanism [282–284]. However, there are other studies that try to study the connection of the late and early Universe, but focus only on the late time cosmology. Among them there are those describing dark energy as quintessence, which base their Lagrangian on an α-attractor model [277, 285–287], or those which study the relation between them and $f(R)$ gravity, from extensions of the Starobinsky R^2 gravity [288], as in Refs. [289, 290]. Others, instead, use the α-attractors as source of dark matter [291].

During inflation, the α-attractors class of models stands out for being able to reproduce the observations, which strongly support concave potential models. CMB Planck sets tight constraints on the tensor-to-scalar ratio, r, with $r < 0.11$ (at 95% C. L.) and the spectral index, n_s, with $n_\mathrm{s} = 0.9649 \pm 0.0042$ (at 95% C. L.), favoring slow-roll models with a concave potential ($V(\phi)'' < 0$) [50], as was already anticipated by WMAP results [15]. In this context, the α-attractor models are able to give the correct predictions thanks to the fact that, for N e-folds [292],

$$n_\mathrm{s} = 1 - 2N^{-1} \quad \text{and} \quad r = 12\alpha N^{-2}\,, \tag{6.1}$$

where α is a parameter shared by all models in this class and is present in their Lagrangian, whose canonical expression is given by

$$\mathcal{L} = \sqrt{-g}\left[\frac{1}{2}M_\mathrm{P}^2 R - \frac{1}{2}(\partial\phi)^2 - \alpha f^2(x)\right]\,, \tag{6.2}$$

where $x = \tanh(\phi/\sqrt{6\alpha})$. The fact that their Lagrangian is the same as the one for canonical

quintessence dark energy models is exploited to connect both inflation and dark energy with the same scalar field.

The α-attractor models are connected with fundamental theories with various fields with local conformal (i.e. rescaling) invariance. This symmetry allows to rewrite the original Lagrangian as a single-field one [292, 293],

$$\mathcal{L} = \sqrt{-g}\left[\frac{1}{2}M_{\rm P}^2 R - \frac{\alpha}{(1-\varphi^2/6)^2}\frac{1}{2}(\partial\varphi)^2 - \alpha f^2\left(\frac{\varphi}{\sqrt{6}}\right)\right] . \tag{6.3}$$

Here, g is the metric and R the Ricci scalar, $M_{\rm P}$ is the Planck mass, and αf^2 is the potential function dependent on the field φ which is measured in $M_{\rm P}$ units. The second order pole in the kinetic term is the reason behind the common predictions for $n_{\rm s}$ and r (Equation 6.1). Finally, in order to obtain its canonical version, one needs to define $\phi = \sqrt{6\alpha}\,\mathrm{arctanh}(\varphi/\sqrt{6})$. In this way, one also pushes the boundaries of the connected region ($\varphi \in (-\sqrt{6}, \sqrt{6})$) to infinity ($\phi \in (-\infty, \infty)$).

We focus here on testing the α-attractor dark energy model against different cosmological observations and physical understanding of the constraints on the parameter space. We use the generalized potential of Ref. [277] and allow the initial field value to vary, since fixing it restricts the phenomenology and can bias the results. Furthermore, we will thoroughly investigate the dependence of the model on each parameter and its initial value conditions showing that cosmological constant-like solutions are generic and do not require any fine-tuning of the model parameters and initial conditions. In addition, we will investigate the tachyonic instabilities noted in Ref. [277] to see if there are signatures of interesting phenomenology, such as clustering dark energy, and if they can cause an observable imprint.

We split the study in three parts. First, Section 6.1 will briefly review the model proposed in Ref. [277] and carefully examine the theory dependence on each parameter (Sections 6.1.1 and 6.1.2) and investigate how the observables change with them, including a quantitative assessment of the tachyonic instability phenomenon in terms of an observable signature (Section 6.1.3). Then, Section 6.2 will confront the model against observational data (described in Section 6.2.1) from CMB (Planck 2015) [294], BAO (BOSS DR12) [49], and the SN Ia (Pantheon) distances in terms of binned $E(z) = H(z)/H_0$ [62]. Section 6.2.2 will show the prior distributions used in the analysis and Sections 6.2.3 and 6.2.4 the results for the cases with only α free and the full model, respectively. The last part of this Chapter (Section 6.3) will show the expected constraints from the next-generation surveys Stage-4 CMB [92], LSST [17], DESI [19] and WFIRST [78], which will be briefly described in Section 6.3.1. Section 6.3.2 will review the multi-tracer Fisher formalism and the computational tools that carry out the computations, while Section 6.3.3 will show and analyze the forecasted constraints. In Section 6.4, we will conclude.

6.1 The α-attractor dark energy model

We will work on the generalized α-attractor potential from [277]. In the language of Equation 6.2, $V(\phi) = \alpha f^2(x)$ is the field potential and, in this case, is given by

$$V(x) = \alpha c^2 \frac{x^p}{(1+x)^{2n}} = \alpha c^2 2^{-2n}(1-y)^p(1+y)^{2n-p} , \tag{6.4}$$

with c, p, n constant parameters and $y \equiv e^{-2\phi/\sqrt{6\alpha}}$. The case $\alpha = 1$, $n = 1$, $p = 2$ corresponds to the Starobinsky model [295–297], working in natural units, i.e. reduced Planck mass $M_{\rm P} = 1$ and speed of light, $c = 1$. We will work on a flat geometry motivated by inflation. Figure 6.1

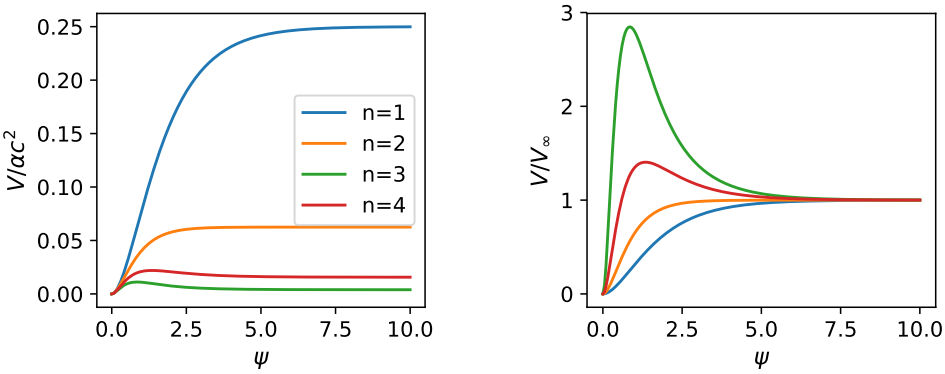

Figure 6.1: Generalized α-attractor potential for different values of n, fixing $p = 2$. For $n > 2$, there is a maximum. The maximum strengthens with n if the potential is normalized to its asymptotic amplitude.

shows the potential for different values of n using the variable $\psi \equiv \phi/\sqrt{\alpha}$, the scaled scalar field, since it is actually what determines the value of $V(x)$. Note how n controls the transition from the flat plateau to the monomial-shaped minimum.

Let us briefly summarize the potential properties before studying thoroughly the dependence on each parameter. The potential interpolates from a power law potential with index p to a cosmological constant fixed value, basically an uplifted (negative) exponential potential, for positive values of the field:

$$V(|\psi| \ll \sqrt{6}) \approx \alpha c^2 6^{-p/2}\, \psi^p \ , \tag{6.5}$$

$$V(\psi \gg \sqrt{6}) \approx \alpha c^2\, 2^{-2n} \left[1 - 2(p-n)\, e^{-2\psi/\sqrt{6}}\right] \xrightarrow[\psi\to\infty]{} \frac{\alpha c^2}{2^{2n}} \ . \tag{6.6}$$

We see that the amount of dark energy in the Universe will be determined by the potential amplitude, αc^2, whose characteristic scale will depend on n as ultimate responsible of the height of the plateau — for a model with $p = 2\,, \alpha = 1$ and $n = 0$, 3, 5, the amplitude $\alpha c^2 \sim 10^{-7}$, 10^{-6}, $10^{-5}\,\mathrm{Mpc}^{-2}$, respectively. Note there is no true cosmological constant: the potential is zero at the minimum.

The α-attractor potential has a maximum at $x_{\max} = p/(2n - p)$ given $n > p$ [277]. Fields starting (from rest) at $x > x_{\max}$ will roll towards infinity and the asymptotic constant potential, i.e. a de Sitter solution, while asymptotically freezing. On the other hand, for $x < x_{\max}$ the field would roll toward the origin along the plateau and eventually (possibly in the future) down toward the zero minimum. However, if it rolls too far off the plateau the kinetic energy rises, forcing the equation of state w far from -1 and it would not be a viable dark energy model today. Therefore we are not concerned with fields rolling past the minimum and so only need to deal with positive field values. Fields with $x < x_{\max}$ basically act like thawing models; they depart from a cosmological constant like behavior.

So far we have talked about the known properties of this model, already studied in Ref. [277]. Now, we will start our detailed study on its dependence on each parameter. We will vary α, n and p. The parameter c is fixed by the closure relation $1 = \sum_i \Omega_i$ (Equation 2.7), where Ω_i is the fractional energy density, i.e. the ratio of the energy density of component i (e.g. matter, dark energy, radiation) to the critical density. To solve the field evolution

$$\ddot{\phi} + 3H\dot{\phi} + V_\phi = 0 \ , \tag{6.7}$$

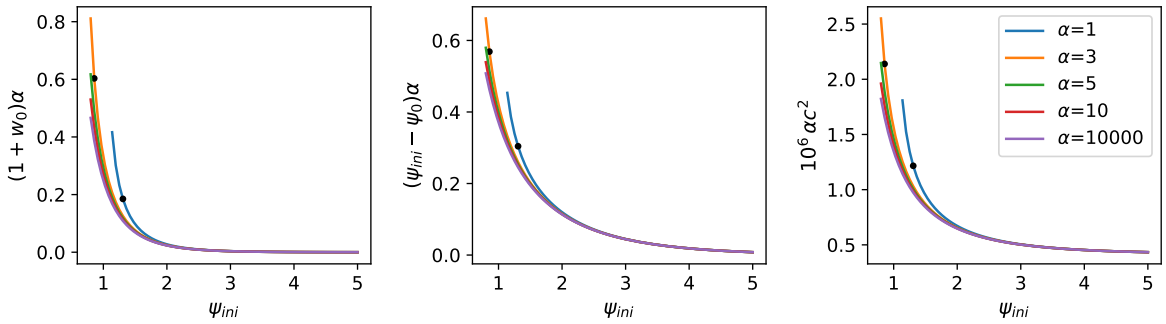

Figure 6.2: The dynamical quantities $(1+w_0)\alpha$ and $(\psi_{\rm ini}-\psi_0)\alpha$ are nearly independent of α for values of $\psi_{\rm ini}$ that deliver $1+w_0<-0.8$ (marked by black dots). Other parameters are fixed to $p=2$ and $n=1$, with c fixed by the density closure relation.

where $V_\phi = {\rm d}V/{\rm d}\phi$, we also need to specify the initial value of the field $\phi_{\rm ini}$ and its velocity $\dot\phi_{\rm ini}$. For a field starting on the nearly flat plateau (and if it starts off the plateau it is not using the α-attractor characteristics) the Hubble friction will freeze the field at early times (we start at $z_{\rm ini}=10^{14}$ in the radiation era) and so we take $\dot\phi_{\rm ini}=0$. Thus $\phi_{\rm ini}$ is the only further parameter. To solve the coupled differential equations that govern the cosmological history we use the `hi_class` Boltzmann code[1] [30, 31].

6.1.1 Dependence on the scaling of the potential (α)

We start our study on the effect of the different parameters varying the simplest one: the scaling α. This has close connections with the underlying particle physics (e.g. supergravity or conformal field theory model). Note that α scales the field value and the potential amplitude, but cannot be removed by a field redefinition since it does not appear in the kinetic terms $\dot\phi^2/2$.

Generally, larger values of α bring the model closer to ΛCDM, as the potential dominates more over the kinetic energy and the plateau is stretched out longer for a given value of ψ. We can make this more quantitative by employing the flow formalism for a thawing field [298],

$$1+w=\frac{4}{27}\left(\frac{V_\phi}{V}\right)^2\Omega_{\rm DE}+\mathcal{O}(V_{,\phi\phi}) \tag{6.8}$$

Since for fields on the plateau, $V_\phi/V\sim 1/\sqrt{\alpha}$, then $1+w\sim 1/\alpha$. We have numerically checked this relation holds until quite recent times and plotted $(1+w_0)\alpha$ in Figure 6.2. Note that in the quintessential inflation model of Ref. [280] they also find $1+w\sim 1/\alpha$, while the CMB tensor to scalar ratio $r\sim\alpha$ so a physics signature is present either in r (if α is large) or w (if α is small). In addition, we can see that for thawing models the field evolution $(\psi_{\rm ini}-\psi_0)\sim 1/\alpha$, where ψ_0 is the value today. This relation comes from

$$(\phi_0-\phi_{\rm ini})=\int_{\rm ini}^0 {\rm d}t\,\dot\phi\approx\int_{\rm ini}^0 {\rm d}t\,\sqrt{\rho_{\rm DE}(1+w)}\,. \tag{6.9}$$

Since the dark energy density changes little for thawing models, one can see that $\sqrt{\alpha}(\psi_{\rm ini}-\psi_0)\sim\sqrt{1+w_0}$ [268]. Effectively, Figure 6.2 shows that for viable models (those with $w_0<-0.8$) these relations hold quite well.

[1] `http://hiclass-code.net`. The implementation of the model was merged into the official code and is publicly available since version 2.0.

Note the initial value of the field plays an important role, with fields with high initial values mimicking the results of a cosmological constant. That is, $w_0 \approx -1$ and $\psi_{\rm ini} - \psi_0 \approx 0$. This is seen in Figure 6.2. Note that when $p > n$ (here $p = 2$, $n = 1$), the potential does not have a maximum and the field will always roll down towards $\psi = 0$. However, sufficiently large initial fields stay on the plateau nearly frozen for the whole evolution history of the Universe. For initial values of the field closer to $\psi = 0$, the parameter α determines when the field starts rolling down and, as a consequence, how fast it moves and how far the equation of state parameter is from the cosmological constant solution. Larger α's slow the field down, keeping it closer to cosmological constant behavior.

The case with $p < n$ has a maximum that causes a different phenomenology depending on the relative size of $\psi_{\rm ini}$ and $\psi_{\rm max}$ so that any field starting at high values ($\psi_{\rm ini} > \psi_{\rm max}$) would roll towards the de Sitter attractor. This case will be studied in detail in Section 6.1.2 and is shown in Figure 6.4.

Finally, the potential amplitude αc^2, responsible for the amount of dark energy in the Universe, which is kept fixed, needs to be adjusted to compensate the loss that comes from the evolving part of the potential, $V/\alpha c^2$. This is shown in the rightmost panel of Figure 6.2. It is fairly insensitive to $\psi_{\rm ini}$, especially for large $\psi_{\rm ini}$ where the field stays nearly frozen. As Equation (6.6) shows, once the amplitude is accounted for, the remaining form of the potential is insensitive to α, so the curves all lie together.

Thus, models will be close to ΛCDM if they either have large α (recall $1 + w_0 \sim 1/\alpha$) or large $\psi_{\rm ini}$. Since allowing them to get larger and larger will give the same physical results, in Section 6.2.2 we pay careful attention to priors for the Monte Carlo analysis.

6.1.2 Dependence on the shape of the potential (p and n)

In this Section we will study how the exponents, p and n, change the field evolution history. We treat them together because, leaving aside the low and high ψ regimes, where the potential is governed by, respectively, p and n separately (Equations 6.6 and 6.5), in the most interesting, intermediate ψ values it is their relative size that matters most.

For completeness, recall that p governs the low ψ regime (Equation 6.5) as $V \propto \psi^p$, and the slope of the potential (for a given n) in the transition between the plateau and the power law regime. The field evolution will be faster and earlier with larger p. Nevertheless, this prescription is only valid in the low-ψ regime and in the case $p > n$. The case with $n > p$, which will be analyzed later, is different because of the appearance of a maximum, whose size, position and steepness is determined by their relative size. The only different case is $p = 0$ because it is the only configuration that exclusively allows the field to grow towards the de Sitter attractor, since the potential is monotonically decreasing. This analysis is confirmed by numerical solution of the evolution equations, as seen for $\alpha = 1$ and $n = 1$, in Figure 6.3.

The exponent n, instead, fixes the asymptotic behavior of $V(\psi)$ as $V \to \alpha c^2 2^{-2n}$ (Equation 6.6) having a direct impact on the potential amplitude. This means that for a fixed amount of present dark energy density, the value of αc^2 must be modified in order to correct the deficit caused by n; thus it shifts up or down as seen in Figure 6.4.

We can also use Figure 6.4 to study the interdependence of both exponents in the intermediate ψ values since $p = 2$ and n ranges from 0 to 5 so that there are solutions with ($p < n$) and without ($p > n$) a potential maximum. In the later case, the potential plateau is slightly inclined towards $V = 0$ and the transition regime that connects it with the power law regime is steeper as $p - n$ grows. This expression also governs the size, slope and position of the maximum when $n > p$. On the one hand, its position is given by $x_{\rm max} = p/(2n - p)$, so that increasing n shifts the potential maximum toward $\psi = 0$. Quantitatively, for the studied cases with $n = 3$, 4, 5, the maximum is located at $\psi_{\rm max} = 1.35$, 0.85, 0.63 . On the other hand, fixing the dark energy

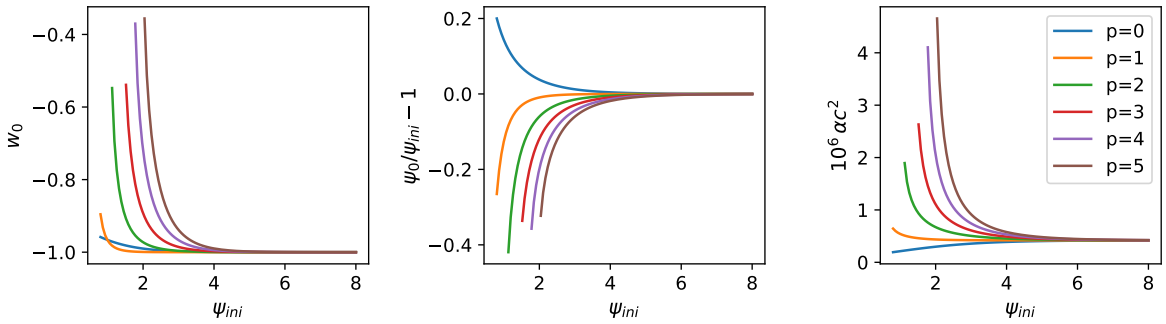

Figure 6.3: The values of w_0, $\psi_0/\psi_{\rm ini} - 1$ and αc^2 are plotted vs $\psi_{\rm ini}$ for various values of p, for a fiducial model with $\alpha = 1$ and $n = 1$. Except for $p = 0$, for which the potential (Equation 6.4) is monotonically decreasing, the exponent p determines the low-ψ shape of the potential. For $p \geq n$, the steepness grows with p, making the field evolve faster (and earlier). The potential amplitude αc^2 varies to compensate for the field evolution in order to preserve the same present dark energy density. Note that viable models with $w_0 < -0.8$ need small p or high $\psi_{\rm ini}$.

content makes the peak higher and steeper: for $n = 3$, 4, 5 the ratio of the potential maximum to its asymptotic value is $V_{\rm max}/V_\infty = 1.40, 2.84, 6.87$, respectively.

Thus, fields starting at $\psi_{\rm ini} > \psi_{\rm max}$ roll down toward ∞ with a velocity dependent on its proximity to the maximum. While fields with $\psi_{\rm ini} \gg \psi_{\rm max}$ remains almost frozen ($w_0 \sim -1$) on the plateau, those with $\psi_{\rm ini} \sim \psi_*$ (ψ_* is the inflection point at $\psi > \psi_{\rm max}$), where the slope is maximal, speed up, departing from the cosmological constant solution (w_0 grows). For $\psi_{\rm ini}$ closer to $\psi_{\rm max}$ the field feels a weaker force and its evolution is slower (w_0 decreases), having as a limit case, $\psi_{\rm ini} = \psi_{\rm max}$, where the field remains frozen for the whole evolution history of the Universe ($w = -1$). Starting at $\psi_{\rm ini} < \psi_{\rm max}$ the field rolls down again, but this time toward $\psi = 0$. The closer to the minimum it starts, the faster it evolves (w_0 grows quickly). Note that the shift in the maximum reduces the available space at $\psi_{\rm ini} < \psi_{\rm max}$ as n grows, e.g. giving the shift of the minimum to the left in Figure 6.4.

6.1.3 Model Predictions and Observables

Now we will focus on the phenomenological predictions of the model given by Equation 6.4. Besides the effects on the background expansion, in Ref. [277] it was suggested that, as a consequence of having $m^2 = V'' < 0$ near the edge of the plateau, one might find some interesting phenomenology, such as clustering dark energy. The field perturbations $\delta\phi_k$ in momentum space becomes [299]

$$\delta\ddot{\phi}_k + 3H\delta\dot{\phi}_k + \left(\frac{k^2}{a^2} - m^2\right)\delta\phi_k = 4\dot{\phi}_k\dot{\Phi} - 2V_{,\phi}\Phi\,, \tag{6.10}$$

in standard Newtonian gauge notation, where the metric perturbations $\Phi = -\Psi$ (following the convention of Equation 2.15).

Since perturbations start growing significantly at horizon entering, we will just consider $k > H$ modes. In addition, Equation 6.10 tell us that the mass term must be $|m^2| \gtrsim k^2/a^2$ in order to change the perturbation growth, bounding the scales sensitive to the imaginary mass to

$$\frac{|m^2|}{H^2} \gtrsim \frac{k^2}{a^2H^2} > 1\,. \tag{6.11}$$

Given that the field starts evolving at late times ($z \sim O(1) - O(10)$) and that the field's mass

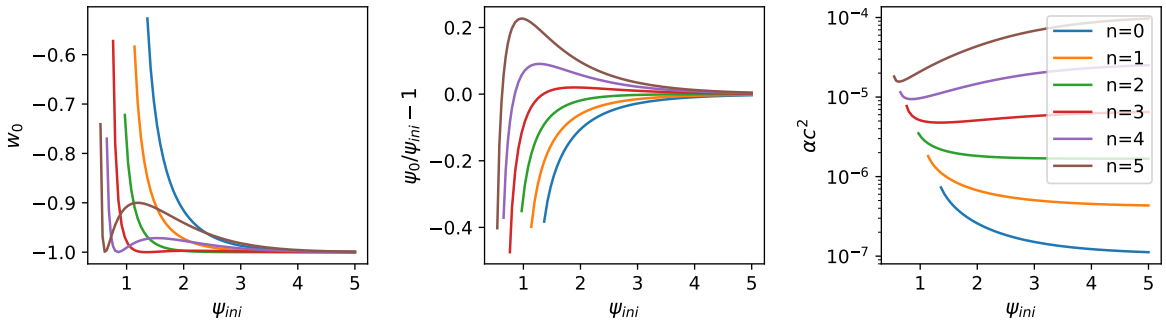

Figure 6.4: As Figure 6.3 but varying with respect to n, with a fiducial model $\alpha = 1$ and $p = 2$. All curves end at the lowest value that gives $\Omega_{\rm DE} \sim 0.7$ today. The relative size of n respect to p changes the potential slope on the plateau: the closer they are, the less pronounced the slope is. This means that as n goes to $p = 2$, the field rolls down later and slower. The potential amplitude αc^2 varies to compensate for the amplitude reduction 2^{-2n} in Equation 6.6 in order to preserve the same present dark energy density. Note that viable models with $w_0 < -0.8$ need $n \approx p$ or high $\psi_{\rm ini}$.

will not be extremely high, the affected wavenumber will be $k \approx 10^{-3}\,{\rm Mpc}^{-1}$, i.e. much larger scales than where precision clustering data lies. In addition, late time evolution implies that perturbations will not have much time to grow.

As a consequence, observing some effect requires a sufficiently large negative mass squared. We have computed the present value of the mass squared term for each model studied in the previous Section, and plotted it in Figure 6.5. One can read from it that models with exponents $n < p$ have only two regions, separated by the inflection point in the transition zone, so that $m^2 < 0$ is expected for high $\psi_{\rm ini}$ and $m^2 > 0$ at low $\psi_{\rm ini}$. On the contrary, as $n > p$ implies the appearance of a maximum, the region with $m^2 < 0$ is bounded by the inflection points. It is important to remark that, given that n makes the maximum steeper as it grows, high n can give rise to sufficiently negative m^2, which, in theory, could be potentially noticeable. Nevertheless, for the sensible models studied here, with no extreme exponents, and compatible with the dark energy density observations, which in the end fixes the potential amplitude, we have found that all models have a similar perturbation growth, just varying a little bit close to the present.

Figure 6.6 illustrates that even the extreme model with with $m^2/H_0^2 \sim -20$ (that indeed has unviable equation of state $w(a) \approx -0.74 - 1.9(1-a)$) shows that perturbations have little effect on the dark energy density or field value for the cosmic history up to the present.

Similarly, the growth function of matter perturbations (Figure 6.7) does not show a significant change with respect to ΛCDM. Since the dark energy equation of state only deviates appreciably from -1 at low redshift, the growth factor is close to that of ΛCDM until recently. Only those models that roll significantly, falling off the plateau show more than percent level deviations.

In those cases, the matter power spectrum as shown in Figure 6.8 is lowered as well, yielding relative differences up to a few percent. Similarly the CMB temperature angular power spectrum (Figure 6.9) departs from ΛCDM. Such deviations can be compared with experimental data letting us rule some models out. In particular, the larger differences at high multipoles are due to the geometric shift in the distance to recombination, anticipating that CMB and BAO galaxy distances will be important to take into account.

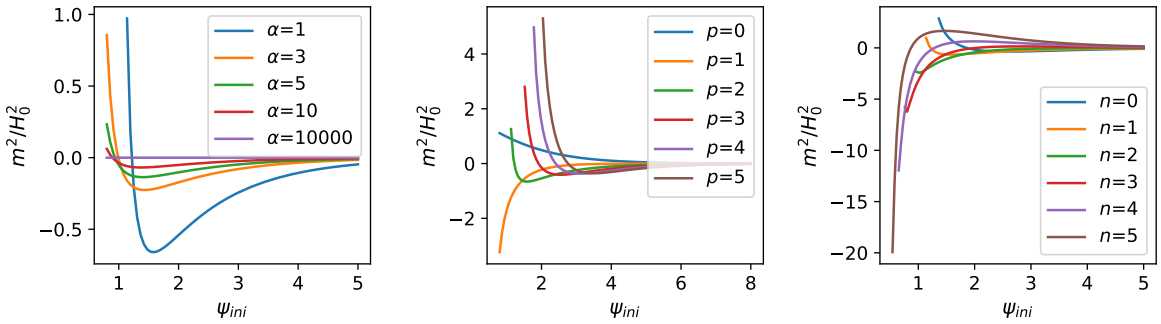

Figure 6.5: The mass squared m^2/H_0^2 can go negative, as is standard for hilltop models, but generally not deeply (relative to H^2) or for long. When $n < p$, there are two regions, delimited by the inflection point in the transition between the power law regime and the plateau, where the mass squared is positive or negative, respectively. On the contrary, if $n > p$, the appearance of a maximum means that $m^2 < 0$ is bounded around it by the two inflection points. As commented in Section 6.1.2, n has a great impact on the relative size of the maximum respect to the plateau, making it also the parameter with greatest impact on m^2.

Distances are integrals over the Hubble parameter (Equation 2.13), i.e.

$$D_{\mathrm{A}} = \frac{1}{1+z}\int_0^z \frac{\mathrm{d}z'}{H(z')}\,, \tag{6.12}$$

for the flat universe we consider. While the Hubble parameter should have its largest deviation from ΛCDM at low redshift, as an integral the distance has increasing deviation with redshift. These quantities are shown in Figure 6.10 and Figure 6.11. Thus we expect that both $z < 3$ measures, e.g. from supernovae and BAO, and high redshift measures from the CMB, will play important roles in constraints.

6.2 Observational constraints

In this Section we will compare the α-attractor model (Equation 6.4) with recent observations. In Section 6.2.1 we will explain the choice of datasets based on the knowledge acquired in previous sections. Then, in Section 6.2.2, we will impose some appropriate and sensible priors which will be needed in the study of the posterior distributions of two iconic cases: that with the exponents of the Starobinsky model ($p = 2$, $n = 1$) but with the scaling allowed to be free, and that with all the parameters freed. We will see that a large portion of the parameter space is ruled out, favoring models close to ΛCDM.

6.2.1 Data sets

We will use the Planck 2015 observations [294], BAO BOSS DR12 [49] and the measurements of $E(z) = H(z)/H_0$, obtained using the latest SNe Ia at $z > 1.5$ [62, 124]. The reason we choose these observations is that Planck sets high redshift constraints, although it also take into account the lower redshift effects through secondary CMB contributions, BAO does at low redshift, where we have found the largest differences, and $E(z)$ imposes direct constraints in the expansion rate up to $z = 1.5$.

In general, CMB observations are used because CMB is affected by the expansion rate, the matter components and inflationary conditions (a good summary of reasons is found in Section 3.1 of this Thesis and Section 2 of Ref. [294]), allowing the constriction of the cosmological

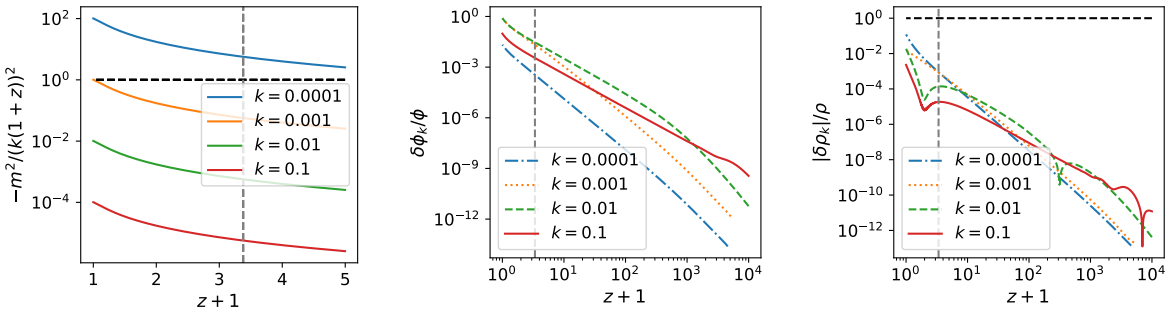

Figure 6.6: Redshift evolution is shown of the mass squared relative to the k^2/a^2 term (left), the normalized field perturbation (middle), and the normalized density perturbation for the model $\alpha = 1$, $\psi_{\rm ini} = 0.542$, $p = 2$ and $n = 5$, the extreme model with $m_0^2/H_0^2 \approx -20$. The vertical dashed line marks the redshift when $|m^2|/H^2 = 1$ and the horizontal one shows $|\delta\rho_k/\rho| = 1$. k is in units of Mpc^{-1}. Recall that the mode with $k = 10^{-4}\,\mathrm{Mpc}^{-1}$ has not yet entered in the horizon. Dark energy density perturbation modes are negligible with respect to its background value during almost the whole evolution history even for this extreme model.

parameters. Indeed, for models close to ΛCDM it allows precise evaluation of them. Furthermore, since deviations from ΛCDM on the power spectrum rise up to few percent (Figures 6.8 and 6.9), Planck and BAO likelihoods could be sensitive to them. BAO set low redshift constraints on H and $D_{\rm M} = (1+z)D_{\rm A}$, where the models' greatest differences with respect to ΛCDM are found. We have chosen the latest released dataset, BAO BOSS DR12 [49], which covers $z \lesssim 0.7$. We have not used Lyman-α BAO measurements, even though they go much deeper in redshift, because they are in tension with Planck and low redshift BAO measurements [300, 301]. For instance, in ΛCDM the discrepancy is approximately 2σ, and our model is phenomenologically too close to ΛCDM to avoid the tension. Lastly, further control on the expansion rate is given by the estimates of $E(z)$ up to $z = 1.5$ using the SN Ia distance observations at $z > 1.5$ [62, 124].

We used the full temperature, polarization and lensing power spectra from Planck 2015 [294]. The main signatures of the model are changes on the cosmological background (at least for models close to a cosmological constant) which can be tested by the Planck compressed likelihood (Table 4 in Ref. [294]). Including the full Planck data allows us to explore potential degeneracies with other cosmological parameters ($A_{\rm s}$, $n_{\rm s}$, $\tau_{\rm reio}$, $\cdots$) and take into account effects in the perturbation growth (i.e. ISW effect). The difference between the full and compress Planck likelihoods is negligible for most of the common parameters, with the largest deviation below 1σ for H_0 and $\Omega_{\rm cdm}h^2$, where $h = H_0/(100\,\mathrm{Mpc}^{-1}\mathrm{km\,s}^{-1})$.

BAO BOSS DR12 measurements [49] are independent of Planck's and are in good agreement with them. Since the most deviating cases are ruled out from the acoustic scale, we can just consider the background quantities and use the consensus BAO-only values suggested in the paper. We have taken them from its electronic archive[2]. Let us note that the actual variables that BAO can measure are $D_{\rm M}(z)/r_{\rm d}$ and $H(z)r_{\rm d}$ (Equation 3.34), which take into account changes in the cosmological parameters and in the pre-recombination energy density era. Since $r_{\rm d}$ is the sound horizon at drag epoch ($z_{\rm d}$), $r_{\rm d} = \int_{z_{\rm d}}^{\infty} \mathrm{d}z\, c_{\rm s}(z)/H(z)$ (Equation 3.10), with $c_{\rm s}$ the speed of sound, and our models are nearly identical to ΛCDM at high redshift, the BAO data informs us of deviations in $D_{\rm M} = (1+z)D_{\rm A}$, i.e. the comoving distance and H.

[2] `https://data.sdss.org/sas/dr12/boss/papers/clustering/ALAM_ET_AL_2016_consensus_and_individual_Gaussian_constraints.tar.gz`

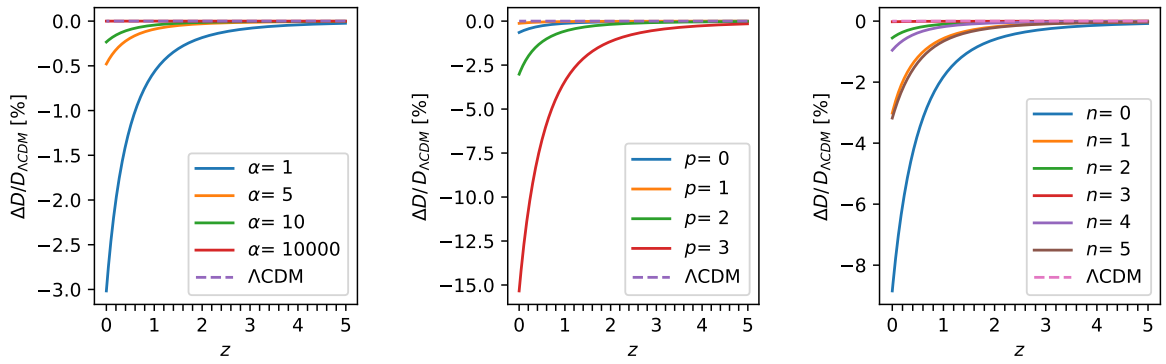

Figure 6.7: The matter density perturbation growth factor D is shown as the relative deviation from ΛCDM for different models varying α, p and n, using $\alpha = 1$, $p = 2$, $n = 1$ and $\psi_{\rm ini} = 1.5$ as the base model. The more the field moves, the more thawing, allowing dark energy to dominate earlier, suppressing matter growth. By contrast, the case with $n = 3$ has the field frozen for $\psi_{\rm ini} > 1$ and so $w_0 \approx -1$ (see the left panel of Figure 6.4). Higher $\psi_{\rm ini}$ would freeze most models in the plateau, decreasing deviations from ΛCDM.

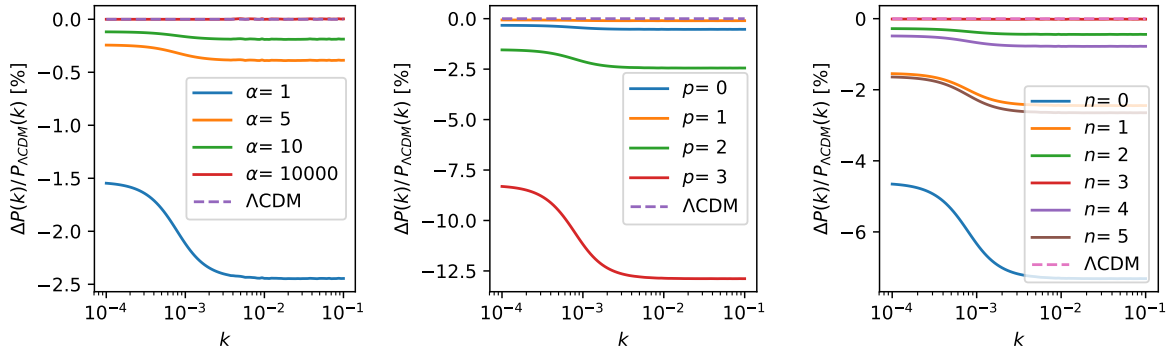

Figure 6.8: The matter power spectrum $P(k)$ is shown as the relative deviation from ΛCDM for different models varying α, p and n, using $\alpha = 1$, $p = 2$, $n = 1$ and $\psi_{\rm ini} = 1.5$ as the base model. The more the field thaws, the more the power spectrum is suppressed.

Finally, $E(z)$ constraints [62] compress the information of a thousand SN Ia distances from the unreleased Pantheon dataset[3] and Hubble Space Telescope, including 15 new discovered supernova at redshift $z > 1.5$. Their measurements are thought to be precise and unbiased estimates of $E(z)$ as long as the expansion rate does not vary much nor have localized features between the specific chosen redshifts, as for our model. Their only assumptions were flatness, not mandatory but convenient, and continuity and smoothness of $E(z)$ in order to parametrize its inverse by its values at different specific redshifts. They used those points to interpolate and recover the whole function, necessary to compute the luminosity distance (Equation 6.12), which they could compare against their selection of well-calibrated SN data.

[3]The Pantheon sample [124] was publicly released after the publication of our paper Ref. [1], on which this Chapter is based, and can be found in `http://dx.DOI.org/10.17909/T95Q4X`.

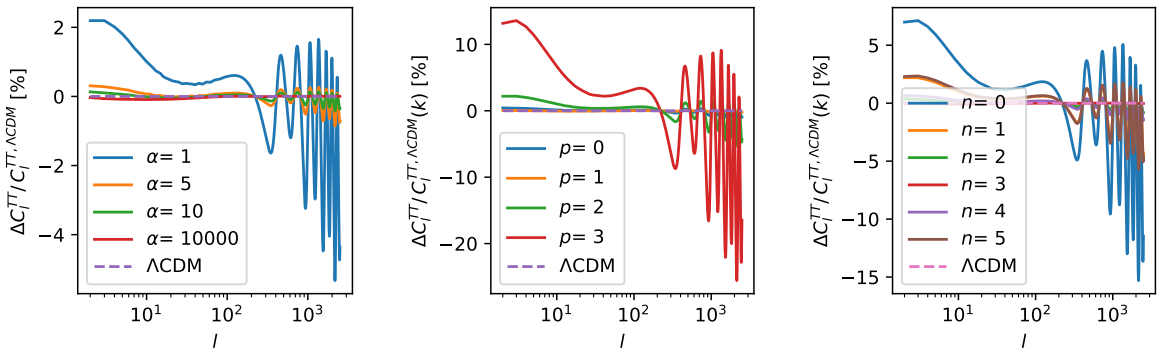

Figure 6.9: Temperature angular power spectrum C_ℓ^{TT} is shown as the relative deviation from ΛCDM for different models varying α, p and n, using $\alpha = 1$, $p = 2$, $n = 1$ and $\psi_{\rm ini} = 1.5$ as the base model. Apart from having different amplitude for low ℓ, the spectrum is shifted in angular scale with respect to that of ΛCDM.

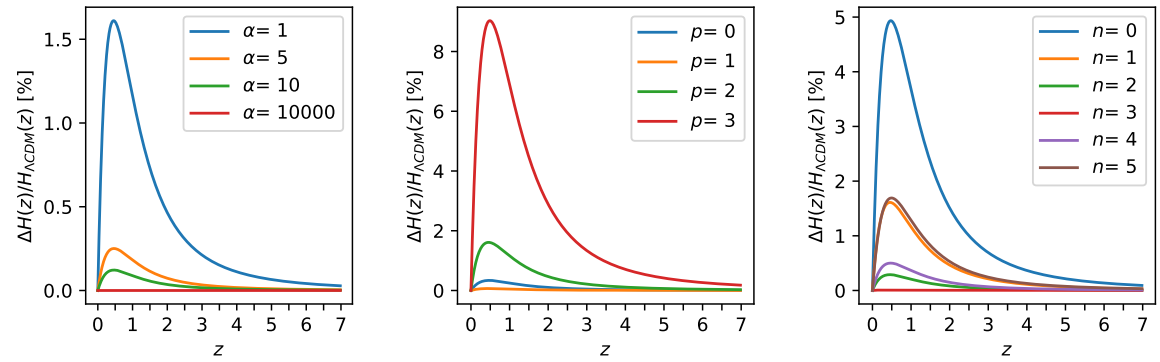

Figure 6.10: Hubble parameter is shown as the relative deviation from ΛCDM for different models varying α, p and n, using $\alpha = 1$, $p = 2$, $n = 1$ and $\psi_{\rm ini} = 1.5$ as the base model. Fields that thaw more have larger expansion rates, modulo the normalization to fixed H_0 today.

6.2.2 MCMC setup

The posterior distribution of the α-attractor model (Equation 6.4) which will be shown in next Section has been obtained by sampling the parameter space with a Markov Chain Monte Carlo (MCMC) method. In particular, we made use of MontePython [36] and CosmoHammer [42] which embeds emcee [41], an implementation of the Goodman and Weare affine invariant ensemble sampler [40]. We chose this algorithm instead of the traditional Metropolis-Hasting to avoid acceptance rate and convergence problems since affine invariant sampling methods are uniformly effective over all the convex bodies with same space dimension and regardless of their shape [40]. In addition, CosmoHammer parallelization allows much faster computations.

The priors are summarized in Table 6.1. Since the parameters for viable models do not vary over much more than an order of magnitude, and no particular values are preferred, a uniform prior is reasonable. This matches well with the MontePython implementation of CosmoHammer which does not allow informative or unbounded priors. As we have seen in Section 6.1, sufficiently high values of the scaling α or the initial field $\psi_{\rm ini}$ all yield ΛCDM-like universes. Also, the exponents, p and n, just under the condition of being close to each other, no matter how high they were, yield more ΛCDM-like results provided that the field had not

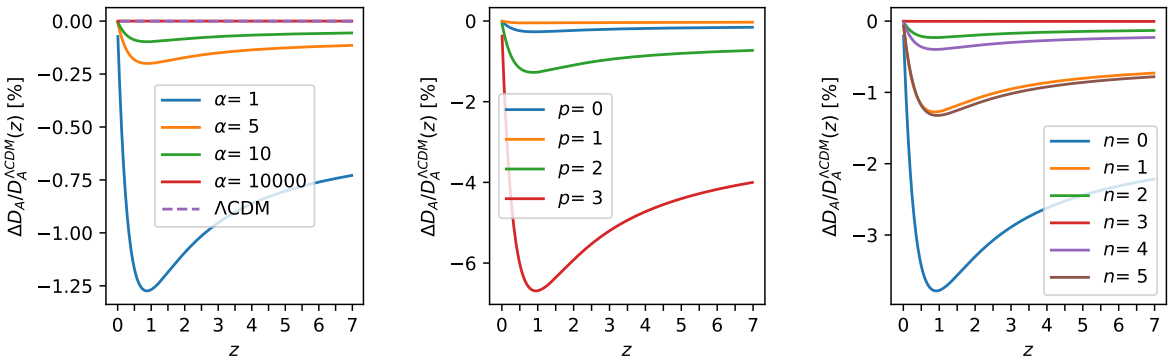

Figure 6.11: Angular distance is shown as the relative deviation from ΛCDM for different models varying α, p and n, using $\alpha = 1$, $p = 2$, $n = 1$ and $\psi_{\rm ini} = 1.5$ as the base model.

Parameter	Range
H_0	[40, 90]
$\Omega_{\rm b}h^2$	[0, 0.04]
$\Omega_{\rm cdm}h^2$	[0, 0.3]
$\dot{\phi}_{\rm ini}$	{0}
$\psi_{\rm ini}$	[0, 3.5]
α	[0, 10]
p	[0, 10]
n	[0, 10]
c	Fixed by $1 = \sum_i \Omega_i$

Table 6.1: Priors used in the MCMC posterior inference. H_0 units are $[\mathrm{km\,s^{-1}Mpc^{-1}}]$ and c is obtained by a bijection method.

started rolling off the plateau too early, i.e. the viable set of models. There is therefore no point in allowing a large range of such high values, which all give essentially ΛCDM. Therefore we bound their space to prevent walkers[4] wasting time in the infinite ΛCDM regime, although we set the bounds large enough to be able to explore all the interesting phenomenology of the model. Finally, in order to accelerate the convergence, we fixed c with the closure relation $1 = \sum_i \Omega_i$, using a bijection method.

6.2.3 Starobinsky form vs ΛCDM

Before studying the full general model posterior distribution, we want to focus on the more constrained case with exponents $p = 2$ and $n = 1$, the one which reduces to the Starobinsky potential when the scaling $\alpha = 1$. Increasing the parameter space in stages will let us understand more easily how the model behaves, letting us check our understanding of its dependence on α and $\psi_{\rm ini}$. Furthermore, the scaling acts as an interpolation between the ΛCDM (high $\psi_{\rm ini}$ or α) and Starobinsky models ($\alpha = 1$).

After studying the autocorrelation times, we decided to use 10 walkers per varied parameter, i.e. 230 walkers in total, and run 1400 iterations, from which we discarded the first 1000 as burn in. Fewer iterations would have sufficed since the slowest autocorrelation function crosses 0

[4]A walker is the equivalent of a chain in a Metropolis-Hasting algorithm, in Goodman-Weare terminology. Note their dynamics are different, though.

Parameter	best-fit	best-fit with $\alpha = 1$	95% limits
$\Omega_{\rm cdm}h^2$	0.1199	0.1192	0.1187 ± 0.0023
H_0	67.8	68.0	$68.1^{+1.1}_{-1.0}$
$10^2\Omega_{\rm b}h^2$	2.216	2.226	$2.221^{+0.039}_{-0.040}$
$10^9 A_{\rm s}$	2.12	2.12	$2.14^{+0.10}_{-0.090}$
$n_{\rm s}$	0.9592	0.9652	$0.9644^{+0.0088}_{-0.0089}$
$\tau_{\rm reio}$	0.063	0.058	$0.068^{+0.024}_{-0.023}$
$\psi_{\rm ini}$	2.61	2.82	> 1.27
α	3.78	1.00	—
$10^7 c^2$	1.45	5.32	< 5.5
w_0	-0.998	-0.995	$-1 \leq w_0 < -0.974$
w_a	-0.0029	-0.0081	$0 > w_a > -0.0413$
m_0^2/H_0^2	-0.09	-0.28	$-0.12^{+0.19}_{-0.25}$
$\chi^2_{\rm min}/2$	5642.099	5646.458	—

Table 6.2: Parameter best fit values and 95% confidence limit for the $p = 2$, $n = 1$ Starobinsky form, allowing α to vary. The $\alpha = 1$ column corresponds to the pure Starobinsky model. H_0 units are $\mathrm{km\,s^{-1}Mpc^{-1}}$ and Mpc^{-2} for c^2. Note that α is unbounded at 95% C. L. (see Figure 6.12).

around 400, but we took a conservative approach given the low time cost. To analyze convergence we used the MontePython [36] internal routine which puts all chains together, ordered by iteration step, splits the resulting chain in three and calculates the Gelman-Rubin test.

The posterior distributions are shown in Figure 6.12 while the quantitative results are in Table 6.2. The first thing to note is that the cosmological parameters are in good agreement with ΛCDM Planck 2015 results [176]. This is related to the fact that our model has a preferred ΛCDM-like regime. In fact, we see that their posterior distribution is unaffected by α and almost any $\psi_{\rm ini}$. The $\psi_{\rm ini}$ posterior distribution, however, has a lower boundary which sets $\psi_{\rm ini} > 1.27$ at 95.4% confidence level. This value is altered by the parameters range choice, as we will see in next Section, and cannot be understood as a general condition. The α–$\psi_{\rm ini}$ figure confirms what we said in Section 6.1.1: the lower α and $\psi_{\rm ini}$ regime is disfavored as a consequence of the fact that a faster evolution of the field yields, for models that match the present dark energy density, a less negative equation of state, which is in tension with data. On the contrary, large α and $\psi_{\rm ini}$ freeze the field evolution getting it closer to $w = -1$, which the data prefer.

The dark energy equation of state parameters w_0 and w_a confirm our previous comments. Their values are close to $w = -1$, regardless of the particular value of α and $\psi_{\rm ini}$. Again, the reason why this happens is that a large value of either one of them can give $w \approx -1$ (see for instance the $\alpha = 10^4$ case in Figure 6.2).

The correlation between w_0 and w_a follows the typical pattern of thawing fields. In Figure 6.13a, we have plotted the w_0–w_a posterior distribution over a random sample of 2×10^4 points colored as a function of the value of the present field mass. Those models with greatest probability follow the thawing relation $w_a \approx -1.6(1+w_0)$ [268]. This leads to tight constraints on w_a. A more subtle effect is the correlation between the equation of state parameters and the field mass, which makes lower mass squared field models be located under those with higher mass squared for the same w_0. Recall that negative mass squared tends to occur for low α models, which also have greater deviations from $w = -1$.

The amplitude parameter c, which we have obtained by requiring $1 = \sum_i \Omega_i$, does not vary much; basically to get $\Omega_{\rm DE,0} \sim 1$, one requires $c^2 \lesssim H_0^2$, hence $c^2 \sim 10^{-7}\,\mathrm{Mpc}^{-2}$. This will change once we let n vary since n affects the height of the plateau and c must compensate any

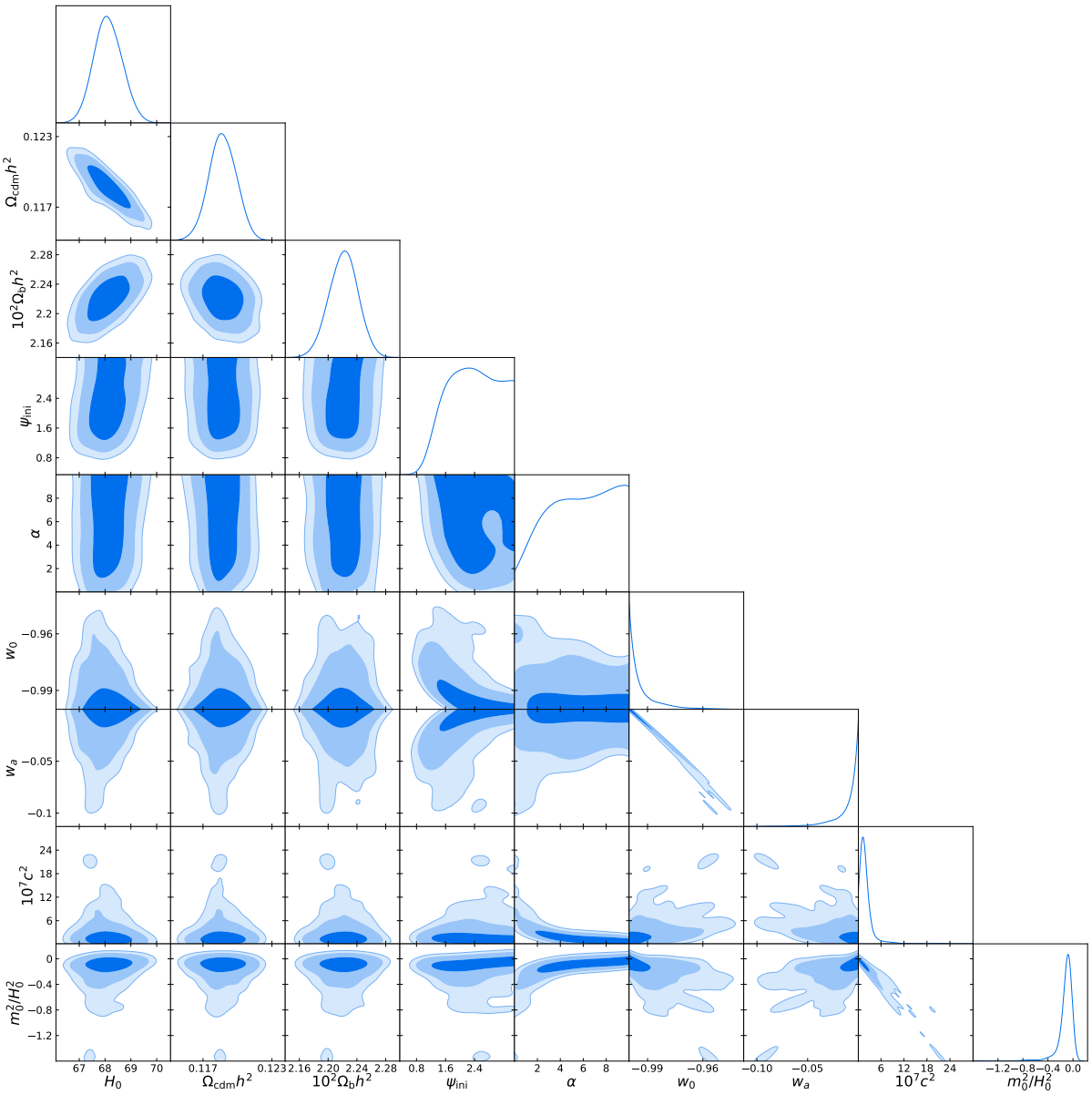

Figure 6.12: Posterior distributions for the Starobinsky form allowing α to vary, with $p = 2$, $n = 1$. The contours show the 68.3%, 95.5%, and 99.7% confidence levels, with darker colors for more probable results. The quantitative results are summarized in Table 6.2.

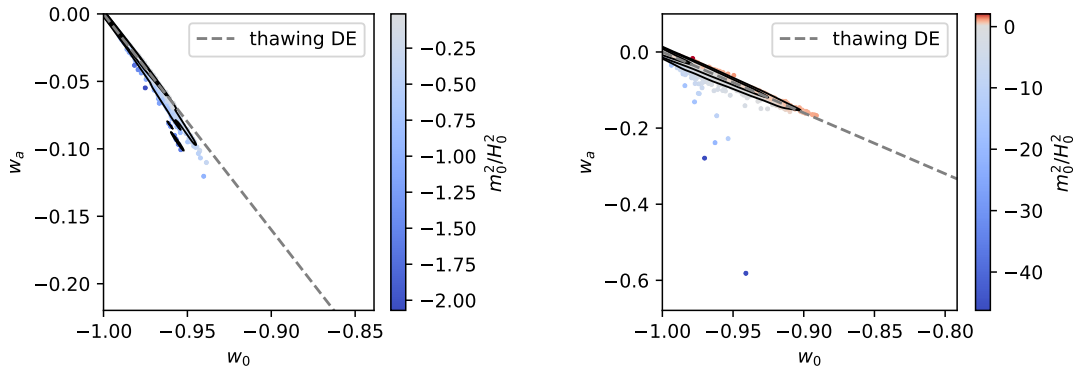

(a) Starobinsky-like ($p = 2$, $n = 1$). (b) General.

Figure 6.13: The w_0–w_a joint posterior distribution is shown for the Starobinsky form (left) and full generalized α-attractor (right) dark energy models (Equation 6.4) over a random sample of 2×10^4 points colored depending on their present field mass. The dashed grey diagonal line represents the usual w_0–w_a relation for thawing models ($w_0 < -0.8$) described in reference [268].

change on the potential to obtain the correct dark energy density. Finally, the present field mass squared, m_0^2/H_0^2, is preferably negative, with 95% C. L. region $(m_0^2/H_0^2)_{95\%C.\ L.} \in (-0.37, 0.07)$. The reason why most solutions are tachyonic is the absence of a maximum in the potencial. In this configuration, the regime with moderate slope, where the field can slow-roll, is found close to the plateau and has $V'' < 0$. However, the $V'' > 0$ regime is that described by a power law and, consequently, the field is quickly speed up. In spite of tachyonic solutions being natural they are not large enough as to play an observable role, given the small effect of even $m^2/H_0^2 \approx -20$ in Section 6.1.3.

Before moving to full model we note that the best-fit Starobinsky form model has $\alpha = 3.78$, well inside the 68% confidence level region, in contrast to the Starobinsky model ($\alpha = 1$), which lies on the 95% C. L. region. In fact, although the $\chi^2_{\rm min}$ difference is relatively small, for one more parameter, the Akaike Information Criterion [302], AIC $= \chi^2 + 2k$, where k is the number of model parameters, tells us that the Starobinsky case is disfavored over the general one ($\mathrm{AIC}_{BF} - \mathrm{AIC}_{\alpha=1\,,BF} = -6.7$). The Schwartz information criterion ($\mathrm{BIC} = \chi^2 + k\log(N)$, where N is the number of data degrees of freedom) [303], however, is more lenient over the $\alpha = 1$ case as it takes into account the size of the data sample. In this case, $|\Delta\mathrm{BIC}| \sim 10^{-1}$, which does not select any model as preferred. It is important to remark that, in both cases, one finds that data prefers ΛCDM-like cosmologies, described by their equations of state which are almost $w = -1$ ($w_0 = 0.998\,, 0.995$, respectively).

6.2.4 Analysis of the full posterior distribution

Finally, we will study the general case with free exponents p and n, as well as α. It will collect all the dependencies we have been describing and let us find the full posterior distribution for the dark energy model proposed by Ref. [277], an α-attractor quintessential model with potential given by Equation 6.4.

For this case the number of walkers per parameter was maintained in 10, giving a total of 250 walkers, the sample iterations were increased to 2500, with 1000 burn in iterations to be discarded, and 1500 iterations to be stored. The extra degrees of freedom had a direct impact on convergence, making it much slower. As before, we checked the autocorrelation time and

Parameter	best-fit	mean ± 95% limits
$\Omega_{\rm cdm}h^2$	0.1186	$0.1183^{+0.0024}_{-0.0022}$
H_0	68.3	$68.2^{+1.0}_{-1.1}$
$10^2\Omega_{\rm b}h^2$	2.224	2.221 ± 0.038
$10^9 A_{\rm s}$	2.15	$2.14^{+0.10}_{-0.098}$
$n_{\rm s}$	0.9640	$0.9649^{+0.0081}_{-0.0087}$
$\tau_{\rm reio}$	0.070	$0.067^{+0.026}_{-0.025}$
$\psi_{\rm ini}$	1.401	> 0.955
α	8.530	—
10^3c^2	3.44×10^{-3}	< 3.89
p	3.140	—
n	4.233	—
$p-n$	-1.1	$0.4^{+6.4}_{-5.2}$
w_0	-1.000	$-1 \leq w_0 < -0.951$
w_a	-0.0006	$0 > w_a > -0.0789$
m_0^2/H_0^2	-0.19	$-0.2^{+1.2}_{-1.1}$
$-\ln\mathcal{L}_{\rm min} = 5641.276$		

Table 6.3: Best fit model for the full potential 6.4. H_0 units are $\mathrm{km\,s^{-1}Mpc^{-1}}$ and $\mathrm{Mpc^{-2}}$ for c^2. Note that α, p and n are unbounded (see Figure 6.14).

computed the Gelman-Rubin test with MontePython [36].

The results are written in Table 6.3. In Figure 6.14 we have plotted the marginalized posterior distribution of the model parameters and the present mass field, leaving aside the cosmological parameters because of their similarities with the results in previous Section, represented in Figure 6.12. Note that the α–$\psi_{\rm ini}$ plot continues to show that $\psi_{\rm ini}$ and the kinetic coefficient α cannot be simultaneously small. Apart from that, all the parameter subspaces tell us something new. For example, the high exponent p disfavors the lower $\psi_{\rm ini}$ regime. As we said in Section 6.1.2, higher p makes the low $\psi_{\rm ini}$ regime steeper, making the field roll faster and changing the expansion rate too much to match the observations. Higher n, changing more the amplitude of the plateau, do not have as strong an effect on the $\psi_{\rm ini}$ range, but does allow for much lower c; note that $n \sim 5$ in the middle of its range can suppress c^2 by a factor $2^{-2n} \sim 1000$.

However, we see that actually it is the difference $p-n$ that mostly matters (see Equation 6.6 and Section 6.1.2), with a strong correlation in the p vs n plane. The mean posterior, with the 95.4% C. L. values, is $p - n = -0.4^{+6.4}_{-5.2}$. Of course, higher values of $\psi_{\rm ini}$ and α make the constraint on $p-n$ weaker as they freeze the field so there is less sensitivity to the shape of the potential.

The m_0^2/H_0^2 distribution is also slightly broader, thanks to the possibility of having a maximum which bounds the region where $V'' < 0$, and makes $V'' > 0$ at the plateau. As we know that slow-roll solutions are mainly placed in those regimes, the 95% C. L. is symmetric around 0, $|m_0^2/H_0^2|_{95\%\text{C. L.}} \sim 1$. Similarly, freeing the exponents allows the w_0–w_a distribution (Figure 6.13) to expand, while continues following the thawing solution, even better than before since allowing $p \approx n$ can give flatter plateaus.

It is important to note that introducing two new parameters has just slightly improved the χ^2 ($\chi^2_{\rm full}/2 = 5641.276 \simeq 5642.098 = \chi^2_{np,\rm fixed}/2$). This makes the Akaike Information Criterion ($|\Delta\mathrm{AIC}| = 2.4$) prefer the simpler model with fixed exponents. The Schwartz criterion is more strict in this case ($|\Delta\mathrm{BIC}| \sim O(10)$), completely rejecting the more complex case. This result is a consequence of the limited phenomenology available in this model, which is mainly described by how much and how fast the field changes, which can be controlled by just α and $\psi_{\rm ini}$.

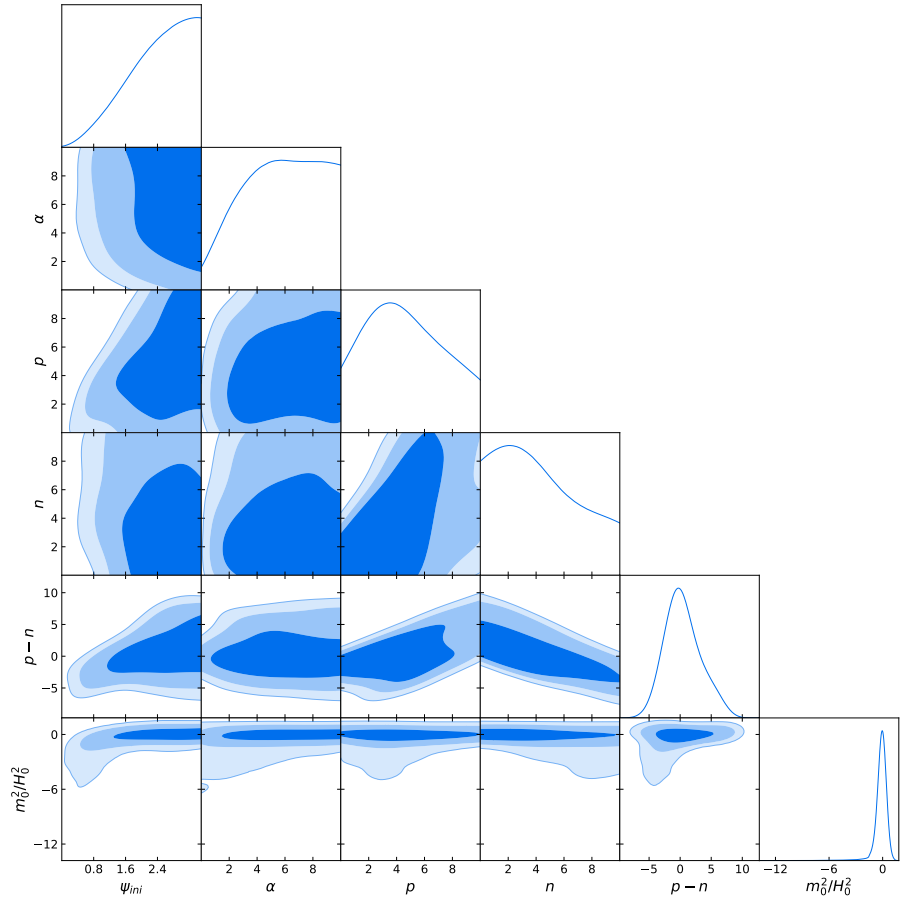

Figure 6.14: Posterior distribution for the generalized α-attractor dark energy model with potential 6.4. The contours show the confidence levels up to 99.7% C. L., with darker colors for more probable results. The quantitative results are summarized in Table 6.3.

Furthermore, the data prefers ΛCDM which is recovered by high α or $\psi_{\rm ini}$. Indeed, the best fit model is almost indistinguishable from ΛCDM, having $(w_0, w_a) = (-1.000, -0.0006)$.

6.3 Prospects of detection with next-generation experiments

It has been seen that the generalized Starobinsky-model has an infinite ΛCDM-like region that makes that, imposing only late time observational constraints (and a true model close to ΛCDM), one can only have lower bounds on the initial position of the field and α and the requirement on the exponents of being of the same order, so that the field slow rolls.

In this Section, we will systematically study how future observations will affect the constraints on the model's parameters. Next spectroscopic experiments generation will reduce the relative error on the angular diameter distance and the Hubble parameter to order of a few percent, while deepening up to $z \sim 3$ [18, 19]. Baryonic Acoustic Oscillations (BAO) measurements will also significantly improve their accuracy, what will be reflected on the parameter constraints. On the other hand, Stage 4-CMB experiments are expected to measure the tensor-to-scalar ratio to order $\sigma(r) \sim 0.001$ [304]. Lowering the r upper-bound below ~ 0.01 might be able to constrain α through Equation 6.1 and, in turn, the initial value of the field. Finally, from the Large Synoptic Survey Telescope [17], a photometric experiment, we will take into account their predictions for galaxy clustering and shear measurements, which will effectively constrain

cosmological parameters by means of precise measurements of the matter power spectrum at different redshifts.

It is important to note that some of these next-generation experiments will overlap, allowing to beat cosmic variance (for certain parameters) when cross-correlations are taken into account [305]. In order to take advantage of this piece of information, we will use the multi-tracer formalism as described in Ref. [58], which is reviewed in Section 6.3.2.

Note that the lower boundary of $\psi_{\rm ini}$ depends on the maximum value accessible for α, since the total evolution of the field is inversely related to α (second item of previous list). As a consequence, constraining α through Equation 6.1 and $n_{\rm s}$ and r measurements could significantly improve the previous result of Section 6.2 cutting out a big portion of the available space for $\psi_{\rm ini}$. Quantitatively,

$$\alpha = \frac{r}{3(1-n_{\rm s})^2}\,, \tag{6.13}$$

so that if Stage 4-CMB experiments measured $r < 0.01$, $\alpha \lesssim 3.5$, which would highly constrain the initial position of the field, restricting its values to positions close to the plateau or the maximum, where the field slow-rolls. It would be even more dramatic if $r \sim 10^{-3}$ (exhausting the intended minimum uncertainty [304]), as $\alpha \sim 0.35$. However, if r remained close to its upper bound value of Planck 2018 results ($r \sim 0.1$) [50], $\alpha \sim 38$. Then, the available space for $\psi_{\rm ini}$ would expand towards values closer to the potential minimum and the inflection points, thanks to the friction α causes.

In this work, we will study the case with $r \lesssim 0.01$, which will allow to explore the regimes in which the model is both close and different to a cosmological constant. The mild upper bound in α ($\alpha \lesssim 3.5$) will restrict $\psi_{\rm ini}$ to values where the field does not roll down fast, but far enough to the plateau and maximum, allowing a mild evolution. A tighter constraint, as that set by the most precise expected measurement of r, $r \sim 10^{-3}$ [304], fixes $\alpha \sim 0.35$, pushing the equation of state towards $w \sim -1$ to avoid the parts of the potential where the field would move fast and yield inviable models, letting alone the maximum (instable), the plateau and their closest points. In addition, we choose to avoid the high α regime (i.e. high r) as it was shown to be unbounded by current data (see previous Section). The only hope of constraining the parameter space relies on finding new data that favors a model sufficiently distinct to ΛCDM and, in that case, our choice of $r \lesssim 0.01$ ($\alpha \lesssim 3.5$) is broad enough to account for a wide range of cosmologies that deviate from ΛCDM.

In Section 6.3.1, the models used to describe the observational probes in our forecast (Stage-4 CMB experiments, the Large Synoptic Survey Telescope [17], DESI [19] and WFIRST [78]) will be introduced. In Section 6.3.2, we will describe the multi-tracer Fisher formalism and the computational tools that we will use. In Section 6.3.3, the results of our forecast will be shown and analyzed.

6.3.1 Observational probes

A cohort of next-generation cosmology experiments will collect an unprecedented amount of data during the next decade, which will allow us to vastly improve our understanding of cosmology. Our forecasts will include two experiments modelled after two of the most promising facilities: CMB Stage-4 and the Large Synoptic Survey Telescope (LSST), which were already introduced in Chapter 3 (and will be further discussed in Chapter 5). Now, the assumptions made to describe these datasets will be described here.

CMB Stage 4

Third-generation CMB experiments, such as ACTPol [73], SPT-3G [74], BICEP2/Keck [75] or Simons Array [76] will be progressively upgraded to an Stage 4 experiment, increasing the number of detectors, frequency channels, and sky coverage, allowing us to cover around 40% of the sky [5], with a white-noise level $\sigma_T \sim 1\mu K$-arcmin in temperature [304].

S4 will measure CMB temperature and polarization anisotropies as well as the reconstructed CMB lensing convergence, among other secondary anisotropies. These measurements will be limited in resolution by the beam size. We assume a Gaussian beam with a full width at half maximum $\theta_{\rm FWHM} = 3$ arcmin. The corresponding noise power spectrum, assuming white noise, is given by

$$N_\ell^x = \sigma_x^2 \exp\left[\ell(\ell+1)\theta^2_{\rm FWHM}/8\log 2\right] , \tag{6.14}$$

where x stands for temperature (T) or polarization maps (E) and σ_x^2 is in units of μK^{2}sr (we assume $\sigma_E = \sigma_T\sqrt{2}$). At large scales, statistical and systematic uncertainties, associated to ground-based facilities such as atmospheric contamination dominate, and therefore we discard multipoles $\ell < 30$ and use the Planck noise levels in this regime [175] (corresponding to $\sigma_T \simeq 30\,\mu$K-arcmin. Furthermore, given the contamination in the temperature power spectrum by astrophysical foregrounds, we choose different scale cuts for polarization ($\ell_{\rm max} = 5000$) and temperature ($\ell_{\rm max} = 3000$) multipoles.

Lensing noise is obtained by quadratic combinations of the CMB maps [306] and estimating the reconstruction noise with the minimum variance weighting, by combinations of the $TT\,, TE\,, TB\,, EB$ and EE individual estimators. This technique significantly reduces the noise of individual estimators which are noise limited at high-ℓ [307]. We include CMB lensing information in the range $30 < \ell < 3000$.

The Large Synoptic Survey Telescope

The Large Synoptic Survey Telescope (LSST) is a photometric Stage 4 experiment that will cover around $20,000\,{\rm deg}^2$ and reach a limit magnitude $r \sim 27$ [17]. Photometric catalogs are dense and deep, which make them excellent for weak lensing studies and multi-probe analyses, where one does not need high accuracy on the spatial distribution of the tracers or clustering statistics at small scales.

Photometric surveys infer the individual galaxies redshifts from their fluxes in a few broad frequency bands and, as a consequence, have large uncertainties in the radial clustering pattern. This procedure, will allow LSST to obtain constraints from different sources: tomographic galaxy clustering and cosmic shear, galaxy cluster counts, SNe Ia and strong lenses. Among these, the combination of galaxy clustering and cosmic shear is the most promising source of information for LSST when combined with measurements of the distance-redshift relation (through e.g. supernovae or baryon acoustic oscillations). We will follow Ref. [308] in the modelling of both tracers.

- Galaxy clustering. For galaxy clustering, the most relevant observable is the shape of the angular power spectrum or the two-point correlation function of the galaxy distribution. In tomographic clustering, we divide the galaxy sample in redshift bins and compute the auto- and cross-correlation functions between them. In order to simplify the analysis, we assume that galaxies can be grouped in two different categories – red galaxies (early-type, elliptical and high-bias) and blue galaxies (late-type, spiral and low-bias). This is just an approximation, since red spiral galaxies exist, for example, but it is based on the strong

[5] This value has been updated in the recent *The CMB-S4 Science Case, Reference Designs and Project Plan* [77] to 70%, which was not available at the time this work (Ref. [2]) was done.

bimodality of the galaxy color space [309]. For instance, red galaxies are less abundant, but show strong features in their spectra that allow to extract more accurate photo-z distributions. Furthermore, they also show a higher clustering amplitude (i.e. they have a larger galaxy bias) than their blue counterparts. In galaxy clustering, the main source of statistical noise is shot noise and, following Ref. [308], the noise power spectra is given by

$$N_\ell^{ij} = \frac{\delta_{ij}}{n^i} \tag{6.15}$$

where n^i is the angular number density of galaxies in the i-th tomographic bin, characterized by its window function $w^i(z)$,

$$n^i = \int_0^\infty \mathrm{d}z\, \bar{N}(z) w^i(z)\,. \tag{6.16}$$

We assume, Gaussian photo-z distributions ($p(z_p|z)$), for which the window function is

$$\begin{aligned} w^i(z) &= \int_{z_0^i}^{z_f^i} \mathrm{d}z_p\, p(z_p|z) & (6.17)\\ &= \frac{1}{2}\left[\mathrm{erf}\left(\frac{z-z_0^i}{\sqrt{2}\sigma_z}\right) - \mathrm{erf}\left(\frac{z-z_f^i}{\sqrt{2}\sigma_z}\right)\right]\,. & (6.18)\end{aligned}$$

Here σ_z is the Gaussian photo-z standard deviation, which we parametrize as $\sigma_z(z) = \sigma_0(1+z)$. We use $\sigma_0 = 0.02$ for red galaxies and $\sigma_0 = 0.05$ for the blue (and the joint, gold, sample) samples as red galaxies have usually more precise photo-z due to their stronger spectral features. Finally, the list of initial and final redshifts for each redshift bin can be found in Table 6.4, and the galaxy distributions in Figure 6.15. Note that the redshift spacing was chosen such that the width of each bin is equal to 3 times the photo-z uncertainty at the center of the bin. This is a compromise between the need to sample the redshift range sufficiently well, and avoiding strong correlations between different bins due to their overlap.

The main source of uncertainty for galaxy clustering is the relation between the galaxy and matter overdensities. On sufficiently large scales, this relation is assumed to be linear, and the proportionality constant is the so-called galaxy bias b [310]. We use a model for the bias of red and blue galaxies as

$$b_{\rm red}(z) = 1+z, \qquad b_{\rm blue} = 1 + 0.84z\,. \tag{6.19}$$

This is motivated by simulations [311] and observations [312], and takes into account the stronger clustering properties of red galaxies.

Given that the linear bias parametrization breaks on small scales, our scale cuts for galaxy clustering need to be more conservative. We will define it in a redshift dependent manner as $\ell_{\rm max}(\overline{z}) = \chi(\overline{z})k_{\rm max}$, where $\overline{z}$ is the mean redshift of the redshift bin, χ is the radial comoving distance and $k_{\rm max}$ is the threshold comoving scale, which we choose to be $k_{\rm max} = 0.2h\,{\rm Mpc}^{-1}$. This is the scale up to which a good estimate of the covariance matrix of the matter power spectrum in the quasi-linear regime can be made at $z = 0$ [313].

As a final remark, we will neglect the effect of magnification bias, given the small effect it has on the final constraints [314].

- Galaxy shear. Weak lensing is an unbiased estimator of the projected matter perturbations, and is quantified by correlating the projected ellipticities of galaxies. We build the

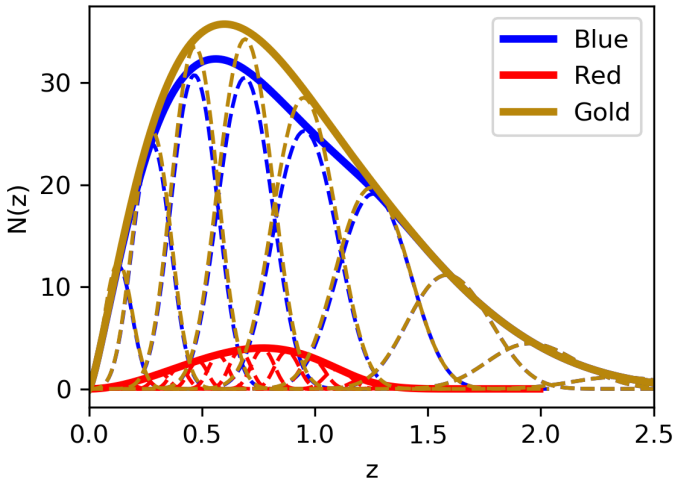

Figure 6.15: Galaxy density distributions for red, blue and gold samples of LSST. Dashed lines show the windows functions ($W^i \propto \bar{N}(z)w^i(z)$) for each redshift bin. Red and blue samples are used for galaxy clustering and the gold sample for weak lensing.

Sample	Redshift bin edges
Blue (cl) Gold (sh)	[0, 0.16, 0.35, 0.57, 0.82, 1.12, 1.46, 1.86, 2.33]
Red (cl)	[0, 0.06, 0.13, 0.20, 0.27, 0.35, 0.43, 0.52, 0.62, 0.72, 0.82, 0.94, 1.1, 1.2, 1.3]

Table 6.4: Redshift bin edges for the angular galaxy density distribution of each sample. cl ≡ clustering; sh ≡ shear. Refer to appendix B.4.2 in Ref [308] for details on the distributions.

shear galaxy sample by grouping together all galaxies in the blue and red samples whose magnitude is above $r \simeq 25.3$. This corresponds to the 'gold sample' of LSST [17] and its distribution and redshift bins can be seen in Figure 6.15 and Table 6.4, respectively. The photo-z distribution is given by Equation 6.18 with $\sigma_0 = 0.05$, as the blue sample. The galaxy shear noise power spectrum is directly proportional to the variance of the intrinsic galaxy ellipticities, and inversely to the angular projected galaxy number density; i.e. $N_\ell^{ij} = \delta_{ij}\sigma_\gamma^2/n^i$. Here, σ_γ includes both the dispersion of the intrinsic galaxy ellipticities and the measurements uncertainties, and is set to $\sigma_\gamma = 0.28$ [17]. We marginalize over shape measurement systematics in the form of a free multiplicative bias parameter for each reshift bin. Other sources of systematic uncertainty, such as intrinsic alignment, shape-measurement systematics or baryonic uncertainties will be neglected. We expect their effect on the constraints on the parameter space of the α-attractor dark energy model to be negligible compared to other sources of systematic uncertainties, particularly the multiplicative bias. We will however impose a scale cut $\ell \leq 2000$ to avoid uncertainties associated with the modelling of baryonic effects in the matter power spectrum [315–321].

Spectroscopic Surveys: DESI and WFIRST

Spectroscopic surveys are especially aimed to study phenomena at smaller scales, like BAO and redshift-space distortions. The high redshift resolution of spectroscopic surveys makes

Tracer	Noise contribution
S4CMB	$N_\ell^x = \sigma_x^2 \exp\left[\ell(\ell+1)\theta^2_{\rm FWHM}/8\log 2\right]$,
gal. cl.	$N_\ell^{ij} = \delta_{ij}/n^i n^j$
gal. sh.	$N_\ell^i = \sigma_\gamma^2/N_\Omega^i$

Table 6.5: Noise contribution to the power spectra for LSST measurements. For S4CMB experiments, the noise level $\sigma_x = \sigma_T$, σ_E, where $\sigma_E/\sqrt{2} = \sigma_T \sim 1\mu K$-arcmin and $\Theta_{\rm FWHM} = 3\,$arcmin. For galaxy clustering (gal. cl.), δ_{ij} is the identity matrix and n^i is the galaxy number in the z-bin i, given by Equation 6.16. For galaxy shear (gal. sh.), the variance of the intrinsic galaxy ellipticities, $\sigma_\gamma = 0.28$ and N_Ω^i is the angular galaxy number density of z-bin i.

a tomographic analysis as described in the previous Section computationally intractable and inefficient. The standard analysis studying the multipoles of the 3D galaxy power spectrum is however not easy to incorporate into our forecasting formalism, in terms of fully characterizing the correlations with overlapping tomographic data.

Instead, we will directly incorporate the BAO forecasts for DESI [19] and WFIRST [18, 78], using the error estimates summarized in Table 6.6. The errors are given on the angular diameter distance ($D_{\rm A} = (1+z)^{-1}\int_0^z {\rm d}z' H^{-1}(z')$) and Hubble parameter ($H(z)$).

DESI [19] will cover $\sim 14000\,{\rm deg}^2$ from the North Hemisphere and target Luminous Red Galaxies (LRGs), Emission Line Galaxies (ELGs) and quasars. Their BAO $D_{\rm A}$ and H error estimations cover 18 redshifts, uniformly distributed in the redshift range $0.05 \leq z \leq 1.85$. The details of their forecast analysis can be found in Ref. [19]. On the other hand, WFIRST will measure redshifts for $\sim 2.6\times 10^7$ galaxies over $\sim 2000\,{\rm deg}^2$. Their forecast assumed the galaxy number densities from from Ref. [78]. We use forecast errors on the BAO parameters over 18 redshift bins, uniformly distributed in $1.05 \leq z \leq 2.75$. Additionally, WFIRST will also be able to measure the expansion of the Universe through SNe Ia. We will include this probe through the forecast for $E(z) = H(z)/H(0)$ from Ref. [62] (see Table 6.7), the same way this was done in Section 6.2. We will neglect correlations between different redshifts as this effect is negligible in comparison with the constraining power of the other experiments. The predictions for $E(z)$ were obtained from a simulation based on Ref. [157], plus an external sample at $z < 0.1$. The predictions for $E(z)$ for WFIRST are based in simulations done by Ref. [157] for WFIRST, where the systematic errors in the adopted model fall below the statistical errors. The number of supernovae in each redshift bin is shown in Table 6.8.

6.3.2 Fisher formalism

This Section summarizes the Fisher formalism introduced in Ref. [58]. Each projected probe (CMB primary and lensing, photometric galaxy clustering and cosmic shear) labelled as a is composed of a number of sky maps $N^a_{\rm maps}$, which can be fully described by their harmonic coefficients ($a^{a,i}_{\ell m}$, $i \in [0, N^a_{\rm maps}]$). They can be grouped into a vector $\mathbf{a}_{\ell m}$, the covariance matrix of which is the power spectrum::

$$\langle \mathbf{a}_{\ell m} \mathbf{a}^\dagger_{\ell' m'} \rangle = \delta_{\ell\ell'}\delta_{mm'}\mathsf{C}_\ell\,. \tag{6.20}$$

Under the assumption of being Gaussian distributed, the likelihood is given by

$$-2\log L = \sum_{\ell_{\rm min}}^{\ell_{\rm max}} \sum_{m=-\ell}^{m=\ell} \left[\mathbf{a}^\dagger_{\ell m}\mathsf{C}_\ell^{-1}\mathbf{a}_{\ell m} + \log(\det(2\pi\mathsf{C}_\ell))\right]\,, \tag{6.21}$$

BAO error predictions					
DESI			WFIRST		
z	$\frac{\sigma_{D_A/s}}{D_A/s}(\%)$	$\frac{\sigma_{Hs}}{Hs}(\%)$	z	$\frac{\sigma_{D_A/s}}{D_A/s}(\%)$	$\frac{\sigma_{Hs}}{Hs}(\%)$
0.05	6.12	12.10	1.05	1.51	2.72
0.15	2.35	4.66	1.15	1.43	2.56
0.25	1.51	2.97	1.25	1.35	2.42
0.35	1.32	2.44	1.35	1.29	2.30
0.45	2.39	3.69	1.45	1.24	2.21
0.65	0.82	1.50	1.55	1.23	2.16
0.75	0.69	1.27	1.65	1.25	2.15
0.85	0.69	1.22	1.75	1.28	2.16
0.95	0.73	1.22	1.85	1.33	2.19
1.05	0.89	1.37	1.95	1.41	2.27
1.15	0.94	1.39	2.05	2.51	3.52
1.25	0.96	1.39	2.15	2.60	3.62
1.35	1.50	2.02	2.25	2.74	3.78
1.45	1.59	2.13	2.35	3.02	4.09
1.55	1.90	2.52	2.45	3.38	4.52
1.65	2.88	3.80	2.55	3.87	5.11
1.75	4.64	6.30	2.65	4.52	5.90
1.85	4.71	6.39	2.75	5.41	6.99

Table 6.6: WFIRST and DESI BAO errors. Respectively, they have been taken from Table VII in Ref. [18] and Tables 2.3 and 2.5 of Ref. [19]. The early-time BAO error predictions from Ly-α and quasars (QSO) have been omitted as they are above the H and D_A partial derivatives (see Figure 6.17) values, having little contribution to the total Fisher matrix.

WFIRST SN Ia $E(z)$ predictions	
z	$\sigma(E(z))(\%)$
0.07	1.3
0.2	1.1
0.35	1.5
0.6	1.5
0.8	2.0
1.0	2.3
1.3	2.6
1.7	3.4
2.5	8.9

Table 6.7: $E(z) = H(z)/H(0)$ estimated relative errors from WFIRST SN Ia. Values have been taken from Table 7 of Ref. [62], based on Ref. [157] simulations plus an external sample at $z < 0.1$.

$z \in$	SN
$[0, 0.1]$	800
$[0.1, 0.4]$	557
$[0.4, 0.8]$	4807
$[0.8, 1.7]$	5892

Table 6.8: Redshift bins and number of supernovae obtained in a realistic simulation of the Imaging All-z observational strategy [157], used in Ref [62] to forecast the uncertainties on $E(z)$. The first 800 SN are assumed to be obtained from a different experiment.

which can be expanded around the maximum in order to find the Fisher matrix

$$F_{\mu\nu} = \sum_{\ell=\ell_{\rm min}}^{\ell_{\rm max}} f_{\rm sky} \frac{2\ell+1}{2} \,{\rm tr}\left(\partial_\mu C_\ell C_\ell^{-1} \partial_\nu C_\ell C_\ell^{-1}\right). \tag{6.22}$$

The covariance matrix of the parameters θ can then be obtained by inverting F. In the previous equation, ∂_μ is the partial derivative respect to the parameter θ_μ and $f_{\rm sky}$ is the sky fraction covered by the considered probes.

Furthermore, we will assume that noise and cosmological signal are uncorrelated in the observed anisotropies, i.e. given $\mathbf{a}_{\ell m} = \mathbf{s}_{\ell m} + \mathbf{n}_{\ell m}$, $\mathsf{C}_\ell = \mathsf{C}_\ell^S + \mathsf{C}_\ell^N = \langle \mathbf{s}_{\ell m} \mathbf{s}_{\ell m}^\dagger \rangle + \langle \mathbf{n}_{\ell m} \mathbf{n}_{\ell m}^\dagger \rangle$, where C_ℓ^S and C_ℓ^N are the signal and noise power spectra.

The Fisher matrix with DESI and WFIRST probes will be computed as

$$F_{\mu\nu} = \sum_i \frac{\partial_\mu q_i \partial_\nu q_i}{\sigma_i^2}, \tag{6.23}$$

where q_i is the measurement of a given quantity q (which stands for $D_{\rm A}(z)$, or $E(z)$) in the i-th redshift bin, and σ_i^2 is the forecasted error on that quantity. This Fisher matrix is added to the one computed for CMB and photometric survey data. This ignores possible correlations between both sets of observables. We do not expect our results to be very sensitive to this assumption.

Finally, all partial derivatives with respect to θ_μ will be computed via finite central differences,

$$\partial_\mu f = \frac{f(\theta_\mu + \delta\theta_\mu) - f(\theta_\mu - \delta\theta_\mu)}{2\delta\theta_\mu} + O(\delta\theta^3). \tag{6.24}$$

In addition, the power spectra, C_ℓ^S, will be obtained using `hi_class` [31], a modified version of CLASS [30] that incorporates Horndeski models [29] without assuming the quasi-static approximation, which ensures results are valid at scales larger than the sound horizon [322]. Finally, we will use the Limber approximation [323] in the full range of scales. The software used to combine all these ingredients is available online[6].

6.3.3 Results

The next generation of data, despite its increase on accuracy, will fail to fully constrain the generalized α-attractor model, as present observations did, if they continue preferring a ΛCDM background evolution. One must recall that this model has an infinite region of the parameter space that is indistinguishable from ΛCDM, corresponding to large α (acts as a friction to the field motion) or having $\psi_{\rm ini}$ on the plateau (or, with more fine tunning, close to a maximum).

[6] `https://gitlab.com/carlosggarcia/GoFish_aatt-forecast/tree/aatt`, a modified version of `https://github.com/damonge/GoFish` (the master branch of the former repository)

Pars.	$\psi_{\rm ini}$	α	p	n	FoM	FoM_{CPL}
Fid (no max).	1.5	2	2	1	–	–
σ	$\lesssim 1$	0.5	$\lesssim 1$	$\lesssim 1$	~ 10	10^3
Fid ($\psi_{\rm ini} < \psi_{\rm max}$).	0.8	2	2	3.5	–	–
σ	0.2	~ 0.5	0.4	1	~ 100	10^2
Fid ($\psi_{\rm ini} > \psi_{\rm max}$).	1.4	2	2	3.5	–	–
σ	2	~ 1	2	2	~ 1	10^4

Table 6.9: Fiducial values and predicted constraints using all probes. Recall that $\psi_{\rm max} = 1.04$. The results with a '$\sim$' sign mean that little changes on the numerical derivative yield changes on the first significant digit. This is consequence of the strong correlations between the model parameters. FoM $\equiv$ FoM($\psi_{\rm ini}$, α, p, n) and $\text{FoM}_{\text{CPL}} \equiv$ FoM(w_0, w_a). The potential shape when $\psi_{\rm ini} < \psi_{\rm max}$ allows for a larger variety of evolutions and, therefore, of w_0–w_a values. This causes a greater FoM_{CPL} than in the other cases.

We will investigate the parameter space that lies 1σ off the best fit result of Section 6.2.4, which is able to differentiate from a cosmological constant. Current observations prefer the cosmological constant-like regime, which correspond to an unbounded region on the parameter space. Therefore, as we said before, if future observations were to continue favoring ΛCDM, they would not be able to constrain the parameter space. At best, they will be able to rise the lower bounds for α and $\psi_{\rm ini}$. As a consequence, the only hope of finding tight constraints relies on new data that favors models slightly different (they still have to be compatible with current observations, at their level of accuracy) to ΛCDM. This regime correspond to the parameters 1σ off the best-fit of Section 6.2.4.

The cosmological parameters have been chosen as in Table 6.3, i.e. $\Omega_{\rm cdm}h^2 = 0.1183$, $\Omega_{\rm b}h^2 = 0.02221$, $h = 0.682$, $10^9 A_{\rm s} = 2.14$, $n_{\rm s} = 0.9649$, $\tau_{\rm reio} = = 0.067$. For the α-attractor parameters, we study two distinct cases, corresponding to models with and without a maximum ($p \geq n$ and $p < n$, respectively). In the first case, the 1σ-off parameters are $\{\psi_{\rm ini},\, \alpha,\, p,\, n\} = \{1.5,\, 2,\, 2,\, 1\}$. In the second case, we choose $\{\alpha, p, n\} = \{2, 2, 3.5\}$ and we study two further options for $\psi_{\rm ini}$: 0.8 and 1.4. This corresponds to the cases with $\psi_{\rm ini}$ smaller and larger than $\psi_{\rm max} = 1.04$ (see Figure 6.16). A summary of the fiducial models and constraints can be found in Table 6.9. In next Sections, we will discuss them in detail. The c parameter, which fixes the potential amplitude, is fixed via the Friedman equation ($1 = \sum_i \Omega_i$).

Case without maximum: $p > n$

The fiducial model parameters are $\{\psi_{\rm ini},\, \alpha,\, p,\, n\} = \{1.5,\, 2,\, 2,\, 1\}$. In Table 6.10 the Figures of Merit (FoM) for different combinations of the experiments are shown. Recall that the FoM is defined by [274]

$$\text{FoM} = (\det C)^{-1/2}. \tag{6.25}$$

In our case, the covariance matrix (C) is obtained inverting the full Fisher matrix and marginalizing over the nuisance and cosmological parameters, so that we describe just the constraining power of the next generation experiments on the parameter space of the α-attractor model.

Table 6.10 shows that LSST galaxy clustering is necessary to be able to constrain the parameter space of the dark energy α-attractor model. The galaxy power spectrum is the observable that is most sensitive to changes on the model parameters, as shown in Figure 6.17. Furthermore, the combination of galaxy clustering and the other probes is able to increase the FoM almost by a factor 2; exhausting the constraining power of future observations. In

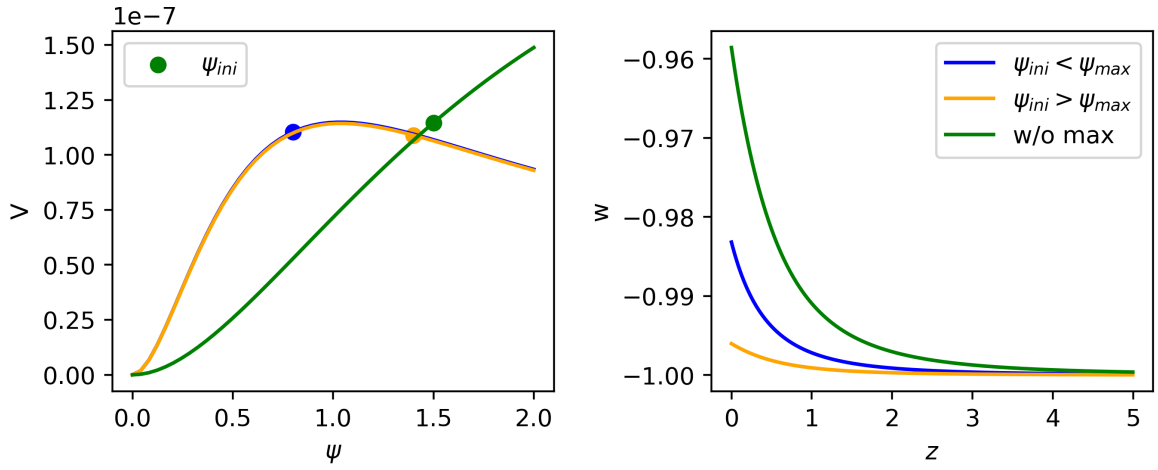

Figure 6.16: Fiducial potentials (V) and equations of state (w). The dots mark the initial position of the field.

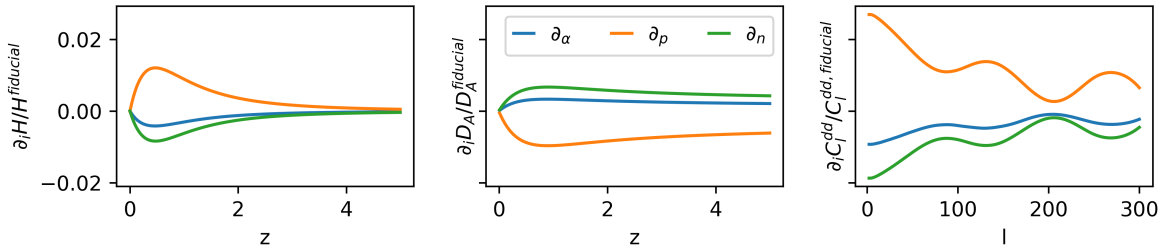

Figure 6.17: Numerical derivatives of the Hubble parameter, angular diameter distance and matter correlation. The computation was done for the case without maximum.

Figure 6.18 we show the predicted 2σ-regions for the cases with all probes, with S4-CMB + BAO + SNIa and S4-CMB + LSST + SNIa. Galaxy clustering would be able to alleviate the degeneracy between α and $\psi_{\rm ini}$ that made it difficult to find good constraints in Section 6.2. The strong degeneracy between $\psi_{\rm ini}$ and the exponents is such that slight variations of one can be compensated with any of the other in order to prevent the field from rolling down the potential too fast.

These constraints in the parameter space can also be seen in the CPL parametrization of dark energy (w_0–w_a) [264, 265]. In fact, one can see a similar improvement on the FoM (Table 6.11) of w_0–w_a as in the model parameters (Table 6.10). The FoM for the CPL parameters has been defined as

$$\mathrm{FoM}(w_0, w_a) = \frac{1}{\mathrm{area}_{1\sigma}(w_0, w_a)}, \tag{6.26}$$

which generalizes Equation 6.25 for a non elliptical shape. It must be noted, however, that the main reason behind the large FoM is due to the fact that this model belongs to the thawing quintessence class, which is known to have little freedom in the w_0–w_a plane [268]. Interestingly, it could be expected to detect a 2σ deviation from a cosmological constant ($w_0 = -1$, $w_a = 0$), provided that the fiducial model were the true one and one included LSST galaxy clustering observations (Figure 6.19). This would not be the case if galaxy clustering were not taken into account. In fact, the weak constraints from the other cosmological probes would shift the w_0–w_a

	FoM($\psi_{\rm ini}$, α, p, n)		
Experiments	w/o max.	$\psi_{\rm ini} < \psi_{\rm max}$	$\psi_{\rm ini} > \psi_{\rm max}$
SN Ia, BAO, gal. sh	–	–	–
S4CMB	–	2×10^{-1}	–
S4CMB + BAO	6×10^{-2}	7×10^{-1}	–
S4CMB + SN Ia	1×10^{-1}	1	–
S4CMB + BAO + SN Ia	1×10^{-1}	2	–
gal. cl	2×10	1×10^{2}	3×10^{-1}
S4CMB + gal.* + SNIa	4×10	3×10^{2}	2
All	4×10	3×10^{2}	2

Table 6.10: Figures of Merit for different combinations of future experiment measurements on the parameter space of the α-attractor model. BAO combines DESI and WFIRST predictions, SN Ia comes from constraints on $E(z)$ using WFIRST forecasts [62] and galaxy clustering (gal. cl) and shear (gal. sh) are those from LSST. The combination of galaxy clustering and shear has been written as gal.*. We have omitted FoM$< 10^{-1}$, considering those as unable to constraint the parameter space.

	FoM(w_0, w_a)		
Experiments	w/o max.	$\psi_{\rm ini} < \psi_{\rm max}$	$\psi_{\rm ini} > \psi_{\rm max}$
S4CMB + BAO + SNIa	6×10^{2}	5×10^{1}	6×10^{2}
S4CMB + gal.* + SNIa	2×10^{3}	2×10^{2}	8×10^{3}
All	2×10^{3}	2×10^{2}	8×10^{3}

Table 6.11: Figures of Merit (Equation 6.25) for different combinations of future experiment on the w_0–w_a parameters. BAO combines DESI and WFIRST predictions, SN Ia comes from constraints on $E(z)$ using WFIRST forecasts [62] and galaxy clustering (gal. cl) and shear (gal. sh) are those from LSST. The combination of galaxy clustering and shear has been written as gal.*.

1σ region towards $w \sim -1$.

The w_0–w_a contours were obtained: first, we diagonalize the covariance matrix (i.e. F^{-1}). We then take samples of the uncorrelated Gaussian distribution and transform-back to the original basis. In doing so, we reject any model with $p < n$ (i.e. models with maximum) and with negative model parameters. Once selected, we used `hi_class` [31] to compute the corresponding w_0–w_a parameters, with w_a computed as $w_a = -dw/d\ln(a)|_{a=1}$). Finally, we used `GetDist` [7] to produce contours of the corresponding samples.

Case with maximum: $p < n$

The fiducial model with maximum is given by $\{\alpha, p, n\} = \{2, 2, 3.5\}$. Given that the potential is not symmetric around the maximum, we will study the forecast potential of the next generation experiments with two fiducial models with initial value of the field so that it is at both sides of the maximum. It is located at $\psi_{\rm max} = 1.04$, and we will consider the cases with $\psi_{\rm ini} = 0.8, 1.4$. The results are shown in Table 6.9, and the quantitative measurement of the constraining power of each probe is shown in Table 6.10. The found contours are shown in Figure 6.20. As before, galaxy clustering will be the most constraining probe. In comparison, the case with $\psi_{\rm ini} < \psi_{\rm max}$ is better constrained, with S4-CMB experiments having a FoM $\sim 10^{-1}$ and, in combination

[7] `https://github.com/cmbant/getdist`

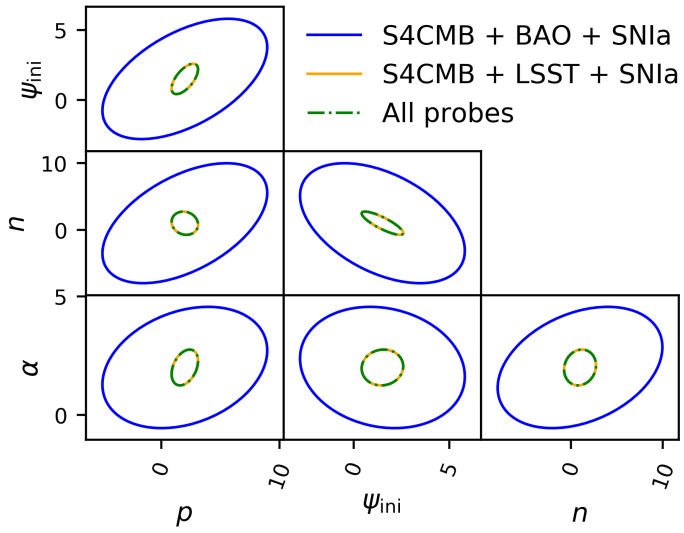

Figure 6.18: 2σ-regions for the model parameters when the potential has no maximum. Note that the maximum constraints are already found for S4CMB + LSST + SNIa.

with BAO and/or SNIa, FoM ~ 1. Using all probes, one can achieve a FoM $\sim 10^2$. However, for the case with $\psi_{\rm ini} > \psi_{\rm max}$, we only reach FoM ~ 1, when using all probes. The asymmetry around the maximum is such that at lower values, the potential slope is much more pronounced (see Figure 6.16), making the model more sensitive to parameters changes. On the contrary, at values of the field greater than the maximum, the potential is softer and asymptotically flat, allowing for greater changes on the parameters that do not impact the final observables. The greater steepness of the potential is also the reason why the case with $\psi_{\rm ini} < \psi_{\rm max}$ is more constrained than the case without maximum (see Figure 6.16), even though the dark energy equation of state of the fiducial model with maximum is closer to $w = -1$ (see Figure 6.21), as a slightly lower $\psi_{\rm ini}$ would make the field end up oscillating fast around 0. It must be noted, however, that it is still 2σ-off the exact $w = -1$.

As in the previous Section, the main restriction on the dark energy CPL parameters comes from being a thawing model. In particular, when $\psi_{\rm ini} < \psi_{\rm max}$, the field cannot start at much lower values than the fiducial $\psi_{\rm ini} = 0.8$, as the field would roll fast towards $\psi = 0$. On the other hand, the constraints allow values of $\psi_{\rm ini}$ that are closer to the maximum and the plateau, in the case with $\psi_{\rm ini} > \psi_{\rm max}$. As a consequence, the most likely parameter combinations that produce a correct late-time acceleration would be those with $w \sim -1$. Finally, the broader 2σ-contours in the $\psi_{\rm ini} < \psi_{\rm max}$ case, despite of having a FoM ~ 100, over the model parameters, are a consequence of the larger range of accessible values of V' (see the potential shape in Figure 6.16), which allows a richer variety of field evolutions. In addition, in all three cases, galaxy clustering is able to increase the FoM(w_0, w_a) by almost an order of magnitude (see Table 6.11). The found contours have been plotted in Figure 6.21

The FoM of the model and CPL parameters reflect the fact that the phenomenology of this model is mainly determined by its thawing nature and the initial position of the field, which determines what part of the potential is going to control the field evolution, and not all its parameters. In particular, the case with largest FoM on the model parameters is that with $\psi_{\rm ini} < \psi_{\rm max}$, while it is the one with lowest FoM(w_0, w_a). Similarly, the configuration with $\psi_{\rm ini} > \psi_{\rm max}$ has the lowest FoM on the model parameters, but the greatest for the CPL parametrization. Finally, although the case without maximum has a FoM(w_0, w_a) of same order as the former, its FoM($\psi_{\rm ini}$, α, p, n) is an order of magnitude larger. Therefore, this shows the

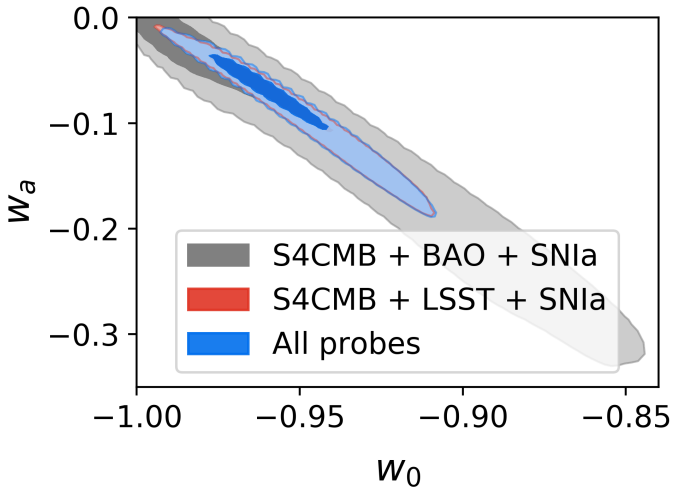

Figure 6.19: 2σ-regions of the w_0–w_a parameters parting from a fiducial model 1σ-off the ΛCDM regime and no maximum. Note that the maximum constraints are already found for S4CMB + LSST + SNIa.

actual degrees of freedom, those that affect the phenomenology, are less than the number of free parameters; which we already know are degenerated. As a consequence, the FoM($\psi_{\rm ini}$, α, p, n) is not a good quantity to inform us about how well constrained is the phenomenology of this model.

6.3.4 Comparison with current constraints

Future observations will be able to greatly constrain the α-attractor model, provided that the true dark energy model were different from a cosmological constant and α could not be arbitrarily large (i.e. $r \lesssim 0.01$). In this case, we have shown that a combination of S4CMB + LSST + SNIa, will greatly improve present results. In fact, they increase by almost an order of magnitude the FoM of both the parameter space and the w_0–w_a parameters, when compared with S4CMB + BAO + SNIa.

A special comment is required for the results in the w_0–w_a plane. In Figure 6.22 we have plotted the w_0–w_a best 2σ-contours, together with the results found in Section 6.2.4. The available space for w_0–w_a greatly depends on the fiducial cosmology used. For instance, if $\psi_{\rm ini} < \psi_{\rm max}$, the parameters are much less constrained. As we discussed in the previous Section, this is caused by the fact that V' can have a broader range of values that will modify the acceleration of the field and, in turn, the evolution of the equation of state. In addition, it also shows that the w_0–w_a CPL parametrization is not sufficient to describe the full evolution of the equation of state. In fact, viable and equivalent cosmologies can be obtained if the equation of state remains $w = -1$ for most of its evolution but grows fast close to the present or in case the equation of state diverged from $w = -1$ at early times but had a more monotonically growth along time. The other two cases are more restricted as the shape of the potential is softer and allows slower evolutions.

The case without maximum is 3σ-off a cosmological constant solution; while the $\psi_{\rm ini} < \psi_{\rm max}$ is 2σ-off. The case with $\psi_{\rm ini} > \psi_{\rm max}$ is concordant with $w = -1$ and is caused by the fact that a mild evolution of the field is allowed given the steepness at that side of the maximum (see Figure 6.16) and the possibility of having $\psi_{\rm ini}$ on the plateau by the loose

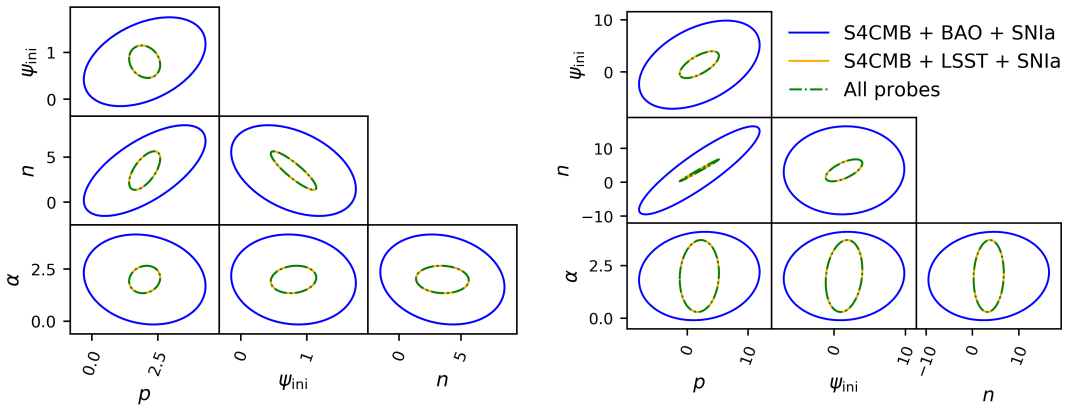

(a) $\psi_{\rm ini} < \psi_{\rm max}$ (b) $\psi_{\rm ini} > \psi_{\rm max}$

Figure 6.20: 2σ-regions for the model parameters when the potential has a maximum. Note that the maximum constraints are already found for S4CMB + LSST + SNIa.

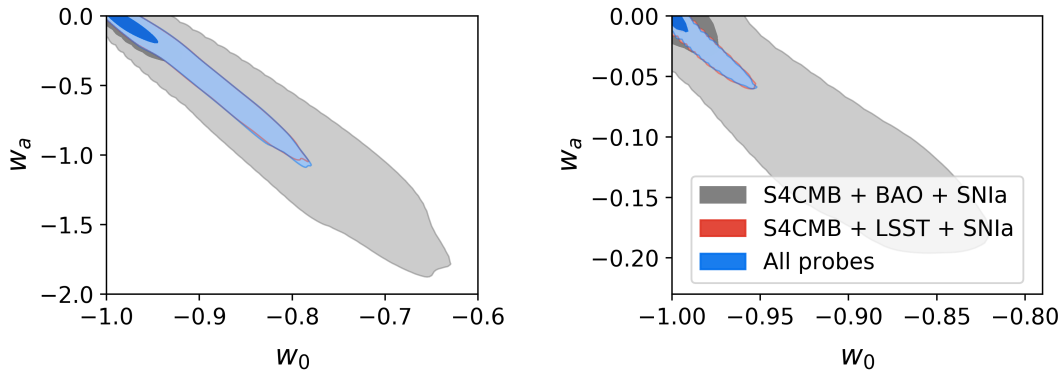

(a) $\psi_{\rm ini} < \psi_{\rm max}$ (b) $\psi_{\rm ini} > \psi_{\rm max}$

Figure 6.21: 2σ-regions of the w_0–w_a parameters parting from a fiducial model 1σ-off the ΛCDM regime. Note that the maximum constraints are already found for S4CMB + LSST + SNIa.

constraints in the parameter space. It is important to note that the case with $\psi_{\rm ini} > \psi_{\rm max}$ is the only for which the constraints beat those imposed by current observations, which have a FoM $\sim 5 \times 10^3$; although, given the mild constraints we have found in the parameter space, comparing the order of magnitude is a more conservative approach. This would be the case for the model without maximum. The reason why our result do not reduce the uncertainty in the w_0–w_a CPL parameters is caused by the fact that the constraints that come from current observations (in blue in Figure 6.22) are showing the preference of current data for a cosmological constant solution as this can be easily recovered thanks to the degeneracies of this model (see Section 6.1.3). In comparison with our current approach, the constraints from Section 6.2 were obtained by random sampling in the full parameter space, with non-informative priors. On the contrary, the constraints found in this work assume a fiducial model 1σ-off a cosmological constant, and do not allow the parameters to change the case of study (e.g. $p < n$ when studying the case without maximum), limiting the possibility of going to the cosmological constant-like regime.

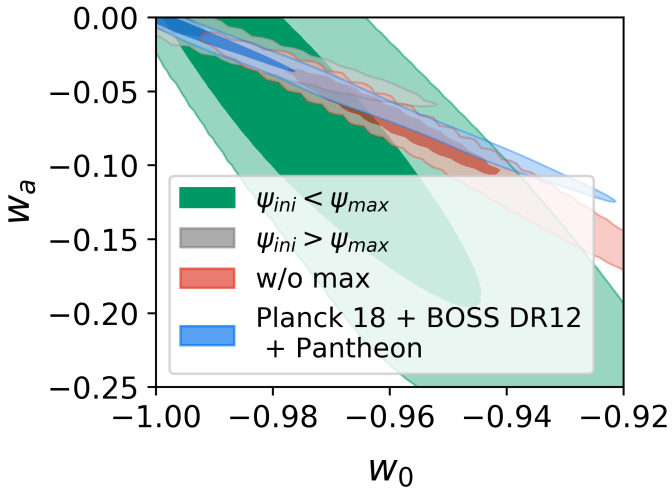

Figure 6.22: w_0–w_a 2σ predicted regions when using all probes, compared with the result found in Section 6.2.4. The case without maximum is 3σ-off a cosmological constant; while the case with $\psi_{\rm ini} < \psi_{\rm max}$ is 2σ-off. Forecast constraints are broader than those imposed by current observations for various reasons. First, we are performing the forecasts around a specific fiducial cosmology, in contrast to the random sampling done in Section 6.2, where they explored all the parameter space without restriction. This shows that current observations favored ΛCDM, which is easily recovered in this model (Section 6.1.3). In addition, a fiducial model 1σ-off a cosmological constant is being used for the forecast analysis. Finally, for the particular case with $\psi_{\rm ini} < \psi_{\rm max}$, the w_0–w_a parameters are not accurate descriptors of the equation of state, as equivalent cosmological evolutions can be obtained if w slowly varies since early times than in the case it remains close to $w = -1$, but close to the present greatly diverges. Nevertheless, the resulting FoM for the $\psi_{\rm ini} > \psi_{\rm max}$ case (8×10^3) is larger than that with current data ($\sim 5 \times 10^3$) and for the case without maximum it is still of the same order of magnitude (2×10^3).

6.4 Conclusions

We have studied the α-attractor dark energy model proposed in Ref. [277], and expressed in Equation 6.4, inspired by the α-attractor class of inflationary models. It is a generalization of the well known Starobinsky potential which correspond to the case with kinetic coefficient $\alpha = 1$ and exponents $p = 2$ and $n = 1$, with no coupling to matter since it is not obtained from a conformal transformation but from gauge fixing the extra degree of freedom associated to the conformal symmetry of the inflationary Lagrangian. This model is appealing because it is able to interpolate between the two most common α-attractor forms used for inflation – the Starobinsky model and the T-model – and also interpolate between power law potential and ΛCDM dark energy regimes at low and high ψ, respectively. This potential also allows, in theory, the existence of clustering dark energy due to tachyonic solutions.

We can summarize the key points of this chapter in the following ideas:

- The model is mainly described by its background evolution, which depends on the parameters in the following way:
  - At viably high ψ, it is in the thawing class, with the field excursion related to the equation of state and the α parameter as $\Delta\psi \sim \sqrt{1+w_0}/\sqrt{\alpha}$ and $1 + w_0 \sim 1/\alpha$ so $\Delta\psi \sim 1/\alpha$.

  - If $p > n$, the field always decreases and its speed is also inversely related to $\psi_{\rm ini}$. In addition, p controls the steepness of the transition regime.
  - If $p < n$, the field can grow towards an asymptotic de Sitter state at infinity if $\psi_{\rm ini} > \psi_{\rm max}$. Around the inflection points, or too close to $\psi = 0$, the field evolution is fast. The exponent n controls the height of the maximum, and the difference $p-n$ controls the characteristic scale of the uplifted exponential potential.

- The MCMC analysis showed that the ΛCDM-like regime is favored by the combined data set of Planck 2015 [294], BAO BOSS DR12 [49] and the $E(z)$ estimate from supernovae [62]:
  - Both the initial field $\psi_{\rm ini}$ and α are pushed to larger values, where the field lingers on the plateau.
  - The case where $p \sim n$ is also favored as it keeps the potential from being too steep (the deviation from a flat plateau becomes second order in the uplifted exponential potential).
  - The tachyonic solutions compatible with the observations have a very mild instability that does not give appreciable dark energy clustering. They are, however, as likely as non-tachyonic ones: $|m_0^2/H_0^2|_{95\%\text{C. L.}} \sim 1$.

- Next-generation experiments effect will depend on the underlying model. In addition:
  - They might be able to distinguish α-attractor dark energy from ΛCDM by 3σ.
  - S4CMB + LSST + SNIa will get the tightest constraints, with a FoM on the model parameters two orders of magnitude better than S4CMB + BAO (DESI & WFIRST) + SNIa, and an order of magnitude on the FoM of w_0–w_a.

We studied the properties of the model and its dependence on the different parameters. We saw that a better variable to understand the field evolution is $\psi = \phi/\sqrt{\alpha}$ instead of ϕ. The kinetic coefficient α (which for inflation models is intimately tied to the geometry of the superconformal field theory space) scales the field so that it determines at what value the field thaws. On the other hand, the reason why one has to consider both ψ and α is that the latter appears explicitly in the potential (but not kinetic) energy, in the frame in which the kinetic term is canonical (Equation 6.2), so that different values of α yield different universe histories. In particular, we saw that the field evolution rate is inversely related to α – higher values of α slow it down.

We showed how the initial position of the field $\psi_{\rm ini}$ played an important role determining how the field would evolve and had to be taken into account. For $p > n$ the field would always roll down but its speed would also decrease as $\psi_{\rm ini}$ grows, placing the field further on the plateau. On the contrary, when $p < n$ the potential has a maximum whose height and position is controlled by the relative size of n and p. In this scenario, the field could roll down towards $\psi = 0$, where the potential behaves like a power law potential $V \propto \phi^p$ (Equation 6.5) or towards $\psi = \infty$, a de Sitter attractor with $V \propto 2^{-2n}$ (Equation 6.6), with speed dependent on the proximity to the inflection points, where the force felt by the field is maximal. This correlates the expansion history with the field mass squared, and with its sign (which depends on which side of the inflection point the field is at present). In particular we have seen (Figure 6.13) that the equation of state parameters w_0 and w_a are ordered so that for a given w_0 the higher mass squared gives higher w_a.

In Section 6.1.3 we briefly studied how the negative mass squared could affect the observables. We saw that it would only have an effect if $|m^2|/H^2 \gtrsim k^2/(a^2H^2) > 1$ (Equation 6.11),

which greatly constrains the relevant modes, leaving just those of order $k \sim 10^{-3}\,\mathrm{Mpc}^{-1}$. Numerically, we studied the most extreme case we had obtained, that with $m^2/H_0^2 \sim -20$. In this case, we saw the mass term became relevant at $z \sim 3$ and that it was just today when it reaches the same order as the mode $k = 10^{-3}\,\mathrm{Mpc}^{-1}$. Therefore, the dark energy density perturbations are not appreciably influenced by the tachyonic instability, except possibly in the future.

For a detailed analysis we constrained the parameter space with MCMC for two α-attractor models. We compared our theoretical predictions with current datasets of CMB (Planck 2015 angular power spectrum, polarization and lensing [294]), BAO (BOSS DR12 [49]) and Supernovae (Pantheon + Hubble Space Telescope compressed [62, 124]). We also discussed how to choose priors since as some parameters get large the models become insensitive to them and indistinguishable from ΛCDM.

The results for the two models were discussed in Sections 6.2.3 and 6.2.4. The first case corresponds to the particular case where the potential is Starobinsky-like but leaving free the α parameter; i.e. fixing $p = 2$ and $n = 1$. We saw that the preferred models are those closer to ΛCDM and the best-fit is almost $w = -1$. Indeed the w_0–w_a behavior closely follows that of thawing dark energy for ψ_{ini} not too small, and this is bounded from below. Furthermore, the other cosmological parameters are compatible with those from Planck 2015 for ΛCDM.

These behaviors hold for the full generalized α-attractor model, with parameters α, p, n. The preferred region continued to be that closer to ΛCDM, and a new way of attaining that was for p and n to be nearly the same. Even though the model had much more freedom, the w_0–w_a behavior (Figure 6.13b) still followed the thawing fit $w_a = -1.6(1 + w_0)$ quite well.

Next-generation experiments will be able to measure the cosmological observables with percent-level precision. For the specific case with a maximum ($p < n$) and $\psi_{\mathrm{ini}} < \psi_{\mathrm{max}}$, we have found an important improvement on the constraints with respect to current bounds. However, this improvement does not translate into a significant reduction of uncertainties in the equation of state parameters under the CPL parametrization. This is due to the restrictions of the model in this space of parameters. On the other hand, the case with $\psi_{\mathrm{ini}} > \psi_{\mathrm{max}}$ is almost insensitive to the additional constraining power of next-generation datasets. Interestingly, in case that true underlying model were that without maximum, and sufficiently distinct from ΛCDM, one could detect a 3σ deviation from a pure cosmological constant; and a 2σ deviation if $\psi_{\mathrm{ini}} < \psi_{\mathrm{max}}$.

The use of CMB-S4 and other future CMB experiments to place constraints on the tensor-to-scalar ratio, r, and the spectral index, n_{s}, to constrain α (see Equation 6.13), is unlikely to provide any significant improvement over the results shown here, since those constraints will still allow for too much freedom, leaving the results shown in Section 6.2 almost untouched.

Finally, the use of tomographic galaxy clustering would be particularly important in order to achieve this. From the analysis of individual probes (see the Figures of Merit in Table 6.10), we have shown that galaxy clustering will be the probe with the most constraining capability, since the galaxy power spectrum is the most sensitive observable (Figure 6.17) to changes in the α-attractor parameters. We find this statement to be true across the different fiducial models studied. In particular, the combination S4CMB + LSST + SNIa will improve the FoM of both the parameter space and w_0–w_a by almost an order of magnitude with respect to the case with S4CMB + BAO + SNIa.

Next-generation experiments will lead us to an unprecedented level of precision in cosmology, allowing us to test our knowledge about the Universe, its origin and dynamical evolution. In this work we have shown how these observations, in particular a combination of CMB, galaxy and SNIa measurements will be able to set constraints on the dark energy α-attractor model and, as a consequence, we would expect that, in general, future surveys will be able to probe whether the late accelerated expansion of the Universe is connected with the one the Universe

started with, i.e. inflation.

Chapter 7

General framework for Modified Gravity

One ring to rule them all, one ring to find them,
One ring to bring them all and in the darkness bind them.

J. R. R. Tolkien[1]

As we commented on Part II, cosmological observations show compelling evidence that the expansion of the Universe is accelerating [15, 43, 49, 60, 61, 276]. While, as yet, we have no clear understanding why, proposals abound involving extra fundamental fields which may or may not modify gravity on large scales. The consensus, for now, is that the way forward is to improve observations. Fortunately, the prospects look good: a slew of powerful surveys mapping out the large scale structure of the Universe over the coming decade should be able to pin down the expansion of the Universe to sub-percent level [17–19, 78, 157].

An effective way of describing the accelerated expansion is to assume that it is driven by an extra, exotic, source of dark energy, with density $\rho_{\rm DE}$ and pressure, $P_{\rm DE}$. One can then define the equation of state of dark energy as

$$w \equiv \frac{P_{\rm DE}}{\rho_{\rm DE}} \tag{7.1}$$

and can, in general, depend on the scale factor of the universe, a, or equivalently, in terms of redshift, $1+z \equiv 1/a$. Characterizing the acceleration of the universe can then be translated into finding an accurate description of $w(a)$ [324]. Indeed, current cosmological surveys targeting dark energy have as their primary goal obtaining accurate measurements of $w(a)$.

It is often useful to use a reduced set of parameters that can accurately describe complex behaviour. A notable example is that of primordial parameters arising from inflation. There one generally has that the evolution of perturbations at early time is governed by an extra field leading to an imprint of quasi-scale invariant perturbations on large scales. These perturbations are incredibly well described by an amplitude, $A_{\rm s}$, a spectra index, $n_{\rm s}$ and a tensor to scalar ratio, r [325]. While one can enlarge this space of parameters, it has been repeatedly shown that these parameters capture the nature of inflationary perturbations with a high degree of accuracy. In particular, one can constrain, using the Cosmic Microwave Background (CMB) for example, the allowed values of $(n_{\rm s}, r)$ and then consider the subspace in this plane which

[1] *The Lord of the Rings: The Fellowship of the Ring* (1954)

corresponds to particular types of inflationary models. In other words it is straightforward to identify the physical priors one should apply to ($n_{\rm s}$, r) for any particular inflationary model.

In this Chapter we want to emulate what has been done in the case of inflation and identify an efficient and accurate parametrization for dark energy models. To do so, we revisit the background parametrization of the scalar field evolution in scalar-tensor theories of gravity. We will attempt to construct an accurate parametrization over a wide range of redshifts and then identify the correct, physical, range of values for this parametrization. I.e. we wish to construct a model for the physical priors, a functional probability distribution function, $P[\vec{\alpha}]$ where $\vec{\alpha}$ is a set of time dependent functions which uniquely describes the family of scalar-tensor theories. Here we focus on the simplest case – quintessence – that is described by a time evolving scalar field, ϕ, with a canonical kinetic term and a potential, $V(\phi)$ [242, 243, 324, 326] (see also [327, 328] for reviews); in this case, the time dependent function that uniquely characterizes a model is $w(a)$. For any particular choice of parametrization, the problem then reduces to studying the distribution of the corresponding parameters $w(a)$ for a wide range of models (i.e. choices of $V(\phi)$) and initial conditions for the scalar field. What we propose to do here is very much in the spirit of Ref. [329] but now we wish to construct a full model for $P[w(a)]$, an approach which can be extended to full scalar-tensor theories further down the line. Note that our method is complementary to what has been done in Ref. [330, 331]. While their aim is to reconstruct $w(a)$ from observations, we use theoretical assumptions.

To go about constructing a prior for $w(a)$ one needs to adopt a parametrization. A wide range of proposals have been put forward that attempt to fully capture its time evolution. A favoured parametrization is [264, 265]

$$w = w_0 + w_a(1-a)\,, \tag{7.2}$$

which can approximate most equations of state close to $a = 1$ and is widely used in current data analysis or in assessing the constraining power of future surveys [43, 332]. While this parametrization has proven to be useful in identifying qualitatively different forms of dark energy, it may not necessarily be accurate enough to fully characterize the time evolution of dark energy over wide range of redshifts. For example, for a particular form of dark energy that we will explore in this Chapter – quintessence – we have that $w \geq -1$ for all a which can be easily violated for certain choices of w_0 and w_a if one chooses to work with Equation 7.2. We shall see, however, that these concerns are not borne out in practice.

Outline: In Section 7.1 we continue the description of quintessence that we outlined on Section 4.2.1, presenting the underlying mathematics but also laying out the various possible regimes that have been identified for the equation of state; in Section 7.2 we discuss in some detail how we establish what are physical priors in quintessence models, singling out thawing models as the most natural in terms of intial conditions (barring the existence of tracking behaviour); in Section 7.3 we discuss the approximation scheme we will use, and present how the required accuracy is evaluated and taking particular care to explain any restrictions; in Section 7.4 we work through a range of models to construct an analytic form for the prior function for the equation of state $w(a)$; in Section 7.5 we apply it to a current selection of data, to illustrate the impact the priors have on current constraints on the equation of state; finally in Section 7.6 we discuss our proposal and its caveats.

7.1 Quintessence.

As we discussed in Section 4.2.1, quintessence is a subclass of the general Horndeski theory. Finding physical priors for the full Horndeski would be our final goal. However, given the little intuition we have for that, we start with a simpler scenario: quintessence. In this context, it was

already pointed out that different theories, with different number of parameters, were actually quite restricted (and similar) when looked in the w_0-w_a space [329]. This suggests that the fundamental degrees of freedom of these theories are much less than those one would naively assume just counting their free parameters. We will use Ref. [329] as starting point.

In quintessence, the energy and pressure densities of the quintessence field are given by Equation 4.33,

$$\rho_{\rm DE} = \frac{1}{2}\dot{\phi}^2 + V(\phi)\,, \tag{7.3}$$

$$P_{\rm DE} = \frac{1}{2}\dot{\phi}^2 - V(\phi)\,, \tag{7.4}$$

where ϕ is the dark energy scalar field sourcing the accelerated expansion of the Universe and $V(\phi)$, its potential energy.

For our analysis, it is useful to follow Ref. [329] and rewrite the potential as $V = M_{\rm P}^2 M_H^2 A U(\phi)$, with

$$U(\phi) = f(\phi) + \sum_{n_{\rm min}}^{n_{\rm max}} c_n \xi_n b_n(\phi)\,, \tag{7.5}$$

where $M_H = 100$ Km s^{-1} Mpc^{-1}, A is the potential amplitude and $f(\phi)$ and $b_n(\phi)$ are a choice of basis functions. The leading order $f(\phi)$ is perturbatively modified by the sum. The lower limit, $n_{\rm min}$, is model specific and the truncation order, $n_{\rm max}$, is randomly chosen. Each perturbation order is weighted by a dimensionless constant, c_n, given by the theory itself and a random contribution from a set of dimensionful constants, ξ_n. These are drawn from a Normal distribution and are meant to increase the different possible $U(\phi)$ expansions. It is useful to rescale the field $\phi \to M_{\rm P}\phi$ and time $t \to M_H^{-1} t$ so that they are dimensionless.

Equations 7.3 and 7.4 already assumed (in accordance with current observations) a homogeneous and isotropic universe where the space-time metric is given by $ds^2 = -dt^2 + a^2(t)(d\vec{r})^2$ (Equation 2.1). The expansion rate can be derived from the Einstein field equations to give, for this metric,

$$H^2 \equiv \left(\frac{\dot{a}}{a}\right)^2 = \frac{1}{3M_{\rm P}^2}\left(\rho + \rho_{\rm DE}\right)\,, \tag{7.6}$$

where the energy density of matter and radiation is ρ. In terms of dimensionless units, the evolution equation for the scalar field is

$$\ddot{\phi} + 3H\dot{\phi} + AU_\phi = 0\,. \tag{7.7}$$

These equations completely define the dynamics of quintessence.

Given the definition of $\rho_{\rm DE}$ and $P_{\rm DE}$, one can use Equations 7.1 and 7.2 to determine the equation of state $w(a)$ and (w_0, w_a). One can envisage two approaches for calculating the latter two parameters. The first one is to consider a Taylor expansion of $w(a)$ around $a = 1$ (the value of the scale factor today) giving

$$w_0 = \frac{\dot{\phi}^2 - 2AU(\phi)}{\dot{\phi}^2 + 2AU(\phi)}, \tag{7.8}$$

$$\frac{dw}{da} = \frac{2A}{\dot{a}\rho_{\rm DE}^2}\left[3U(\phi)\dot{\phi}^2 H + U_{,\phi}\dot{\phi}\rho(\phi)\right]. \tag{7.9}$$

where the commas "$,\phi$" are partial derivatives with respect to ϕ and the dots are derivatives with respect to the cosmological time. Alternatively one can simply fit the expression in Equation 7.2 over a range of redshifts.

As we saw in Section 4.2.1, it turns out that (w_0, w_a) is a useful diagnostic for the types of behaviour that arise. In particular they allow us to distinguish between two broadly different types of regimes [266, 267] (see Figure 7.1). In the first regime, the equation of state can be different from -1 in the past but evolves towards -1 as the dynamics of the scalar field freezes with the expansion of the Universe. This is often called the *freezing* or *cooling* regime and is satisfied (for special choices of initial conditions) by, for example, potentials of the form $U \sim \phi^{-n}$. In the second regime, the equation of state starts close to -1 and evolves towards larger values as the Universe expands. Often called the *thawing regime*, it arises, e.g. in potentials of the form $\mathcal{P} \sim \phi^n$.

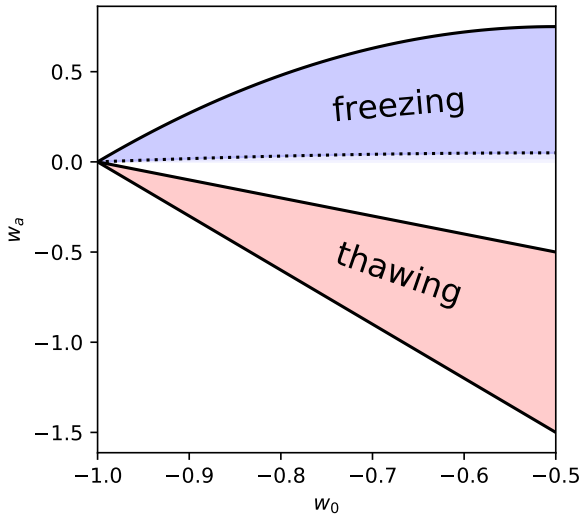

Figure 7.1: A schematic of the loci of *freezing* and *thawing* models on the (w_0, w_a) plane.

Whether the quintessence field is in the freezing or thawing regime not only depends on the form of the potential but also depends heavily on the initial conditions one is considering. Furthermore, it is possible to choose potentials such that the intermediate and late time behaviour is an attractor, independent of initial conditions. Models endowed with this behaviour are known as *tracker* models. In practice, and without tracking, natural initial conditions inevitably lead to thawing behaviour (as we will discuss in Section 7.2) and, in this Chapter, we will focus on characterizing these models thoroughly.

In this Chapter we will consider a comprehensive suite of dark energy models (see [327, 328] for a broad range). Building on the choices of Ref. [329] we will explore and characterize the following subclasses of *thawing* potentials given by Equation 7.5 and represented in Table 7.1:
Monomial: $V \sim \phi^N$; N can be positive, such as the case of a massive Klein-Gordon field ($N = 2$) or a scale-invariant field ($N = 4$); or negative. Both cases lead to thawing behavior, provided one solves the evolution equation from early times. It has been argued that a negative N would lead to freezing behaviour [266, 267]; however, this is only true if the initial conditions are set at low redshift (see Figure 7.2) or the kinetic energy is similar to the potential energy at the origin and $V(\phi_\mathrm{i}) \gg V(\phi_0)$ (see discussion in next Section). In general, starting from deep inside the radiation epoch, the Hubble parameter is large ($\ddot{\phi} + 3\dot{\phi}H \approx 0$) and freezes the field ($\dot{\phi} = \dot{\phi}_\mathrm{i} a^{-3}$), which only starts evolving at late times (thawing). In addition, the early dark energy constraints from CMB and Big-Bang Nucleosynthesis (BBN) ($\sim 1\%$ [175, 294]), limits the maximum value of $\dot{\phi}_\mathrm{i}$. Recall that, during kination, $\rho_{DE} \sim \dot{\phi}^2 = \dot{\phi}_\mathrm{i}^2 a^{-6}$.
Effective Field Theory (EFT): V is sum of monomials suitably weighted by the corrected powers of a mass scale consistent with the view that it arises as a consistent low energy limit of a

theory. This series represents corrections from operators representing high-energy physics. The series converges if the parameter $\epsilon_{\rm F}$ is small, required by the super-Planckian shift symmetry that imposes $\epsilon_{\rm F} < 1$. We will call $n_{\rm Q}$ to the number of quantum corrections.
Modulus: $V \sim \epsilon_{\rm D}^n e^{\lambda_n \phi}$; the vacua potential of theories with higher order dimensions are usually proportional to exponentials of the field [327]. We consider here weighted sums of them, where $\epsilon_{\rm D}$ is the compactification scale. In addition, we parametrize $\lambda_n = \alpha(p_{\rm D} - n)$, so that λ_n can be positive or negative, depending on the order of the term, and weighted by α.
Axion: $V \sim 1 + \cos(\epsilon_{\rm F}\phi)$ where $\epsilon_{\rm F}$ is related to the symmetry breaking scale; these potential arise in theories where the field is a pseudo-nambu Goldstone boson. Note that we are interested in a regime different of that in which axions contribute to dark matter, in which the field oscillates around a minimum of the potential and the equation of state averages to zero.

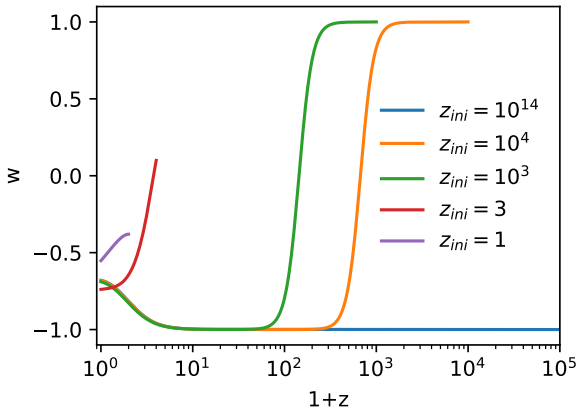

Figure 7.2: Effect of the initial conditions on the dynamics of the model $U \propto \phi^{-2}$ with initial conditions $\phi_{\rm i} = M_{\rm P}$ and $\phi'_{\rm i} \equiv {\rm d}\phi/{\rm d}\tau|_{\rm i} = H_0$. Just starting the integration close enough $z = 0$ the initial velocity of the field can survive and yield a freezing behavior.

Model	$b_n(\phi)$	c_n	$n_{\rm min}$	$f(\phi)$	$\phi_{\rm i}$
Monomial	0	–	–	ϕ^N	$[1, 7]$
EFT	ϕ^n	$(\epsilon_{\rm F})^n$	$p_{\rm E}$	$\sum_{i=2,4} \xi_i (\epsilon_{\rm F}\phi)^i$	$[1, 10]_{\log_{10}}$
Modulus	$e^{\alpha(p_{\rm D}-n)\phi}$	$(\epsilon_{\rm D})^n$	0	0	$[-1, 1]$
Axion	$\cos(n\epsilon_{\rm F}\phi)$	$(\epsilon_{\rm NP})^{n-1}$	2	$1 + \cos\epsilon_{\rm F}\phi$	$[-\frac{\pi}{\epsilon_{\rm F}}, \frac{\pi}{\epsilon_{\rm F}}]$

Table 7.1: Elements of the potential (Equation 7.5) for the studied models. Note that for EFT, $\phi_{\rm i} \in [1, 10]_{\log_{10}}$ stands for $\log_{10}(\phi_{\rm i}) \in [0, 1]$.

7.2 Establishing Physical Priors

Before we attempt to construct an efficient and comprehensive parametrization of quintessence models it is useful to explore the broad characteristics one might expect if one focuses on what we determine to be physical priors. We will focus on (w_0, w_a), very much along the lines of Ref. [266, 267, 329, 333]. This will allow us to explain and make explicit our choices that then lead to a distribution of dynamical behaviours for each individual model.

We can split the choices into a) cosmological parameters that affect that background evolution b) parameters in the action (or more specifically, the potential $V(\phi)$ and c) initial conditions for the scalar field. With regards to a) we chose to be sufficiently general but not overly so, or the analysis is impractical. This means that we choose to vary cosmological parameters that most directly affect the background evolution and which play off against the scalar field evolution. Specifically, we restrict ourselves to just h (where the Hubble constant is $H_0 = 100\,h\,\mathrm{km\,s^{-1}Mpc^{-1}}$) and the fractional density of cold dark matter today, $\Omega_{\rm cdm}$. We choose the ranges $h \in U[0.6, 0.8]$ and $\Omega_{\rm cdm} \in U[0.15, 0.34]$. It is important to note that ranges are chosen to be broad enough so that we do not bias our result, but we do not explore regimes that are clearly ruled out by current observations (e.g. $H_0 = 0$) [2]. In particular, $\Omega_{\rm cdm}$ priors might seem too broad in comparison with typical constraints. However, they were enlarged to allow for compatible results with tomographic weak lensing constraints from KiDS-450 [14] or CFHTLenS [334], which gave weaker constraints on $\Omega_{\rm m}$.

With regards to parameters in the potential, the choices are more subtle. In principle one should work within the framework of effective field theory and only include terms ("operators") with a suitable dimensionfull weighting and dimensionless parameters of $O(1)$. Indeed, one of the options makes this philosophy explicit – the case of EFT – and generally we obey this principle. Nevertheless, if used bluntly, this can severely restrict the range of behaviours; indeed it will be overwhelming dominated by a cosmological constant. We take care to allow for more general behaviour to be able to emerge.

We should note that alternatives are permissible where naturalness still plays a role (e.g. in the case of monomial potentials that break shift symmetry) or where other symmetry principles may be at play (as in the case of scale invariant potentials or axion like potentials). Furthermore, more complex operators arising from the low energy limit of higher dimensional theories and their variants (where, for example, factors of $e^{\lambda\phi}$ might emerge) are also considered.

Finally, we need to address the initial conditions for the scalar field. We assume that the initial conditions are established deep in the radiation era and there we can identify two different regimes. In the first case, the expansion of the Universe will have damped the evolution such that, in full generality, $\dot{\phi} = 0$. We can, again, use the view point of effective field theory and assume that the amplitude of the scalar field is of a $O(1)$ in terms of either Planck units or the fiducial mass scale which is used for dimensionful power counting. Alternatively, one can assume that the scalar field "scales" or "tracks" initially, i.e. that its background energy density follows that of radiation. In that case the initial value and velocity is uniquely determined by the background cosmology.

We have chosen these ranges in cosmological and potential parameters as well as in the initial conditions for the scalar field to span as broad a set of possibilities as are physically credible, very much in the spirit of Ref. [329]. A list of the ranges is presented in Table 7.2 where the parameters are described in Section 7.1. This does mean that we are excluding what we consider unphysical possibilities such as, for example, starting the scalar field with an arbitrary velocity at some low redshift – there is simply no physical mechanism that would put it there. Or, for example, we do not consider hugely disparate sets of parameters in the potential, as the small parameters would receive large radiative corrections in the absence of a symmetry protecting them.

We also avoid having too many higher order terms in the potential, controlled by $n_{\rm max}$ and $n_{\rm Q}$, as that would make their contribution negligible. In the same way we don't have either too low or too high values of the weighting constants $\epsilon_{\rm F,NP,D}$ that would make the higher order

[2] The other parameters are left as the hi_class default, i.e. Planck 2013 values. In general, these parameters will have little effect in our result, except, perhaps, for the lack of massive neutrinos, whose effect is degenerate with DE and could have a small impact when used with data.

Parameter	Model	Dist.
A	All	Fixed by $1 = \sum_i \Omega_i$
ξ_n	All	$\mathcal{N}(0, 1)$
N	Monomial	$\mathrm{U}_{\mathbb{Z}}[1, 7)$
$n_{\max}$	Modulus, Axion	$\mathrm{U}_{\mathbb{Z}}[10, 20]$
n_{Q}, p_{E}	EFT	$\mathrm{U}_{\mathbb{Z}}[5, 10]$
$\log_{10} \epsilon_{\mathrm{F,NP,D}}$	EFT, Modulus, Axion	$\mathrm{U}[-3, -1)$
p_{D}	Modulus	$\mathrm{U}_{\mathbb{Z}}[1, 5]$
α	Modulus	$\mathrm{U}[0, 1]$

Table 7.2: Parameters distributions. $\mathrm{U}[a, b]$ stands for the uniform distribution between a and b and $\mathrm{U}_{\mathbb{Z}}$ is the uniform distribution in the integers.

terms either stop contributing or explode. Similarly, we choose α and p_{D} priors for Modulus so that the exponent size is controlled, despite allowing for unlikely large values such as e^5. For the monomial case, large N values would make the potential too steep making the field evolve too fast and yielding unphysical or highly tuned results. Finally, the ξ_n constants weigh randomly higher order term in the potential, leading us to take their values from a Normal distribution.

In Figure 7.3 we can get an idea of the dominant type of behaviour for the class of models we consider, in terms of the equation of state. Focusing, for now, on the solid contours, we can see that these models lead exclusively to thawing models. The only way to change this behaviour (unless the potential tracks the dominant energy density) is to give the scalar field large initial velocities at late time (see Figure 7.2); these are completely unphysical as they correspond to unacceptable velocities in the radiation era – i.e. there is no physical mechanism for achieving these velocities and hence, such evolution cannot be, in any way considered part of a set of physical priors. We note that, in the analysis of Ref. [333] such unphysical initial conditions were considered by starting the integration of the background at late redshifts ($z = 3$). This prevents the expansion of the universe to dilute the initial conditions and hence the unnatural prevalence of freezing models in their analysis. We also note that this plot pretty much reflects the findings of Ref. [329].

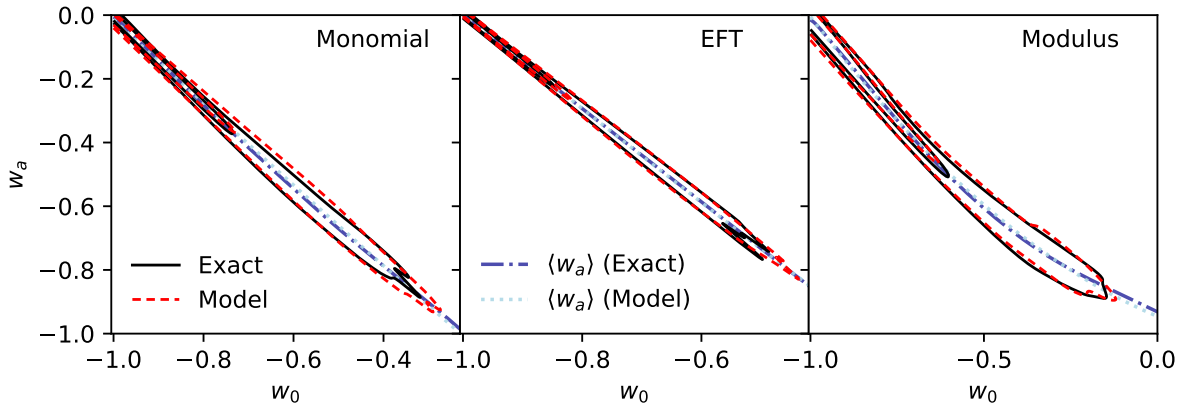

Figure 7.3: w_0-w_a distributions for the Monomial (left panel), EFT (central panel) and Modulus (right panel). All these models have $w_a \neq 0$, while Axion can be described just with $w_0 \leq -1 + 10^{-4}$ (95% C.L.). In this Figure we are comparing the prior distributions found for w_0-w_a fitting the observables (the *Exact*); i.e. minimizing Equation 7.12; and the distributions obtained with our analytic approximation (*Model*), i.e. with Equation 7.13-7.16.

Freezing models can be obtained in at least two situations. In *tracker models*, solutions exist in which the quintessence energy density is a fraction of the dominant matter component, e.g. radiation at early times. This early dark energy contributes to the expansion rate throughout cosmic history and is thus subject to constraints from CMB and BBN [294]. Generic initial conditions will cause the field to be frozen at $\rho_{\rm DE} \sim V(\phi_{\rm i})$, entering the tracking behavior when $V \sim \rho$. A tracking behaviour at all epochs can be achieved through an exponential potential, although a change on $V_{,\phi}/V$ is necessary for the field to freeze in Ref. [335, 336]. Other freezing models can be obtained with inverse power-law potential (i.e. monomial with $N < 0$) [337, 338]. In this case the field evolves with a fixed equation of state, rather than track the dominant matter component. However such a simple potential does not successfully freeze to $w \sim -1$ at low redshift unless N is close to zero, effectively recovering the cosmological constant behaviour, cf. Figure 7.4. In both cases, freezing behaviour requires that the initial conditions for the field are so that $V(\phi_{\rm i}) \gg V(\phi_0)$ ($\rho_{\rm DE}(\phi_{\rm i}) \gg \rho_{\rm DE}(\phi_0)$) – only thawing behavior can occur if the initial energy density of quintessence is small, as it is the case for the priors used here. Neither purely exponential or inverse power-law potentials can act as viable freezing models – we will leave the study of other potentials with freezing behavior for a future work.

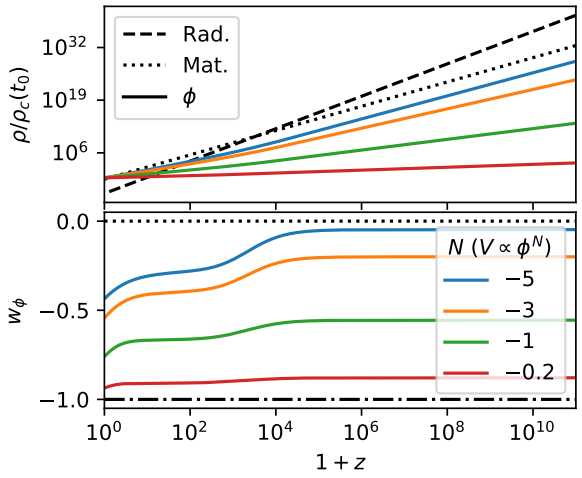

Figure 7.4: Freezing behavior for inverse power-law potentials (monomial quintessence $N < 0$). Freezing behavior is possible if the energy density of the field is significant at early times $V(\phi_{\rm i}) \gg V(\phi_0)$ (upper panel). However, in order to achieve $w(z = 0) \approx -1$ the potential needs to be very flat ($N \approx 0$), a requirement that pushes the model towards a Λ limit (lower panel).

7.3 Parameterizing quintessence

We now proceed to describe the method by which we compress information about the quintessence component in such a way as to retain as much information as necessary for a reliable model comparison or likelihood analysis. In this Chapter, as it is customary, we choose to work with the equation of state w, which enters into the equations of the observables through the energy density:

$$\rho_{\rm DE} = \rho^{(0)}_{\rm DE} \exp\left[-3 \int_0^{\log(a)} {\rm d}[\log(a')]\,[1 + w(a')]\right] . \tag{7.10}$$

The Hubble rate, H, and the angular diameter distance, $D_{\rm A}$, only depend on the energy densities:

$$H^2 \propto \sum_i \rho_i \,,$$
$$D_{\rm A} = \int_0^z \frac{{\rm d}z'}{H(z)} \,,$$

while the growth rate of structure, $f = {\rm d}(\ln \delta_{\rm m})/{\rm d}(\ln a)$ (where $\delta_{\rm m}$ is the matter density contrast) also depends (mildly) on w:

$$(1+z)\frac{{\rm d}f}{{\rm d}z} = \frac{1}{2}\left(1 - \sum_i \frac{3w_i\rho_i}{H^2}\right) f + f^2 - \frac{3}{2}\Omega_M(z) \,.$$

In choosing a parametrisation, one has to assess how well it approximates the dynamics it is supposed to represent. To do so, one needs some kind of measure. For example, it should be good enough that evolution of distinct classes of models, once parameterised, are easily distinguishable. In practice this means one needs to construct realisations of this evolution (the equation of state, w, in this case) from a realistic priors for a particular class of models and check that the parametrisation follows these realisations faithfully and in such a way that it is clearly distinguishable from another class of models.

There is also a practical guide for the quality of the parametrisation. Ultimately we will use it to generate mock observables that will be compared to data. We are looking forward and assuming that the quality of the data will be such that we will have, at most, percent errors on the observables. This means that we should aim to have a parametrisation which is accurate at the sub-percent level but not much more. Another way of stating it is that the systematic errors arising from our modelling of the dark energy evolution (through the parametrisation) should be of the same order as (or marginally smaller than) the statistical and systematic errors arising from the observations themselves.

We will use the latter criteria as a practical guide in determining the quality of our parametrisation. The observables we will focus on are the angular diameter distance, $D_{\rm A}(z)$, the growth rate, $f(z)$, and the Hubble parameter, over the range of redshifts which will be covered by the next generation of data sets. This is key (and a novel aspect) of the approach in this Chapter.

Our starting point is a finite series expansion of w,

$$w = \sum_{m=0}^{M} c_m (1-a)^m \,, \tag{7.11}$$

Note this parametrization does not break at high order and that higher terms contribute more at early times ($a \to 0$). It will be convenient to denote $\mathbf{c} = (c_1, c_2, \cdots, c_m)$.

While it is clear that the larger the number of coefficients (i.e the larger the M), the more accurate the parametrisation, we, naturally, want to come up with the most economical parametrization. Even though the equation of state can have a difficult evolution, the results of Ref. [329] and the fact that it will only be relevant when dark energy is not negligible, lead us to believe that it should, universally, be described by a combination of a few smooth functions. We shall see that, for thawing models of quintessence, which is the focus of this work, the parametrization of Equation 7.2 is sufficient. This means we need to find a probabality distribution function for (w_0, w_a), $\mathcal{P}[w_0, w_a]$.

Our approach is as follows [3]. For each class of theories, we generate a large number of possible evolutions for w, using the approach described in Section 7.2. We work with hi_class

[3]Our code can be found in `https://gitlab.com/carlosggarcia/horndeski-priors`

[31, 32], a modified version of the Boltzmann code CLASS [30] that incorporates Horndeski theories [29, 239, 240], to solve the cosmological equations and obtain the exact observables for each realization. In addition, the parameters of the model must be chosen so that we are able to reproduce the phenomenology of the given model, with mild restrictions based on stability and more fundamental physics. Given an ensemble of models, parameters are obtained fitting w_0 and w_a so that they minimize the error on the observables at specific redshifts; i.e. minimizing

$$\chi^2 = \sum_i \frac{(\mathcal{O}(\vec{c}) - \mathcal{O}(\phi))_i^2}{\sigma^2_{\mathcal{O}_i}}\,, \tag{7.12}$$

where $\mathcal{O}(\phi)_i$ stands for the exact D_A, H and f at the specific redshift z_i, computed solving the field equation and, therefore, depends on the specific choice of the model parameters in Table 7.1. On the other hand, $\mathcal{O}(\vec{c})$ stands for the observables computed using the parametrized w. As we will see, $\mathcal{O}(\vec{c}) \equiv \mathcal{O}(w_0, w_a)$. Finally, $\sigma_{\mathcal{O}_i}$ is the desired precision, which, in all cases, we choose it to be lower than 1% at low redshift (i.e. $z < z_\mathrm{low} = 10$) [17–19], and 0.3% at recombination for D_A [87]. Note that, using the parametrization it is possible that w crosses $w = -1$. To allow for such models that, however, reproduce the observables accurately, we use the fluid equations with the Parametrized post-Friedmann (PPF) approximation [339], already implemented in `CLASS`.

Equation 7.12 neglects the fact that the observables are, in general, correlated. However, we can safely disregard this contribution as Equation 7.12 suffices to achieve the goal precision. This will be seen in following Section.

With this machinery in hand, we can study the probability distribution functions (PDFs) of (w_0, w_a) and from them we are able to generate the PDFs for the observables, D_A, H and f.

7.4 Results

We now proceed to construct a distribution function for w_0 and w_a. To begin with, we generate ensembles of cosmologies for each of the models. We follow the procedure we discussed in Section 7.2 to generate $20,000$ realizations for each class of models, which we have seen is enough to produce stable results. Given the extra accuracy we need for $D_\mathrm{A}(z_\mathrm{rec})$, we weight the low redshift observables with $\sigma_{\mathcal{O}_i} = 10^{-3}$ and $\sigma_{D_\mathrm{A}(z_\mathrm{rec})} = 10^{-4}$ for the angular diameter distance point at recombination in Equation 7.12. These variables are different than our threshold for the allowed maximum allowed errors. They are set lower to ensure the maximum errors are below our threshold (i.e. 1% at low redshift and 0.3% for $D_\mathrm{A}(z_\mathrm{rec})$).

Revisiting Figure 7.3, we note that the contours for (w_0, w_a) all have similar characteristics: a long degeneracy direction (given by the dotted line) towards the bottom right while a reasonable tight distribution along the (quasi)-orthogonal direction. This is characteristic of thawing models, as has been previously observed in Ref. [268, 329]. In the end, the field evolution for thawing models is just a slow (to be physically viable) roll down of the potential and, consequently, produces similar effects. We will exploit this structure further down.

To begin with, as explained before, we check the quality of this parametrization by generating our proxies for the observables, now with (w_0, w_a) and comparing, model by model, with the original full calculation. In Figure 7.5 we can see that, apart from a very few outliers, most models lie well within our target precision. In other words, using (w_0, w_a) we generate observables which agree with those calculated from the full evolution to better than our threshold. This gives us confidence that describing $w(a)$ in terms of two parameters is good enough for any of the planned surveys.

It is interesting to see how well the parametrized $w(a)$ approximates the full one as a function of redshift. In Figure 7.6 we plot the maximum deviation between the two. We can

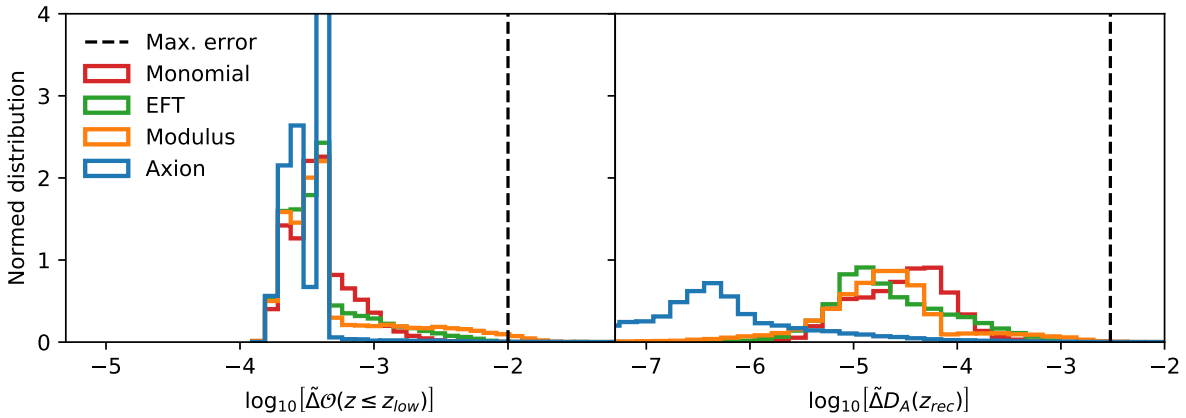

Figure 7.5: Distribution of the maximum relative error of the observables for each Quintessence model compared to its fit in the $(w_0,\, w_a)$ plane, i.e. $\tilde{\Delta}\mathcal{O} \equiv |\mathcal{O}(\text{Fit})/\mathcal{O}(\text{Quintessence}) - 1|$. In the left panel $\mathcal{O}$ stands for any observable among H, f or D_A, whichever gives the maximum error at low redshift ($z < z_\text{low} = 10$). In the right panel we show the maximum error at recombination for the angular diameter distance $D_\text{A}(z_\text{rec})$.

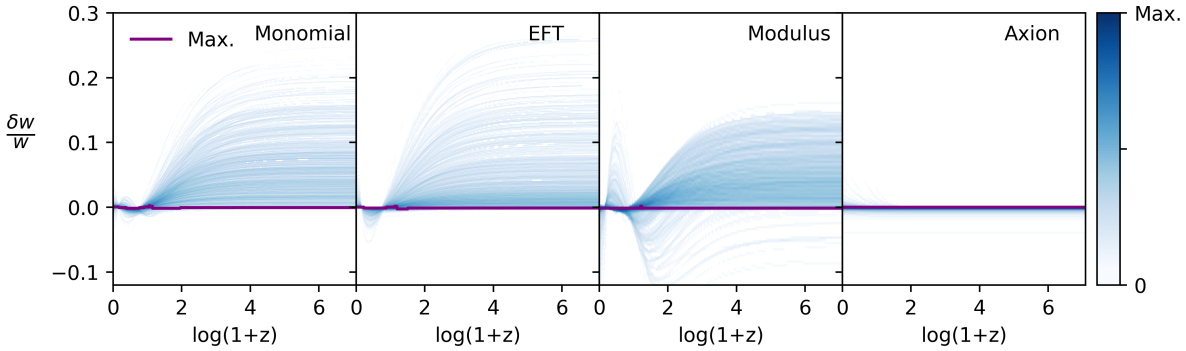

Figure 7.6: Density plots, one for each Quintessence model, showing the time evolution of the relative difference between $w(a)$ obtained from the original realization and after fitting it in the $(w_0,\, w_a)$ plane. Darker colors indicate the presence of more models with that particular relative difference at that redshift. The purple lines show the maximum density for each model.

see that for $z > 1$, the differences are appreciable. This is, of course, to be expected. The dark energy density at those redshift is sufficiently subdominant and will contribute very little to the observables.

With the distributions in hand for (w_0, w_a) we can construct an analytic model. We assume that the distribution can be factorized into

$$\mathcal{P}[w_0, w_a] = \mathcal{P}[w_a|w_0]\mathcal{P}[w_0]\,. \tag{7.13}$$

We can see in Figure 7.7, the $\mathcal{P}[w_0]$ for each model (solid line) is sharply peaked at $w_0 = -1$. While an exponential is a reasonable approximation, we find that

$$\mathcal{P}[w_0] = A_1 e^{-\left(\frac{w_0}{w_1}\right)^{\alpha_1}} + A_2 e^{-\left(\frac{w_0}{w_2}\right)^{\alpha_2}} \tag{7.14}$$

is more robust and can cover more models. In Figure 7.7 we see that approximate form as a dashed line.

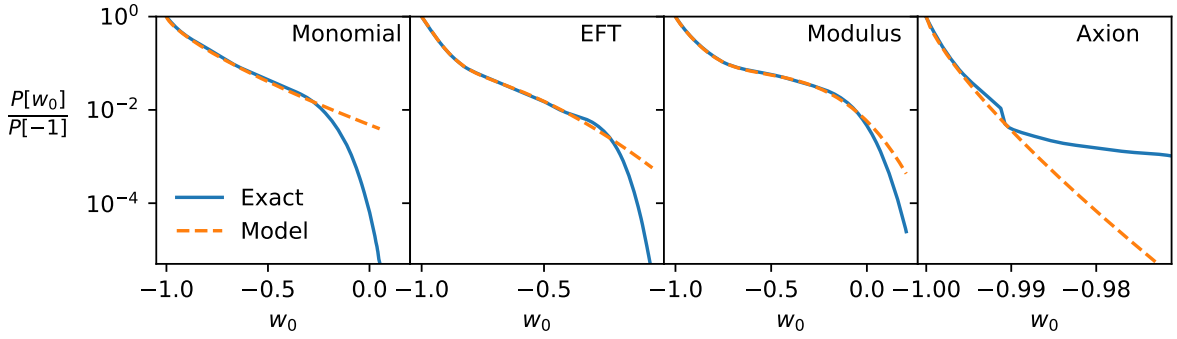

Figure 7.7: For each model, we show the exact (blue solid lines) probability distribution of w_0 normalized to 1 for $w_0 = -1$. The approximate analytic model defined in Equation 7.14 is also shown (orange dashed lines). It is possible to appreciate the excellent agreement between the two curves down to probabilities of 10^{-2}, which includes the region preferred by the data in most models.

Model	A_1	w_1	α_1	A_2	w_2	α_2
Axion	737	0.775	-1.08×10^{-3}	0	-	-
Monomial	8.21	0.734	0.102	0	-	-
EFT	12.9	1.01	0.0499	1.05	1.76	0.383
Modulus	8.13	0.890	0.0712	0.535	3.95	0.803

Table 7.3: Fit parameters for $\mathcal{P}[w_0]$ (Equation 7.14) model distributions.

From the contour plots in Figure 7.3 we can also see that there is a well defined degeneracy direction in (w_0, w_a) (the dotted lines). The degeneracy line, $\bar{w}_a(w_0)$ is well approximated by a quadratic polynomial

$$\bar{w}_a(w_0) \simeq \beta_0 + \beta_1 w_0 + \beta_2 w_0^2 \,. \tag{7.15}$$

We now want to look at the conditional probability, $\mathcal{P}[w_a|w_0]$. From Figure 7.8 we can see that, for each value of w_0, the distribution is peaked around $\bar{w}_a(w_0)$ and well approximated by a Gaussian. We thus use the ansatz

$$\mathcal{P}[w_a|w_0] = \frac{1}{\sqrt{2\pi\sigma^2(w_0)}} e^{-\left(\frac{w_a - \bar{w}_a(w_0)}{2\sigma(w_0)}\right)^2} , \tag{7.16}$$

where the variance is given by

$$\sigma(w_0) \simeq \sigma_0 + \sigma_1 w_0 + \sigma_2 w_0^2 \,. \tag{7.17}$$

The fits to these parameters for each class of models are given in Tables 7.3 and 7.4, respectively. Although they are given with high accuracy, we have found that small changes do not affect the w_0-w_a distribution and, specially, the distributions of the observables. Nevertheless, we are cautious and use three significant figures. The study of the minimum required accuracy goes beyond the scope of this work.

We can now revisit the contour plots, comparing the original ones with those from our analytical model. In Figure 7.3 we overlay the two sets and, unsurprisingly, find very close agreement. The final step is now to sample from the analytic priors to generate the observables and compare them with those generated by the full scalar field evolution. In Figure 7.9 we

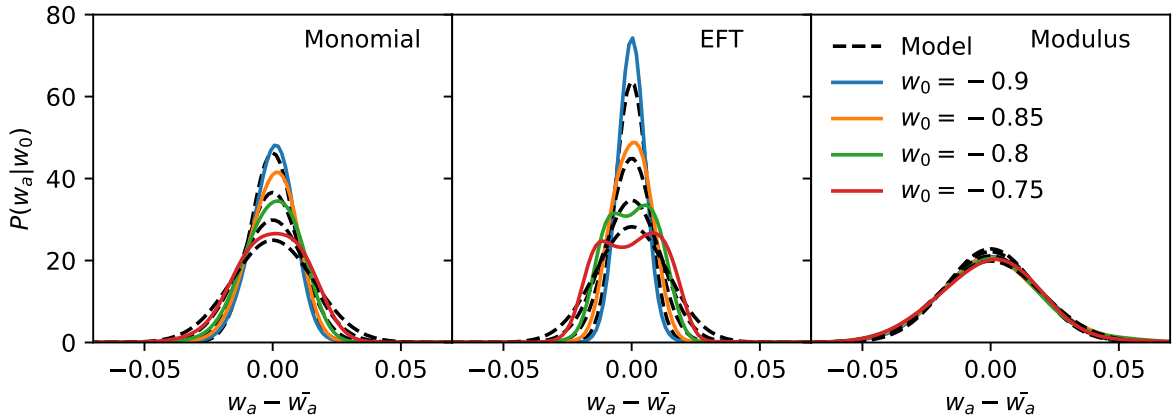

Figure 7.8: For each model, Axion excluded since it can be parametrized solely in terms of w_0, we show the conditional probability distribution of w_a given specific values of w_0 (colored solid lines). Dashed black lines represent the same curves obtained using our analytic approximation, Equation 7.16. The parameters of this equation have been obtained through a global fitting. This explains the discrepancy between the solid and dashed curves, but it does not affect the observables as shown in Figure 7.9.

Model	β_0	β_1	β_2	σ_0	σ_1	σ_2
Monomial	-1.28	-1.21	0.0564	0.0769	0.108	0.0357
EFT	-1.43	-1.35	0.0882	0.0556	0.0577	0.00320
Modulus	-0.946	-0.460	0.481	0.0755	0.121	0.0628

Table 7.4: Fit parameters for $\mathcal{P}[w_a|w_0]$ (Equation 7.16) model distributions. Recall that $\langle w_a \rangle(w_0, \beta_i)$ and $\sigma(w_0, \sigma_i)$ are given by Equations 7.15 and 7.17, respectively.

overlay the contours for the case with the largest differences, i.e. for the Modulus model at redshift $z = 1$. We find an excellent agreement between the two, giving us confidence that the analytic priors can be used as reasonably accurate representation of the quintessence space in future cosmological analysis. It must be noted that we checked the truth of this statement for all models at different redshifts ($z = 0.1$, 0.5, 1.0, 2.0, 5.0, and 10). In Section 7.5, we will study the impact of these analytic priors when used in combination with actual data and see that they considerably increase the constraining power of the data.

In general, the analytic expression are stable under changes of the parameters' priors. We checked the stability of the results by approximately doubling or halving the width of the prior distributions and saw that, even though (in a very few cases) the actual numbers change, the new distributions can be still parametrized by Equations 7.14 and 7.16. In particular, we saw that Monomial and EFT distributions remain unchanged, while the distributions for Axion and, more significantly, Modulus varied. The exponential potential of Modulus makes it more sensitive to changes on the field.

In the following lines we summarize some key, individual, features of each model.
Monomial: The two parameters, w_0-w_a, suffice to reproduce the observables accurately. In fact, minimizing the χ^2 with the observables (Equation 7.12) yields equivalent distributions to those obtained fitting the actual curves (i.e. w) at low redshift. The probability distribution of w_0, $P[w_0]$, is correctly reproduced with just one of the exponentials in Equation 7.14. The parametrized w goes to lower values than the original one, meaning that, for a large fraction of the models, one needs $w < -1$ at early times to effectively recover the model.

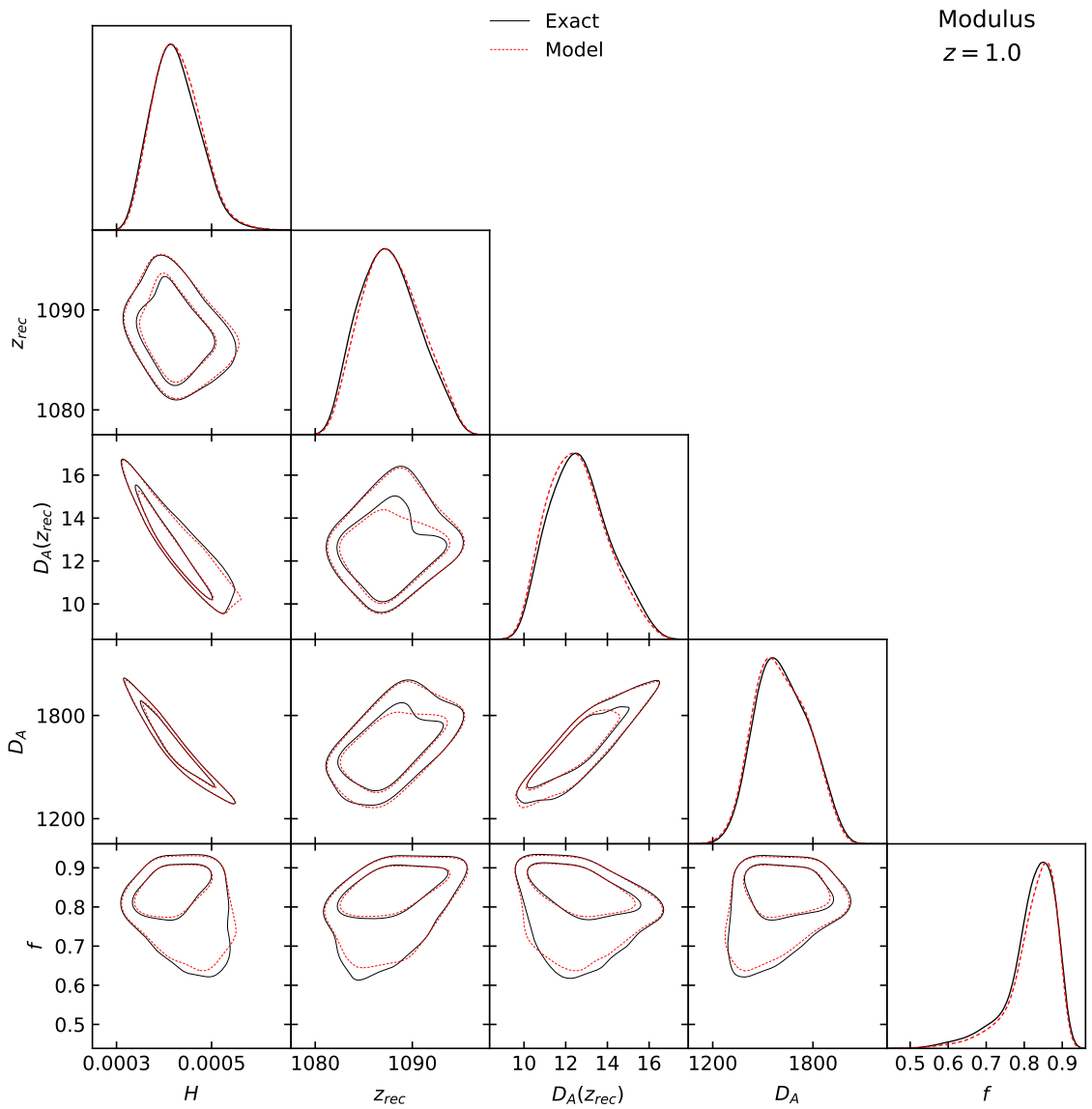

Figure 7.9: Distributions of the observables obtained integrating the field equations of motion (solid black line) compared to those obtained sampling from our parametrization. These are the results for modulus at redshift $z = 1$, which was the case we found largest differences. However, they are small and will have little impact when the analytic expressions are used in combination with data.

EFT: The two parameters, w_0-w_a, suffice to reproduce the observables accurately. In contrast with the monomial case, fitting w at low redshift yields different distributions for the parameters. This is consequence of faster evolutions of the field close to $z = 0$. In addition, our prior on $\phi_{\rm i}$ substantially enlarge the w_0-w_a distribution in comparison with that in Ref. [329]. This is consequence of having initial values of the field considerably lower than $1/\epsilon_{\rm F}$ and forcing the Friedmann equation to hold today. While in Ref. [329] $\phi_{\rm i} \in [-1/\epsilon_{\rm F}, 1/\epsilon_{\rm F}]$ (with $\log_{10}(\epsilon_{\rm F}) \in [-3, -1]$), we imposed a fixed range $\phi_{\rm i} \in [1, 10]$; the smaller $(\epsilon_{\rm F}\phi)^n$ terms that enter into the potential, force the potential to be (substantially) larger, leading to a large derivative, $V_{,\phi}$.
Modulus: The two parameters, w_0-w_a, suffice to reproduce the observables accurately. The more complicated dynamics are reflected in both the fit performance and the way w is recovered in

comparison with the original: the errors on the observables, although good enough, have longer tails relative to other models; in addition, in contrast with previous cases, many models have $w(w_0, w_a) > w(z)$ at early times.
Axion: Just one parameter is needed to reproduce the observables accurately: w_0. In this case, the field remains frozen for almost all its history and just starts moving very close to the present. As in the previous case, $w(w_0) > w(z)$ at early times, in a form that compensates the (small) late time evolution of the field, but does not change the early universe dynamics.

7.5 Comparison with current data

In this Section we present the constraints on the equation of state from current cosmological data and combine them with the analytical priors of previous section. Let us briefly go through the method. We do a Bayesian analysis, sampling through w_0 and w_a along with the standard cosmological parameters in a Markov Chain Monte Carlo (MCMC) with `MontePython` [36, 37] using the Metropolis-Hastings algorithm [38, 39]. We have used the Gelman-Rubin convergence criterion [340], requiring $R - 1 < 0.01$.

We have used the following datasets:
CMB: From Planck 2015 [176, 341, 342], we use the high ℓ temperature autocorrelation (TT) likelihood, in the range $\ell = 30 - 2508$, along with the likelihood of the joint autocorrelations of the temperature (TT), the E and B polarization modes (EE and BB) and the cross-correlation of the temperature with the E-polarization mode (TE) for $\ell = 2 - 29$ and the lensing likelihood (with temperature and polarisation lensing reconstruction) in the multipole range $\ell = 40 - 400$.
BAO: We use Baryon Acoustic Oscillation (BAO) measurements from 6dFGS survey [343], the SDSS DR7 Main Galaxy Sample (MGS) [344], and BOSS DR12 [49]. The first two measure the expansion history through the redshift-distance and redshift-Hubble relations combined through the relation, $D_{\rm V} = (D_{\rm A}^2(1+z)^2 z/H)^{1/3}$, where $D_{\rm V}$ is the angle-averaged distance, $D_{\rm A}$ – the angular diameter distance and z is the redshift BOSS DR12 constrains both the angular diameter distance, $D_{\rm A}$ and the Hubble parameter, H. We do not consider the correlation between the BOSS measurements and the 6dF and MGS survey as those surveys cover different patches of the sky and hence any such correlation would be negligible.
RSD: We use Redshift Space Distortions (RSD) measurements derived form from 6dFGS [345] and BOSS DR12 [49], where for BOSS we use the full covariance between the 3 $f(z)\sigma_8(z)$ measurements at different redshifts and the BAO measurements of $H(z)$ and $D_{\rm A}(z)$.
SNe Ia: We use the new Pantheon Supernovae (SNe) Ia sample [124], which combines observations from the Pan-STARRS1 Medium Deep Survey at redshift $0.03 < z < 0.65$ with ones from the SDSS, SuperNova Legacy Survey (SNLS), and various low-redshift and HST samples. In total 1048 SNe Ia in the redshift range $0.01 < z < 2.3$.

We note that, throughout, we assume that the cross-correlation between the different datasets is negligible. To obtain the combined constraints from data and theory we implemented the priors as a likelihood module[4] in `MontePython` and plotted the results with the python package for analysing MCMC samples GetDist [346].

We begin by showing the results of a likelihood analysis without including our model for the theoretical priors in the left hand panel Figure 7.10. The likelihood analysis with uniform priors on the equation of state parameters prefers a distinct direction in the (w_0, w_a) plane which, interestingly, is not colinear with the $\bar{w}_a(w_0)$ we derived in the previous section; this is clear from the overlay of the theoretical priors (and was already apparent in Ref. [329]). The Axion model, as has been repeatedly mentioned, is a special case, with an equation of state which is

[4]Available at: `https://gitlab.com/carlosggarcia/horndeski-priors/tree/master/montepython_lkl_quint_thawing_priors`

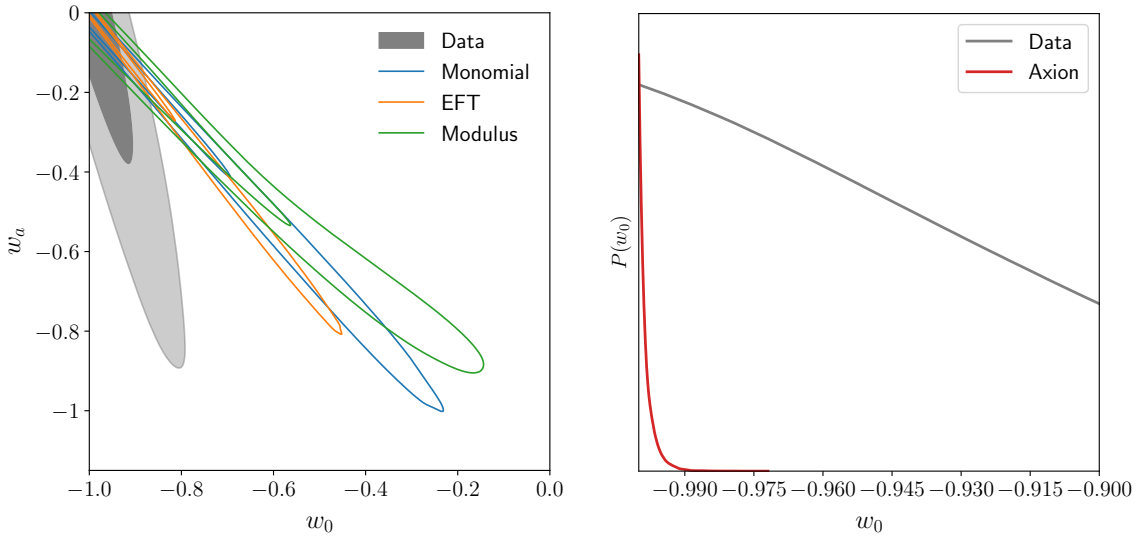

Figure 7.10: Distribution of (w_0, w_a) for the CMB+BAO+RSD+SN combined datasets and the theoretical priors. On the left panel we show Monomial, Modulus and EFT and on the right panel Axion quintessence priors.

very concentrated at $w_0 = -1$. For this model, we compare the widths of the posterior from the likelihood analysis with uniform priors on (w_0, w_a) with the theoretical priors studied in this Chapter; clearly the theoretical prior is much tighter than the posterior. As mentioned above, Figure 7.10, to some extent, echoes similar plots used in contour plots for (n_s, r) for constraining the inflationary landscape. There one tends to plot inflationary "tracks" for specific models, overlaying the contours from a likelihood analysis assuming uniform priors for (n_s, r).

Even though the two sets of contours overlap, i.e. there is no "tension" between them, we do not expect them to be aligned: very different physical considerations go into generating each set. Our choices were broad and uninformative in order to completely explore the phenomenology of the studied models. Furthermore the operational assumptions to build the analytical approximations of the PDF's cannot bias our result as they almost perfectly recover the exact w_0-w_a distributions.

If we invert the perspective and plot the theoretical priors individually and then incorporate them in the likelihood analysis of the current data, we see the power of combining the two. In the left hand side of Figure 7.11, we can see a substantial reduction in the areas of the contours when the data is folded in. We see that the width of the likelihood contours of (w_0, w_a) in the analysis that included the theoretical priors is a factor of few times smaller than for the theoretical priors alone. While one would expect the uncertainty in (w_0, w_a) for the combination of priors and data to be substantially better than for an analysis with uniform priors and data, we can see how the non-colinearity of the prior and data contours works to our advantage and that, even with current data, combining with theoretical priors gives us greatly improved constraints.

To emphasize the power of including correct theoretical priors, in Table 7.5 we present constraints on (w_0, w_a) for the likelihood analysis with uniform priors and with theoretical priors. Clearly there is a dramatic improvement in constraints. For completeness, again, we single out the case of the Axion model in the right hand panel of Figure 7.11 to see that in this case the prior is so tightly centred at $w_0 = -1$, combining it with data (also centred at ~ -1) does not improve the constraints significantly.

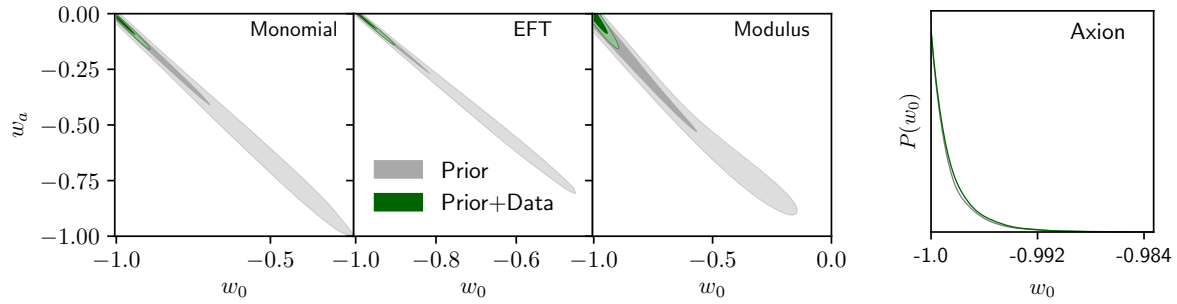

Figure 7.11: Constraints (w_0, w_a) for the four different quintessence model from the CMB+BAO+RSD+SN combined datasets combined with the priors.

Data	$w_0 = -1.012 \pm 0.088$	$w_a = 0.05 \pm 0.36$
Data + Monomial	$w_0 = -0.966 \pm 0.027$	$w_a = -0.058 \pm 0.036$
Data + EFT	$w_0 = -0.968 \pm 0.023$	$w_a = -0.040 \pm 0.035$
Data + Modulus	$w_0 = -0.967 \pm 0.025$	$w_a = -0.054 \pm 0.037$
Data + Axion	$w_0 = -0.9983 \pm 0.0020$	$w_a = 0.0$

Table 7.5: Confidence limits of w_0 and w_a for the combined data set CMB+BAO+RSD+SN (Data) and the data combined with the theoretical priors for each model.

7.6 Discussion

In this Chapter we have proposed a simple, analytic model, for the priors of the equation of state, $w(a)$ of thawing quintessence. We have developed it for four specific thawing models but are confident it could be extended to any thawing model, given the observed similarities on the (w_0, w_a) space [268, 329]. It can now be used to either demarcate the physically allowed subset of the (w_0, w_a) plane or incorporated into any future MCMC parameter estimation analysis. In Section 7.5 we have trialled our proposal with existing data.

The prior for the equation of state factorizes easily into one probability distribution function for w_0 and another for w_a conditional on the value of w_0. The model we propose is reasonably robust on the choice of fundamental parameters for each theory (i.e. fundamental constants in the quintessence action and initial values of the scalar field). We mean by this that the priors are unchanged when we vary these fundamental parameters or that the shape of the priors remains invariant (albeit with smaller or larger variances). We believe our choice of fundamental parameters is physical, erring on the conservative side. As a result, any future likelihood analysis is greatly simplified and it is no longer necessary to run the full scalar field dynamics to find the correct distribution of (w_0, w_a).

One interesting, and important, consequence of having accurate physical priors is that, within the context of thawing models, constraints on (w_0, w_a) are greatly improved. While this is not initially surprising – the physical priors we have characterized are much more restrictive than the usual uniform priors one uses for (w_0, w_a) – the fact that the orientation of the prior distribution relative to that of the posterior constructed from the uniform prior with data also plays a key role. In fact, even though the posterior constructed from a uniform prior with data is much broader than the theoretical prior, the fact that they are not co-linear means that combining the two greatly improves the constraints on (w_0, w_a) relative to the prior alone. As the data improves, we except this situation to be further exacerbated.

We have focused on thawing models but our approach must be extended to other models. Within the scope of quintessence, we have touched on tracker models which lead to freezing behaviour (we do not believe non-tracking, freezing models are physically realistic; these models need to be tuned so that $V(\phi_{\rm i}) \gg V(\phi_0)$ and a sufficiently flat potential to correctly approximate to $w \sim -1$, as is exemplified in Figure 7.4). Tracking models are not amenable to such a simple parametrization. One possible reason is due to the "quasi-nonanalyticity" of $w(a)$: in this case, the shape of the equation of state mimics that of rational functions which do not have well behaved Taylor expansions. Nevertheless, there may be alternative ways of parametrizing the equation of state (through, for example Pade approximants) that are amenable to the treatment here.

Naturally, we would like go beyond quintessence and we have tried to couch the task in as general way as possible, as a first step in completely characterizing Horndeski theories. For the case of quintessence, it has been an easy first step given that quintessence models have been extensively studied for over two decades and there is a detailed understanding of how the scalar field evolves in these scenarios. In the case of more general Horndeski theories, pockets have been studied well (such as Galileons or extended Jordan-Brans-Dicke theories) but a complete, generic framework for the scalar field evolution is still lacking. Only once such a framework is in hand can one start discussing physical priors for the parametrized versions of these theories, the $\mathcal{P}[\vec{\alpha}]$ discussed in the introduction.

Chapter 8

Building analytic likelihoods for Large Scale Structure

We saw in Chapter 3 that the two-point correlation of different fields projected on the celestial sphere is one of the most common observables used in the analysis of large datasets in astrophysics, from studies of the Cosmic Microwave Background (CMB) [347–357] to Large Scale Structure (LSS) and weak lensing surveys [358–366]. Using these two-point functions, one achieves a high level of data compression (with respect to the size of the raw datasets – time-ordered data, images or catalogs). They can also be directly used to constrain cosmological and astrophysical parameters assuming that one can model their likelihood. This is usually done by assuming that the two-point functions are Gaussianly distributed, which is often a good approximation due to the central limit theorem [367, 368]. In this case, the only obstacle that remains is being able to estimate the covariance matrix of a set of two-point correlators. Since the form of this covariance directly affects the posterior parameter uncertainties, a precise determination of it is of paramount importance. In Large Scale Structure experiments, this has often been resolved by making use of one's own data through resampling techniques [369–373], or by generating a large number of mock realizations [374–376]. With the advent of the larger current and future surveys, the increasing size of the data vector and of the volume to be simulated has made this solution impractical, and fully analytical and hybrid estimators are now being used.

The problem of producing accurate analytical estimates of the covariance matrix for Large Scale Structure data has seen significant progress in the last few years [377–382]. As described in Ref. [383], the covariance matrix receives three main contributions:

- **Gaussian covariance:** this is the contribution to the covariance from the disconnected part of the trispectrum of the different fields involved (also called the "disconnected" covariance). In simpler terms, this is the covariance matrix one would obtain if all fields involved were Gaussianly distributed.

- **Connected non-Gaussian covariance:** this is the contribution from the connected trispectrum (which would vanish if all fields were Gaussianly distributed).

- **Super-sample covariance:** this is the additional coupling between different scales induced by density fluctuations on scales larger than the volume mapped. This term also vanishes for Gaussian fields.

On most scales relevant for cosmological studies, the Gaussian contribution dominates the error budget, although the connected and super-sample terms cannot be neglected [383]. The

Gaussian contribution is trivial to compute for fields observed over the full sky:

$$\mathrm{Cov}\left(C_\ell^{ab}, C_\ell^{cd}\right) = \delta^K_{\ell\ell'}\frac{C_\ell^{ac}C_\ell^{bd} + C_\ell^{ad}C_\ell^{bc}}{2\ell+1}, \tag{8.1}$$

where C_ℓ^{xy} is the angular power spectrum between two maps x and y on multipole ℓ. Unfortunately, the presence of a sky mask in general induces non-trivial couplings between different ℓ's, which must be accurately estimated in order to produce unbiased evaluations of the parameter likelihood [384].

In this Chapter, we will present and generalize methods developed in the context of CMB experiments to account for the impact of survey geometry on the Gaussian part of the power spectrum covariance matrix [342, 385–391][1], and will study in detail the performance of these methods for Large Scale Structure and weak lensing datasets. We have also implemented these approximations in the public code `NaMaster`[2] [35], making the computation of accurate Gaussian covariance matrices significantly simpler for the community.

The Chapter is structured as follows: Section 8.1 presents the methods and approximations used to calculate accurate covariances. In Section 8.2 we test the methods against Gaussian simulations and study their performance as well as their impact on the final cosmological parameter estimation. We then summarize our results and conclude in Section 8.3. Appendix 8.A presents the performance of these methods in the flat-sky approximation, and we provide technical details of the software implementation in Appendix 8.B.

8.1 Analytical Gaussian covariances

8.1.1 Preliminaries

We will deal with spin-0 and spin-2 fields defined on a 2-dimensional space. In two dimensions, spin-s fields in general have two components $\mathbf{a}(\mathbf{x}) = (a_1(\mathbf{x}), a_2(\mathbf{x}))$[3]. Forming a complex number from these components, $a_1 + ia_2$, spin-s fields transform, under a coordinate rotation with angle ψ, as $a_1 + ia_2 \to (a_1 + ia_2)\exp(i\,s\psi)$. Thus, spin-0 fields are invariant under rotations, and are usually expressed as real-valued fields with a single component.

Given a field $\mathbf{a}(\mathbf{x})$, with 1 (spin-0) or 2 components (spin-2), defined on the coordinates $\mathbf{x}$, we define its generalized Fourier coefficients as

$$\mathbf{a}_\mathbf{k} = \sum_\mathbf{x} \Delta^2 x\ \mathsf{E}^\dagger_\mathbf{k}(\mathbf{x})\,\mathbf{a}(\mathbf{x}), \tag{8.2}$$

where the operator $\sum_\mathbf{x} \Delta^2 x$ denotes an integral or sum over all values of the coordinates $\mathbf{x}$, and $\mathsf{E}^\dagger_\mathbf{k}(\mathbf{x})$ are a set of orthogonal functions. We will also assume that the $\mathsf{E}^\dagger_\mathbf{k}(\mathbf{x})$ are a *complete* set of basis functions, in which case:

$$\sum_\mathbf{x} \Delta^2 x\ \mathsf{E}^\dagger_\mathbf{k}(\mathbf{x})\mathsf{E}_\mathbf{l}(\mathbf{x}) = \mathbb{1}\Delta^x(\mathbf{k},\mathbf{l}), \tag{8.3}$$

$$\sum_\mathbf{k} \Delta^2 k\ \mathsf{E}_\mathbf{k}(\mathbf{x})\mathsf{E}^\dagger_\mathbf{k}(\mathbf{y}) = \mathbb{1}\Delta^k(\mathbf{x},\mathbf{y}), \tag{8.4}$$

[1] See also Ref. [392] for a similar application to the problem of 3D power spectrum covariances.

[2] `https://github.com/LSSTDESC/NaMaster`

[3] E.g. for CMB polarization, a spin-2 field, these components are the Stokes parameters (Q, U), while for cosmic shear the two components are usually labeled (γ_1, γ_2).

where $\sum_{\mathbf{k}} \Delta^2 k$ denotes an integral over all possible generalized Fourier coefficients $\mathbf{k}$, and Δ^x and Δ^k are generalized delta functions, defined through their action on functions of $\mathbf{x}$ or $\mathbf{k}$:

$$\sum_{\mathbf{k}} \Delta^2 k \; f(\mathbf{k}) \Delta^x(\mathbf{k}, \mathbf{l}) \equiv f(\mathbf{l}), \tag{8.5}$$

$$\sum_{\mathbf{x}} \Delta^2 x \; f(\mathbf{x}) \Delta^k(\mathbf{x}, \mathbf{y}) \equiv f(\mathbf{y}). \tag{8.6}$$

For a spin-s quantity, $\mathsf{E}_{\mathbf{l}}(\mathbf{x})$ can be written in terms of two spin-raising and spin-lowering operators, $\eth$ and $\bar{\eth}$, and a set of scalar orthogonal functions $q(\mathbf{l}, \mathbf{x})$ as:

$$\mathsf{E}_{\mathbf{l}}(\mathbf{x}) = -\frac{\beta_{\ell,s}}{2} \begin{pmatrix} \eth^s + \bar{\eth}^s & i(\eth^s - \bar{\eth}^s) \\ -i(\eth^s - \bar{\eth}^s) & \eth^s + \bar{\eth}^s \end{pmatrix} q(\mathbf{l}, \mathbf{x}), \tag{8.7}$$

where $\beta_{\ell,s}$ is a normalization factor defined in Table 8.1.

Finally, we will assume that all fields are Gaussian stochastic fields that are additionally statistically isotropic. As a consequence of the latter, different generalized Fourier modes are uncorrelated:

$$\langle \mathbf{a}_{\mathbf{k}} \mathbf{b}_{\mathbf{l}}^\dagger \rangle \equiv \mathsf{C}_\ell^{ab} \, K \, \Delta^x(\mathbf{k}, \mathbf{l}), \tag{8.8}$$

where K is a volume factor (see below) and C_k^{ab} is the power spectrum. Defined this way, the power spectrum is a matrix, with elements

$$\left\langle a_{\mathbf{k}}^\alpha \left(b_{\mathbf{l}}^\beta \right)^* \right\rangle \equiv \left(\mathsf{C}_\ell^{ab} \right)_{\alpha\beta} K \, \Delta^x(\mathbf{k}, \mathbf{l}), \tag{8.9}$$

where a^α is the α-th element of field $\mathbf{a}$. It will often be useful in what follows to think of C_ℓ^{ab} as a 1-dimensional vector that we will denote by $\mathrm{vec}(\mathsf{C}_\ell^{ab})$. To do so, we simply map the two indices (α, β) into a single number A, such that $\mathrm{vec}(\mathsf{C}_\ell^{ab})_A = (\mathsf{C}_\ell^{ab})_{\alpha\beta}$.

All the functions and operators above can be specialized to fields defined on the sphere or the 2D plane (flat sky approximation) as described in Table 8.1.

8.1.2 The pseudo-C_ℓ method

This section provides a very brief introduction to the pseudo-C_ℓ power spectrum estimator. Further details can be found in e.g. [35, 356, 386]. In any practical situation we do not have access to maps of a given field $\mathbf{a}$ over the full sky, but rather to a weighted or masked version of them

$$\tilde{\mathbf{a}}(\mathbf{x}) \equiv w_a(\mathbf{x}) \mathbf{a}(\mathbf{x}), \tag{8.10}$$

where w_a is commonly called the "mask". Due to the convolution theorem, the generalized Fourier coefficients of the masked field will be a convolution of the mask and true field coefficients:

$$\begin{aligned} \tilde{\mathbf{a}}_{\mathbf{l}} &= \sum_{\mathbf{k}} \Delta^2 k \left[\sum_{\mathbf{x}} \Delta^2 x \; w^a(\mathbf{x}) \, \mathsf{E}_{\mathbf{l}}^\dagger(\mathbf{x}) \, \mathsf{E}_{\mathbf{k}}(\mathbf{x}) \right] \mathbf{a}_{\mathbf{k}} \\ &\equiv \sum_{\mathbf{k}} \Delta^2 k \; {}^a\mathsf{M}_{\mathbf{lk}} \, \mathbf{a}_{\mathbf{k}}, \end{aligned} \tag{8.11}$$

where we have defined the mode-coupling coefficients ${}^a\mathsf{M}_{\mathbf{lk}}$ in the second line.

Symbol	Curved sky	Flat sky (continuum $\to$ discretized)
$\mathbf{l}$	(ℓ, m)	(l_x, l_y)
$\sum_{\mathbf{l}} \Delta^2 l$	$\sum_{\ell=0}^{\infty} \sum_{m=-\ell}^{\ell}$	$\int \frac{dl^2}{2\pi} \to \sum_{\mathbf{l}} \frac{2\pi}{L_x L_y}$
$\Delta^x(\mathbf{l}, \mathbf{l}')$	$\delta^K_{\ell\ell'} \delta^K_{mm'}$	$2\pi\, \delta^D(\mathbf{l} - \mathbf{l}') \to \delta^K_{l_x l'_x} \delta^K_{l_y l'_y} \frac{L_x L_y}{(2\pi)^2} 2\pi$
$\mathbf{x}$	$\hat{\boldsymbol{\theta}} \equiv (\theta, \varphi)$	(x, y)
$\sum_{\mathbf{x}} \Delta^2 x$	$\int_0^{\phi} d\phi \int_{-1}^{1} d(\cos\theta)$	$\int \frac{dx^2}{2\pi} \to \sum_{\mathbf{x}} \frac{L_x L_y}{2\pi N_x N_y}$
$\Delta^k(\mathbf{x}, \mathbf{y})$	$\delta^D(\cos\theta - \cos\theta') \delta^D(\varphi - \varphi')$	$2\pi\, \delta^D(\mathbf{x} - \mathbf{y}) \to \delta^K_{xx'} \delta^K_{yy'} \frac{N_x N_y}{L_x L_y} 2\pi$
$q(\mathbf{l}, \mathbf{x})$	$Y_{\ell m}(\hat{\boldsymbol{\theta}})$	$e^{i\mathbf{l}\cdot\mathbf{x}}$
$\eth\, {}_s f$	$-(\sin\theta)^s \left(\partial_\theta + i \frac{\partial_\varphi}{\sin\theta}\right) (\sin\theta)^{-s}\, {}_s f(\hat{\boldsymbol{\theta}})$	$(\partial_x - i\partial_y)\, {}_s f$
$\bar{\eth}\, {}_s f$	$-(\sin\theta)^{-s} \left(\partial_\theta - i \frac{\partial_\varphi}{\sin\theta}\right) (\sin\theta)^{s}\, {}_s f(\hat{\boldsymbol{\theta}})$	$(\partial_x + i\partial_y)\, {}_s f$
$\beta_{\ell,s}$	$\sqrt{\frac{(\ell - s)!}{(\ell + s)!}}$	ℓ^{-s}
K	1	$(2\pi)^{-1}$

Table 8.1: Lookup table describing the generalized notation introduced in Section 8.1.1 for quantities defined on the sphere (second column) and on the flat 2D plane (third column). For the flat-sky case, we also provide expressions for a discretized, finite 2D plane with periodic boundary conditions. In this case, the map has dimensions (L_x, L_y) subdivided into (N_x, N_y) equi-spaced pixels in (x, y). δ^D and δ^K are the Dirac and Kronecker delta functions respectively.

Correlating the generalized Fourier coefficients of two masked fields therefore yields a mode-coupled version of their true underlying power spectrum:

$$\begin{aligned}\left\langle \tilde{\mathbf{a}}_{\mathbf{l}} \tilde{\mathbf{b}}_{\mathbf{l}}^{\dagger} \right\rangle =& \sum_{\mathbf{k}} \Delta^2 k \sum_{\mathbf{q}} \Delta^2 q \; {}^{a}\mathsf{M}_{\mathbf{lk}} \left\langle \mathbf{a}_{\mathbf{k}} \mathbf{b}_{\mathbf{q}}^{\dagger} \right\rangle {}^{b}\mathsf{M}_{\mathbf{lq}}^{\dagger} \\ =& K \sum_{\mathbf{k}} \Delta^2 k \; {}^{a}\mathsf{M}_{\mathbf{lk}} \mathsf{C}_{k}^{ab} \, {}^{b}\mathsf{M}_{\mathbf{lk}}^{\dagger} \end{aligned} \tag{8.12}$$

The pseudo-C_ℓ estimator then proceeds in two steps:

1. We first bin different $\mathbf{l}$ modes into sets of them called bandpowers (typically bands of similar ℓ or annuli of flat-sky Fourier modes spanning a range of radii). Let us denote a given bandpower by its index q. We must note that it is more appropriate to use bandpower-averaged spectra when the underlying spectrum does not vary much within each ℓ bin. When this is not the case, it is often useful to apply ℓ-weights (such as $D_\ell \equiv \ell(\ell+1)C_\ell/(2\pi)$). Let us note that the Large Scale Structure spectra discussed in this work are sufficiently flat that the binning used in the simulations of Section 8.2.1 is appropriate for this formalism. The binned pseudo-power spectrum is:

$$\tilde{\mathsf{C}}_{q}^{ab} = \sum_{\mathbf{l}\in q} B_{q}^{\mathbf{l}} \, \tilde{\mathbf{a}}_{\mathbf{l}} \tilde{\mathbf{b}}_{\mathbf{l}}^{\dagger}, \tag{8.13}$$

   where the bandpower weights are normalized such that $\sum_{\mathbf{l}\in q} B_q^{\mathbf{l}} = (K\Delta^x(\mathbf{0}))^{-1}$.

2. Then, the correlation between bandpowers induced by the mode-coupling coefficients is partially reversed by multiplying $\tilde{\mathsf{C}}_q^{ab}$ by the so-called binned "mode-coupling matrix" $\mathcal{M}$, giving the final estimator

$$\mathrm{vec}\left(\hat{\mathsf{C}}_{q}^{ab}\right) = \sum_{q'} \left(\mathcal{M}^{-1}\right)_{qq'} \mathrm{vec}\left(\tilde{\mathsf{C}}_{q'}^{ab}\right). \tag{8.14}$$

   The main advantage of the pseudo-C_ℓ estimator is that the mode-coupling matrix $\mathcal{M}$ is directly related to the coupling coefficients ${}^{a}\mathsf{M}_{\mathbf{ll}'}$, and can be computed analytically making use of methods that scale like ℓ_{max}^3 (see e.g. [356]).

For completeness, the mode-coupling matrices for flat-sky and curved-sky fields are given by [35]:

- **Curved sky.** After averaging over the harmonic number m, the mode-coupling matrices are:

$$\left\langle \frac{1}{2\ell+1} \sum_{m=-\ell}^{\ell} \mathrm{vec}\left[\tilde{\mathbf{a}}_{\mathbf{l}} \tilde{\mathbf{b}}_{\mathbf{l}}^{\dagger}\right] \right\rangle = \sum_{\ell'} \mathsf{M}_{\ell\ell'}^{s_a s_b} \mathrm{vec}\left[\mathsf{C}_{\ell'}^{ab}\right], \tag{8.15}$$

  with

$$\mathsf{M}_{\ell\ell'}^{00} = (2\ell'+1)\,\Xi_{\ell\ell'}^{00}(w_a, w_b), \quad \mathsf{M}_{\ell\ell'}^{02} = (2\ell'+1)\,\Xi_{\ell\ell'}^{0+}(w_a, w_b)\,\mathbb{1}, \tag{8.16}$$

$$\mathsf{M}_{\ell\ell'}^{22} = (2\ell'+1) \begin{pmatrix} \Xi_{\ell\ell'}^{++} & 0 & 0 & \Xi_{\ell\ell'}^{--} \\ 0 & \Xi_{\ell\ell'}^{++} & -\Xi_{\ell\ell'}^{--} & 0 \\ 0 & -\Xi_{\ell\ell'}^{--} & \Xi_{\ell\ell'}^{++} & 0 \\ \Xi_{\ell\ell'}^{--} & 0 & 0 & \Xi_{\ell\ell'}^{++} \end{pmatrix}, \tag{8.17}$$

where

$$\Xi^{00}_{\ell\ell'}(w,v) \equiv \sum_{\ell''} \frac{P^{wv}_{\ell''}}{4\pi} \begin{pmatrix} \ell & \ell' & \ell'' \\ 0 & 0 & 0 \end{pmatrix}^2 \tag{8.18}$$

$$\Xi^{0+}_{\ell\ell'}(w,v) \equiv \sum_{\ell''} \frac{P^{wv}_{\ell''}}{4\pi} \begin{pmatrix} \ell & \ell' & \ell'' \\ 0 & 0 & 0 \end{pmatrix} \begin{pmatrix} \ell & \ell' & \ell'' \\ 2 & -2 & 0 \end{pmatrix} \tag{8.19}$$

$$\Xi^{\pm\pm}_{\ell\ell'}(w,v) \equiv \sum_{\ell''} \frac{P^{wv}_{\ell''}}{4\pi} \begin{pmatrix} \ell & \ell' & \ell'' \\ 2 & -2 & 0 \end{pmatrix}^2 \frac{1 \pm (-1)^{\ell+\ell'+\ell''}}{2}. \tag{8.20}$$

Here the 2-by-3 matrix-like quantities are the Wigner 3-j symbols, and

$$P^{vw}_{\ell} \equiv \sum_{m=-\ell}^{\ell} v_{\ell m} w^*_{\ell m}. \tag{8.21}$$

- **Flat sky.** In this case the averaging over the Fourier-space azimuth happens while binning into bandpowers, and therefore the unbinned mode-coupling matrix is defined before binning. Assuming flat bandpowers, such that $B^{\mathbf{l}}_q = (2\pi)^2/(L_x L_y N_q)$, where N_q is the number of Fourier-space modes in the q-th bandpower:

$$\left\langle \mathrm{vec}\left[\tilde{\mathsf{C}}^{ab}_q\right]\right\rangle = \sum_{\mathbf{l}\in q} \frac{1}{N_q} \sum_{\mathbf{k}} \mathsf{M}^{s_a s_b}_{\mathbf{lk}}\, \mathrm{vec}\left[\mathsf{C}^{ab}_k\right] \tag{8.22}$$

with

$$\mathsf{M}^{00}_{\mathbf{l}\,\mathbf{k}} \equiv \bar{\Xi}^{00}_{\mathbf{lk}}, \tag{8.23}$$

$$\mathsf{M}^{02}_{\mathbf{l}\,\mathbf{k}} \equiv \begin{pmatrix} \bar{\Xi}^{0+}_{\mathbf{lk}} & -\bar{\Xi}^{0-}_{\mathbf{lk}} \\ \bar{\Xi}^{0-}_{\mathbf{lk}} & \bar{\Xi}^{0+}_{\mathbf{lk}} \end{pmatrix} \tag{8.24}$$

$$\mathsf{M}^{22}_{\mathbf{l}\,\mathbf{k}} \equiv \begin{pmatrix} \bar{\Xi}^{++}_{\mathbf{lk}} & -\bar{\Xi}^{+-}_{\mathbf{lk}} & -\bar{\Xi}^{+-}_{\mathbf{lk}} & \bar{\Xi}^{--}_{\mathbf{lk}} \\ \bar{\Xi}^{+-}_{\mathbf{lk}} & \bar{\Xi}^{++}_{\mathbf{lk}} & -\bar{\Xi}^{--}_{\mathbf{lk}} & -\bar{\Xi}^{+-}_{\mathbf{lk}} \\ \bar{\Xi}^{+-}_{\mathbf{lk}} & -\bar{\Xi}^{--}_{\mathbf{lk}} & \bar{\Xi}^{++}_{\mathbf{lk}} & -\bar{\Xi}^{+-}_{\mathbf{lk}} \\ \bar{\Xi}^{--}_{\mathbf{lk}} & \bar{\Xi}^{+-}_{\mathbf{lk}} & \bar{\Xi}^{+-}_{\mathbf{lk}} & \bar{\Xi}^{++}_{\mathbf{lk}} \end{pmatrix}, \tag{8.25}$$

where

$$\bar{\Xi}^{00}_{\mathbf{lk}} = \left(\frac{2\pi}{L_x L_y}\right)^2 (w_a)_{\mathbf{l}-\mathbf{k}} (w_b)^*_{\mathbf{l}-\mathbf{k}}, \tag{8.26}$$

$$\bar{\Xi}^{0+}_{\mathbf{lk}} = \left(\frac{2\pi}{L_x L_y}\right)^2 (w_a)_{\mathbf{l}-\mathbf{k}} (w_b)^*_{\mathbf{l}-\mathbf{k}} \cos 2\Delta\varphi, \tag{8.27}$$

$$\bar{\Xi}^{0-}_{\mathbf{lk}} = \left(\frac{2\pi}{L_x L_y}\right)^2 (w_a)_{\mathbf{l}-\mathbf{k}} (w_b)^*_{\mathbf{l}-\mathbf{k}} \sin 2\Delta\varphi, \tag{8.28}$$

$$\bar{\Xi}^{++}_{\mathbf{lk}} = \left(\frac{2\pi}{L_x L_y}\right)^2 (w_a)_{\mathbf{l}-\mathbf{k}} (w_b)^*_{\mathbf{l}-\mathbf{k}} \cos^2 2\Delta\varphi, \tag{8.29}$$

$$\bar{\Xi}^{+-}_{\mathbf{lk}} = \left(\frac{2\pi}{L_x L_y}\right)^2 (w_a)_{\mathbf{l}-\mathbf{k}} (w_b)^*_{\mathbf{l}-\mathbf{k}} \cos 2\Delta\varphi\, \sin 2\Delta\varphi, \tag{8.30}$$

$$\bar{\Xi}^{--}_{\mathbf{lk}} = \left(\frac{2\pi}{L_x L_y}\right)^2 (w_a)_{\mathbf{l}-\mathbf{k}} (w_b)^*_{\mathbf{l}-\mathbf{k}} \sin^2 2\Delta\varphi, \tag{8.31}$$

and $\Delta\varphi$ is the relative angle between $\mathbf{l}$ and $\mathbf{k}$.

Before we move on to covariances, it is worth considering the case of unmasked field (i.e $w^a(\mathbf{x}) = 1$ everywhere). In this case ${}^a\mathsf{M}_{\mathbf{ll}'} = \mathbb{1}\Delta^x(\mathbf{l}, \mathbf{l}')$, and therefore different modes are uncorrelated (as should have been obvious). In a non-ideal case where the mask is still sufficiently well behaved (i.e. masks without too much small-scale structure), we can still expect the coupling coefficients ${}^a\mathsf{M}_{\mathbf{ll}'}$ to be sharply peaked around $\mathbf{l} = \mathbf{l}'$.

8.1.3 Covariance matrices

So far we have not assumed anything about the statistics of the fields, other than the fact that they are isotropic (Equation 8.8). This section presents a method to estimate the disconnected part of the power spectrum covariance for the pseudo-C_ℓ estimator.

Let A and F be the vector indices corresponding to the pairs of field indices (α, β) and (ϕ, γ), respectively, and let us start by considering the covariance

$$\Sigma^{AF}_{\mathbf{ll}'} \equiv \left\langle \tilde{a}^\alpha_{\mathbf{l}} \tilde{b}^{\beta *}_{\mathbf{l}} \tilde{f}^\phi_{\mathbf{l}'} \tilde{g}^{\gamma *}_{\mathbf{l}'} \right\rangle - \left\langle \tilde{a}^\alpha_{\mathbf{l}} \tilde{b}^{\beta *}_{\mathbf{l}} \right\rangle \left\langle \tilde{f}^\phi_{\mathbf{l}'} \tilde{g}^{\gamma *}_{\mathbf{l}'} \right\rangle \tag{8.32}$$

The covariance of the binned bandpowers $\tilde{\mathsf{C}}$ can then be computed as

$$\mathrm{Cov}\left(\mathrm{vec}\left(\tilde{\mathsf{C}}^{ab}_q\right)_A, \mathrm{vec}\left(\tilde{\mathsf{C}}^{fg}_{q'}\right)_F\right) = \sum_{\mathbf{l}\in q} B^{\mathbf{l}}_q \sum_{\mathbf{l}'\in q'} B^{\mathbf{l}'}_{q'} \Sigma^{AF}_{\mathbf{ll}'}. \tag{8.33}$$

which can then be used to estimate the covariance of the mode-decoupled bandpowers multiplying it by the inverse mode-coupling matrix twice. I.e., schematically:

$$\mathrm{Cov}\left(\hat{\mathsf{C}}\right) = \mathcal{M}^{-1} \cdot \mathrm{Cov}\left(\tilde{C}\right) \cdot \left(\mathcal{M}^{-1}\right)^T, \tag{8.34}$$

where we have suppressed all indices for simplicity. The problem of estimating the pseudo-C_ℓ covariance therefore reduces to estimating $\Sigma^{AC}_{\mathbf{ll}'}$.

We now make use of Wick's theorem, which states that, for Gaussian fields, $\langle a\, b\, f\, g\rangle = \langle a\, b\rangle\langle f\, g\rangle + \langle a\, f\rangle\langle b\, g\rangle + \langle a\, g\rangle\langle b\, f\rangle$. In this case, the expression for $\Sigma^{AF}_{\mathbf{ll}'}$ reads:

$$\begin{aligned}\Sigma^{AF}_{\mathbf{ll}'} = &\left[K \sum_{\mathbf{k}} \Delta^2 k\ {}^a M^{\alpha\alpha'}_{\mathbf{lk}}\ {}^g M^{\gamma\gamma'*}_{\mathbf{l}'\mathbf{k}} C^{ag,(\alpha'\gamma')}_k\right]\left[K \sum_{\mathbf{q}} \Delta^2 q\ {}^b M^{\beta\beta'*}_{\mathbf{lq}}\ {}^f M^{\phi\phi'}_{\mathbf{l}'\mathbf{q}} C^{bf,(\beta'\phi')}_q\right]^* \\ &+ \left((g,\gamma) \leftrightarrow (f,\phi)\right),\end{aligned} \tag{8.35}$$

where we implicitly sum over repeated indices (e.g. α'), and the second term is equivalent to the first one after swapping the roles of fields $\mathbf{f}$ and $\mathbf{g}$. Without any further approximations, for each pair $(\mathbf{l}, \mathbf{l}')$, we would need to perform two 2-dimensional integrals, and therefore the calculation would scale like ℓ^6_{max}, quickly becoming unfeasible.

Under the assumption that the coupling coefficients $M_{\mathbf{lk}}$ are sharply peaked around $\mathbf{l} = \mathbf{k}$, we can simplify the expression above approximating the power spectra as constants within the support of the coupling coefficients [385]. Explicitly, we approximate

$$C^{ag,(\alpha'\gamma')}_k C^{bf,(\beta',\phi')}_q \simeq C^{ag,(\alpha'\gamma')}_{(\ell} C^{bf,(\beta',\phi')}_{\ell')} \equiv \frac{1}{2}\left(C^{ag,(\alpha'\gamma')}_\ell C^{bf,(\beta',\phi')}_{\ell'} + C^{ag,(\alpha'\gamma')}_{\ell'} C^{bf,(\beta',\phi')}_\ell\right).$$

In this case, the expression for $\Sigma^{AF}_{\mathbf{ll}'}$ simplifies to

$$\Sigma^{AF}_{\mathbf{ll}'} = K^2 C^{ag,(\alpha'\gamma')}_{(\ell} C^{bf,(\beta',\phi')}_{\ell')}\ {}^{ag}W^{\alpha\gamma,\alpha'\gamma'}_{\mathbf{ll}'}\left({}^{bf}W^{\beta\phi,\beta'\phi'}_{\mathbf{ll}'}\right)^* + \left((g,\gamma) \leftrightarrow (f,\phi)\right), \tag{8.36}$$

where we have defined the covariance coupling coefficients

$$ {}^{ab}W^{\alpha\beta,\alpha'\beta'}_{\mathbf{ll'}} = \sum_{\mathbf{k}} \Delta^2 k \; {}^{a}M^{\alpha\alpha'}_{\mathbf{lk}} \left({}^{b}M^{\beta\beta'}_{\mathbf{l'k}} \right)^* . \tag{8.37} $$

In order to compute these coefficients, let us start by defining the quantities

$$ {}^{ab}I^{\pm s_a,\pm s_b}_{\mathbf{ll'}} \equiv \sum_{\mathbf{k}} \Delta^2 k \sum_{\mathbf{x}} \Delta^2 x \sum_{\mathbf{y}} \Delta^2 y \, w_a(\mathbf{x}) w_b(\mathbf{y}) \, q^{\pm s_a}_{\mathbf{lk}}(\mathbf{x}) \, \left[q^{\pm s_b}_{\mathbf{l'k}}(\mathbf{y}) \right]^* , \tag{8.38} $$

where s_a is the spin of field $\mathbf{a}$, and

$$ q^{\pm s}_{\mathbf{lk}}(\mathbf{x}) \equiv \frac{\beta_{\ell,s}\beta_{k,s}}{2} \left(\left[\eth^s q(\mathbf{l},\mathbf{x}) \right]^* \eth^s q(\mathbf{k},\mathbf{x}) \pm \left[\bar{\eth}^s q(\mathbf{l},\mathbf{x}) \right]^* \bar{\eth}^s q(\mathbf{k},\mathbf{x}) \right) . \tag{8.39} $$

Now, in what follows, we will be concerned with the auto- and cross-correlations of spin-0 and spin-2 fields. Thus, to simplify the notation, we will enumerate the different types of coupling coefficients that exist for a spin-0 field with a single component that we will call δ, in analogy to the projected galaxy overensity, and for a spin-2 field, $\boldsymbol{\gamma}$, with E and B components, γ_E and γ_B, in analogy to the cosmic shear field. With this setup, all the possible non-zero $W^{\alpha\beta,\alpha'\beta'}_{\mathbf{ll'}}$ can be expressed in terms of the $I^{\pm s_a,\pm s_b}_{\mathbf{ll'}}$ as follows:

$$ W^{\delta\delta,\delta\delta}_{\mathbf{l,l'}} = I^{0,0}_{\mathbf{ll'}}; \tag{8.40} $$

$$ W^{\delta\gamma_E,\delta\gamma_E}_{\mathbf{l,l'}} = W^{\delta\gamma_B,\delta\gamma_B}_{\mathbf{l,l'}} = I^{0,+2}_{\mathbf{l,l'}}; \quad W^{\delta\gamma_E,\delta\gamma_B}_{\mathbf{l,l'}} = -W^{\delta\gamma_B,\delta\gamma_E}_{\mathbf{l,l'}} = -i\, I^{0,-2}_{\mathbf{l,l'}}; \tag{8.41} $$

$$ W^{\gamma_E\gamma_E,\gamma_E\gamma_E}_{\mathbf{l,l'}} = W^{\gamma_E\gamma_B,\gamma_E\gamma_B}_{\mathbf{l,l'}} = W^{\gamma_B\gamma_E,\gamma_B\gamma_E}_{\mathbf{l,l'}} = W^{\gamma_B\gamma_B,\gamma_B\gamma_B}_{\mathbf{l,l'}} = I^{+2,+2}_{\mathbf{ll'}} \tag{8.42} $$

$$ W^{\gamma_E\gamma_E,\gamma_B\gamma_B}_{\mathbf{l,l'}} = W^{\gamma_B\gamma_B,\gamma_E\gamma_E}_{\mathbf{l,l'}} = -W^{\gamma_B\gamma_E,\gamma_E\gamma_B}_{\mathbf{l,l'}} = -W^{\gamma_E\gamma_B,\gamma_B\gamma_E}_{\mathbf{l,l'}} = I^{-2,-2}_{\mathbf{ll'}} \tag{8.43} $$

$$ W^{\gamma_E\gamma_E,\gamma_E\gamma_B}_{\mathbf{l,l'}} = -W^{\gamma_E\gamma_B,\gamma_E\gamma_E}_{\mathbf{l,l'}} = W^{\gamma_B\gamma_E,\gamma_B\gamma_B}_{\mathbf{l,l'}} = -W^{\gamma_B\gamma_B,\gamma_B\gamma_E}_{\mathbf{l,l'}} = -i\, I^{+2,-2}_{\mathbf{ll'}} \tag{8.44} $$

$$ W^{\gamma_E\gamma_E,\gamma_B\gamma_E}_{\mathbf{l,l'}} = W^{\gamma_E\gamma_B,\gamma_B\gamma_B}_{\mathbf{l,l'}} = -W^{\gamma_B\gamma_E,\gamma_E\gamma_E}_{\mathbf{l,l'}} = -W^{\gamma_B\gamma_B,\gamma_E\gamma_B}_{\mathbf{l,l'}} = i\, I^{-2,+2}_{\mathbf{ll'}}. \tag{8.45} $$

Thus, in principle, we only need to compute 7 different types of terms ($I^{0,0}$, $I^{0,\pm2}$, $I^{\pm2,\pm2}$ and $I^{\pm2,\mp2}$)). In order to simplify these expressions further, we follow [388, 390] and neglect all gradients of the masks[4], which allows us to relate the different $I^{\pm s_a,\pm s_b}$ through the following set of identities:

$$ \begin{aligned} \sum_{\mathbf{x}} \Delta^2 x \, w(\mathbf{x}) \left(\bar{\eth}^2 q(\mathbf{l},\mathbf{x}) \right)^* \bar{\eth}^2 q(\mathbf{k},\mathbf{x}) &= \sum_{\mathbf{x}} \Delta^2 x \, w(\mathbf{x}) \eth^2 q^*(\mathbf{l},\mathbf{x}) \, \bar{\eth}^2 q(\mathbf{k},\mathbf{x}) \\ &= \sum_{\mathbf{x}} \Delta^2 x \, q^*(\mathbf{l},\mathbf{x}) \, \eth^2 \left(\bar{\eth}^2 q(\mathbf{k},\mathbf{x}) w(\mathbf{x}) \right) \\ &\simeq \sum_{\mathbf{x}} \Delta^2 x \, q^*(\mathbf{l},\mathbf{x}) \, \left(\eth^2 \bar{\eth}^2 q(\mathbf{k},\mathbf{x}) \right) w(\mathbf{x}) \\ &= \frac{1}{\beta^2_{k,2}} \sum_{\mathbf{x}} \Delta^2 x \, q^*(\mathbf{l},\mathbf{x}) \, q(\mathbf{k},\mathbf{x}) w(\mathbf{x}) \qquad (8.46) \\ &= \sum_{\mathbf{x}} \Delta^2 x \, q^*(\mathbf{l},\mathbf{x}) \, \left(\bar{\eth}^2 \eth^2 q(\mathbf{k},\mathbf{x}) \right) w(\mathbf{x}) \\ &= \sum_{\mathbf{x}} \Delta^2 x \, \bar{\eth}^2 \left(w(\mathbf{x}) \, q^*(\mathbf{l},\mathbf{x}) \right) \eth^2 q(\mathbf{k},\mathbf{x}) \\ &\simeq \sum_{\mathbf{x}} \Delta^2 x \, w(\mathbf{x}) \, \left(\eth^2 \, q(\mathbf{l},\mathbf{x}) \right)^* \eth^2 q(\mathbf{k},\mathbf{x}), \qquad (8.47) \end{aligned} $$

[4]It is worth noting that it is possible in principle to avoid this approximation, as demonstrated in Ref. [387].

where we have made repeated use of integration by parts.

Using these identities together with the completeness relation of the basis functions, it is possible to simplify the expressions for the $I^{\pm s_a,\pm s_b}$:

$$ {}^{ab}I^{0,0}_{\mathbf{ll}'} = {}^{ab}I^{0,+2}_{\mathbf{ll}'} = {}^{ab}J^{0}_{\mathbf{ll}'}; \quad {}^{ab}I^{+2,+2}_{\mathbf{ll}'} = {}^{ab}J^{+}_{\mathbf{ll}'}; \tag{8.48} $$

$$ {}^{ab}I^{+2,-2}_{\mathbf{ll}'} = {}^{ab}I^{-2,+2}_{\mathbf{ll}'} = {}^{ab}J^{-}_{\mathbf{ll}'}; \quad {}^{ab}I^{0,-2}_{\mathbf{ll}'} = {}^{ab}I^{-2,-2}_{\mathbf{ll}'} = 0, \tag{8.49} $$

where we have defined

$$ {}^{ab}J^{0}_{\mathbf{ll}'} = \sum_{\mathbf{x}} \Delta^2 x \; (w_a w_b)\,(\mathbf{x})\, q(\mathbf{l},\mathbf{x}) \; \left[q(\mathbf{l}',\mathbf{x})\right]^*, \tag{8.50} $$

$$ {}^{ab}J^{\pm}_{\mathbf{ll}'} = \sum_{\mathbf{x}} \Delta^2 x \; (w_a w_b)\,(\mathbf{x})\, q^{\pm 2}_{\mathbf{ll}'}(\mathbf{x}). \tag{8.51} $$

Thus, the only surviving non-zero coupling coefficients are

$$ W^{\delta\delta,\delta\delta}_{\mathbf{l},\mathbf{l}'} = W^{\delta\gamma_E,\delta\gamma_E}_{\mathbf{l},\mathbf{l}'} = W^{\delta\gamma_B,\delta\gamma_B}_{\mathbf{l},\mathbf{l}'} = J^{0}_{\mathbf{ll}'}; \tag{8.52} $$

$$ W^{\gamma_E\gamma_E,\gamma_E\gamma_E}_{\mathbf{l},\mathbf{l}'} = W^{\gamma_E\gamma_B,\gamma_E\gamma_B}_{\mathbf{l},\mathbf{l}'} = W^{\gamma_B\gamma_E,\gamma_B\gamma_E}_{\mathbf{l},\mathbf{l}'} = W^{\gamma_B\gamma_B,\gamma_B\gamma_B}_{\mathbf{l},\mathbf{l}'} = J^{+}_{\mathbf{ll}'} \tag{8.53} $$

$$ \begin{aligned} W^{\gamma_E\gamma_E,\gamma_E\gamma_B}_{\mathbf{l},\mathbf{l}'} &= -W^{\gamma_E\gamma_B,\gamma_E\gamma_E}_{\mathbf{l},\mathbf{l}'} = W^{\gamma_B\gamma_E,\gamma_B\gamma_B}_{\mathbf{l},\mathbf{l}'} = -W^{\gamma_B\gamma_B,\gamma_B\gamma_E}_{\mathbf{l},\mathbf{l}'} = \\ &= -W^{\gamma_E\gamma_E,\gamma_B\gamma_E}_{\mathbf{l},\mathbf{l}'} = -W^{\gamma_E\gamma_B,\gamma_B\gamma_B}_{\mathbf{l},\mathbf{l}'} = W^{\gamma_B\gamma_E,\gamma_E\gamma_E}_{\mathbf{l},\mathbf{l}'} = W^{\gamma_B\gamma_B,\gamma_E\gamma_B}_{\mathbf{l},\mathbf{l}'} = -i\, J^{-}_{\mathbf{ll}'}. \end{aligned} \tag{8.54} $$

We have reduced the problem of computing the covariance in Equation 8.35 to the problem of computing the coupling coefficients 8.37 entering Equation 8.36, and we have now shown that there are only 3 independent coefficients, given by Equation 8.50. In order to simplify the calculation further, it is now useful to inspect these results for the specific case of fields defined on the sphere.

Covariances for curved skies

As described in Section 8.1.2, in the curved-sky estimator it is common to first average over the harmonic number m as part of the bandpower binning operation. Let us, therefore, define

$$ \tilde{C}^{a_\alpha b_\beta}_{\ell} = \frac{1}{2\ell+1} \sum_{m=-\ell}^{\ell} (\tilde{a}_\alpha)_{\ell m} (\tilde{b}_\beta)^*_{\ell m}. \tag{8.55} $$

The covariance of these objects, under the approximation in Equation 8.36, can be computed as:

$$ \mathrm{Cov}\left(\tilde{C}^{a_\alpha b_\beta}_{\ell}, \tilde{C}^{f_\phi g_\gamma}_{\ell'}\right) = C^{a_{\alpha'} f_{\phi'}}_{(\ell} C^{b_{\beta'} g_{\gamma'}}_{\ell')} \, {}^{af}_{bg}\mathcal{W}^{\alpha\phi,\alpha'\phi'}_{\beta\gamma,\beta'\gamma'}(\ell,\ell') + ((g,\gamma) \leftrightarrow (f,\phi))\,, \tag{8.56} $$

where we have defined the symbols

$$ {}^{af}_{bg}\mathcal{W}^{\alpha\phi,\alpha'\phi'}_{\beta\gamma,\beta'\gamma'}(\ell,\ell') \equiv \sum_{m=-\ell}^{\ell} \sum_{m'=-\ell'}^{\ell'} \frac{{}^{af}W^{\alpha\phi,\alpha'\phi'}_{\mathbf{ll}'} \left({}^{bg}W^{\beta\gamma,\beta'\gamma'}_{\mathbf{ll}'}\right)^*}{(2\ell+1)(2\ell'+1)}. \tag{8.57} $$

These quantities involve terms of the form:

$$ {}^{af}_{bg}\mathcal{J}^{XY}_{\ell\ell'} \equiv \sum_{m=-\ell}^{\ell} \sum_{m'=-\ell'}^{\ell'} \frac{{}^{af}J^{X}_{\mathbf{ll}'} \left({}^{bg}J^{Y}_{\mathbf{ll}'}\right)^*}{(2\ell+1)(2\ell'+1)} \tag{8.58} $$

Making use of the completeness relation for the Wigner 3-j symbols, it is possible to show, that these can be written as:

$$ {}^{af}_{bg}\mathcal{J}^{00}_{\ell\ell'} = \Xi^{00}_{\ell\ell'}(w_a w_f, w_b w_g), \quad {}^{af}_{bg}\mathcal{J}^{0+}_{\ell\ell'} = \Xi^{0+}_{\ell\ell'}(w_a w_f, w_b w_g), \tag{8.59} $$

$$ {}^{af}_{bg}\mathcal{J}^{++}_{\ell\ell'} = \Xi^{++}_{\ell\ell'}(w_a w_f, w_b w_g), \quad {}^{af}_{bg}\mathcal{J}^{--}_{\ell\ell'} = \Xi^{--}_{\ell\ell'}(w_a w_f, w_b w_g), \tag{8.60} $$

$$ {}^{af}_{bg}\mathcal{J}^{+-}_{\ell\ell'} = {}^{af}_{bg}\mathcal{J}^{-+}_{\ell\ell'} = {}^{af}_{bg}\mathcal{J}^{0-}_{\ell\ell'} = 0, \tag{8.61} $$

where the $\Xi^{XY}_{\ell\ell'}$ are defined in Equation 8.18. Thus, computationally speaking, the problem of computing covariance matrices reduces to that of computing the same coupling coefficients needed for the computation of the pseudo-C_ℓ power spectra themselves, except now they involve product of two masks, rather than the masks alone. Using the same notation as in Equation 8.40, the only non-zero $\mathcal{W}$ coefficients are:

$$ \mathcal{W}^{\delta\delta,\delta\delta}_{\delta\delta,\delta\delta} = \mathcal{W}^{\delta\delta,\delta\delta}_{\delta\gamma_X,\delta\gamma_X} = \mathcal{W}^{\delta\gamma_X,\delta\gamma_X}_{\delta\gamma_Y,\delta\gamma_Y} = \mathcal{J}^{00} \tag{8.62} $$

$$ \mathcal{W}^{\delta\delta,\delta\delta}_{\gamma_X\gamma_Y,\gamma_X\gamma_Y} = \mathcal{W}^{\delta\gamma_Z,\delta\gamma_Z}_{\gamma_X\gamma_Y,\gamma_X\gamma_Y} = \mathcal{J}^{0+} \tag{8.63} $$

$$ \mathcal{W}^{\gamma_X\gamma_Y,\gamma_X\gamma_Y}_{\gamma_W\gamma_Z,\gamma_W\gamma_Z} = \mathcal{J}^{++} \tag{8.64} $$

$$ \begin{aligned} &\mathcal{W}^{\gamma_X\gamma_E,\gamma_X\gamma_B}_{\gamma_Y\gamma_E,\gamma_Y\gamma_B} = \mathcal{W}^{\gamma_X\gamma_E,\gamma_X\gamma_B}_{\gamma_B\gamma_Y,\gamma_E\gamma_Y} = \mathcal{W}^{\gamma_B\gamma_X,\gamma_E\gamma_X}_{\gamma_B\gamma_Y,\gamma_E\gamma_Y} = \\ &\quad \mathcal{W}^{\gamma_X\gamma_B,\gamma_X\gamma_E}_{\gamma_Y\gamma_B,\gamma_Y\gamma_E} = \mathcal{W}^{\gamma_X\gamma_B,\gamma_X\gamma_E}_{\gamma_E\gamma_Y,\gamma_B\gamma_Y} = \mathcal{W}^{\gamma_E\gamma_X,\gamma_B\gamma_X}_{\gamma_E\gamma_Y,\gamma_B\gamma_Y} = -\mathcal{J}^{--} \end{aligned} \tag{8.65} $$

$$ \begin{aligned} &\mathcal{W}^{\gamma_X\gamma_B,\gamma_X\gamma_E}_{\gamma_Y\gamma_E,\gamma_Y\gamma_B} = \mathcal{W}^{\gamma_X\gamma_B,\gamma_X\gamma_E}_{\gamma_B\gamma_Y,\gamma_E\gamma_Y} = \mathcal{W}^{\gamma_E\gamma_X,\gamma_B\gamma_X}_{\gamma_B\gamma_Y,\gamma_E\gamma_Y} = \\ &\quad \mathcal{W}^{\gamma_X\gamma_E,\gamma_X\gamma_B}_{\gamma_Y\gamma_B,\gamma_Y\gamma_E} = \mathcal{W}^{\gamma_X\gamma_E,\gamma_X\gamma_B}_{\gamma_E\gamma_Y,\gamma_B\gamma_Y} = \mathcal{W}^{\gamma_B\gamma_X,\gamma_E\gamma_X}_{\gamma_E\gamma_Y,\gamma_B\gamma_Y} = \mathcal{J}^{--}, \end{aligned} \tag{8.66} $$

where (X, Y, Z, W) stand for either E or B, and where we have suppressed all redundant indices (including $\ell\ell'$). Any pseudo-C_ℓ covariance element can then be found by replacing these results in Equation 8.56. Some explicit examples for common terms can be found in Appendix A.3.3 of Ref. [390].

Covariances for flat skies

Similar results hold in the case of flat skies. As mentioned in Section 8.1.2, in this case averaging over the Fourier-space azimuth happens while binning into bandpowers. Under the assumption that the underlying power spectra are roughly constant within each bandpower, in this case, the covariance matrix of the bandpowers defined in Equation 8.13 takes the form:

$$ \mathrm{Cov}\left(\tilde{C}_q^{a_\alpha b_\beta}, \tilde{C}_{q'}^{f_\phi g_\gamma}\right) = C_{(q}^{a_{\alpha'} f_{\phi'}} C_{q')}^{b_{\beta'} g_{\gamma'}} \sum_{\mathbf{l}\in q} \frac{1}{N_q} \sum_{\mathbf{l}'\in q'} \frac{1}{N_{q'}} \, {}^{af}_{bg}\bar{\mathcal{W}}^{\alpha\phi,\alpha'\phi'}_{\beta\gamma,\beta'\gamma'}(\mathbf{l},\mathbf{l}') + ((g,\gamma) \leftrightarrow (f,\phi)) \,, \tag{8.67} $$

where the coefficients $\bar{\mathcal{W}}$ are related to the mode-coupling coefficients $\bar{\Xi}$ defined in Equation 8.26, in the same way that the curved-sky coefficients $\mathcal{W}$ were related to the Ξ:

$$ \bar{\mathcal{W}}^{\delta\delta,\delta\delta}_{\delta\delta,\delta\delta} = \bar{\mathcal{W}}^{\delta\delta,\delta\delta}_{\delta\gamma_X,\delta\gamma_X} = \bar{\mathcal{W}}^{\delta\gamma_X,\delta\gamma_X}_{\delta\gamma_Y,\delta\gamma_Y} = \bar{\mathcal{J}}^{00} \tag{8.68} $$

$$ \bar{\mathcal{W}}^{\delta\delta,\delta\delta}_{\gamma_X\gamma_Y,\gamma_X\gamma_Y} = \bar{\mathcal{W}}^{\delta\gamma_Z,\delta\gamma_Z}_{\gamma_X\gamma_Y,\gamma_X\gamma_Y} = \bar{\mathcal{J}}^{0+} \tag{8.69} $$

$$ \bar{\mathcal{W}}^{\gamma_X\gamma_Y,\gamma_X\gamma_Y}_{\gamma_W\gamma_Z,\gamma_W\gamma_Z} = \bar{\mathcal{J}}^{++} \tag{8.70} $$

$$ \begin{aligned} &\bar{\mathcal{W}}^{\gamma_X\gamma_E,\gamma_X\gamma_B}_{\gamma_Y\gamma_E,\gamma_Y\gamma_B} = \bar{\mathcal{W}}^{\gamma_X\gamma_E,\gamma_X\gamma_B}_{\gamma_B\gamma_Y,\gamma_E\gamma_Y} = \bar{\mathcal{W}}^{\gamma_B\gamma_X,\gamma_E\gamma_X}_{\gamma_B\gamma_Y,\gamma_E\gamma_Y} = \\ &\quad \bar{\mathcal{W}}^{\gamma_X\gamma_B,\gamma_X\gamma_E}_{\gamma_Y\gamma_B,\gamma_Y\gamma_E} = \bar{\mathcal{W}}^{\gamma_X\gamma_B,\gamma_X\gamma_E}_{\gamma_E\gamma_Y,\gamma_B\gamma_Y} = \bar{\mathcal{W}}^{\gamma_E\gamma_X,\gamma_B\gamma_X}_{\gamma_E\gamma_Y,\gamma_B\gamma_Y} = -\bar{\mathcal{J}}^{--} \end{aligned} \tag{8.71} $$

$$ \begin{aligned} &\bar{\mathcal{W}}^{\gamma_X\gamma_B,\gamma_X\gamma_E}_{\gamma_Y\gamma_E,\gamma_Y\gamma_B} = \bar{\mathcal{W}}^{\gamma_X\gamma_B,\gamma_X\gamma_E}_{\gamma_B\gamma_Y,\gamma_E\gamma_Y} = \bar{\mathcal{W}}^{\gamma_E\gamma_X,\gamma_B\gamma_X}_{\gamma_B\gamma_Y,\gamma_E\gamma_Y} = \\ &\quad \bar{\mathcal{W}}^{\gamma_X\gamma_E,\gamma_X\gamma_B}_{\gamma_Y\gamma_B,\gamma_Y\gamma_E} = \bar{\mathcal{W}}^{\gamma_X\gamma_E,\gamma_X\gamma_B}_{\gamma_E\gamma_Y,\gamma_B\gamma_Y} = \bar{\mathcal{W}}^{\gamma_B\gamma_X,\gamma_E\gamma_X}_{\gamma_E\gamma_Y,\gamma_B\gamma_Y} = \bar{\mathcal{J}}^{--}, \end{aligned} \tag{8.72} $$

and, as before,

$$ {}^{af}_{bg}\bar{\mathcal{J}}^{00}_{\ell\ell'} = \bar{\Xi}^{00}_{\ell\ell'}(w_a w_f, w_b w_g), \quad {}^{af}_{bg}\bar{\mathcal{J}}^{0+}_{\ell\ell'} = \bar{\Xi}^{0+}_{\ell\ell'}(w_a w_f, w_b w_g), \tag{8.73} $$

$$ {}^{af}_{bg}\bar{\mathcal{J}}^{++}_{\ell\ell'} = \bar{\Xi}^{++}_{\ell\ell'}(w_a w_f, w_b w_g), \quad {}^{af}_{bg}\bar{\mathcal{J}}^{--}_{\ell\ell'} = \bar{\Xi}^{--}_{\ell\ell'}(w_a w_f, w_b w_g), \tag{8.74} $$

$$ {}^{af}_{bg}\bar{\mathcal{J}}^{+-}_{\ell\ell'} = {}^{af}_{bg}\bar{\mathcal{J}}^{-+}_{\ell\ell'} = {}^{af}_{bg}\bar{\mathcal{J}}^{0-}_{\ell\ell'} = 0. \tag{8.75} $$

8.1.4 Approximate covariances

When presenting our results in Section 8.2, we will compare the true covariance matrix, estimated from a large number of Gaussian simulations, with the analytical covariance estimated under different approximations. In descending order of complexity, these are:

1. The narrow-kernel approximation (labeled **NKA** here), described in the previous sections. This approximation assumes that the support of the harmonic-space masks (represented by the mode-coupling coefficients in e.g. Equation 8.15) is small compared to the variation of the true power spectrum with ℓ. Additionally, it neglects all derivatives of the sky mask when accounting for the spin nature of the fields involved.

2. The **spin-0** approximation corresponds to a simplified version of the NKA in which the spin nature of all fields involved is completely ignored, and all fields, including the E- and B-mode components of a spin-2 field, are treated as spin-0 quantities.

3. The mode-counting approximation (labeled **MC** here), commonly known as the *Knox formula* [393], which applies the result found for full-sky observations (Equation 8.1) to masked fields, corrected by an overall factor that accounts to the loss of modes due to the sky mask. In this case, the covariance is simply given by:

$$ \mathrm{Cov}\left(C_q^{ab}, C_{q'}^{cd}\right) = \delta^K_{qq'} \frac{C_q^{ad}C_q^{bc} + C_q^{ac}C_q^{bd}}{(2\ell_q+1)\, f_{\rm sky}\, N_q}, \tag{8.76} $$

   where ℓ_q is the mean multipole in the q-th bandpower, N_q is the number of multipoles assigned to it, and $f_{\rm sky}$ is the available sky fraction.

8.2 Results

8.2.1 Simulations

In order to quantitatively study the performance of the analytical approximations for the power spectrum covariance matrix introduced in Section 8.1, we generate a large number of Gaussian simulations including a number of realistic observational effects.

Each simulation is a set of maps corresponding to a number of spin-0 and spin-2 fields that are drawn as Gaussian random fields following a set of input power spectra that include all relevant cross-correlations between different fields. We generate simulations for two types of fields modeled after the two main Large Scale Structure observables of photometric redshift surveys:

- Spin-0 fields, corresponding to maps of the overdensity of galaxies within a given redshift bin projected on the sphere. In keeping with the notation introduced in Section 8.1.3, we will label these fields as δ^a, where the index a denotes the redshift bin.

- Spin-2 fields, corresponding to maps of the cosmic shear measured from the projected shapes of galaxies in a given redshift bin. We will label these fields $\boldsymbol{\gamma}^a = (\gamma^a_E, \gamma^a_B)$ where, again, the index a denotes the redshift bin.

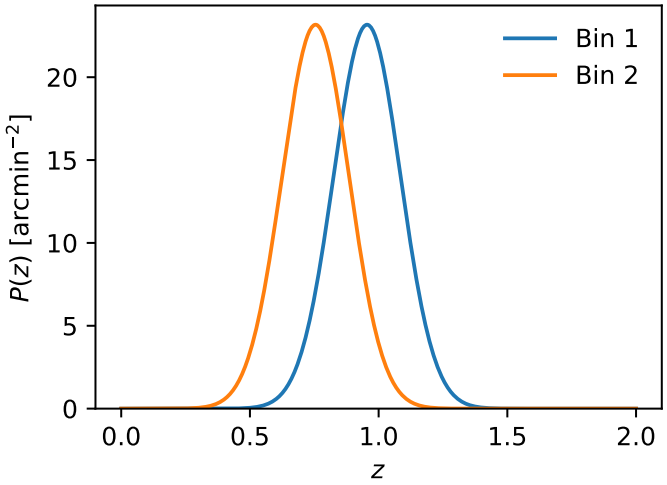

Figure 8.1: Redshift distributions assumed for the Gaussian simulations used in this analysis.

The cross-correlation between two of these fields can be written as:

$$C_\ell^{ab} = S_\ell^{ab} + N_\ell^{ab}, \tag{8.77}$$

where S and N are the power spectra of the cosmological signal and noise respectively. We model the signal part for δ and γ_E as:

$$S_\ell^{ab} = \int d\chi \frac{W_\ell^a(\chi)\, W_\ell^b(\chi)}{\chi^2}\, P\left(k = \frac{\ell + 1/2}{\chi}, z\right), \tag{8.78}$$

where χ is the comoving radial distance, $z \equiv z(\chi)$ is the corresponding redshift in the lightcone, $P(k, z)$ is the matter power spectrum. The window functions are given by [394][5]:

$$\begin{aligned} W_\ell^\delta(\chi) &= b(z)\, H(z)\, p_z(z), \\ W_\ell^\gamma(\chi) &= f_\ell \frac{3H_0^2\Omega_\mathrm{m}}{2}(1+z)\chi \int dz'\, p_z(z')\, \frac{\chi(z') - \chi}{\chi(z')}, \end{aligned} \tag{8.79}$$

where $H(z)$ is the expansion rate in units where the speed of light is $c = 1$, $H_0 \equiv H(z = 0)$, $b(z)$ is the linear galaxy bias, p_z is the normalized redshift distribution of galaxies within the redshift bin, and

$$f_\ell \equiv \frac{\sqrt{(\ell+2)(\ell+1)\ell(\ell-1)}}{(\ell+1/2)^2}. \tag{8.80}$$

We assume zero signal for the shear B-modes.

The noise power spectrum is diagonal (i.e. zero between different fields and redshift bins), and is given by:

$$N_\ell^{\delta\delta} = \frac{1}{n_\Omega}, \quad N_\ell^{\gamma_E\gamma_E} = N_\ell^{\gamma_B\gamma_B} = \frac{\sigma_\gamma^2}{n_\Omega}, \tag{8.81}$$

where n_Ω is the mean number density of galaxies in units of sterad^{-2} (see below), and $\sigma_\gamma = 0.28$ is the intrinsic shape scatter per ellipticity component.

[5]See Ref. [33] and references therein for details about these calculations.

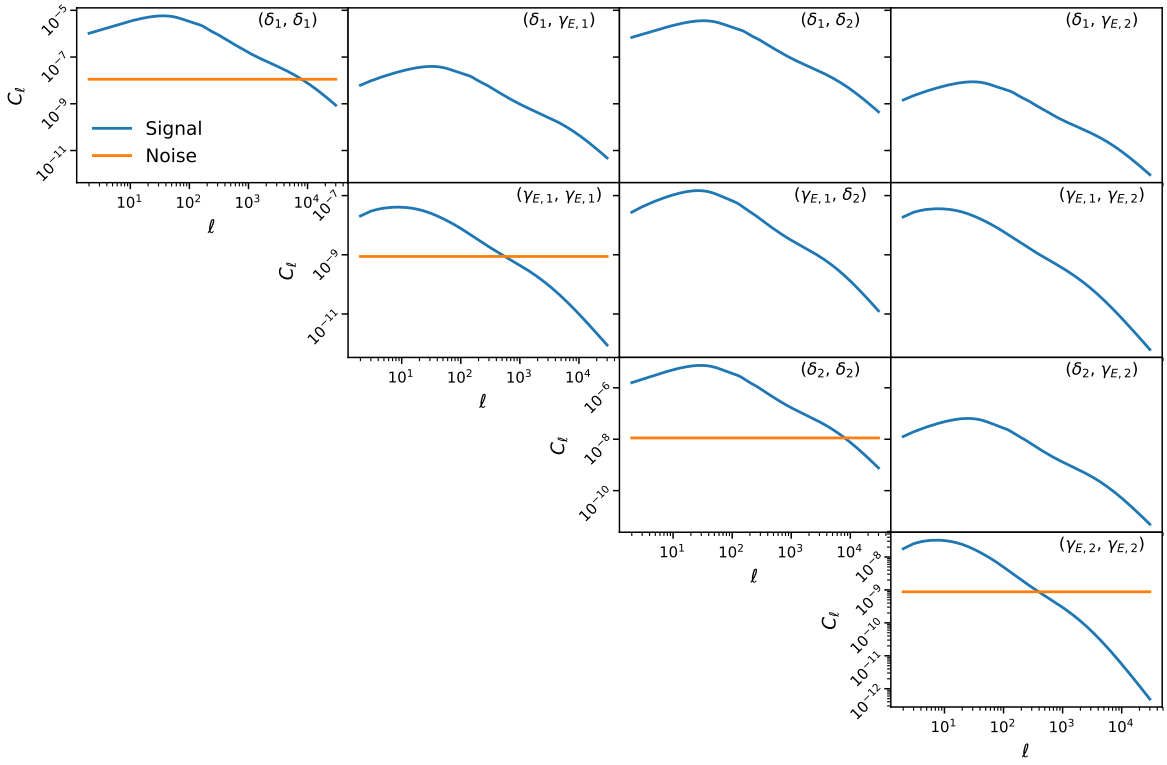

Figure 8.2: Signal (blue) and noise (orange) power spectra for the different observables used in our simulations. Note that the signal for shear B-modes (γ_B) is zero, and the noise is the same as that of γ_E. The different panels show different cross-correlations between δ and γ_E in two redshift bins.

We consider the case of auto- and cross-correlations between all fields in two redshift bins, with redshift distributions modeled as Gaussians with width $\sigma_z = 0.13$ centered around redshifts 0.75 and 0.95, with number densities $n_\Omega = 7.5\,\mathrm{arcmin}^{-2}$. The corresponding redshift distributions $p_z(z)$ are shown in Figure 8.1. For simplicity we use a constant bias $b(z) = 1$. For these specifications, we generate signal power spectra using the Core Cosmology Library (`CCL` [33]) for cosmological parameters $(\Omega_{\rm cdm}, \Omega_{\rm b}, h, A_{\rm s}, n_{\rm s}) = (0.27, 0.045, 0.67, 2.1\times10^{-9}, 0.96)$. The resulting non-zero signal and noise power spectra are shown in Figure 8.2.

After generating a set of Gaussian maps, we mask them making use of a realistic sky mask. This mask has three main components: a cut in declination based on the expected sky coverage of LSST [395], a more conservative Galactic cut using the dust reddening data from [396] and a set of 100 randomly positioned holes with a radius of 1 degree. To explore the case of cross-correlations between fields with different masks, we generated two masks for the two redshift bins above, consisting of two different sets of random holes. These masks are shown in Figure 8.3.

We have also explored the impact of the presence of sky contaminants on the estimate of the covariance matrix. As described in Ref. [35], the presence of a small contamination from observational systematics in the data can be accounted for through a technique known as *mode deprojection* [397–399]. In this method, the contamination is modeled as a linear contribution at the map level from contaminants with a known template. Mode deprojection then consists on projecting the data onto the subspace of modes that are perpendicular to those templates, effectively removing all modes from the map that "look like" any of the contaminants. This

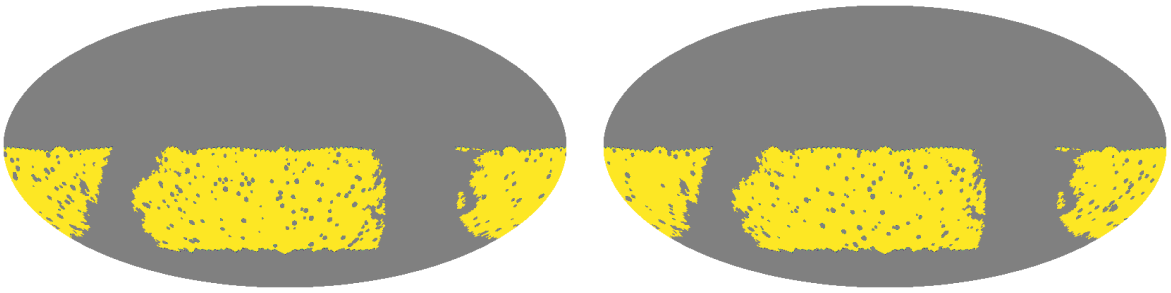

Figure 8.3: Sky masks used in our analysis for bins 1 and 2 (left and right panels respectively). As explained in the text, these masks have three main components: a cut in declination based on the expected sky coverage of LSST [395], a more conservative Galactic cut using the dust reddening data from [396] and a set of 100 randomly positioned holes with a radius of 1 degree. The same mask is assumed for the galaxy overdensity δ and cosmic shear $\boldsymbol{\gamma}$ for simplicity.

removal of modes has been shown to provide unbiased estimates of the power spectrum, however it could potentially affect the power spectrum uncertainties due to the loss of statistical power. To study this effect, we have also generated contaminant maps of two types:

- **Large-scale contaminants:** Gaussian random maps with a red spectrum of the form $C_\ell \propto (\ell+1)^\beta$, where β is a random number chosen within the range $\beta \in (-1,-3)$.
- **Small-scale contaminants:** Gaussian random maps with a flat spectrum $C_\ell = \text{const.}$

In both cases, we fixed the amplitude of the contaminant power spectrum such that it would yield a 10% contamination in the data power spectrum at $\ell = 400$. For spin-2 fields, we assumed the same power spectrum for E and B modes, with no cross-correlation between them. The resulting contaminant power spectra are shown in Figure 8.4. When exploring the effects of mode deprojection, we generated 100 contaminant maps of both types and added them to each simulated realization. We then deprojected the full set of 100 contaminant templates from the simulated maps and computed the corresponding unbiased power spectra. Note that, in what follows, our fiducial results do not include the effects of mode deprojection. These are discussed separately.

For our fiducial results, we generated a set of 20,000 random simulations. This number was chosen in order to recover the covariance matrix for all possible auto- and cross-correlations with sufficient accuracy. All simulations were generated as `HEALPix`[6] [400] maps with resolution $N_{\rm side} = 512$. We then used `NaMaster` to compute all possible power spectra for each simulation using narrow bandpowers of width $\Delta\ell = 3$ from $\ell = 2$ to $\ell = 1023$. Finally, we used the power spectra from the simulations to estimate the sample covariance matrix

$$\mathrm{Cov}(\mathbf{C}) = \frac{1}{N_{\rm sim}-1}\sum_{i=1}^{N_{\rm sim}} \left(\mathbf{C}_i - \bar{\mathbf{C}}\right)\cdot\left(\mathbf{C}_i - \bar{\mathbf{C}}\right)^T, \tag{8.82}$$

where $\mathbf{C}_i$ is the vector of all possible power spectra for the i-th realization, and $\bar{\mathbf{C}}$ is the mean of this vector over all realizations. The comparison of this sample covariance with the analytical approximations described above is presented in the next sections.

[6] `http://healpix.sourceforge.net`

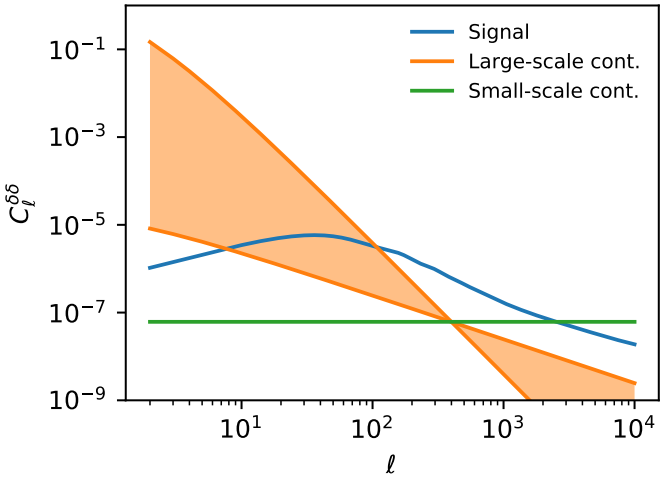

Figure 8.4: Input (signal + noise) power spectrum for the galaxy overdensity in the first redshift bin (blue line). The orange band shows the range of power spectra used for the 100 large-scale contaminant templates used to study the impact of contaminant deprojection on the covariance matrix. The green line shows the power spectrum used to generate small-scale contaminants. The amplitudes of the contaminant power spectra were fixed by imposing a 10% contamination level in the power spectrum at $\ell = 400$. The same approach was used for the cosmic shear maps, with independent contaminants defined in γ_E and γ_B.

8.2.2 Qualitative comparison

As a first step, we visually compare the main properties of the sample covariance matrix estimated from the simulations and the NKA, Spin-0 and MC approximations described in the previous section. Figure 8.5 shows four rows of the covariance matrix of different auto- and cross-correlations. The rows correspond to bandpowers centered on multipoles $\ell_q \simeq 60$, 90, 120 and 150. The upper panels show results for the non-zero power spectra (δ-δ, δ-γ_E and γ_E-γ_E), with the solid blue, dashed orange and dotted green lines showing results for the sample covariance matrix, the analytical covariance using the NKA approximation and their difference, respectively. For comparison, the black stars show the diagonal covariance matrix elements predicted by the MC approximation (Equation 8.76). We find an excellent agreement between the simulated and analytical covariances, with very small deviations in the amplitude of the diagonal and first few off-diagonal elements.

The bottom panel in Figure 8.5 shows the same rows of the covariance matrix for power spectra involving B-modes (and therefore with zero signal expectation value). In this case we find significant differences, at the level of $30 - 50\%$, on the covariance matrix elements, with the analyticial prediction underestimating the error bars overall. This is expected and can be understood as follows: the presence of a sky mask mixes E and B modes. Although this mixing can be accounted for at the level of the power spectrum through the pseudo-C_ℓ estimator, the leaked modes contribute to the variance. This is particularly significant for power spectra involving B-modes, since the E-mode amplitude is significantly larger, especially at $\ell \lesssim 200$, as can be seen in Figure 8.2. Thus, if the effects of E-B mixing caused by the sky mask are not accurately accounted for in the estimation of the covariance matrix for power spectra involving B-mode maps, we can expect a misestimation of the contribution to the covariance from the leaked E modes that would underpredict the uncertainties. This is not a problem for power

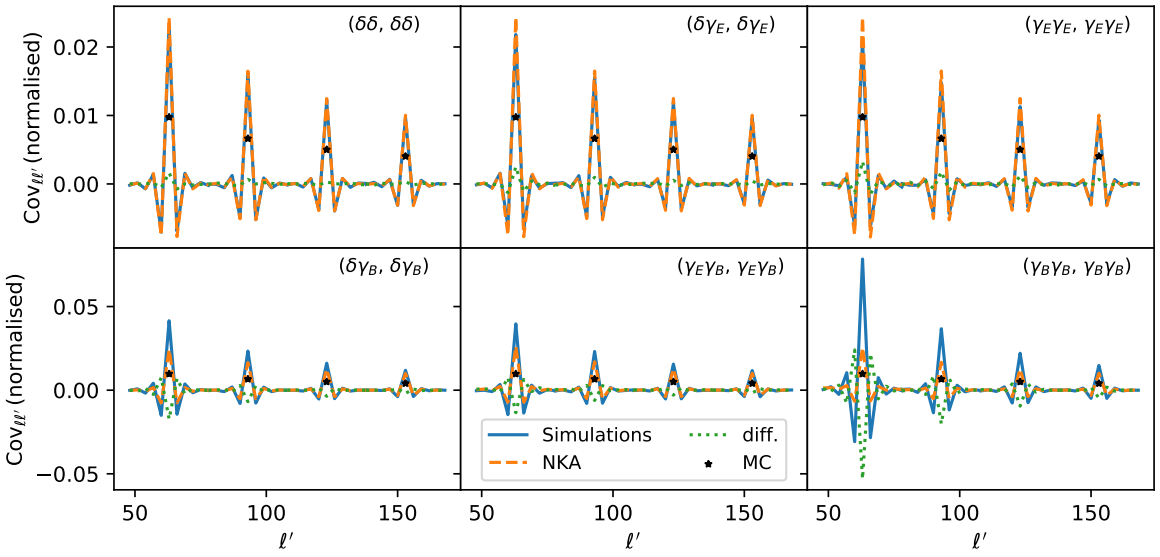

Figure 8.5: Four rows of the covariance matrix for different power spectra. The top panels show the cases of spectra with non-zero signal, involving δ and γ_E, while the bottom panels show cases involving B-modes. In each panel we show rows of the covariance matrix for $\ell = 60$, 90, 120 and 150, which peak at those central values. The different lines show the results for the sample covariance matrix (solid blue), its NKA estimator (dashed orange) and the difference between both (dotted green). The black stars show the mode-counting approximation to the covariance matrix (Equation 8.76). To facilitate the visualization of the different rows, we have divided them by $C_\ell^{aa}C_\ell^{bb} + (C_\ell^{ab})^2$, the numerator of Equation 8.76, for the two fields, a and b, that are being correlated in each case. The NKA method is able to recover the covariance with high accuracy for all field combinations that do not involve B modes, yielding visibly poorer results otherwise.

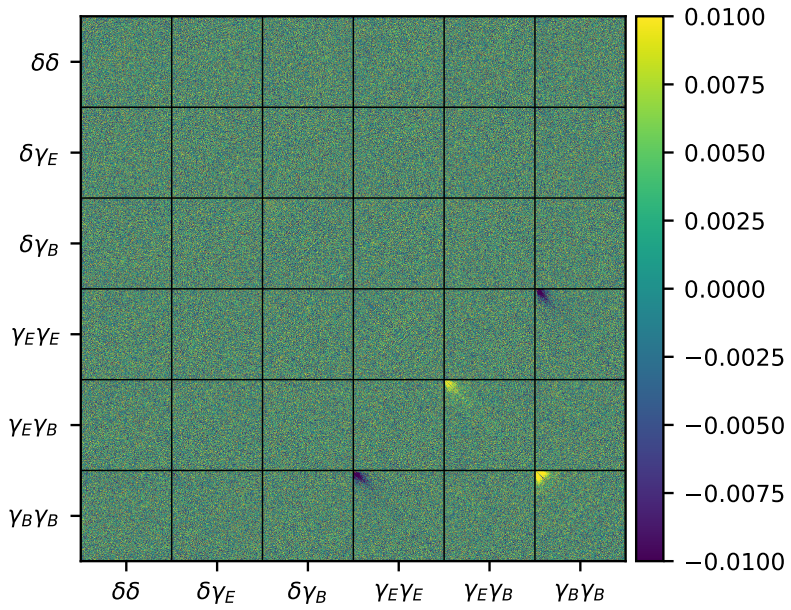

Figure 8.6: Difference between the correlation matrices associated to the sample covariance matrix and its estimate with the NKA method including all possible correlations between δ and $\boldsymbol{\gamma}$ in a single redshift bin. While the NKA estimator is able to recover the covariance matrix to high accuracy in most cases, it is not able to reproduce the off-diagonal correlations between different bandpowers in cases involving B modes.

spectra involving only E modes, since the only B modes that leak into them are those associated with noise, and they have the same amplitude as the noise E modes move into the B-mode map.

This is further illustrated by Figure 8.6. The figure shows, for the case of a single redshift bin, the difference (not the relative difference, to avoid problems dividing by 0) between the correlation matrices associated with the sample covariance matrix and the NKA estimate[7]. While the differences between both matrices are small for all elements involving δ and γ_E, all terms involving B-modes show a significant disagreement, particularly the $\gamma_E\gamma_E$-$\gamma_B\gamma_B$, $\gamma_E\gamma_B$-$\gamma_E\gamma_B$ and $\gamma_B\gamma_B$-$\gamma_B\gamma_B$ boxes.

We thus conclude that while the NKA estimator is able to recover the covariance matrix for the non-zero power spectrum elements (i.e. those involving δ and γ_E) with high accuracy, a more sophisticated approach would be needed in order to obtain a precise estimate of the uncertainties for components involving B-modes. This is not a major concern, since B-mode power spectra are predominantly used as null tests, while cosmological parameter constraints are driven by the analysis of δ and γ_E. For completeness, Figure 8.7 shows the difference between the correlation matrices for the sample covariance and the NKA estimator for all non-zero cross-correlations between different bins in the case of two redshift bins with different small-scale masks, where

[7]The correlation matrix is defined as $r_{ij} = \mathrm{Cov}_{ij}/\sqrt{\mathrm{Cov}_{ii}\mathrm{Cov}_{jj}}$

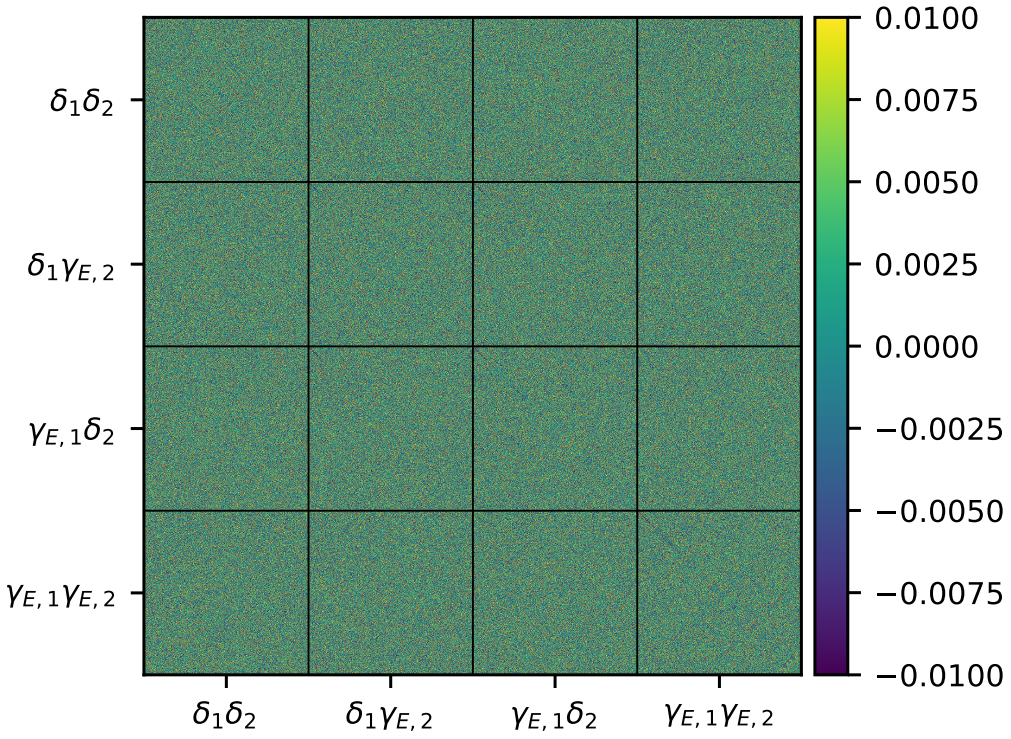

Figure 8.7: Same as Figure 8.6 for all cross-correlations between δ and γ_E measured in two different redshift bins.

we find a similarly good agreement.

8.2.3 Quantitative comparison

In order to quantify the validity of our analytical approximations, we need to compare the NKA covariance with the sample covariance estimated from the simulations. However, comparing two matrices is not as straightforward as comparing their elements one by one. The covariance between far-away bandpowers is expected to be very close to zero, and therefore a direct comparison of those elements would easily yield large relative differences simply due to the statistical noise in the sample covariance matrix. We will therefore quantify the differences between the different covariances making use of scalar quantities formed from them. The impact of the analytical approximations on the final parameter constraints will then be described in detail in Section 8.2.4.

As a first test to quantify the differences between covariance matrices, we compute the relative difference between their eigenvalues. This is shown in Figure 8.8 for a data vector

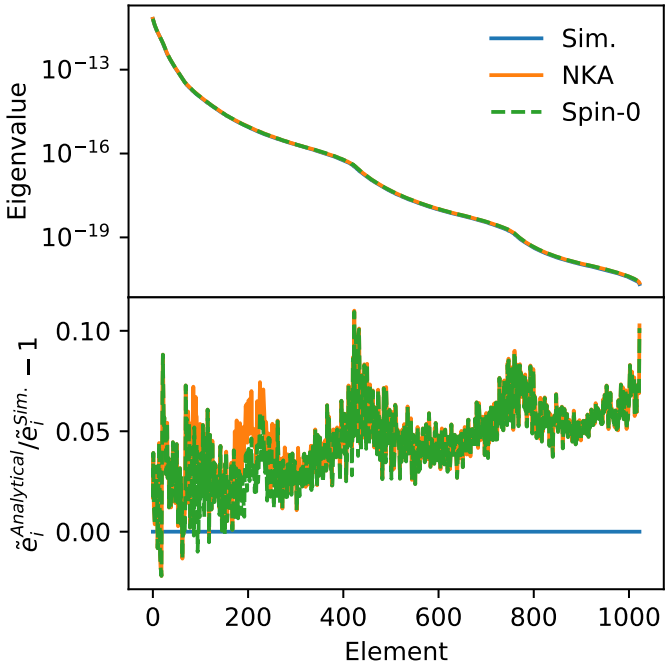

Figure 8.8: Eigenvalues of the single-bin covariance matrices for all power spectra involving δ and γ_E. Results are shown for the sample covariance (solid blue), the NKA estimator (solid orange) and the spin-0 approximation (dashed green). The NKA and spin-0 estimators are able to recover the covariance eigenvalues with an accuracy $\lesssim 5\%$.

combining all auto- and cross-correlations between δ and γ_E for a single redshift bin. The eigenvalues of both matrices are roughly similar, with relative differences of about 5%. The figure also shows the eigenvalues of the covariance matrix estimated using the Spin-0 approximation, which achieves a similar level of precision (even marginally higher in some cases).

Another scalar quantity that can be used to compare different covariances is the χ^2. For a given random data vector $\mathbf{d}$ with mean $\mathbf{m}$ and covariance matrix Cov, this is given by

$$\chi^2 = (\mathbf{d} - \mathbf{m})^T \cdot \mathrm{Cov}^{-1} \cdot (\mathbf{d} - \mathbf{m}) \,. \tag{8.83}$$

We compute this quantity for a data vector $\mathbf{d}$ composed of different auto- and cross-correlations for each of the 20,000 Gaussian simulations, with $\mathbf{m}$ given by the mean over all simulations and different choices of covariance matrix. Figure 8.9 shows the distribution of χ^2 values for the three non-zero power spectra in the case of a single bin: δ-δ, δ-γ_E and γ_E-γ_E. The histograms show the distribution for the sample covariance matrix (blue), and the analytical NKA and Spin-0 estimators (orange and green, respectively). We additionally plot the theoretical χ^2 distribution under the assumption that the underlying data vector is Gaussianly distributed (red dashed lines). In the simplest case of purely spin-0 quantities (leftmost panel), we find an excellent agreement between the different distributions. In the cases involving the spin-2 fields, we see noticeable differences between the distributions found with the sample covariance and the approximate ones. These differences are small, corresponding to less of a 2 and 4% shift in the mean χ^2 for the δ-γ_E and γ_E-γ_E cases, respectively, and a negligible variation in the width of the distributions. We therefore expect these differents to have a negligible effect on the posterior parameter distributions, as we show explicitly in Section 8.2.4. The fact that these differences appear only for power spectra involving spin-2 quantities indicate that the NKA and

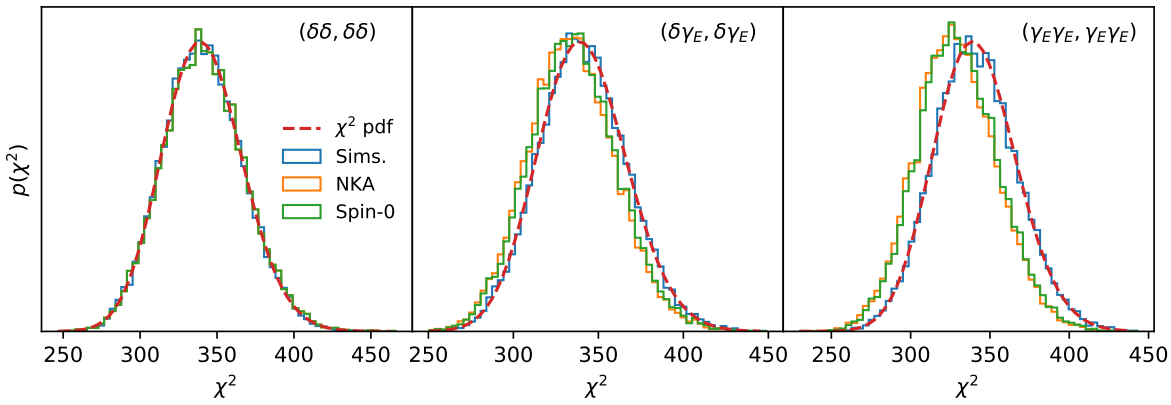

Figure 8.9: χ^2 distributions for the cases without γ_B-modes. We compare the distributions obtained with the covariance matrix computed directly from the simulated power spectra (blue) and the two different analytical methods: NKA (orange) and spin-0 (green). In addition, the theoretical χ^2 distribution has been included (dashed red). The distribution extracted from the simulation follows the theoretical expectation almost perfectly in all cases. In the cases of $\delta \times \gamma_E$ and $\gamma_E \times \gamma_E$, we observe small shifts in the peak χ^2, of $\sim$ 2-4%, while their width is recovered accurately (a difference $\lesssim 2\%$). We will show that these differences are due to the inaccuracy of the analytical approximations on the largest scales, and that they have a completely negligible impact on the final cosmological parameter constraints.

spin-0 methods are imperfect at describing the additional mode coupling caused in the presence of a mask for higher-spin fields. This is rather obvious in the case of the spin-0 approximation but, interestingly, we find that the NKA and Spin-0 predictions yield results that are almost indistinguishable from each other. We therefore conclude that the additional approximation made in the NKA method for spin-2 fields – neglecting the spatial derivatives of the mask – is effectively equivalent to ignoring the spin nature of the fields involved. Note, however, that this is not the case for B-modes, where the NKA estimator outperforms the spin-0 approximation by up to one order of magnitude, even though its accuracy is very poor (as we described in the previous section). For completeness, Figure 8.10 shows the distribution of χ^2 values for a data vector composed of all possible auto- and cross-correlations of δ and γ_E for the case of two redshift bins, where similar conclusions hold.

We have also explored the impact of contaminant deprojection on the different covariance matrix estimates. The loss of modes due to deprojection can potentially increase the variance of the power spectrum estimates, affecting the accuracy with which an analytical estimator would be able to recover the covariance. Figure 8.11 shows the diagonal of the covariance matrix for the δ-δ, δ-γ_E and γ_E-γ_E power spectra. Each panel displays the diagonal for the sample covariance matrix estimated from simulations without contaminants or contaminant deprojection (blue line), the sample covariance from simulations with contaminants and contaminant deprojection (dashed orange line) and for the NKA covariance (green line). We see that the power spectrum uncertainties are almost indistinguishable with or without deprojection, and that those relative differences are much smaller than the differences between the sample covariance and the NKA estimator. We therefore conclude that, except in the case where a very large set of contaminant maps are deprojected (comparable with the number of unmasked pixels in the map), the analytical approximation to the covariance matrix should be as accurate as in the absence of contaminants (i.e. accurate enough).

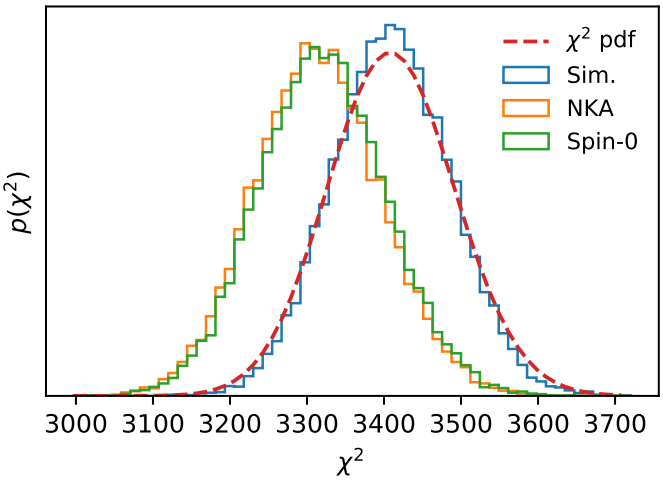

Figure 8.10: Same as Figure 8.9 for the combination of all correlations between δ and γ_E for two redshift bins, where similar conclusions hold. In this case, the differences in the distribution means and widths are less than 3% and 7%, respectively.

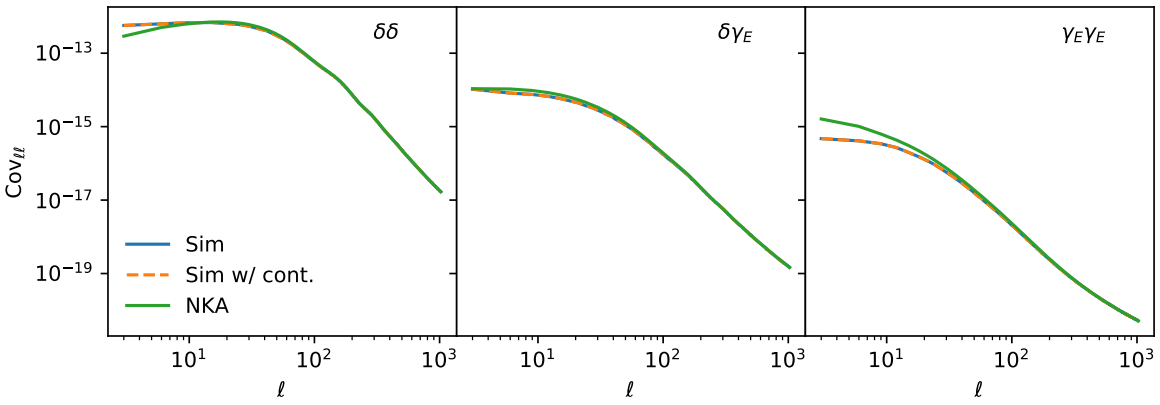

Figure 8.11: Diagonal of the covariance matrix estimated from simulations without contaminants (solid blue), with 200 contaminants deprojected (dashed orange) and the NKA estimator (solid green). The differences between the simulated cases are significantly smaller than those associated with the NKA estimator. The NKA method is therefore equally valid to approximate the covariance even in the presence of contaminant deprojection.

Figure 8.11 serves also to illustrate another important point. In all our tests we find that the largest differences between the sample and NKA covariances occur on large scales. For δ-δ correlations, the effect is limited to the first few multipoles ($\ell \lesssim 10$), while for γ_E-γ_E we are only able to recover the sample covariance errors within 5% for $\ell \gtrsim 40$. This is the main source of the small mismatch observed in Figure 8.9. Note, however, that most of the cosmological information is obtained from the higher multipoles, due to their higher statistical weight, and, as we will show in the next section, the effect on the final parameter constraints is negligible. If accurate covariance matrix elements are needed on these large scales for cosmic shear, they can be estimated alternatively making use of fast, low resolution simulations (e.g. `HEALPix` $N_{\rm side} = 64$ maps), or computed exactly as in Ref. [388, 390].

8.2.4 Impact on parameter estimation

Ultimately, the most important test to judge the accuracy of the analytical covariance matrix estimators implemented here is to study their impact on the posterior distribution of cosmological parameters derived from power spectrum measurements. Assuming flat priors and a fiducial Gaussian likelihood approximation [367], in which the covariance matrix is computed only once for the fiducial model, the posterior distribution for parameters $\vec{\theta}$ is simply given by:

$$-2\log p(\vec{\theta}|\hat{\mathbf{C}}) = \left(\hat{\mathbf{C}} - \mathbf{C}(\vec{\theta})\right)^T \cdot \mathrm{Cov}^{-1} \cdot \left(\hat{\mathbf{C}} - \mathbf{C}(\vec{\theta})\right) + \mathrm{const.}, \tag{8.84}$$

where $\hat{\mathbf{C}}$ is a vector of power spectrum measurements, Cov is their covariance matrix, and $\mathbf{C}(\vec{\theta})$ is their theoretical prediction for parameters $\vec{\theta}$. It is worth noting that this Gaussian likelihood is not accurate on large scales, where the small number of modes invalidates the application of the central limit theorem. Even in this regime, the likelihood can be approximated through the method described in Ref. [367], which still requires an accurate estimate of the power spectrum covariance.

We explore $\log p(\vec{\theta}|\hat{\mathbf{C}})$ for the two parameters $\vec{\theta} \equiv (\Omega_{\rm cdm}, \sigma_8)$, for a data vector composed of all possible auto- and cross-correlations between δ and γ_E in the case of two redshift bins described in Section 8.2.1. In this simple two-dimensional scenario, we simply sample the distribution in a regular grid of 100 by 100 points for each parameter. We construct a data vector $\hat{\mathbf{C}}$ from the theoretical prediction for the experimental setup described in Section 8.2.1, and produce theoretical predictions for it at each grid point using `CCL`. Note that, when evaluating the posterior for the sample covariance matrix, one needs to correct for the finite number of simulations used to construct the covariance. In most situations this can be done simply by rescaling the inverse covariance matrix by a factor given by [401]

$$\mathrm{Cov}^{-1} \longrightarrow \frac{N_s - 2 - N_{\rm data}}{N_s - 1}\,\mathrm{Cov}^{-1}, \tag{8.85}$$

where $N_s = 20,000$ is the number of samples used to estimate the covariance, and $N_{\rm data} = 3510$ is the number of data points.

The 68% and 95% confidence level contours associated with the posterior distributions for the sample covariance and the NKA estimator are shown in Figure 8.12. We find that both distributions agree with each other remarkably well, and that the 1σ errors for each parameter agree for both covariances up to 0.3%. Note that, since we have not included any statistical noise in the data vector $\hat{\mathbf{C}}$, the relative difference in the means of both distributions is zero by construction (since Equation 8.84 is bounded from below by zero). When adding Gaussian statistical noise compatible with the sample covariance matrix, we observe small differences (smaller than 0.3σ) in the best fit parameters found with both covariance matrices. These

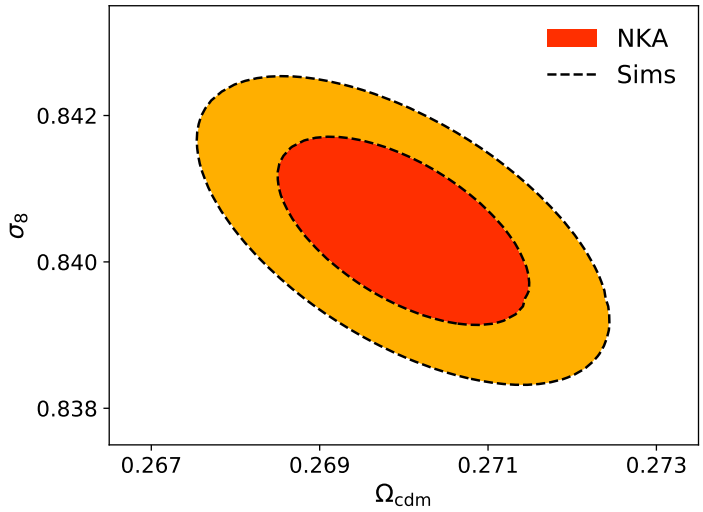

Figure 8.12: 1σ and 2σ contours for $\Omega_{\rm cdm}$ and σ_8 found from two different estimates of the power spectrum likelihood for a dataset containing all possible cross-power spectra between δ and γ_E for two redshift bins. The filled contours correspond to the parameter likelihood evaluated using the NKA estimator for the power spectrum covariance matrix, while the dashed black contours correspond to the same calculation done with the sample covariance matrix corrected by the factor in Equation 8.85. In both cases we assume a Gaussian likelihood. We find a remarkably good agreement between both likelihoods, highlighting the negligible impact of the approximations involved in the NKA method on the final parameter estimates.

differences, however, are not systematic, and we have verified that averaging over several noise realizations does not yield biased best-fit parameters.

We therefore conclude that the analytical approximations for the power spectrum covariance matrix explored here are able to reproduce the true posterior distribution of cosmological parameters to very high accuracy.

8.3 Discussion

Estimating accurate covariance matrices for projected two-point correlators is an ubiquitous problem in modern cosmology [402–404], but it is particularly relevant for Large Scale Structure datasets. This problem is further complicated in this case, in comparison with e.g. CMB experiments, by two factors: the fact that the fields involved are non-Gaussian at some level and the arguably higher complexity of the sky masks used in optical datasets. The main impact of survey geometry is the statistical coupling it induces between different Fourier/harmonic modes, which must be accurately characterized in order to obtain reliable estimates of the posterior distribution for cosmological parameters. In this Chapter we have focused on the impact of survey geometry on the dominant Gaussian (i.e. disconnected) part of the covariance matrix.

We have described and generalized existing analytical approaches to estimate the covariance matrix for pseudo-C_ℓ power spectrum estimators [385, 386, 390], and implemented them in the public code `NaMaster` [35], making it straightforward to fully account for the effects of survey geometry on the data uncertainties. With these approximations, computationally speaking, the problem of estimating a covariance matrix is as complex as that of computing the power spectrum itself, and scales with the number of pixels in the map as $N_{\rm pix}^{3/2}$. We leave for future

work the study of the impact of extra complications, as position-dependent noise, on their performance.

The main finding of this Chapter is the excellent performance of the analytical methods described in Section 8.1.3. We have shown that the NKA estimator (see Section 8.1.4) is able to recover the covariance matrix for all power spectra with non-zero signal expectation value (i.e. those involving the galaxy overdensity δ or the E-mode shear γ_E), as well as the posterior distribution for cosmological parameters, to a high degree of accuracy.

More in detail, we have also found that the impact of contaminant deprojection on the covariance matrix, through the corresponding loss of modes, is negligible unless a very large number of contaminant templates are removed. This simplifies the procedure to estimate covariance matrices for galaxy clustering data, which are particularly sensitive to a large number of astrophysical and observational systematics. Additionally, we have found that, although the NKA estimator is accurate enough, it is not able to perfectly capture the additional effects of mode coupling that are present for spin-2 fields, and that a simpler approach treating the shear E modes as a spin-0 object is able to reach similar levels of accuracy. Due to the imperfect treatment of the E/B mixing caused by the sky mask in the NKA estimator, we also find that the predicted covariance matrix for any power spectra involving B modes differs significantly from the true sample covariance, and, therefore, this approach cannot be used to reliably estimate the uncertainties of B-mode power spectra. Likewise, we find that the NKA estimator yields inaccurate estimates of the power spectrum uncertainties on the largest scales ($\ell \lesssim 50$). Although these modes carry a substantially smaller statistical weight, if more accurate covariances are needed on these large scales, they can be easily computed making use of fast low-resolution simulations or exactly following Refs. [388, 390].

In spite of these shortcomings, we find that the approximations described in this Chapter are able to provide estimates of the power spectrum covariance matrix that are sufficiently accurate for current and future tomographic Large Scale Structure cosmological datasets. The main advantage of this approach is the computational cost, which is comparable to that of estimating the power spectrum in the first place, and which scales with pixel resolution in a similar way. This is, therefore, significantly less time-consuming than generating large numbers of mock datasets (even simple Gaussian or log-normal realizations), and more reliable than the traditional jackknife resampling techniques. The method, in all its generality, is currently implemented in the public code `NaMaster`. Future extensions to this work will focus on improving the estimator for power spectra involving B modes, and incorporating the impact of E/B-mode purification [405–407].

8.A Flat sky

We have repeated the analysis described in Section 8.2 on flat-sky realizations, making use of the flat-sky implementation of `NaMaster`. We generate Gaussian realizations of the galaxy overdensity and shear maps making use of flat-sky extensions of the methods described in Section 8.2.1. In this case we use a high-resolution mask constructed from the bright-object mask distributed with the first data release of the HSC collaboration [408] for the VVDS field, which is shown in Figure 8.13.

We find similar levels of accuracy in the NKA and spin-0 estimators compared to the curved-sky case. The higher resolution and smaller area of these simulations allow us to focus on the small-scale galaxy clustering and lensing power spectra, covering the range of multipoles $\ell \in (120, 17640)$ in constant bandpowers of width $\Delta\ell = 240$. On these small scales, the shear power spectrum is more dominated by noise (e.g. see Figure 8.2), and therefore there is roughly the same power in E and B modes. This reduces the sensitivity of the method to an inaccurate

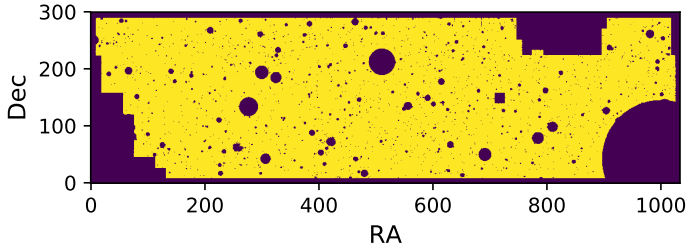

Figure 8.13: Flat-sky mask used in the study of the analytical methods presented in this work in the flat-sky regime. The mask was constructed from the bright-object mask distributed with the first data release of the HSC collaboration [408] for the VVDS field. As in the curved-sky case, it is used both for galaxy clustering and shear for simplicity.

treatment of E/B leakage, and the agreement between the sample covariance matrix and the NKA estimator improves significantly. This can be seen in Figure 8.14, which shows the χ^2 distributions for all possible power spectra (including those including B modes) in the case of a single redshift bin. In all cases we find a good agreement between the χ^2 distributions derived from all covariance matrix estimates (sample covariance, NKA and spin-0 in blue, orange and green respectively), which also accurately follow the expected χ^2 distribution for the corresponding number of degrees of freedom (red dashed line).

8.B Software implementation

In addition to the code functionality described in Section 3 of Ref. [35], we have now included the capability to estimate Gaussian covariance matrices using the NKA method. This functionality is structured around a `python` class called `NmtCovarianceWorkspace`. These objects are used to compute and store the covariance mode-coupling coefficients in Equations 8.59 and 8.73. They are initialized from two pairs of fields corresponding to the two power spectra for which the covariance is required. Once initialized, these coefficients can be reused for any other set of fields with the same combination of sky masks. `NaMaster` then provides routines to estimate covariance matrix elements making use of the coupling coefficients stored in a `NmtCovarianceWorkspace` object and best-guess power spectra for the fields involved using Equations 8.56 and 8.67. Further details about the implementation and practical examples can be found in `https://namaster.readthedocs.io/en/latest/sample_covariance.html`.

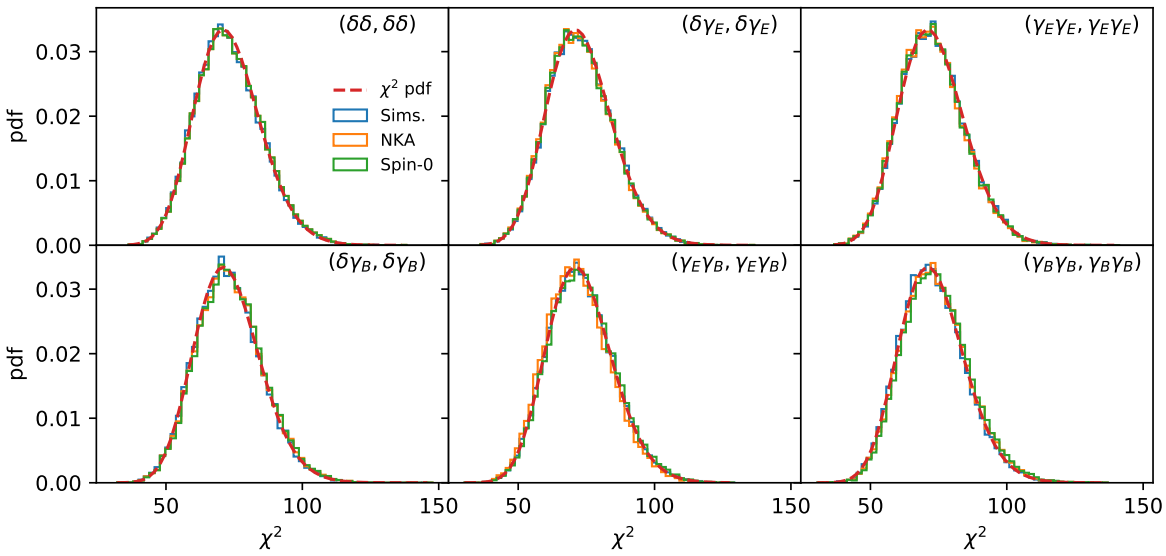

Figure 8.14: Same as Figure 8.9 for flat-sky fields. This figure additionally shows the χ^2 distributions for power spectra involving B-modes. For the smaller scales covered by these flat-sky simulations, the NKA and spin-0 estimators work remarkably well, even for B-mode spectra. The distribution mean shift and width difference is of about $\lesssim 2\%$ for all cases.

Chapter 9

The history of structure growth

In Chapter 2 we saw that current observations of the Universe are well described by the Standard Cosmological Model, ΛCDM. According to this model and current observations (e.g. Ref. [43]), the energetic content of the Universe is mainly due to dark energy ($\sim 70\%$) and dark matter ($\sim 25\%$), followed by baryonic matter ($\sim 5\%$), The contribution of photons and neutrinos; i.e. radiation, to the total energy density is negligible today. All this content is necessary to explain current observations.

Dark energy is introduced to explain the accelerated expansion of the Universe, first seen with Type Ia supernovae (SNe Ia) [60, 61] but also with Cosmic Microwave Background (CMB) [15, 43, 45–48] and Large Scale Structure (LSS) (e.g. Refs. [22, 49, 409]) observations. On the other hand, CMB and LSS observations also require dark matter in order to increase the growth rate of structure formation and match the observations. This was early realized using galaxy distribution measurements [359, 409–416].

As it was seen in Chapter 3, the main target of Large Scale Structure surveys are the positions and shapes of galaxies. Galaxy clustering is one of the main tracers of matter; however, the way we model the relation between the observed properties of clustering and the underlying matter distribution is source of biases. On the contrary, the shear field is an unbiased tracer of the matter distribution. This is a consequence of the fact that the galaxies shape deformation is caused by the weak lensing effect produced by all kinds of matter, and not only galaxies, found by their photons in their way to us. Cosmic shear, however, is more difficult to detect and needs a larger sample for an accurate description of the shear field. This is the reason why it has taken longer to produce competitive constraints on the cosmological parameters, which have been achieved in the last 15 years [14, 51, 334, 417–424].

Galaxy clustering and shear observations give complementary information of the matter distribution of the Universe. While the former directly maps overdensities on the matter field, the shear field gives information of the matter distribution that photons find in their way to us, in a integrated way. Subject to different systematics, the correlation of both observations allow to break the degeneracies that exist between the galaxy bias and cosmological parameters [425]. This feature will be used in forthcoming LSS studies. In fact, with the advent of next-generation LSS surveys, increasing the number of galaxies sampled by orders of magnitude and achieving a new level of accuracy, surveys such as LSST [34], DESI [19] or Euclid [79] will be able to reduce the uncertainty on the cosmological parameters to the order of 1%, even beating the cosmic variance for some parameters due to the overlapping of many of these surveys [58, 305].

In addition to galaxy maps, one can also include an extra probe. The CMB weak lensing convergence field has been mapped with great accuracy [426] and can be correlated with the other probes. CMB photons have travelled from recombination ($z \sim 1100$) to us. In this way, CMB lensing is giving us information of all matter since the Universe is transparent.

In addition, since CMB photons are mainly affected by weak lensing at $0.5 \leq z \leq 3$ [427], there will be a clear overlapping with LSS surveys which are currently reaching $z \sim 2$. This constitutes an additional form of cross-correlation with galaxy clustering and cosmic shear. In fact, this have been studied by the Dark Energy Survey (DES). They took measurement of the galaxy distribution and the shear field and correlated them with the SPT-Planck convergence field (excluding its auto-correlation) [22, 428]. Among other things, they were interested on the value of the parameter that measures the granularity of matter, $S_8 \equiv \sigma_8 \sqrt{\Omega_m/0.3}$, with σ_8 the root mean square amplitude of the linear mass fluctuation at $8\,\mathrm{h}^{-1}\,\mathrm{Mpc}$, and found $S_8 = 0.782^{+0.019}_{-0.025}$ and $\Omega_\mathrm{m} = 0.260^{+0.029}_{-0.019}$ in agreement with Planck's results [43]. In this way, their result contradicted the earlier findings reported by the Kilo Degree Survey (KiDS). KiDS, using tomographic weak lensing, found, first, a mild discrepancy of 2.3σ on S_8 with respect to the Planck's value [14], However, later analysis increased it to 3.2σ [51].

We want to explore further this discrepancy between both surveys. We want to analyze the temporal evolution of S_8 and check whether the compatibility between DES and Planck's data persists as a function of cosmic time. For that, we will use the DES Y1 data release [429, 430] that includes their galaxy clustering and shear maps and the publicly available CMB convergence map made by the Planck collaboration [426]. We will describe them further in next Section. In a later stage, we will do the same with KiDS-450 data and compare both outcomes.

This work is organized as follow. First, in Section 9.1 we will briefly describe the DES (Section 9.1.1) and Planck (Section 9.1.2) datasets. In Section 9.2, we will describe the maps we will be using and how we built them (Section 9.2.1), how we compute the angular power spectra (Section 9.2.2) from observations and theory and how we estimate the observations covariance matrix (Section 9.2.3) that we will use to build the likelihood. Next, in Section 9.2.4, we will show how we take into account possible deviations from the ΛCDM linear matter growth that will be also observationally constrained. Finally, in Section 9.3, we will outline the process needed to obtain the time evolution of S_8.

9.1 Datasets description

In this Chapter we will briefly describe the dataset that will be used in the analysis of the temporal evolution of the perturbation growth. We will describe the DES Year-1 galaxy clustering and shear maps [429, 430], and the Planck 2015 CMB weak lensing convergence field map [426].

9.1.1 Dark Energy Survey: galaxy clustering and tomographic shear

The DES Year 1 data release is publicly available and covers $1786\,\mathrm{deg}^2$ in griz after coaddition and before masking [429, 430]. DES aims to cover $5000\,\mathrm{deg}^2$ in 5 filter bands called *grizY*. The measurements are taken from the Cerro Tololo Inter-American Observatory (CTIO) with the 4 m Blanco Telescope, using the 570-megapixel Dark Energy Camera (DECam [431]). The 10σ limiting magnitude of the galaxy sample is $g = 23.4$, $r = 23.2$, $i = 22.5$, $z = 21.8$ and $Y = 20.1$ [429, 430]. This sample can be divided in two: the *tracer* and *source* galaxies. Each of them is used to build a different kind of map: *tracer* galaxies are used for galaxy clustering maps and *source* galaxies for weak lensing shear maps. The resulting maps are publicly available in `https://des.ncsa.illinois.edu/releases/y1a1`.

The tracer galaxies are redMaGiC-selected galaxies, a sample of Red Luminous Galaxies obtained with an algorithm that is able to find the galaxy photo-z with an error $\sigma_z = 0.017(1+z)$ [432]. This sample has been validated by cross-correlation with a spectroscopic sample [433]. The redMaGiC sample, by construction, has a constant comoving density in redshift and the selection criterion only depends on the comoving density, $\bar{n}$, and a luminos-

	Edges of the redshift bins
Tracers	0.15, 0.3, 0.45, 0.6, 0.75, 0.9
Sources	0.2, 0.43, 0.63, 0.9, 1.3

Table 9.1: z-bin edges for DES galaxy samples [21]. Lens and source galaxies correspond to, respectively, galaxies samples used for galaxy clustering and shear field maps.

ity threshold, $L_{\rm min}$, which determines if the galaxy is bright enough to be considered. The redMaGiC sample is divided in three: a high-density sample ($\bar{n} = 10^{-3}$, $L_{\rm min} = 0.5L_*$), a high-luminosity sample ($\bar{n} = 4 \times 10^{-4}$, $L_{\rm min} = L_*$) and a higher-luminosity sample ($\bar{n} = 10^{-4}$, $L_{\rm min} = 1.5L_*$); where the comoving densities $\bar{n}$ have been given in units of galaxies/$(h^{-1}{\rm Mpc})^3$ and $h \equiv H_0/100\,{\rm km\,sec^{-1}\,Mpc^{-1}}$ parametrizes the current value of the Hubble parameter. The tracer galaxy sample is divided in five different redshift bins (see Table 9.1 and top panel of Figure 9.1). The high-density subsample correspond to the lowest three redshift bins, while the other two are populated with both high-luminosity and higher-luminosity galaxies. In order to avoid contamination of systematic effects, the patchier region is masked out leaving only the smoother part that will be used in the analysis. This is called the "SPT" region [430] and covers 1321 deg^2 [430]. The same mask is applied to the *source* sample.

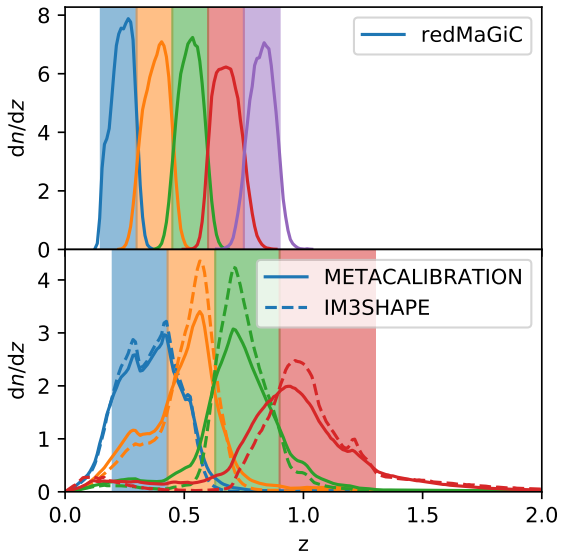

Figure 9.1: Galaxy density distribution per redshift bin. The top panel correspond to the galaxy sample used to construct the galaxy clustering map, while those in the bottom panel were used for the shear maps. The latter were obtained with two different approaches named `METACALIBRATION` and `IM3SHAPE`. See Section 9.1.1 for further details.

The source galaxy is used to estimate the weak lensings shear field, measuring the statistical alignment of the galaxy shapes. For that, DES used two different algorithms: `METACALIBRATION` and `IM3SHAPE` [434]. `METACALIBRATION` [435, 436] fits a 2D Gaussian model for each galaxy to the pixel data in bands r, i and z exposures convolved by its corresponding point-spread function (PSF). In order to calibrate the shear estimator, this process is repeated with artificially sheared images, allowing to determine the response of the estimator. It also calibrates shear-dependent selection effects that could bias the statistics a few percents (see e.g. Refs. [424, 434, 436, 437]). `IM3SHAPE` [438], instead, maximizes the likelihood set of parameters fitting a bulge of a disc

Priors			
Parameter	Prior	Parameter	Prior
Cosmology		**Lens photo-z bias**	
$\Omega_{\rm m}$	$U(0.1, 0.9)$	$\Delta z_{\rm g}^1$	$\mathcal{N}(0.0, 0.007)$
$A_{\rm s}/10^{-9}$	$U(0.5, 5.0)$	$\Delta z_{\rm g}^1$	$\mathcal{N}(0.0, 0.007)$
$n_{\rm s}$	$U(0.87, 1.07)$	$\Delta z_{\rm g}^2$	$\mathcal{N}(0.0, 0.007)$
w_0	-1	$\Delta z_{\rm g}^3$	$\mathcal{N}(0.0, 0.006)$
$\Omega_{\rm b}$	$U(0.03, 0.07)$	$\Delta z_{\rm g}^4$	$\mathcal{N}(0.0, 0.01)$
h_0	$U(0.55, 0.91)$	$\Delta z_{\rm g}^5$	$\mathcal{N}(0.0, 0.01)$
$\Omega_\nu h^2$	0	**Source photo-z bias**	
$\Omega_{\rm K}$	0	$\Delta z_{\rm s}^1$	$\mathcal{N}(-0.001, 0.016)$
τ	0.08	$\Delta z_{\rm s}^2$	$\mathcal{N}(-0.019, 0.013)$
		$\Delta z_{\rm s}^3$	$\mathcal{N}(0.009, 0.011)$
		$\Delta z_{\rm s}^4$	$\mathcal{N}(-0.018, 0.022)$
Galaxy bias		**Intrinsic Alignments**	
$b_{\rm g}^i$	$U(0.8, 3.0)$	$A_{\rm IA,0}$	$U(-5.0, 5.0)$
Shear Calibration bias		$\eta_{\rm IA}$	$U(-5.0, 5.0)$
m^i	$\mathcal{N}(0.012, 0.023)$	z_0	0.62

Table 9.2: Prior distribution of the different parameters entering the analysis. They can be uniform (U) or Gaussian ($\mathcal{N}$) distributions, depending on the a priori knowledge of these variables (see Section 9.1). Note that the prior distributions related to the parameters of the DES dataset have been taken from Table 1 of Ref. [22]. As it is customary, $U(a, b)$ and $\mathcal{N}(\mu, \sigma)$ describe a uniform distribution with boundaries (a, b) and a Gaussian distribution with mean μ and variance σ, respectively. The index i in $b_{\rm g}^i$ and m^i run over the different redshift bins.

model to the galaxies' r-band measurements. This estimator is biased and calibrated using catalogs that resemble the DES Y1 dataset [434, 439].

In both cases, the biases, parametrized by m^i for each redshift bin i, modify the true shear field, $\gamma^{\rm true}$, multiplicatively, so that $\gamma^{\rm obs} = (1 + m^i)\gamma^{\rm true}$ is the observed shear. These m^i must be considered free parameters in the forthcoming analysis. The main contribution of the `METACALIBRATION` bias comes from the impact of neighboring galaxies on the estimation of th galaxy shapes. On the other hand, in the case of `IM3SHAPE`, the imperfections in the image simulations are the main cause. The physically motivated priors can be seen in Table 9.2 and were determined in the analysis of the systematic errors of Ref [434].

The final sample is highly reduced respect to the full Y1 Gold catalog after applying conservative cuts on the signal-to-noise ratio and galaxy size. Once applied, the `METACALIBRATION` sample contains 26 million galaxies up to magnitude ~ 23 in the r-band on the area of interest; i.e. the SPT region. The `METACALIBRATION` sample was chosen over that of `IM3SHAPE` in the cosmological analysis of DES on Refs. [21, 22]. The reason is that the former contains a higher number density and `METACALIBRATION` is considered a more secure technique than `IM3SHAPE` [21, 434].

Apart from correctly estimating the shear, the redshift distribution of the source galaxy sample is also needed. The redshift probability density, $p_{\rm BPZ}(z)$, of each galaxy is determined using the BPZ algorithm [440]. Details on the process can be found on Ref. [441]. In turn,

galaxies are assigned to one of the four redshift bins of Table 9.1, based on the mean value of their $p_{\rm BPZ}(z)$. In the case of `METACALIBRATION`, it is assigned based on the value of the galaxy photo-z estimated by its own pipeline. The resulting redshift distributions are shown in Figure 9.1.

The photometrically derived redshift distributions, $n^i_{\rm PZ}(z)$, are considered a shifted version of the true distribution, $n^i(z)$, to account for their corresponding uncertainties. Mathematically,

$$n^i(z) = n^i_{\rm PZ}(z - \Delta z^i)\,, \tag{9.1}$$

where we are evaluating the distribution $n^i_{\rm PZ}$ at $z - \Delta z^i$, not multiplying both terms. Note that this equation is valid both for the tracer and source galaxy samples. Furthermore, note that in cosmological analysis, the Δz^i must be kept free and varied with the others parameters. Their prior distributions are based on physical considerations (see Ref. [21]) and shown in Table 9.2.

It was shown in Refs. [21, 441] that the exact form of the redshift distribution $n^i(z)$ has a negligible impact on the cosmological posterior distribution if their mean redshift, Δz^i, are allowed to vary. Therefore, the estimated distribution $n_{\rm PZ}$ does not need to be very accurate.

9.1.2 Planck CMB convergence weak lensing

CMB weak lensing is an extra probe that can be used together with LSS galaxy clustering and shear maps. While the latter allow for tracking the matter distribution and growth rate at different redshifts, CMB is a localized sourced, well understood and very close to a Gaussian distribution, making the reconstruction of the mass or weak lensing potential maps, much easier.

Furthermore, CMB is affected by all matter along the line of sight between us and the last scattering surface, being mainly affected by matter at $0.5 \lesssim z \lesssim 3$ (e.g. [427]). This, however, does not give information on the temporal evolution of the growth rate. It is its correlation with the other tracers (galaxy clustering and shear, for instance) which can provide us with it.

The CMB convergence map that we will use for our analysis will be the publicly released of Planck 2015 [426]. We use this map instead of the SPT-Planck combined map [428], that was used in DES analysis [22], because although its overlapping with DES observed area is not as good as the SPT-Planck combined map, it allows us to easily extend our work to other LSS surveys like KiDS [14, 51].

Planck observes in nine different frequency bands ranging from 30 GHz to 857 GHz. From these, the 143 GHz and 217 GHz channels have most of the information at small scales ($\ell > 1000$). Their beams are well approximate by a Gaussian with full-width-at-half-maximum (FWHM) of $7'$ and $5'$, respectively. Their noise is almost white in the scales $1000 \lesssim \ell \lesssim 3000$, with values of $\sim 30\,\mu$K arcmin and $\sim 60\,\mu$K arcmin in temperature and polarization, respectively, for the 143 GHz band. For the 217 GHz one, the noise values are $\sim 40\,\mu$K arcmin and $\sim 95\,\mu$K arcmin, respectively.

The Planck collaboration reconstructed the weak lensing field [426] from inverse-variance filtered CMB multipoles with the quadratic estimator of Okamoto & Hu [442]. This gives five different estimators, $\hat{\phi}^{TT}$, $\hat{\phi}^{TE}$, $\hat{\phi}^{EE}$, $\hat{\phi}^{EB}$ and $\hat{\phi}^{TB}$ that will enter in the minimum-variance estimator, $\hat{\phi}$. The primordial B-modes are neglected and, therefore, the $\hat{\phi}^{BB} \sim 0$. The filters used mask the Milky Way and bright point sources (such as clusters) and applies bandpass filters to scales $100 \leq \ell \leq 2048$. In addition, the SMICA-specific masks are also applied, which inpaint some of the masked points to avoid statistical problems with the whole map [443]. With all these masks applied, the usable sky fraction is $f_{\rm sky} = 67.3\%$ [426].

The lensing potential is enhanced at large scales, possibly causing leakages when cutting the map. This is prevented working with the convergence κ weak lensing field [426],

$$\hat{\kappa}^{MV}_{\ell m} = \frac{1}{2}\ell(\ell+1)\hat{\phi}^{MV}_{\ell m}\,. \tag{9.2}$$

In contrast with the lensing potential, κ has a whiter power spectrum and noise [444]. Therefore, this is the quantity that will be used in our analysis.

One must note when working with the resulting convergence map that the scales $\ell < 8$ are considered unstable and must be removed from the analysis [426]. Furthermore, the small scale resolution limited by the beam size of Planck satellite imposes also a large-ℓ upper bound. We conservatively chose $\ell_{\rm max} = 2000$. Therefore, the scale range of interest in this work is $8 \leq \ell \leq 2000$.

9.2 Analysis

In the following Section 9.2.1 we will describe how DES and Planck data is processed to build the galaxy clustering, shear and convergence maps that will go into the analysis. In addition, we will show how we estimate the noise, multiplicative bias and other corrections that must be undertaken to recover the underlying fields that can be compared with the theoretical predictions. For that, we will be working in Fourier space with the angular power spectra, C_ℓ^{ab}, where $a\,, b$ can be any of the fields considered on this work; i.e. galaxy overdensity ($\delta_{\rm g}$), the shear E-mode (γ_E) or the CMB convergence (κ). In Section 9.2.2 we will compute the angular power spectra of the observations and our fiducial model. This will be used in Section 9.2.3 to estimate the data likelihood. Finally, in Section 9.2.4, we will show how we incorporate in our analysis possible deviations from ΛCDM, by parametrizing a linear perturbation of its linear growth factor. This parametrization will also be constrained later with the LSS and CMB observations.

9.2.1 Maps

In the previous Section we have explained the datasets that will be used in our analysis. DES [429, 430] and Planck [426] have made their data publicly available. We built and worked with the corresponding maps with `HEALPix` [1] [400] with $N_{\rm side} = 4096$. The maps are described below and have been summarized in Table 9.3:

- Galaxy clustering DES maps. Five maps, one per redshift bin (see Table 9.1 and Figure 9.1). Each pixel contains information about the number of galaxies in it, N_p. All of them share the same mask, W_p^δ.

- Galaxy shear DES maps. 16 maps in total, four per redshift bin. Each redshif bin map has its own mask, $W_p^{\gamma,i}$. Each redshift bin has, in addition, a map of $W_p^{\gamma,i} e_{1,p}$ and $W_p^{\gamma,i} e_{2,p}$, where e_1 and e_2 are the two different components of the shear field, and a map of $W_p^{\gamma,i}(1+m)_p^i$, where m is the multiplicative bias. The subindex p referres to the value of those quantities in a given pixel p.

- CMB convergence maps. Two maps: one map of the convergence κ_p and the mask, W_p^κ.

The mapped quantities, however, cannot be directly compared with theoretical predictions. Only the CMB convergence map can be directly used. Instead, those related with galaxy clustering and shear must be first transformed. The galaxy number counts must be transformed to the overdensity of galaxies and the shear modes must be obtained free of the multiplicative bias and mask contribution. These transformations will be seen below.

[1] `http://healpix.sourceforge.net`

	Maps	Variable
Galaxy clustering	5	N_p^i
	1	W_p^δ
Galaxy shear	4	$W_p^{\gamma,i} e_{1,p}$
	4	$W_p^{\gamma,i} e_{2,p}$
	4	$W_p^{\gamma,i}(1+m)_p^i$
	4	$W_p^{\gamma,i}$
CMB Convergence	1	κ_p
	1	W_p^κ

Table 9.3: Summary of the maps used in the present study. The index p runs over all pixels of the map and the index i over all maps redshift bins. N_p is the number of galaxies per pixel, $e_{1,p}$ and $e_{2,p}$ are the first and second shear modes, m_p^i is the multiplicative bias of pixel p and redshift bin i and κ_p is the value of the convergence field in pixel p. Galaxy clustering maps all share the same mask.

Galaxy clustering

The galaxy number counts maps can be converted to overdensity maps taking into account that the galaxy overdensity field, δ_p, is given by

$$\delta_p = \frac{N_p}{\bar{N} w_p} - 1\,, \tag{9.3}$$

where N_p is the number of galaxies in pixel p, $\bar{N} = \sum_p N_p / \sum_p w_p$ is the mean number of galaxies per pixel and w_p is the value of the mask field, $W^\delta(p)$, at pixel p. w_p is included multiplying $\bar{N}$ in Equation 9.3 in order to correctly address the relative weight of the given pixel; i.e. to take into consideration the possibility of computing δ_p in a fraction of a pixel.

Noise. Galaxy clustering observations suffer of shot noise. We need to remove it in order to compare the statistics of the overdensity field with our theoretical predictions. For that, we first realize that the angular momentum of shot noise is

$$\widetilde{N}_\ell = \int \frac{\mathrm{d}^2\Theta}{4\pi} (W^\delta(\Theta))^2 \sigma^2_{\bar{N}}(\Theta)\,, \tag{9.4}$$

where Θ covers the whole area of the sky and $\sigma_n(\Theta)$ the variance of the overdensity distribution. Given that galaxies follow a Poisson distribution and taking into account the contribution of the mask, $W^\delta(\Theta)$, $\sigma_{\bar{N}}(\Theta)^2 = 1/\bar{N} W^\delta(\Theta)$. As a consequence,

$$\widetilde{N}_\ell = \frac{1}{\bar{N}} \int \frac{\mathrm{d}^2\Theta}{4\pi} W^\delta(\Theta)\,, \tag{9.5}$$

which, in a pixelated map, becomes

$$\widetilde{N}_\ell = \frac{A_{\rm pix}}{\bar{N}} \frac{\sum_p w_p}{N_{\rm pix}} = \frac{1}{\bar{N}_\Omega} \frac{\sum_p w_p}{N_{\rm pix}}\,, \tag{9.6}$$

where $\bar{N}_\Omega$ is the mean angular number of galaxies per steradian. In the computation of the integral we had into account that in `HEALPix` [400], the total area of the sphere is 4π and that the area of a pixel is given by $A_{\rm pix} = 4\pi/N_{\rm pix}$.

The tilde in the previous expression is there to remind ourselves that surveys masks couple different angular momenta. In order to obtain the decoupled noise power spectrum, which we

can compare with theoretical predictions, we need to multiply by the inverse mode coupling matrix, M, i.e.

$$N_\ell = M^{-1}\bar{N}_\ell\,. \tag{9.7}$$

See Section 9.2.2 for further information on how we compute the angular power spectrum in this work.

Galaxy tomographic weak lensing shear

In this case, we focus on the galaxies shape deformation due to weak lensing. The pixelated images return the averages of the shear modes of the galaxies within. For instance, if the individual galaxies in a pixel p have shear modes $e_\alpha(p) = \sum_{i\in p} e_{\alpha\, i}$, the resulting averaged values for that pixel will be

$$\bar{e}_\alpha(p) = \frac{\sum_{i\in p} e_{\alpha\, i} w_i}{\sum_{i\in p} w_i}\,, \tag{9.8}$$

where we had into account the effect of the survey mask, $W^{\gamma_\alpha}(p) = \sum_{i\in p} w_i$, which modifies the observed value by $e_\alpha \to W^{\gamma_\alpha} e_\alpha$.

The observed ellipticity is not, however, only caused by weak lensing. It can also have a non-negligible contribution of systematics. In fact, the DES sample has a non-zero mean ellipticity, $\langle e_\alpha\rangle \sim 10^{-4}$, from unclear origin that must be removed in each redshift-bin [434]. Therefore,

$$e_\alpha(p) = \bar{e}_\alpha(p) - \langle e_\alpha\rangle = \frac{w e_\alpha(p)}{w(p)} - \frac{\sum_p w(p) e_\alpha(p)}{\sum_p w(p)}\,. \tag{9.9}$$

Finally, we have to take into account the multiplicative bias. In this work we approximate it, simply, by

$$\langle 1+m\rangle \equiv 1 + \langle m\rangle = \frac{\langle \sum_{i\in p}(1+m)_i w_i\rangle}{\langle w\rangle} = \frac{\sum_p \sum_{i\in p}(1+m)_i w_i}{\sum_p w}\,, \tag{9.10}$$

where the average is over all pixels. More complex estimations could be done as, for example, averaging patches of the sky instead of the whole sky. In any case,

$$e_\alpha(p) = \left[\frac{w e_\alpha(p)}{w(p)} - \frac{\sum_p w(p) e_\alpha(p)}{\sum_p w(p)}\right] \frac{1}{1+\langle m\rangle}\,. \tag{9.11}$$

Noise. We account for the shear noise by averaging over the power spectra of 10 shear modes maps obtained randomly rotating each galaxy.

CMB convergence weak lensing

In the case of the convergence map of CMB (κ), we only have to take into account the geometrical mode coupling produced by the mask as the statistics of κ is directly comparable with theoretical predictions. This effect will be described in the following Section.

9.2.2 Angular power spectra

We have seen in Section 9.1 that DES and Planck surveys cover large portions of the sky with an overlapping area of $\sim 1300\,\mathrm{deg}^2$. As a consequence, the flat-sky approximation does not remain valid. In addition, as we mentioned before, we will be working in the Fourier space, with the angular power spectrum, C_ℓ. In the following two Sections we will describe its computation using the maps described in the previous Section, as well as, from a given cosmological model.

Observed C_ℓ

We compute the observed angular power spectrum, C_ℓ, using the pseudo-C_ℓ estimator [35], implemented in `NaMaster` [2]. For two discrete fields, $\mathbf{a}(\mathbf{x})$ and $\mathbf{b}(\mathbf{x}')$, their Fourier transformed version are $\mathbf{a_k}$ and $\mathbf{b_l}$, where $\mathbf{k} = (k, m_k)$ and $\mathbf{l} = (\ell, m_\ell)$. In Fourier space, the power spectrum is then given by

$$\langle \mathbf{a_k} \mathbf{b_l}^\dagger \rangle = C_\ell^{ab} \delta_{k\ell} \delta_{m_k m_\ell} \,, \tag{9.12}$$

where the fields a and b can have spin 0 or 2. This means that in the first case, a would be a scalar, while in the second case, a would be a vector with 2 components, $a = (a^1, a^2)$, that under rotations of angle ψ transforms as $a^1 + ia^2 \to (a^1 + ia^2)\exp(i\,2\psi)$, written in complex form.

Although the power spectrum of different modes is zero, the presence of a mask changes that. With a mask, the fields become $\tilde{a}(\mathbf{x}) = w_a(\mathbf{x})a(\mathbf{x})$ and $\tilde{b}(\mathbf{x}) = w_b(\mathbf{x})b(\mathbf{x})$, and their Fourier transform is not longer diagonal,

$$\tilde{\mathbf{a}}_\mathbf{l} = \sum_\mathbf{k} \Delta^2 k \, {}^a\mathsf{M}_{\mathbf{lk}} \mathbf{a_k} \,, \qquad \tilde{\mathbf{b}}_\mathbf{l} = \sum_\mathbf{k} \Delta^2 k \, {}^b\mathsf{M}_{\mathbf{lk}} \mathbf{a_k} \,, \tag{9.13}$$

where ${}^a\mathsf{M}_{\mathbf{lk}}$ and ${}^b\mathsf{M}_{\mathbf{lk}}$ are mode coupling matrices completely defined by the masks, w_a and w_b. For w_a,

$${}^a\mathsf{M}_{\mathbf{lk}} = \sum_\mathbf{x} \Delta^2 x \; w^a(\mathbf{x}) \, \mathsf{E}_\mathbf{l}^\dagger(\mathbf{x}) \, \mathsf{E}_\mathbf{k}(\mathbf{x}) \,. \tag{9.14}$$

With this, their power spectrum is now

$$\langle \tilde{\mathbf{a}}_\mathbf{l} \tilde{\mathbf{b}}_\mathbf{l}^\dagger \rangle = \sum_\mathbf{k} \Delta^2 k \; {}^a\mathsf{M}_{\mathbf{lk}} \, C_k^{ab} \, {}^b\mathsf{M}_{\mathbf{lk}}^\dagger \,. \tag{9.15}$$

In order to recover the true power spectrum, C_k^{ab}, we use the pseudo-C_ℓ, estimator [35]. First we bin the mode scales, $\mathbf{l}$, into bandpowers of index q, $\mathbf{l} \in q$. For this work, we have chosen 39 bandpowers from $\ell = 0$ to $\ell = 12288 = 3N_{\rm side}$ [3]. In order to avoid the small steps of logarithmic spacing at low-ℓ, we choose a linear binning at that regime and a logarithmic binning at large-ℓ. From $\ell = 0$ to $\ell = 240$, inclusive, the bandwidth is constant and its value is $\Delta\ell = 30$. From $\ell = 247$ to $\ell = 12288$, the bandpowers are log-spaced. In these bandpowers, the power spectra does not change much and we can average their value, resulting on

$$\tilde{C}_q^{ab} = \sum_{\mathbf{l}\in q} B_q^\mathbf{l} \tilde{a}_\mathbf{l} \tilde{b}_\mathbf{l}^\dagger \,, \tag{9.16}$$

with normalized bandpower weights $B_q^\mathbf{l}$ (i.e. $\sum_{\mathbf{l}\in q} B_q^\mathbf{l} = 1$).

Inside the bandpowers support, the mode coupling matrix is invertible and we can recover an estimation of the true power spectrum. The estimator is called $\hat{C}_q^{ab}$ and is given by

$$\hat{C}_q^{ab} = \sum_{q'} (\mathcal{M}^{-1})_{qq'} \tilde{C}_q^{ab} \,, \tag{9.17}$$

where $\mathcal{M}$ is the binned mode-coupling matrix.

For completeness, note that for curved sky, the power spectra is given by

$$\langle C_{\ell m}^{ab} \rangle = \sum_\ell M_{\ell\ell'}^{s_a s_b}(w_a, w_b) \mathcal{C}_{\ell'}^{ab} \,, \tag{9.18}$$

[2] `https://github.com/LSSTDESC/NaMaster`

[3] $\ell_q = \{0, 30, 60, 90, 120, 150, 180, 210, 240, 272, 309, 351, 398, 452, 513, 582, 661, 750, 852, 967, 1098, 1247, 1416, 1608, 1826, 2073, 2354, 2673, 3035, 3446, 3914, 4444, 5047, 5731, 6508, 7390, 8392, 9529, 10821, 12288\}$

where the average is over the harmonic number m. The dependence on the fields' spin has been made explicit in the mode-coupling matrix $M_{\ell\ell'}^{s_a s_b}(w_a, w_b)$, as well as that on the maks, w_a, w_b. The value of the mode-coupling matrices can be see in Chapter 8 and Ref. [35].

The angular power spectra of the DES and Planck observations have been plotted in Figure 9.2, together with the theoretical power spectra that we will discuss in the following Section and the observational estimated errors that will be computed in Section 9.2.3.

Theoretical C_ℓ

We compute the angular power spectra using the `Core Cosmology Library` [4] [33]. We will work under the Limber approximation [323], following the DES analysis [429]. This approximation can be used given that we do not explore very large angular scales and that the galaxy selection functions are slowly varying with redshift [434]. In the Limber approximation, the angular power spectra is given by an integral along the path of sight of the matter distribution weighted accordingly. Mathematically,

$$C_\ell^{a_\alpha b_\beta} = \int \mathrm{d}\chi \frac{q_{a_\alpha}(\chi) q_{b_\beta}(\chi)}{\chi^2} P_{\mathrm{NL}}\left(\frac{\ell + 1/2}{\chi}, z(\chi)\right), \tag{9.19}$$

where χ is the comoving distance, q_{a_α} is the weight function for the field a with component α, and P_{NL} is the non-linear matter power spectrum. The kernel or weight functions $q(\chi)$ are given by

$$q_\kappa = \frac{3\Omega_{\mathrm{m}} H_0^2}{2c^2} \frac{\chi}{a(\chi)} \frac{\chi^* - \chi}{\chi^*}, \tag{9.20}$$

in the case of CMB weak lensing convergence field and where the * means evaluated at recombination. The other two weight functions are

$$q_{\gamma^i} = \frac{3\Omega_{\mathrm{m}} H_0^2}{2c^2} \frac{\chi}{a(\chi)} \int_\chi^{\chi_h} \mathrm{d}\chi' \frac{n_{\mathrm{s}}^i(z(\chi')) \frac{\mathrm{d}z}{\mathrm{d}\chi'}}{\bar{n}_s^i} \frac{\chi' - \chi}{\chi'}, \tag{9.21}$$

for the weak lensing shear galaxy fields and

$$q_\delta = b_{\mathrm{g}}^i \frac{n_{\mathrm{g}}^i(z(\chi))}{\bar{n}_{\mathrm{g}}^i} \frac{\mathrm{d}z}{\mathrm{d}\chi}, \tag{9.22}$$

for the galaxy clustering overdensity field. In these expressions, $n_s^i(z)$ and $n_{\mathrm{g}}^i(z)$ are the redshift distribution corresponding to the i-th redshift bin of the source and tracer galaxies (see Figure 9.1), and $\bar{n}_s^i$ and $\bar{n}_{\mathrm{g}}^i$ are the mean galaxy distribution of the redshift bin of their respective galaxy population. The galaxy clustering bias is parametrized additively, as usual, by b_{g}^i.

In addition to the galaxy clustering bias, we have to introduce the effects affecting the shear field: the intrinsic alignments and the multiplicative bias. The intrinsic alignments are introduced in the shear field by changing the kernel function

$$q_{\gamma^i} \to q_{\gamma^i} - A(z(\chi)) \frac{n_{\mathrm{s}}^i(z(\chi))}{\bar{n}_s^i} \frac{\mathrm{d}z}{\mathrm{d}\chi}, \tag{9.23}$$

where

$$A(z) = A_{\mathrm{IA},0} \left(\frac{1+z}{1+z_0}\right)^{\eta_{\mathrm{IA}}} \frac{0.0139\Omega_{\mathrm{m}}}{D(z)}, \tag{9.24}$$

[4] `https://github.com/LSSTDESC/CCL`

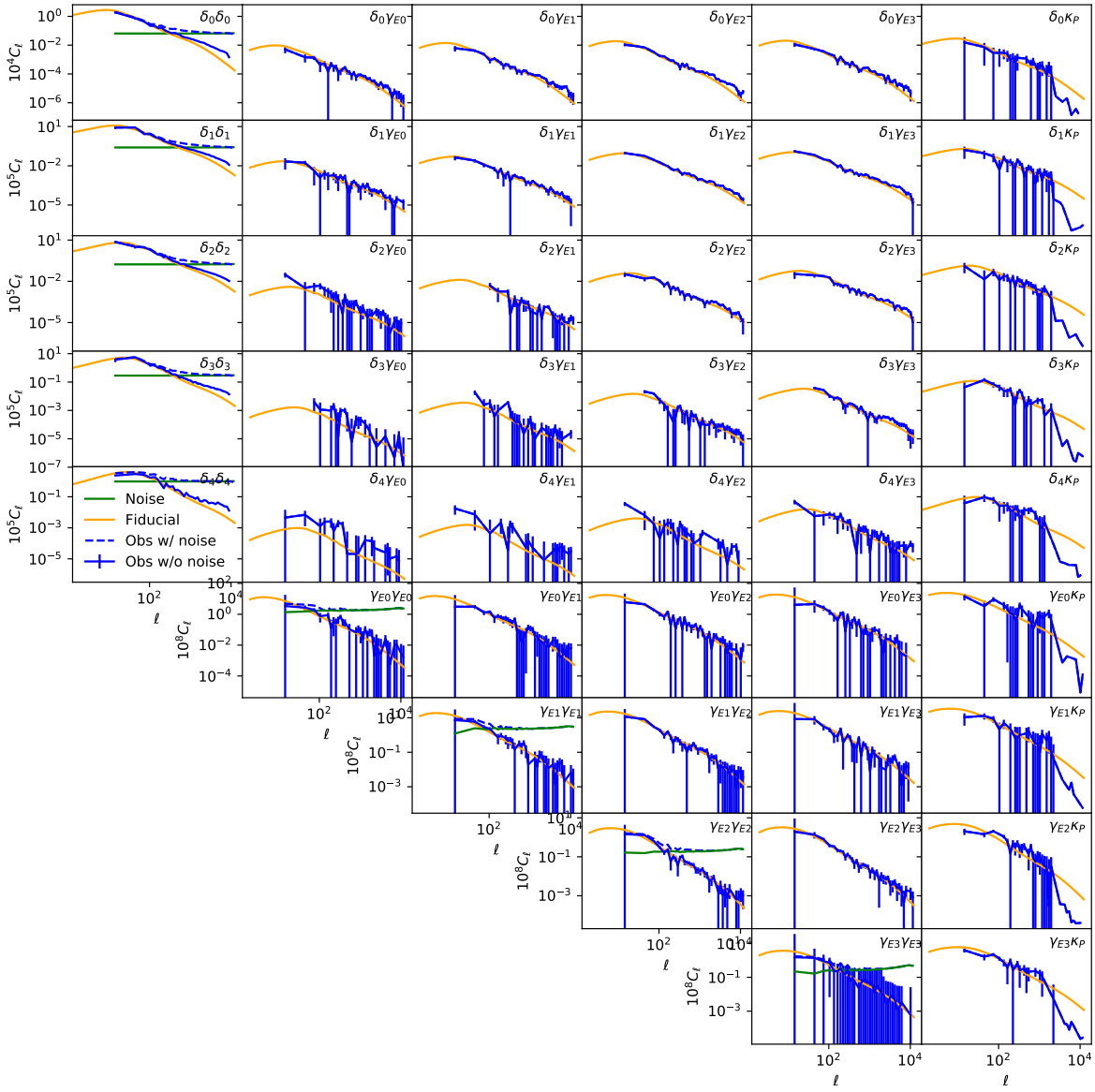

Figure 9.2: Angular power spectra used in our study. They are the auto and cross correlations for galaxy clustering (δ), shear-E mode (γ_E) and CMB weak lensing convergence (κ) fields, from DES and Planck collaborations, respectively. We have overplotted the observed power spectra of DES and Planck surveys with its approximated error (blue) and the fiducial power spectra theoretically parametrized (orange). In addition, we have included the noise contribution (green). The dashed-blue line correspond to the observe power spectra with noise. We have removed for clarity the points for which the numerical computations gave $C_\ell < 0$. The theoretical C_ℓ have been computed with `CCL` with $\Omega_{\rm cdm} = 0.2121$, $\Omega_{\rm b} = 0.0479$, $h = 0.685$, $\sigma_8 = 0.821$ and $n_{\rm s} = 0.973$ and biases $b_{\rm g}^i = (1.41, 1.60, 1.60, 1.91, 1.96)$.

and where $A_{\rm IA,0}$ and $\eta_{\rm IA}$ are two free parameter, z_0 is the redshift pivot point that is fixed to $z = 0.62$ and $D(z)$ is the linear growth factor. Finally, the multiplicative bias transforms all shear field by a factor $(1+m)^i$; i.e. $e_\alpha^{{\rm obs},i} = (1+m^i)e_\alpha^{{\rm true},i}$. Consequently,

$$C_\ell^{\gamma^i X^j,{\rm obs}} = (1+m)^i C_\ell^{\gamma^i X,{\rm true}}\,, \qquad C_\ell^{\gamma^i\gamma^j,{\rm obs}} = (1+m)^i(1+m)^j C_\ell^{\gamma^i\gamma^j,{\rm true}}\,, \tag{9.25}$$

where we have omitted the shear field component index and explicitly written the redshift bin dependence i, j and $X = \delta$, κ.

For completion, recall that the true redshift distribution is a shifted version of the estimated one; $n^{\rm true}(z) = (n^{\rm obs}(z-\Delta z)$, where Δz depends on each redshift bin (i) and galaxy population type (gt); i.e. $\Delta z = \Delta z^i_{\rm gt}$.

The prior distribution for all free parameters parametrizing the biases ($b^i_{\rm g}$, $A_{\rm IA,0}$, $\eta_{\rm IA}$, m^i and $\Delta z^i_{\rm gt}$) are shown in Table 9.2.

9.2.3 Covariance

Estimating accurately the covariance matrix is of key importance as it will be used to build the likelihood that will be used to constrain the growth redshift evolution in following Sections. The covariance matrix for Large Scale Structure has three main contributions:

- Gaussian or disconnected part. This contribution is the largest of the three. It accounts for the modes scales not causally connected. It comes from the randomly distributed matter perturbations and would be the only contribution if all fields were perfectly Gaussian distributed.

- Non-Gaussian or connected part. It is produced by the interaction of sub-horizon modes, yielding higher order correlations.

- Super Sample Covariance (SSC). It is produced by the mode coupling induced by density perturbations on scales larger than the mapped volume.

In order to estimate the Gaussian part of the covariance matrix we have followed Refs. [3, 385] (Chapter 8) and used the Narrow Kernel Approximation (NKA). The NKA was shown to be an accurate representation of the disconnected part of the covariance matrix and able to recover the correct posterior distribution of cosmological parameters.

In the following lines we will skim through the basics of the NKA. First, let us note that the covariance of a two generic power spectra is given by (Equation 8.35)

$$\mathrm{Cov}(\tilde{C}_\ell^{ab}, \tilde{C}_{\ell'}^{cd}) = \left[K\sum_{\mathbf{k}} \Delta^2 k\; M^a_{\mathbf{lk}}\, M^d_{\mathbf{l'k}} C_k^{ad}\right]\left[K\sum_{\mathbf{q}} \Delta^2 q\; M^b_{\mathbf{lq}}\, M^c_{\mathbf{l'q}} C_q^{bc}\right]^* + (c \leftrightarrow d)\,. \tag{9.26}$$

For LSS power spectra, we can assume that different modes are not highly coupled and make the approximation $M_{\mathbf{kq}} \sim \delta_{kq}$. Furthermore, we can take the power spectra to be constant within the support of the mode coupling matrix as the LSS power spectra is sufficiently slow varying. In this case,

$$C_k^{ad} C_q^{bc} \sim C_{(\ell}^{ad} C_{\ell')}^{bc} \equiv \frac{1}{2}\left(C_\ell^{ad} C_{\ell'}^{bc} + C_{\ell'}^{ad} C_\ell^{bc}\right)\,. \tag{9.27}$$

Using this approximation, the covariance matrix is then given by (Equation 8.36)

$$\mathrm{Cov}(\tilde{C}_\ell^{ab}, \tilde{C}_{\ell'}^{cd}) = K^2 C_{(\ell}^{ad} C_{\ell')}^{bc} W_{\ell\ell'}^{ad} (W_{\ell\ell'}^{bc})^* + (c \leftrightarrow d)\,. \tag{9.28}$$

In curved sky, the angular power spectrum is described by Equation 9.18, and the previous expression becomes (Equation 8.56)

$$\begin{aligned}\mathrm{Cov}(\tilde{C}_\ell^{ab}, \tilde{C}_{\ell'}^{cd}) &= C_{(\ell}^{ad} C_{\ell')}^{bc} \sum_{m=-\ell}^{\ell} \sum_{m=-\ell'}^{\ell'} W_{\ell\ell'}^{ad} (W_{\ell\ell'}^{bc})^* + (c \leftrightarrow d) \\ &= C_{(\ell}^{ad} C_{\ell')}^{bc} \, {}^{ad}_{bc}\mathcal{W} + (c \leftrightarrow d)\,. \end{aligned} \tag{9.29}$$

The value of the symbols $\mathcal{W}$ can be found in the previous Chapter, in Equations 8.63-8.66. These equations do have an extra approximation that we have not mentioned before: they neglect the gradient of the mask. This set of approximations constitute the Narrow Kernel Approximation.

It was shown in Chapter 8 (Ref. [3]) that the NKA accurately estimates the covariance matrix and is able to return the correct posterior distribution of cosmological parameters when used in MCMC's. In order to estimate the covariance matrix with the NKA, we will use its public implementation in `NaMaster` [35].

The non-Gaussian causally connected and super-sample covariance parts have not been considered yet. We will include these contributions in a later stage of the project.

In Figure 9.2 we show the angular power spectra that will enter in our likelihood, obtained with our theoretical approach, together with those from DES and Planck's observations, with the estimated errors. The theoretical power spectra were computed with the fiducial model: $\Omega_{\rm cdm} = 0.2121$, $\Omega_{\rm b} = 0.0479$, $h = 0.685$, $\sigma_8 = 0.821$, $n_{\rm s} = 0.973$ and biases $b_{\rm g}^i = (1.41, 1.60, 1.60, 1.91, 1.96)$; and are compatible with the observed ones, within the scales of interests; i.e. those well approximated linearly and not dominated by noise. Following this idea, we have built the likelihood with the scale cuts in Table 9.4. For galaxy clustering power spectra, $C_\ell^{\delta_i\delta_j}$, we have excluded the non-linear comoving scales above $k_{\rm max} = 0.1\,{\rm h^{-1}Mpc^{-1}}$, related with the maximum ℓ by $\ell_{\rm max} = \chi k_{\rm max}$, with χ the radial comoving distance. For the shear power spectra, $C_\ell^{\gamma_i\gamma_j}$, we removed the scales for which the baryonic effects contributed more than a 2%; i.e. the scales for which $C_\ell^{\rm baryons}/C_\ell^{\rm no\ baryons} - 1 > 2\%$. For the cross galaxy clustering–shear power spectra, $C_\ell^{\delta_i\gamma_j}$, we chose the smallest $\ell_{\rm max}$ given by previous methods. For the power spectra involving the CMB convergence field, $C_\ell^{\delta_i\kappa}$ and $C_\ell^{\gamma_i\kappa}$, we chose the method used for the $\delta_i\delta_j$ and $\gamma_i\gamma_j$ cases, respectively. Finally, the reconstruction of the convergence map and Planck's beam size (see Section 9.1.2 and Ref. [426]) limits its scales to $8 < \ell < 2000$. All these constraints result on a C_ℓ vector composed of 326 elements.

9.2.4 Parametrization of the growth

We want to find the time evolution of the $S_8(z)$ parameter. Since the ΛCDM power spectra is compatible with observations, we do not want to explore very different regimes. The way we introduce a small deviation from ΛCDM is by a linear perturbation on the linear growth,

$$D(z) \simeq D_{\Lambda{\rm CDM}}(1 + d(z))\,. \tag{9.30}$$

Here we have called $D_{\Lambda{\rm CDM}}$ to the value of the linear growth D in absence of any variation and $d(z)$ the small variation that we have introduce. The main reason to use this parametrization, instead of the more common $f = {\rm d}\log(\delta_{\rm m})/{\rm d}\log(a) = \Omega_{\rm m}^\gamma$, is that Equation 9.30 easily propagates to the definition of the power spectra, which is then given by

$$P_k = (1 + d(z))^2 P_{\Lambda{\rm CDM}}\,. \tag{9.31}$$

This makes our computations much simpler and can be easily generalized.

δ_1- 145	δ_2- 225	δ_3- 298	δ_4- 371	δ_5- 435
$\gamma_{E1}-\gamma_{E1}$ 101	$\gamma_{E1}-\gamma_{E2}$ 115	$\gamma_{E1}-\gamma_{E3}$ 129	$\gamma_{E1}-\gamma_{E4}$ 137	$\gamma_{E1}-\kappa$ [8, 172]
	$\gamma_{E2}-\gamma_{E2}$ 135	$\gamma_{E2}-\gamma_{E3}$ 156	$\gamma_{E2}-\gamma_{E4}$ 167	$\gamma_{E2}-\kappa$ [8, 210]
		$\gamma_{E3}-\gamma_{E3}$ 188	$\gamma_{E3}-\gamma_{E4}$ 207	$\gamma_{E3}-\kappa$ [8, 263]
			$\gamma_{E4}-\gamma_{E4}$ 235	$\gamma_{E4}-\kappa$ [8, 325]

Table 9.4: Likelihood scale cuts. The single numbers correspond to the range $[0, \ell_{\rm max}]$, except for the κ field for which it becomes $[8, \ell_{\rm max}]$. These ranges exclude the non-linear scales $k > 0.1\,{\rm h}^{-1}{\rm Mpc}^{-1}$ for the power spectra involving galaxy clustering and scales for which the baryonic effects contribute more than 2% for the rest. More information about our choice of scale cuts can be found in the text. The CMB convergence field, κ, is restricted to scales $8 < \ell < 2000$ [426], limiting the lower scales of the C_ℓ. Note that this is also true for the $C_\ell^{\delta_i\kappa}$, although we have omitted it from the table for clarity.

In order to investigate the evolution of $S_8(z)$, we will parametrize $d(z)$, obtain the corresponding power spectrum and compare it with the observed one. Using a Metropolis-Hasting algorithm we will explore the parameter space and find the observable-compatible evolution of $d(z)$ and, in turn, of $S_8(z)$.

The first parametrization that we will explore, is the naive polynomial expansion. We will go up to fourth order; i.e.

$$d(z) = \sum_{n=1}^{4} d_n \left(\frac{z}{1+z}\right)^n . \tag{9.32}$$

Note that $z/(1+z) = 1-a$; i.e we are Taylor expanding around $z = 0$ and that we have removed the zeroth-order term d_0 because it is degenerated with the amplitude of the primordial scalar perturbations, $A_{\rm s}$.

9.3 Preliminary results: testing the Gaussian covariance matrix and the modified growth with d_1

We implemented the likelihood as described in the previous Section in `MontePython` [36, 37]. Using the prior distributions shown in Table 9.2 we run a Monte Carlo Markov Chain (MCMC) with the Metropolis-Hastings algorithm [38, 39]. We determined convergence with the Gelman-Rubin criterion [340], requiring $R < 0.01$.

First, we have to test the goodness of the estimation of the Gaussian covariance matrix. For that, we run a MCMC without modifying the growth; i.e. we replicate DES work [22]. As can be see in Table 9.5, we find constraints that are compatible with those of DES [22]. However, the χ^2 of the best-fit model, $\chi^2 = 462$, is high for the number of degrees of freedom (d.o.f.) that we have. In fact, the power spectrum vector size is 326 and the number of free parameters is 25, making d.o.f. $= 326 - 25 = 301$. Then, $\chi^2/{\rm d.o.f.} = 1.53$, which is far from 1. This could be consequence of having only taken into account the Gaussian part of the likelihood, when it is known that in most cases one cannot neglect the non-Gaussian parts [383]. However, it could also be that our fiducial model is not accurate enough as some parameters ($h = 0.685$

	ΛCDM		Modified Growth			ΛCDM		Modified Growth	
Param.	best-fit	mean$\pm\sigma$	best-fit	mean$\pm\sigma$	Param.	best-fit	mean$\pm\sigma$	best-fit	mean$\pm\sigma$
Cosmology									
Varied					**Derived**				
d_1	...	...	-0.24	$-0.26^{+0.22}_{-0.29}$					
$10^9 A_s$	1.96	$2.02^{+0.27}_{-0.49}$	2.13	$2.40^{+0.44}_{-0.71}$					
n_s	0.974	$0.956^{+0.041}_{-0.084}$	0.889	$0.961^{+0.036}_{-0.087}$	Ω_m	0.259	$0.284^{+0.028}_{-0.041}$	0.256	$0.274^{+0.026}_{-0.040}$
$10^2\Omega_b$	5.00	$4.23^{+0.40}_{-1.2}$	4.26	$4.16^{+0.40}_{-1.1}$	S_8	0.806	0.783 ± 0.029	0.844	0.845 ± 0.067
Ω_{cdm}	0.209	$0.242^{+0.027}_{-0.041}$	0.214	$0.233^{+0.024}_{-0.040}$	σ_8	0.868	0.811 ± 0.074	0.914	0.89 ± 0.11
h_0	0.837	$0.713^{+0.091}_{-0.11}$	0.837	0.730 ± 0.093					
Nuisance									
Galaxy bias					**Lens photo-z bias** ($\times 10^3$)				
b_g^1	1.34	$1.43^{+0.12}_{-0.15}$	1.32	$1.37^{+0.12}_{-0.16}$	Δz_g^1	-5.7	-4.7 ± 6.7	-5.5	-4.5 ± 6.7
b_g^2	1.67	$1.79^{+0.15}_{-0.18}$	1.65	$1.76^{+0.13}_{-0.18}$	Δz_g^2	3.3	2.2 ± 6.5	3.2	2.9 ± 6.5
b_g^3	1.61	$1.72^{+0.14}_{-0.17}$	1.62	$1.74^{+0.13}_{-0.17}$	Δz_g^3	-7.4	-3.7 ± 5.6	0.8	-3.2 ± 5.6
b_g^4	2.01	$2.12^{+0.16}_{-0.20}$	2.03	$2.19^{+0.17}_{-0.22}$	Δz_g^4	-1.2	-0.4 ± 8.8	4.7	0.7 ± 8.9
b_g^5	2.08	$2.20^{+0.17}_{-0.21}$	2.14	$2.30^{+0.20}_{-0.25}$	Δz_g^5	-1.7	2.0 ± 9.8	-1.5	2.0 ± 9.7
Shear Calibration bias					**Source photo-z bias**				
m^1	0.000	0.013 ± 0.023	0.018	0.013 ± 0.023	Δz_s^1	-0.012	-0.001 ± 0.014	0.000	-0.001 ± 0.014
m^2	0.017	0.006 ± 0.022	0.009	0.004 ± 0.022	Δz_s^2	0.000	0.003 ± 0.011	0.007	0.003 ± 0.011
m^3	0.038	0.031 ± 0.021	0.024	0.028 ± 0.021	Δz_s^3	0.003	0.0025 ± 0.0096	0.009	0.0016 ± 0.0097
m^4	-0.012	0.006 ± 0.021	0.012	0.009 ± 0.021	Δz_s^4	-0.004	-0.007 ± 0.019	-0.012	-0.013 ± 0.020
Intrinsic Alignments									
$A_{IA,0}$	0.26	$0.32^{+0.13}_{-0.15}$	0.33	$0.34^{+0.13}_{-0.15}$	η_{IA}	-4.3	$-1.68^{-3.2}_{+0.90}$	-2.8	$-2.15^{+0.70}_{-2.8}$

Table 9.5: Best fit, mean posterior distribution values and 68% C. L. ranges obtained with DES galaxy clustering and shear maps and Planck's CMB convergence field map. We show the cases with and without modified growth. The results of the ΛCDM case are compatible at 1σ level for most parameters and less than 2σ for all with DES results [22]. The ΛCDM minimum $\chi^2 = 462$ and d.o.f. = 301, so that χ^2/d.o.f. = 1.53. For the modified growth $\chi^2 = 461$ and d.o.f. = 300, so that χ^2/d.o.f. = 1.54. These values are far from 1, indicating that our likelihood is not well estimated. It will be partially caused by the lack of the non-Gaussian parts of the likelihood, which have not been considered so far. In addition, it might point that our Gaussian covariance matrix is not well estimated and need to be recomputed with a better fiducial model. This will be clarified when introduced the non-Gaussian parts of the likelihood.

and the biases $b_i = (1.41, 1.60, 1.60, 1.91, 1.96)$) are a bit far from the best-fit values, although compatible within 1σ (see Table 9.5). Once we have introduced the non-Gaussian parts, it will become clear if we have, or not, to reestimate the Gaussian covariance with a new fiducial model closer to the best fit.

Once the likelihood is correctly estimated, having a χ^2/d.o.f. ~ 1, we will proceed to constrain the modification of the growth (Equation 9.30). Here, we will constrain the polynomial parametrization of the linear perturbation around the ΛCDM growth (Equation 9.32). As a first step, we will only incorporate the linear order, with coefficient d_1. This will be just a skim to show the prospects of this project. In the future, a more complex parametrization or other statistical techniques, such as Gaussian processes, will be explored in order to accurately describe the evolution of $S_8(z)$.

For now, we have constrained the parameter d_1, with an uninformative unbounded prior distribution, together with all the other parameters shown in Table 9.2 with their priors. The

results are shown in Table 9.5 and are compatible with the case with no modified growth. In fact, $d_1 = -0.26^{+0.22}_{-0.29}$; i.e. compatible (at 1.2σ level) with the ΛCDM ($d_1 = 0$) case. As in the previous case with no modified growth, the minimum $\chi^2/\text{d.o.f.} = 1.54$ is far from 1, showing the same kind of concerns mentioned above.

In Figure 9.4, we show the 1- and 2D posterior distributions found in our MCMC for the cases with and without modifying the growth. We have omitted h, Ω_b and n_s as their posterior distribution is dominated by their priors. In addition, all the b^i_g, m^i, Δz^i_g and Δz^i_s have Gaussian posterior distributions. Therefore, we have only included the b^0_g as example. As it was seen from the quantitative results of Table 9.5, the results are compatible. In addition, the posterior distribution of d_1, together with Ω_m, σ_8 and A_s, is shown in Figure 9.5. It slightly prefers negative values, i.e. a lower growth rate than in ΛCDM. Figure 9.5 shows that d_1 is degenerated with A_s, so that if one grows the other is reduced. Consequently, d_1 is anticorrelated with σ_8, i.e. lower values of d_1 push σ_8 to higher values (as a consequence of the higher A_s needed to match the observations).

Finally, we show in Figure 9.3 the kind of result we aim with this work. In it we show the temporal evolution of $S_8(z) = D(z)S_8(z=0)$ compatible with DES and CMB observations for the case with and without modifying the growth. We show the mean and 1σ posterior values. In order to compute those, we computed the growth, $D(z)$, for the mean and 1σ values of the cosmological parameters in Table 9.5. As one could naively expect, the S_8 with the modified growth has wider 1σ regions than that of ΛCDM. This is a consequence of the extra degree of freedom introduced in the analysis, d_1. Furthermore, as we saw before, the evolutions of S_8 with and without modifying the growth are compatible, although the former tends to prefer lower values of S_8, specially around $z \sim 2$, favored by the slight negative preference of d_1.

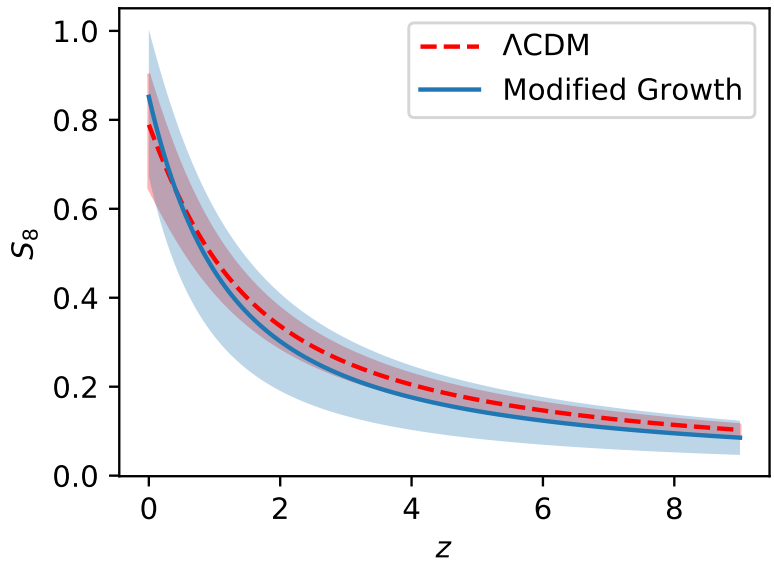

Figure 9.3: $S_8(z)$ evolution for the ΛCDM and modified growth cases. The lines show the evolution predicted with the mean posterior values obtained in the MCMC's. The shaded regions show the regions covered by the S_8 parameter with cosmological parameters at 1σ of the mean value.

9.4 Discussion

In this Chapter we have discussed an ongoing project on the study of the S_8 tension. For that, we have used the DES Y1 catalogs [429, 430] to build 5 different maps of galaxy clustering and 4 maps of the shear field. These correspond to 5 and 4 redshift bins that reach $z \sim 0.9$ and $z \sim 1.3$ (see Table 9.1), respectively. In addition, we included Planck's CMB convergence field map [426].

We implemented the likelihood in MontePython in order to find the constraints to the evolution of S_8. The likelihood was estimated with the Narrow Kernel Approximation [3, 385], presented in Chapter 8. This was shown to be fast and accurate and reliable in MCMC's. At the current stage of the project, the only part of the likelihood taken into account has been the Gaussian part. In the future, we will also include the non-Gaussian terms: the causally connected part and the super-sample covariance.

We tested the likelihood by reproducing DES results [22]. We found compatible results, although the best fit $\chi^2/\text{d.o.f.} = 1.53$ is far from 1. One of the reasons for this discrepancy must be the lack of the non-Gaussian parts of the covariance matrix, which are known to be necessary in most cases [383]. In addition, it could also be that the fiducial model we used to estimate the Gaussian part of the likelihood is not accurate enough, although the largest differences with the best-fit model are within the 1σ confidence level. Once we have introduced the non-Gaussian parts of the likelihood it will become clear if we need to reestimate the Gaussian part with a new fiducial model closer to the best fit.

Nevertheless, for the shake of showing the kind of results we aim with this project, we have constrained the evolution of $S_8(z)$ in a more general case that accounts for small deviations from the ΛCDM growth (Equation 9.30). For simplicity, we have just considered a linear order perturbation of $D_{\Lambda\text{CDM}}$, so that it becomes $D(z) = [1 + d_1(1-a)]D_{\Lambda\text{CDM}}(z)$. DES and CMB observations constrained $d_1 = -0.26^{+0.22}_{-0.29}$, being compatible (at 1.2σ) with the exact ΛCDM evolution. The other parameters varied were also compatible with ΛCDM results (see Figure 9.4 and Table 9.5). It was shown that d_1 is anticorrelated with σ_8 and A_s, meaning that slower growth histories push A_s (and, consequently, σ_8) to higher values in order to match the observations. The evolutions of $S_8(z)$ (Figure 9.3) obtained with and without having modified the growth yield compatible results, in consonance with the other parameters. The main difference is the larger uncertainty area on $S_8(z)$ when the growth is modified, which allows lower values, especially around $z \sim 2$.

In the future, we will include the non-Gaussian parts of the likelihood, which will reveal if the minimum $\chi^2/\text{d.o.f.} \sim 1$. In case it is kept far from 1, we will then need to reestimate the Gaussian part of the likelihood. Once we are able to correctly reproduce DES results, we will explore different modifications of the growth and different parametrizations, which will allow us to constrain the $S_8(z)$ evolution. When we have achieved this objective, we will repeat our study with KiDS-450 data [14, 51], which will give us a different evolution of $S_8(z)$. In the end, we will compare the evolutions from DES and KiDS, as we did in Figure 9.3, revealing the moment when both surveys disagree on the estimation of $S_8(z)$. We are confident this will let us gain insight into the S_8 tension.

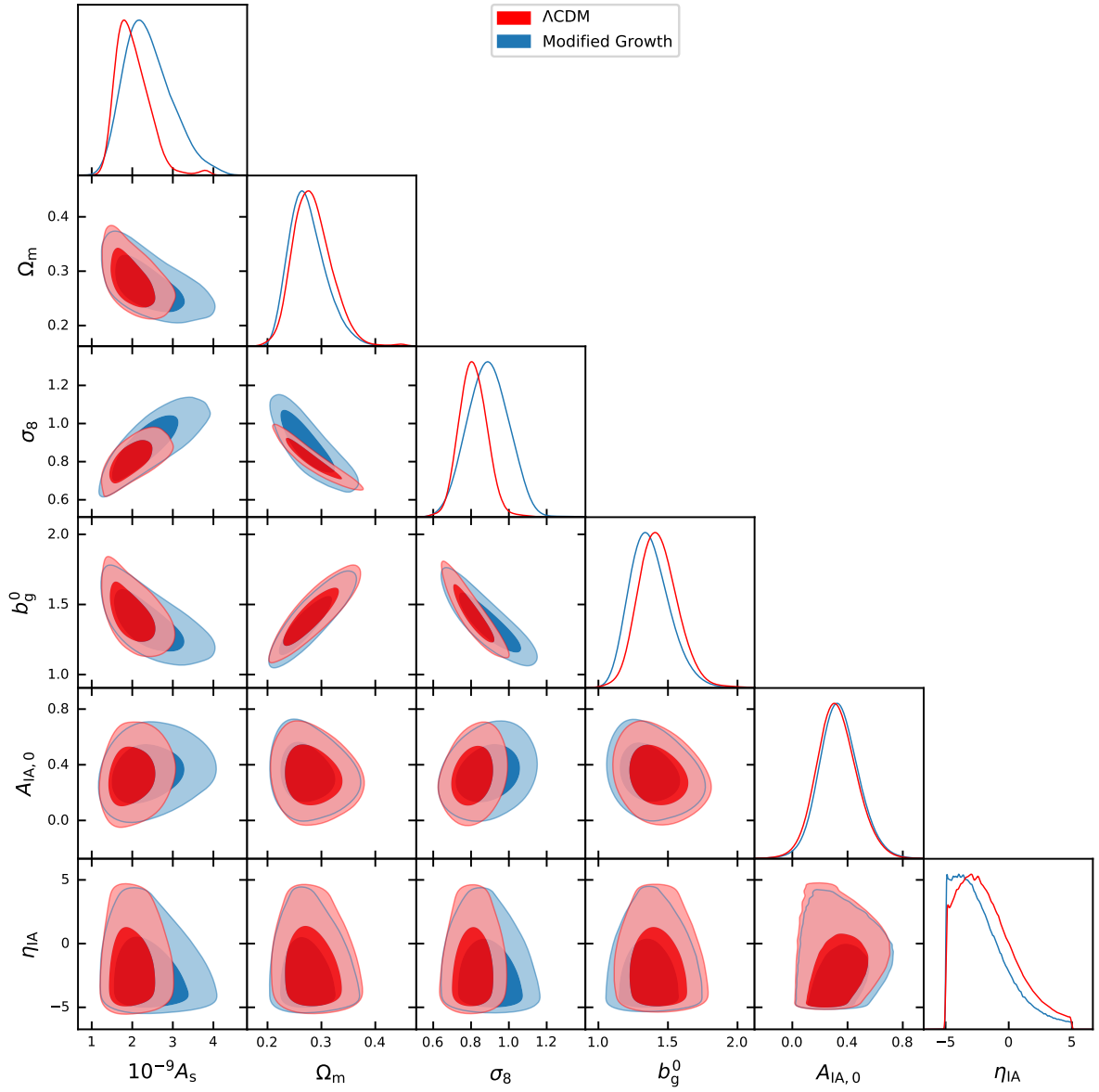

Figure 9.4: Posterior distribution for different parameters of the analysis showing the 1 and 2σ C. L. regions for the case with and without varying growth. We see only a small difference among them, mainly in the σ_8 and A_s parameters, which are pushed to larger values. The distributions of the missing nuisance parameters (Δz^i, m^i, b^i) are Gaussian and similar to that of b_g^1 and have been omitted.

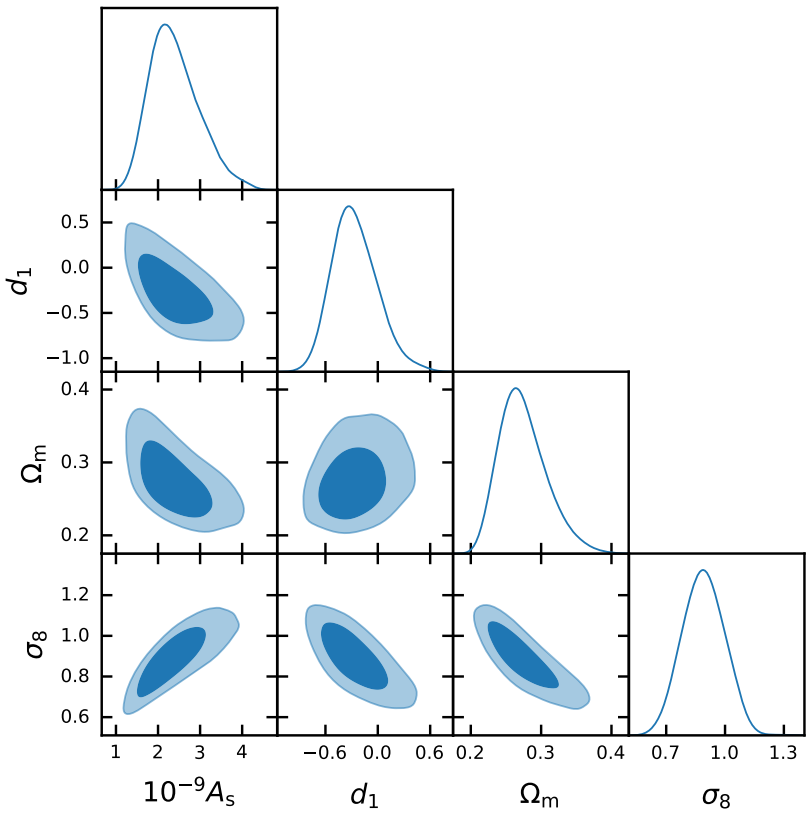

Figure 9.5: Posterior distribution of d_1, σ_8, Ω_m and A_s showing the 1 and 2σ C. L. regions with modified growth.

Part IV

Conclusions

Chapter 10

Conclusions

This Thesis aims to be a contribution on the large quest that is understanding dark energy and the expansion of the Universe. The next decade, with the first observations of the next-generation cosmological surveys, will be an inflection point on our knowledge of the Universe. The amount of data that will be collected and its depth will give us an accurate picture of the structure and evolution of our Universe up to really early times. This will give stringent constraints on the accelerated expansion of the Universe and the growth of structure.

As we have seen, the expansion rate and the structure growth are two topics that are now under debate. There are contradictory estimations that support, or not, the existence of a tension between early (CMB) and late (local) time measurements of the H_0 and σ_8 parameters. These results might be signaling the rupture of the Standard Cosmological Model, ΛCDM. If this is the case, the next-generation data will make it clear. It is, therefore, of vital importance to study alternative cosmological models that could explain these tensions. Furthermore, even in the case the new data supported ΛCDM once again, we will still be challenged by the fundamental problems of ΛCDM. As we saw in Section 2.3, the cosmological constant is highly fine tuned and seems to be incompatible with our knowledge of particle physics, taking into account that the predicted value form the vacuum energy of the Universe disagrees by 120 orders of magnitude with the value compatible with current observations. In comparison, alternative models of Gravity could explain the accelerated expansion without a cosmological constant.

In Chapter 6, we studied the α-attractor dark energy model, a quintessence model that links the accelerated expansion epochs of dark energy and inflation. In this model, the accelerated expansion of the Universe would be driven by a remnant of the scalar field that produced inflation. We showed that the lack of constraints on the initial position of the field allowed for an infinite-large cosmological constant like region in the parameter space. As a consequence, the α-attractor dark energy could, indeed, explain current observations. More interestingly, the increased power of next-generation surveys might be able to distinguish it from ΛCDM up to 3σ.

Although this is an interesting result, it will probably not be the only model able to fit the current observations and be detectable by forthcoming data. In fact, we would have to repeat our analysis with every single model in order to be sure that we are keeping the most favored by data. This is clearly intractable, specially given the amount of data that we will have from next-generation surveys. We need an alternative approach in order to extract the maximum information available in next-generation data. This new procedure will have to be efficient and accurate to match the expected precision on the cosmological parameters (for ΛCDM), which will be of order 1%. We addressed this problem in Chapter 7.

In Chapter 7, instead of looking at individual models, we proposed to parametrize in a common way the functions that characterize their phenomenology. In this way, we could find

the priors that come with the theory itself; i.e. looking just at stability conditions and the requirement of having an accelerated expansion. These priors could then be readily compared with the observational constraints, easily identifying their agreement or disagreement. As a first step to do the same for more general theories, and, finally, for Horndeski, we focused on the simplest modification of General Relativity: quintessence. For quintessence, we showed that the phenomenology of thawing quintessence is well described up to recombination by just two parameters: the usual w_0–w_a. In fact, we proposed an alternative way of obtaining w_0 and w_a: to choose them so that they best reproduce the observables. These derived prior distributions could then be compared with the constraints from current observations. By doing so, we found that large regions of the w_0–w_a space, compatible with observations, were actually excluded by the theoretical priors.

This result exemplifies our idea of how having an accurate parametrization of Horndeski and their corresponding theoretical priors would allow for an efficient validation of Modified Gravity models with observational data. In fact, one would only have to constrain the parameters once with data, and impose the theoretical priors, which is much faster than exploring the posterior distribution with an observational likelihood. In this way, it will easily show the compatibility between theory and data. However, an alternative point of view might be seen more powerful. With no theoretical prior, data can favor regions of the parameter space that are not well motivated by fundamental physics and, therefore, we could end up just translating the cosmological constant problem to more general theories. In this sense, the theoretical priors of models well based on fundamental physics would delimit the parameter space to the subspace compatible with the underlying laws of physics.

Going back to data, it is important to note that the correct estimation of the posterior distribution of the parameter space of any model or parametrization depends on how well described the likelihood is. Estimating the likelihood is not necessarily simple, however. In this Thesis, we have focused on building an accurate approximation of the Gaussian part of the LSS likelihood (Chapter 8), its largest contribution. It has, however, other two contributions that cannot be neglected: the non-Gaussian (connected) and the Super Sample Covariance parts. Although, the Gaussian part can be analytically computed, its exact computation scales as $O(\ell^6_{\rm max})$, which is intractable for the small scales accessible by next-generation surveys, such as LSST. With our approximation, that we called the Narrow Kernel Approximation (NKA), we were able to reproduce correctly the covariance matrix terms involving the galaxy clustering and shear E-mode, with an scaling of $O(\ell^3_{\rm max})$. As a consequence, the NKA was also shown to be able to accurately recover the posterior distribution of the cosmological parameters.

We implemented the NKA in `NaMaster`, a unified framework to work with the pseudo-C_ℓ formalism, developed by the LSST Dark Energy Scientific Collaboration. In addition, the NKA has been already used by the LSST DESC in the analysis of the galaxy clustering Subaru Hyper Suprime-Cam, with which it shares important similarities in depth, bands and primary data reduction and catalog generation. This similitude allows to use its data to test LSST DESC implemented methods [273]. In addition, the NKA is being used in our ongoing project on tracking the growth history of the Universe (Chapter 9), using LSS (DES and, in the near future, KiDS-450) and CMB (Planck) data. The idea with this work is to gain insight into the tension on the σ_8 parameter found by KiDS [14, 51]. For now, we have shown how we estimate the likelihood and compute the theoretical power spectra. In addition, we tested our estimation by comparing with DES results [22] showing compatible results, although with a high χ^2 that might come from the not yet implemented non-Gaussian parts of the likelihood. In order to allow for deviations from ΛCDM, we linearly perturbed its linear growth, $D(z) = [1+d_1(1-a)]D_{\Lambda{\rm CDM}}(z)$, and constrained the d_1 parameter. We obtained the observationally compatible evolution of $S_8(z)$ with and without the modified growth, finding both compatible. In the future, we will

repeat this analysis with KiDS data [14, 51], and obtain its corresponding $S_8(z)$ evolution. By comparing the DES and KiDS $S_8(z)$ results, we aim to identify when (and hopefully why) the DES and KiDS S_8 parameters start to diverge.

As a summary, next-generation surveys will come with unprecedented deep and precise data that will probably finally unravel the evolution history of our Universe. It will definitely show if our Universe can still be described by ΛCDM or a new model will be needed. In this quest for understanding the gravitational interaction on large scales we have investigated suitable models that reproduce current observations and could be detectable with next-generation data (Chapter 6). We have also looked for efficient ways of using forthcoming data by accurately parametrizing general theories of Modified Gravity and finding general and fundamental priors, which can easily show if the parameter space regions favored by data correspond to theories of Gravity well ground on fundamental physics (Chapter 7). Furthermore, we have developed and implemented an accurate and efficient approximation of the Gaussian part of the LSS likelihood (Chapter 8) that is already being used in LSS studies by the LSST Collaboration and ourselves. We are using it on our ongoing project on tracking the growth of structure in the Universe using LSS and CMB data, to explore the S_8 tension shown in KiDS analyses (Chapter 9).

The next years will be of incredible interest for the cosmological and astrophysical community and, probably, the general public. The new unprecedented amount of data, covering large areas of the sky and compiled in a daily basis, will reveal the still hidden parts and events of the cosmos. It will not only improve our knowledge about astrophysics, but might also reveal new astrophysical processes. The forthcoming data will also bring us a precise 3D map of the Large Scale Structure of the Universe, thousands of new SNe Ia, quasars and other objects of interests, giving us a precise description of the evolution history of the Universe. Next years will again test the ever-standing Standard Cosmological Model, ΛCDM, and from this test, the quest for a new dark energy or Modified Gravity Standard Model might begin.

List of acronyms

	Acronym	Meaning
Observations	BAO	Baryon Acoustic Oscillations
	CMB	Cosmic Microwave Background
	FWHM	Full Width at Half Maximum
	GW	Gravitational Wave
	LSS	Large Scale Structure
	QSO	Quasar
	RSD	Redshift Distorsions
	SN	Supernova
	SN Ia	Type Ia Supernova
Software	`CCL`	Core Cosmology Library
	`hi_class`	Horndeski in CLASS
	`CLASS`	Cosmic Linear Anisotropy Solving System
Surveys	ACTPol	Atacama Cosmology Telescope Polarimeter
	BOSS	Baryon Oscillation Spectroscopic Survey
	BOSS DR12	BOSS - Data Release 12
	CFHTLenS	The Canada-France-Hawaii Telescope Lensing Survey
	COBE	Cosmic Background Explorer
	DES	Dark Energy Survey
	DESI	Dark Energy Scientific Instrument
	HST	Hubble Space Telescope
	KAGRA	Kamioka Gravitational Wave Detector
	KiDS	Kilo-Degree Survey
	LIGO	Laser Interferometer Gravitational-Wave Observatory
	LISA	Laser Interferometer Space Antenna
	LSST	Large Synoptic Spectroscopic Telescope
	IPTA	International Pulsar Timing Array
	PTA	Pulsar Timing Array
	SDSS	Sloan Digital Sky Survey
	SKA	Square Kilometer Array
	SNLS	Supernova Legacy Survey
	SPT-3G	South Pole Telescope - 3rd Generation
	WFIRST	Wide Field Infrared Space Telescope
	WMAP	Wilkinson Microwave Anisotropy Probe
Theory	AIC	Akaike Information Criterion
	BIC	Bayesian Information Criterion or Schwartz Information Criterion
	BF	Best fit
	CDM	Cold Dark Matter
	C. L.	Confidence Level

	CPL	Chevallier-Polarski-Linder
	DE	Dark Energy
	EFT	Effective Field Theory
	EP	Equivalence Principle
	EEP	Einstein Equivalence Principle
	EH	Einstein-Hilbert
	FLRW	Friedman-Lemaître-Robertson-Walker
	MG	Modified Gravity
	WEP	Weak Equivalence Principle
	SEP	Strong Equivalence Principle

Table: Main acronyms used in the text.

List of variables

Variable	Meaning	Equation
a	Scale factor	Eq. 2.1
$\alpha_{\rm K}$	Kineticity (Bellini-Sawicki function)	Eq. 4.21
$\alpha_{\rm B}$	Braiding (Bellini-Sawicki function)	Eq. 4.25
$\alpha_{\rm M}$	Planck-mass run rate (Bellini-Sawicki function)	Eq. 4.26
$\alpha_{\rm T}$	Tensor excess (Bellini-Sawicki function)	Eq. 4.27
C_ℓ	Angular power spectrum	Eq. 2.74
c	Speed of light	...
$c_{\rm gw}$	Speed of gravitational waves	...
$c_{\rm s}$	Sound speed	Eq. 2.19
δ_i	Overdensity of fluid i	Eq. 2.18
$D_{\rm A}$	Angular diameter distance	Eq. 2.13
$D_{\rm L}$	Luminous distance	Eq. 2.14
φ	Scalar field	...
ϕ	Scalar field, azimuthal angle or grav. potential. Check in Chapter.	...
Φ	Scalar perturbation to metric $g_{\mu\nu}$	Eq. 2.15
FoM	Figure of Merit	Eq. 6.25
$g_{\mu\nu}$	Metric tensor	Eq. 2.1
g	Metric tensor determinant	Eq. 2.3
G	Gravitational constant	...
$G_{\mu\nu}$	Einstein tensor	Eq. 2.4
$\mathcal{H}$	$\mathcal{H} = aH$	...
H	Hubble parameter	Eq. 2.2
H_0	Current value of Hubble parameter (i.e. $H(z=0)$)	...
h	$H/100\,{\rm Mpc}^{-1}$	...
$\hbar$	Reduced Planck constant	...
$\mathbf{k}$	Wavevector	Eq. 2.28
k	Wavenumber	Eq. 2.28
ℓ	Angular mode	Eq. 2.73
$\mathcal{L}$	Lagrangian	...
$\lambda_{\rm J}$	Jeans scale	Eq. 2.39
Λ	Cosmological constant	Eq. 2.9
M	Absolute magnitude	...
m	Relative magnitude	Eq. 3.65
$M_{\rm P}$	Planck mass	...
$\mathbf{n}$	Direction of line of sight unit vector	Eq. 3.12
n_s	Spectral index	Eq. 2.100
N_ℓ	Noise angular power spectrum	...
Ω_i	Fractional energy density; i.e $8\pi G\rho_i/3H^2$	Eq. 2.7

P	Power spectrum	Eq. 2.70
p_i	Pressure density of fluid i	Eq. 2.4
$\mathcal{P}_\ell$	Legendre polynomial of order ℓ	...
Ψ	Scalar perturbation to metric $g_{\mu\nu}$	Eq. 2.15
r	Tensor-to-scalar ratio	Eq. 2.99
ρ_i	Energy density of fluid i	Eq. 2.4
$R_{\mu\nu}$	Ricci tensor	Eq. 2.4
R	Ricci scalar	Eq. 2.3
S	Action	...
σ	Error or Variance	...
σ_8	Root mean square of δ_m in a sphere of radius $R = 8h^{-1}\,\mathrm{Mpc}$	Eq. 3.20
σ_T	Thomson scattering cross section	Eq. 2.64
S_8	$S_8 = \sigma_8\sqrt{\Omega_m/0.3}$	...
t	Cosmic or proper time	Eq. 2.1
τ	Conformal time	Eq. 2.1
$T_{\mu\nu}$	Energy-momentum tensor	Eq. 2.4
V	Potential	Eq. 2.84
w	Equation of state ($w = p/\rho$)	Eq. 2.5
W	Window function	Eq. 3.54
w^i	Window function of redshift bin i	Eq. 6.18
ξ	Correlation function	Eq. 2.70
$Y_{\ell m}(\theta, \phi)$	The Laplace's spherical harmonics	...
z	Redshift	Eq. 2.11

Table: Main variables used throughout the text. The fluid i can be radiation (r), matter (m), cold dark matter (c or cdm), baryonic matter (b), dark energy (DE), neutrinos (ν), photons (γ), etc. The meaning of some of them might be different in certain parts of the text.

List of notation

Notation	Meaning
f_0	Current value of f; i.e. $f(z=0)$
$f_{\rm ini}$	Initial value of f. Sometimes also written as f_i.
$\bar{f}$	Mean value of f
$\hat{f}$	Estimator of f
δf	Perturbation of f
δ_i	Overdensity; i.e. $\delta f/\bar{f}$
δ_k	Density perturbation in Fourier space with mode k
$\delta_{\mathbf{k}}$	Density perturbation in Fourier space with mode $\mathbf{k}$
∇_μ	Covariant derivative
∇^2	Laplacian; i.e. $\nabla^2 \equiv \nabla^\mu \nabla_\mu$
$\dot{f}$	$\mathrm{d}f/\mathrm{d}t$
$f_{\mathbf{k}}$	Fourier transform of f
$f_{,x}$	$\partial f/\partial x$
f'	$\partial f/\partial \tau$

Table: Common notation used throughout the text. f is a function.

List of Tables

List of Figures

Bibliography

[1] C. García-García, E. V. Linder, P. Ruíz-Lapuente and M. Zumalacárregui, *Dark energy from α-attractors: phenomenology and observational constraints*, *JCAP* **1808** (2018) 022 [1803.00661].

[2] C. García-García, P. Ruíz-Lapuente, D. Alonso and M. Zumalacárregui, *α-attractor dark energy in view of next-generation cosmological surveys*, *JCAP* **1907** (2019) 025 [1905.03753].

[3] C. García-García, D. Alonso and E. Bellini, *Disconnected pseudo-C_l covariances for projected large-scale structure data*, *JCAP* **2019** (2019) 043 [1906.11765].

[4] C. García-García, E. Bellini, P. G. Ferreira, D. Traykova and M. Zumalacárregui, *Theoretical priors in scalar-tensor cosmologies: Thawing quintessence*, *Phys. Rev.* **D101** (2020) 063508 [1911.02868].

[5] C. García-García, D. Alonso, E. Bellini, P. G. Ferreira, E.-M. Mueller and P. Ruiz-Lapuente, *S_8 time evolution in view of KiDS-450, DES-Y1 and Planck CMB data*, *In preparation* [200M.XXXXX].

[6] S. Dodelson, *Modern Cosmology*. Academic Press, Amsterdam, 2003.

[7] S. Weinberg, *Cosmology*. Oxford University Press, Oxford, 2008.

[8] P. Ruiz-Lapuente, *Dark Energy: Observational and Theoretical Approaches*. 2010.

[9] L. Amendola and S. Tsujikawa, *Dark Energy*. Cambridge University Press, 2015.

[10] B. J. T. Jones, *Precision Cosmology: The First Half Million Years*. Cambridge University Press, 2017, 10.1017/CBO9781139027809.

[11] T. Clifton, P. G. Ferreira, A. Padilla and C. Skordis, *Modified gravity and cosmology*, *Physics Reports* **513** (2012) 1 [1106.2476].

[12] L. Heisenberg, *A systematic approach to generalisations of General Relativity and their cosmological implications*, *Phys. Rept.* **796** (2019) 1 [1807.01725].

[13] M. Ishak, *Testing General Relativity in Cosmology*, *Living Rev. Rel.* **22** (2019) 1 [1806.10122].

[14] H. Hildebrandt, M. Viola, C. Heymans, S. Joudaki, K. Kuijken, C. Blake et al., *KiDS-450: cosmological parameter constraints from tomographic weak gravitational lensing*, *MNRAS* **465** (2017) 1454 [1606.05338].

[15] WMAP collaboration, *Nine-Year Wilkinson Microwave Anisotropy Probe (WMAP) Observations: Cosmological Parameter Results*, *Astrophys. J. Suppl.* **208** (2013) 19 [1212.5226].

[16] Planck collaboration, *Planck 2013 results. I. Overview of products and scientific results*, *Astron. Astrophys.* **571** (2014) A1 [1303.5062].

[17] LSST Science, LSST Project collaboration, *LSST Science Book, Version 2.0*, 0912.0201.

[18] A. Font-Ribera, P. McDonald, N. Mostek, B. A. Reid, H.-J. Seo and A. Slosar, *DESI and other dark energy experiments in the era of neutrino mass measurements*, *JCAP* **1405** (2014) 023 [1308.4164].

[19] DESI collaboration, *The DESI Experiment Part I: Science,Targeting, and Survey Design*, 1611.00036.

[20] A. G. Riess, S. Casertano, W. Yuan, L. M. Macri and D. Scolnic, *Large Magellanic Cloud Cepheid Standards Provide a 1% Foundation for the Determination of the Hubble Constant and Stronger Evidence for Physics beyond ΛCDM*, *ApJ* **876** (2019) 85 [1903.07603].

[21] DES collaboration, *Dark Energy Survey year 1 results: Cosmological constraints from galaxy clustering and weak lensing*, *Phys. Rev. D* **98** (2018) 043526 [1708.01530].

[22] DES, SPT collaboration, *Dark Energy Survey Year 1 Results: Joint Analysis of Galaxy Clustering, Galaxy Lensing, and CMB Lensing Two-point Functions*, *Phys. Rev.* **D100** (2019) 023541 [1810.02322].

[23] W. L. Freedman, B. F. Madore, D. Hatt, T. J. Hoyt, I. S. Jang, R. L. Beaton et al., *The Carnegie-Chicago Hubble Program. VIII. An Independent Determination of the Hubble Constant Based on the Tip of the Red Giant Branch*, *ApJ* **882** (2019) 34 [1907.05922].

[24] T. Shanks, L. M. Hogarth and N. Metcalfe, *Gaia Cepheid parallaxes and 'Local Hole' relieve H_0 tension*, *MNRAS* **484** (2019) L64 [1810.02595].

[25] B. Carter, *Large number coincidences and the anthropic principle in cosmology.*, in *Confrontation of Cosmological Theories with Observational Data*, M. S. Longair, ed., vol. 63 of *IAU Symposium*, pp. 291–298, Jan, 1974.

[26] T. Padmanabhan, *Dark Energy: Mystery of the Millennium*, in *Albert Einstein Century International Conference*, J.-M. Alimi and A. Füzfa, eds., vol. 861 of *American Institute of Physics Conference Series*, pp. 179–196, Nov, 2006, astro-ph/0603114, DOI.

[27] G. Dvali, S. Hofmann and J. Khoury, *Degravitation of the cosmological constant and graviton width*, *Phys. Rev. D* **76** (2007) 084006 [hep-th/0703027].

[28] J. M. Ezquiaga and M. Zumalacárregui, *Dark Energy in light of Multi-Messenger Gravitational-Wave astronomy*, *Frontiers in Astronomy and Space Sciences* **5** (2018) 44.

[29] G. W. Horndeski, *Second-order scalar-tensor field equations in a four-dimensional space*, *Int. J. Theor. Phys.* **10** (1974) 363.

[30] D. Blas, J. Lesgourgues and T. Tram, *The Cosmic Linear Anisotropy Solving System (CLASS) II: Approximation schemes*, *JCAP* **1107** (2011) 034 [1104.2933].

[31] M. Zumalacárregui, E. Bellini, I. Sawicki, J. Lesgourgues and P. G. Ferreira, *hi_class: Horndeski in the Cosmic Linear Anisotropy Solving System*, *JCAP* **1708** (2017) 019 [1605.06102].

[32] E. Bellini, I. Sawicki and M. Zumalacárregui, *hi_class: Background Evolution, Initial Conditions and Approximation Schemes*, 1909.01828.

[33] N. E. Chisari, D. Alonso, E. Krause, C. D. Leonard, P. Bull, J. Neveu et al., *Core Cosmology Library: Precision Cosmological Predictions for LSST*, *ApJS* **242** (2019) 2 [1812.05995].

[34] The LSST Dark Energy Science Collaboration, R. Mandelbaum, T. Eifler, R. Hložek, T. Collett, E. Gawiser et al., *The LSST Dark Energy Science Collaboration (DESC) Science Requirements Document*, *arXiv e-prints* (2018) arXiv:1809.01669 [1809.01669].

[35] D. Alonso, J. Sanchez, A. Slosar and LSST Dark Energy Science Collaboration, *A unified pseudo-C_ℓ framework*, *MNRAS* **484** (2019) 4127 [1809.09603].

[36] B. Audren, J. Lesgourgues, K. Benabed and S. Prunet, *Conservative Constraints on Early Cosmology: an illustration of the Monte Python cosmological parameter inference code*, *JCAP* **1302** (2013) 001 [1210.7183].

[37] T. Brinckmann and J. Lesgourgues, *MontePython 3: boosted MCMC sampler and other features*, 1804.07261.

[38] N. Metropolis, A. W. Rosenbluth, M. N. Rosenbluth, A. H. Teller and E. Teller, *Equation of state calculations by fast computing machines*, *J. Chem. Phys.* **21** (1953) 1087.

[39] W. K. Hastings, *Monte Carlo Sampling Methods Using Markov Chains and Their Applications*, *Biometrika* **57** (1970) 97.

[40] J. Goodman and J. Weare, *Ensemble samplers with affine invariance*, *Communications in applied mathematics and computational science* **5** (2010) 65.

[41] D. Foreman-Mackey, D. W. Hogg, D. Lang and J. Goodman, *emcee: The mcmc hammer*, *PASP* **125** (2013) 306 [1202.3665].

[42] J. Akeret, S. Seehars, A. Amara, A. Refregier and A. Csillaghy, *CosmoHammer: Cosmological parameter estimation with the MCMC Hammer*, 1212.1721.

[43] Planck collaboration, *Planck 2018 results. VI. Cosmological parameters*, 1807.06209.

[44] D. J. Fixsen, *The temperature of the cosmic microwave background*, *The Astrophysical Journal* **707** (2009) 916–920.

[45] WMAP collaboration, *First year Wilkinson Microwave Anisotropy Probe (WMAP) observations: Foreground emission*, *Astrophys. J. Suppl.* **148** (2003) 97 [astro-ph/0302208].

[46] Planck collaboration, *Planck 2013 results. XXIII. Isotropy and statistics of the CMB*, *Astron. Astrophys.* **571** (2014) A23 [1303.5083].

[47] Planck collaboration, *Planck 2015 results. XVI. Isotropy and statistics of the CMB*, *Astron. Astrophys.* **594** (2016) A16 [1506.07135].

[48] Planck collaboration, *Planck 2018 results. VII. Isotropy and Statistics of the CMB*, 1906.02552.

[49] BOSS collaboration, *The clustering of galaxies in the completed SDSS-III Baryon Oscillation Spectroscopic Survey: cosmological analysis of the DR12 galaxy sample*, *Mon. Not. Roy. Astron. Soc.* **470** (2017) 2617 [1607.03155].

[50] Planck collaboration, *Planck 2018 results. X. Constraints on inflation*, 1807.06211.

[51] F. Köhlinger et al., *KiDS-450: The tomographic weak lensing power spectrum and constraints on cosmological parameters*, *Mon. Not. Roy. Astron. Soc.* **471** (2017) 4412 [1706.02892].

[52] A. G. Riess, S. Casertano, D. Kenworthy, D. Scolnic and L. Macri, *Seven Problems with the Claims Related to the Hubble Tension in arXiv:1810.02595*, *arXiv e-prints* (2018) arXiv:1810.03526 [1810.03526].

[53] S. M. Carroll, *Spacetime and Geometry: An Introduction to General Relativity*. Cambridge University Press, 2019, 10.1017/9781108770385.

[54] S. Weinberg, *Anthropic bound on the cosmological constant*, *Phys. Rev. Lett.* **59** (1987) 2607.

[55] T. Padmanabhan, *Dark energy and gravity*, *General Relativity and Gravitation* **40** (2008) 529 [0705.2533].

[56] T. Padmanabhan, *Dark Energy and its Implications for Gravity*, *arXiv e-prints* (2008) arXiv:0807.2356 [0807.2356].

[57] C. de Rham, S. Hofmann, J. Khoury and A. J. Tolley, *Cascading gravity and degravitation*, *JCAP* **2008** (2008) 011 [0712.2821].

[58] D. Alonso and P. G. Ferreira, *Constraining ultralarge-scale cosmology with multiple tracers in optical and radio surveys*, *Phys. Rev.* **D92** (2015) 063525 [1507.03550].

[59] J. C. Mather et al., *Measurement of the Cosmic Microwave Background spectrum by the COBE FIRAS instrument*, *Astrophys. J.* **420** (1994) 439.

[60] Supernova Search Team collaboration, *Observational evidence from supernovae for an accelerating universe and a cosmological constant*, *Astron. J.* **116** (1998) 1009 [astro-ph/9805201].

[61] Supernova Cosmology Project collaboration, *Measurements of Omega and Lambda from 42 high redshift supernovae*, *Astrophys. J.* **517** (1999) 565 [astro-ph/9812133].

[62] A. G. Riess et al., *Type Ia Supernova Distances at $z > 1.5$ from the Hubble Space Telescope Multi-Cycle Treasury Programs: The Early Expansion Rate*, 1710.00844.

[63] LIGO Scientific Collaboration and Virgo Collaboration collaboration, *Observation of gravitational waves from a binary black hole merger*, *Phys. Rev. Lett.* **116** (2016) 061102.

[64] C. de Rham and S. Melville, *Gravitational Rainbows: LIGO and Dark Energy at its Cutoff*, *Phys. Rev. Lett.* **121** (2018) 221101 [1806.09417].

[65] L. Lombriser and A. Taylor, *Breaking a Dark Degeneracy with Gravitational Waves*, *JCAP* **1603** (2016) 031 [1509.08458].

[66] D. Bettoni, J. M. Ezquiaga, K. Hinterbichler and M. Zumalacárregui, *Speed of Gravitational Waves and the Fate of Scalar-Tensor Gravity*, *Phys. Rev.* **D95** (2017) 084029 [1608.01982].

[67] J. Sakstein and B. Jain, *Implications of the Neutron Star Merger GW170817 for Cosmological Scalar-Tensor Theories*, *Phys. Rev. Lett.* **119** (2017) 251303 [1710.05893].

[68] P. Creminelli and F. Vernizzi, *Dark Energy after GW170817 and GRB170817A*, *Phys. Rev. Lett.* **119** (2017) 251302 [1710.05877].

[69] J. M. Ezquiaga and M. Zumalacárregui, *Dark Energy After GW170817: Dead Ends and the Road Ahead*, *Phys. Rev. Lett.* **119** (2017) 251304 [1710.05901].

[70] T. Baker, E. Bellini, P. G. Ferreira, M. Lagos, J. Noller and I. Sawicki, *Strong Constraints on Cosmological Gravity from GW170817 and GRB 170817A*, *Phys. Rev. Lett.* **119** (2017) 251301 [1710.06394].

[71] B. P. Abbott, R. Abbott, T. D. Abbott, F. Acernese, K. Ackley, C. Adams et al., *Gravitational Waves and Gamma-Rays from a Binary Neutron Star Merger: GW170817 and GRB 170817A*, *ApJL* **848** (2017) L13 [1710.05834].

[72] B. P. Abbott, R. Abbott, T. D. Abbott, F. Acernese, K. Ackley, C. Adams et al., *A gravitational-wave standard siren measurement of the Hubble constant*, *Nature* **551** (2017) 85 [1710.05835].

[73] E. Calabrese et al., *Precision Epoch of Reionization studies with next-generation CMB experiments*, *JCAP* **1408** (2014) 010 [1406.4794].

[74] SPT-3G collaboration, *SPT-3G: A Next-Generation Cosmic Microwave Background Polarization Experiment on the South Pole Telescope*, *Proc. SPIE Int. Soc. Opt. Eng.* **9153** (2014) 91531P [1407.2973].

[75] BICEP2, Keck Array collaboration, *Improved Constraints on Cosmology and Foregrounds from BICEP2 and Keck Array Cosmic Microwave Background Data with Inclusion of 95 GHz Band*, *Phys. Rev. Lett.* **116** (2016) 031302 [1510.09217].

[76] POLARBEAR collaboration, *The POLARBEAR-2 and the Simons Array Experiment*, *J. Low. Temp. Phys.* **184** (2016) 805 [1512.07299].

[77] K. Abazajian et al., *CMB-S4 Science Case, Reference Design, and Project Plan*, 1907.04473.

[78] D. Spergel et al., *Wide-Field InfraRed Survey Telescope-Astrophysics Focused Telescope Assets WFIRST-AFTA Final Report*, 1305.5422.

[79] EUCLID collaboration, *Euclid Definition Study Report*, 1110.3193.

[80] K. Somiya, *Detector configuration of KAGRA-the Japanese cryogenic gravitational-wave detector*, *Classical and Quantum Gravity* **29** (2012) 124007 [1111.7185].

[81] LIGO Scientific Collaboration, J. Aasi, B. P. Abbott, R. Abbott, T. Abbott, M. R. Abernathy et al., *Advanced LIGO*, *Classical and Quantum Gravity* **32** (2015) 074001 [1411.4547].

[82] F. Acernese, M. Agathos, K. Agatsuma, D. Aisa, N. Allemandou, A. Allocca et al., *Advanced Virgo: a second-generation interferometric gravitational wave detector*, *Classical and Quantum Gravity* **32** (2015) 024001 [1408.3978].

[83] P. Amaro-Seoane, H. Audley, S. Babak, J. Baker, E. Barausse, P. Bender et al., *Laser interferometer space antenna*, 2017.

[84] R. N. Manchester and IPTA, *The International Pulsar Timing Array*, *Classical and Quantum Gravity* **30** (2013) 224010 [1309.7392].

[85] P. E. Dewdney, P. J. Hall, R. T. Schilizzi and T. J. L. W. Lazio, *The Square Kilometre Array*, *IEEE Proceedings* **97** (2009) 1482.

[86] J. Silk, *Cosmic black body radiation and galaxy formation*, *Astrophys. J.* **151** (1968) 459.

[87] S. Joudaki, M. Kaplinghat, R. Keeley and D. Kirkby, *Model independent inference of the expansion history and implications for the growth of structure*, *Phys. Rev.* **D97** (2018) 123501 [1710.04236].

[88] R. K. Sachs and A. M. Wolfe, *Perturbations of a cosmological model and angular variations of the microwave background*, *Astrophys. J.* **147** (1967) 73.

[89] E. Martinez-Gonzalez, J. L. Sanz and J. Silk, *Anisotropies in the Microwave Sky Due to Nonlinear Structures*, *ApJL* **355** (1990) L5.

[90] W. Hu and M. J. White, *A CMB polarization primer*, *New Astron.* **2** (1997) 323 [astro-ph/9706147].

[91] M. J. Rees and D. W. Sciama, *Large scale Density Inhomogeneities in the Universe*, *Nature* **217** (1968) 511.

[92] K. N. Abazajian, P. Adshead, Z. Ahmed, S. W. Allen, D. Alonso, K. S. Arnold et al., *CMB-S4 Science Book, First Edition*, *arXiv e-prints* (2016) arXiv:1610.02743 [1610.02743].

[93] A. S. Bolton, D. J. Schlegel, É. Aubourg, S. Bailey, V. Bhardwaj, J. R. Brownstein et al., *Spectral Classification and Redshift Measurement for the SDSS-III Baryon Oscillation Spectroscopic Survey*, *Astron. Journal* **144** (2012) 144 [1207.7326].

[94] A. Dey, D. J. Schlegel, D. Lang, R. Blum, K. Burleigh, X. Fan et al., *Overview of the DESI Legacy Imaging Surveys*, *Astron. Journal* **157** (2019) 168 [1804.08657].

[95] N. Kaiser, *Clustering in real space and in redshift space*, *MNRAS* **227** (1987) 1.

[96] É. Aubourg, S. Bailey, J. E. Bautista, F. Beutler, V. Bhardwaj, D. Bizyaev et al., *Cosmological implications of baryon acoustic oscillation measurements*, *Phys. Rev. D* **92** (2015) 123516 [1411.1074].

[97] E. V. Linder, *Cosmic growth history and expansion history*, *Phys. Rev. D* **72** (2005) 043529 [astro-ph/0507263].

[98] E. V. Linder and R. N. Cahn, *Parameterized beyond-Einstein growth*, *Astroparticle Physics* **28** (2007) 481 [astro-ph/0701317].

[99] A. J. S. Hamilton, *Measuring Omega and the Real Correlation Function from the Redshift Correlation Function*, *ApJL* **385** (1992) L5.

[100] W. Saunders, M. Rowan-Robinson and A. Lawrence, *The spatial correlation function of IRAS galaxies on small and intermediate scales*, *MNRAS* **258** (1992) 134.

[101] N. Kaiser, *Weak Gravitational Lensing of Distant Galaxies*, *ApJ* **388** (1992) 272.

[102] W. Hu, *Power Spectrum Tomography with Weak Lensing*, *ApJL* **522** (1999) L21 [astro-ph/9904153].

[103] S. A. Thomas, F. B. Abdalla and J. Weller, *Constraining modified gravity and growth with weak lensing*, *MNRAS* **395** (2009) 197 [0810.4863].

[104] R. Mandelbaum, U. Seljak, R. J. Cool, M. Blanton, C. M. Hirata and J. Brinkmann, *Density profiles of galaxy groups and clusters from SDSS galaxy-galaxy weak lensing*, *MNRAS* **372** (2006) 758 [astro-ph/0605476].

[105] W. Godłowski, *Remarks on the Methods of Investigations of Alignment of Galaxies*, *ApJ* **747** (2012) 7 [1110.2245].

[106] C. Li, Y. P. Jing, A. Faltenbacher and J. Wang, *The Detection of the Large-scale Alignment of Massive Galaxies at z ~0.6*, *ApJL* **770** (2013) L12 [1303.1965].

[107] A. Tenneti, S. Singh, R. Mandelbaum, T. di Matteo, Y. Feng and N. Khandai, *Intrinsic alignments of galaxies in the MassiveBlack-II simulation: analysis of two-point statistics*, *MNRAS* **448** (2015) 3522 [1409.7297].

[108] Y. Rong, S.-X. Yi, S.-N. Zhang and H. Tu, *Radial alignment of elliptical galaxies by the tidal force of a cluster of galaxies*, *MNRAS* **451** (2015) 2536 [1506.01800].

[109] N. Chisari, S. Codis, C. Laigle, Y. Dubois, C. Pichon, J. Devriendt et al., *Intrinsic alignments of galaxies in the Horizon-AGN cosmological hydrodynamical simulation*, *MNRAS* **454** (2015) 2736 [1507.07843].

[110] S. Hilbert, D. Xu, P. Schneider, V. Springel, M. Vogelsberger and L. Hernquist, *Intrinsic alignments of galaxies in the Illustris simulation*, *MNRAS* **468** (2017) 790 [1606.03216].

[111] T. Okumura and Y. P. Jing, *The Gravitational Shear-Intrinsic Ellipticity Correlation Functions of Luminous Red Galaxies in Observation and in the ΛCDM Model*, *ApJL* **694** (2009) L83 [0812.2935].

[112] R. Mandelbaum, C. Blake, S. Bridle, F. B. Abdalla, S. Brough, M. Colless et al., *The WiggleZ Dark Energy Survey: direct constraints on blue galaxy intrinsic alignments at intermediate redshifts*, *MNRAS* **410** (2011) 844 [0911.5347].

[113] B. Joachimi, R. Mandelbaum, F. B. Abdalla and S. L. Bridle, *Constraints on intrinsic alignment contamination of weak lensing surveys using the MegaZ-LRG sample*, *A&A* **527** (2011) A26 [1008.3491].

[114] J. Blazek, R. Mandelbaum, U. Seljak and R. Nakajima, *Separating intrinsic alignment and galaxy-galaxy lensing*, *JCAP* **2012** (2012) 041 [1204.2264].

[115] S. Singh, R. Mandelbaum and S. More, *Intrinsic alignments of SDSS-III BOSS LOWZ sample galaxies*, *MNRAS* **450** (2015) 2195 [1411.1755].

[116] M. Tonegawa, T. Okumura, T. Totani, G. Dalton, K. Glazebrook and K. Yabe, *The Subaru FMOS galaxy redshift survey (FastSound). V. Intrinsic alignments of emission-line galaxies at $z \sim 1.4$*, *Publications of the ASJ* **70** (2018) 41 [1708.02224].

[117] R. Massey, H. Hoekstra, T. Kitching, J. Rhodes, M. Cropper, J. Amiaux et al., *Origins of weak lensing systematics, and requirements on future instrumentation (or knowledge of instrumentation)*, *MNRAS* **429** (2013) 661 [1210.7690].

[118] J. T. A. de Jong, G. A. Verdoes Kleijn, K. H. Kuijken and E. A. Valentijn, *The Kilo-Degree Survey*, *Experimental Astronomy* **35** (2013) 25 [1206.1254].

[119] A. G. Riess, W. H. Press and R. P. Kirshner, *Using SN-Ia light curve shapes to measure the Hubble constant*, *Astrophys. J.* **438** (1995) L17 [astro-ph/9410054].

[120] Supernova Cosmology Project collaboration, *Measurements of the cosmological parameters Omega and Lambda from the first 7 supernovae at z¿=0.35*, *Astrophys. J.* **483** (1997) 565 [astro-ph/9608192].

[121] M. Sullivan, A. Conley, D. A. Howell, J. D. Neill, P. Astier, C. Balland et al., *The dependence of Type Ia Supernovae luminosities on their host galaxies*, *MNRAS* **406** (2010) 782 [1003.5119].

[122] N. Suzuki, D. Rubin, C. Lidman, G. Aldering, R. Amanullah, K. Barbary et al., *The Hubble Space Telescope Cluster Supernova Survey. V. Improving the Dark-energy Constraints above z > 1 and Building an Early-type-hosted Supernova Sample*, *ApJ* **746** (2012) 85 [1105.3470].

[123] R. Amanullah, C. Lidman, D. Rubin, G. Aldering, P. Astier, K. Barbary et al., *Spectra and Hubble Space Telescope Light Curves of Six Type Ia Supernovae at 0.511 < z < 1.12 and the Union2 Compilation*, *ApJ* **716** (2010) 712 [1004.1711].

[124] D. M. Scolnic et al., *The Complete Light-curve Sample of Spectroscopically Confirmed Type Ia Supernovae from Pan-STARRS1 and Cosmological Constraints from The Combined Pantheon Sample*, 1710.00845.

[125] A. Rest, D. Scolnic, R. J. Foley, M. E. Huber, R. Chornock, G. Narayan et al., *Cosmological Constraints from Measurements of Type Ia Supernovae Discovered during the First 1.5 yr of the Pan-STARRS1 Survey*, *ApJ* **795** (2014) 44 [1310.3828].

[126] D. Scolnic, A. Rest, A. Riess, M. E. Huber, R. J. Foley, D. Brout et al., *Systematic Uncertainties Associated with the Cosmological Analysis of the First Pan-STARRS1 Type Ia Supernova Sample*, *ApJ* **795** (2014) 45 [1310.3824].

[127] A. G. Riess, R. P. Kirshner, B. P. Schmidt, S. Jha, P. Challis, P. M. Garnavich et al., *BVRI Light Curves for 22 Type IA Supernovae*, *Astron. Journal* **117** (1999) 707 [astro-ph/9810291].

[128] S. Jha, R. P. Kirshner, P. Challis, P. M. Garnavich, T. Matheson, A. M. Soderberg et al., *UBVRI Light Curves of 44 Type Ia Supernovae*, *Astron. Journal* **131** (2006) 527 [astro-ph/0509234].

[129] M. Hicken, P. Challis, S. Jha, R. P. Kirshner, T. Matheson, M. Modjaz et al., *CfA3: 185 Type Ia Supernova Light Curves from the CfA*, *ApJ* **700** (2009) 331 [0901.4787].

[130] C. Contreras, M. Hamuy, M. M. Phillips, G. Folatelli, N. B. Suntzeff, S. E. Persson et al., *The Carnegie Supernova Project: First Photometry Data Release of Low-Redshift Type Ia Supernovae*, *Astron. Journal* **139** (2010) 519 [0910.3330].

[131] G. Folatelli, M. M. Phillips, C. R. Burns, C. Contreras, M. Hamuy, W. L. Freedman et al., *The Carnegie Supernova Project: Analysis of the First Sample of Low-Redshift Type-Ia Supernovae*, *Astron. Journal* **139** (2010) 120 [0910.3317].

[132] M. D. Stritzinger, M. M. Phillips, L. N. Boldt, C. Burns, A. Campillay, C. Contreras et al., *The Carnegie Supernova Project: Second Photometry Data Release of Low-redshift Type Ia Supernovae*, *Astron. Journal* **142** (2011) 156 [1108.3108].

[133] J. A. Frieman, B. Bassett, A. Becker, C. Choi, D. Cinabro, F. DeJongh et al., *The Sloan Digital Sky Survey-II Supernova Survey: Technical Summary*, *Astron. Journal* **135** (2008) 338 [0708.2749].

[134] R. Kessler, A. C. Becker, D. Cinabro, J. Vand erplas, J. A. Frieman, J. Marriner et al., *First-Year Sloan Digital Sky Survey-II Supernova Results: Hubble Diagram and Cosmological Parameters*, *ApJS* **185** (2009) 32 [0908.4274].

[135] M. Sako, B. Bassett, A. C. Becker, P. J. Brown, H. Campbell, R. Wolf et al., *The data release of the sloan digital sky survey-ii supernova survey*, *Publications of the Astronomical Society of the Pacific* **130** (2018) 064002.

[136] J. Guy, M. Sullivan, A. Conley, N. Regnault, P. Astier, C. Balland et al., *The Supernova Legacy Survey 3-year sample: Type Ia supernovae photometric distances and cosmological constraints*, *A&A* **523** (2010) A7 [1010.4743].

[137] M. Sullivan, J. Guy, A. Conley, N. Regnault, P. Astier, C. Balland et al., *SNLS3: Constraints on Dark Energy Combining the Supernova Legacy Survey Three-year Data with Other Probes*, *ApJ* **737** (2011) 102 [1104.1444].

[138] A. Conley, J. Guy, M. Sullivan, N. Regnault, P. Astier, C. Balland et al., *Supernova Constraints and Systematic Uncertainties from the First Three Years of the Supernova Legacy Survey*, *ApJS* **192** (2011) 1 [1104.1443].

[139] A. G. Riess, P. E. Nugent, R. L. Gilliland, B. P. Schmidt, J. Tonry, M. Dickinson et al., *The Farthest Known Supernova: Support for an Accelerating Universe and a Glimpse of the Epoch of Deceleration*, *ApJ* **560** (2001) 49 [astro-ph/0104455].

[140] Supernova Search Team collaboration, *Type Ia supernova discoveries at z ¿ 1 from the Hubble Space Telescope: Evidence for past deceleration and constraints on dark energy evolution*, *Astrophys. J.* **607** (2004) 665 [astro-ph/0402512].

[141] Supernova Cosmology Project collaboration, *Precision Measurement of The Most Distant Spectroscopically-Confirmed Supernova Ia with the Hubble Space Telescope*, *Astrophys. J.* **763** (2013) 35 [1205.3494].

[142] A. G. Riess et al., *New Hubble Space Telescope Discoveries of Type Ia Supernovae at z¿=1: Narrowing Constraints on the Early Behavior of Dark Energy*, *Astrophys. J.* **659** (2007) 98 [astro-ph/0611572].

[143] O. Graur, S. A. Rodney, D. Maoz, A. G. Riess, S. W. Jha, M. Postman et al., *Type-Ia Supernova Rates to Redshift 2.4 from CLASH: The Cluster Lensing And Supernova Survey with Hubble*, *ApJ* **783** (2014) 28 [1310.3495].

[144] S. A. Rodney, A. G. Riess, L.-G. Strolger, T. Dahlen, O. Graur, S. Casertano et al., *Type Ia Supernova Rate Measurements to Redshift 2.5 from CANDELS: Searching for Prompt Explosions in the Early Universe*, *Astron. Journal* **148** (2014) 13 [1401.7978].

[145] W. L. Freedman and B. F. Madore, *The Hubble Constant*, *ARA&A* **48** (2010) 673 [1004.1856].

[146] S. H. Suyu et al., *H0LiCOW – I. H0 Lenses in COSMOGRAIL's Wellspring: program overview*, *Mon. Not. Roy. Astron. Soc.* **468** (2017) 2590 [1607.00017].

[147] K. C. Wong et al., *H0LiCOW XIII. A 2.4% measurement of H_0 from lensed quasars: 5.3σ tension between early and late-Universe probes*, 1907.04869.

[148] K. Blum, E. Castorina and M. Simonović, *Could quasar lensing time delays hint to cored dark matter halos, instead of H_0 tension?*, 2001.07182.

[149] Gaia Collaboration, A. G. A. Brown, A. Vallenari, T. Prusti, J. H. J. de Bruijne, C. Babusiaux et al., *Gaia Data Release 2. Summary of the contents and survey properties*, *A&A* **616** (2018) A1 [1804.09365].

[150] T. Shanks, L. Hogarth and N. Metcalfe, *H_0 Tension: Response to Riess et al arXiv:1810.03526*, *arXiv e-prints* (2018) arXiv:1810.07628 [1810.07628].

[151] D. Scolnic, S. Perlmutter, G. Aldering, D. Brout, T. Davis, A. Filippenko et al., *The Next Generation of Cosmological Measurements with Type Ia Supernovae*, *Astro2020: Decadal Survey on Astronomy and Astrophysics* **2020** (2019) 270 [1903.05128].

[152] E. C. Bellm, S. R. Kulkarni, M. J. Graham, R. Dekany, R. M. Smith, R. Riddle et al., *The zwicky transient facility: System overview, performance, and first results*, *Publications of the Astronomical Society of the Pacific* **131** (2018) 018002.

[153] R. J. Foley, D. Scolnic, A. Rest, S. W. Jha, Y. C. Pan, A. G. Riess et al., *The Foundation Supernova Survey: motivation, design, implementation, and first data release*, *MNRAS* **475** (2018) 193 [1711.02474].

[154] J. L. Tonry, L. Denneau, A. N. Heinze, B. Stalder, K. W. Smith, S. J. Smartt et al., *ATLAS: A High-cadence All-sky Survey System*, *Publications of the ASP* **130** (2018) 064505 [1802.00879].

[155] C. S. Kochanek, B. J. Shappee, K. Z. Stanek, T. W. S. Holoien, T. A. Thompson, J. L. Prieto et al., *The All-Sky Automated Survey for Supernovae (ASAS-SN) Light Curve Server v1.0*, *Publications of the ASP* **129** (2017) 104502 [1706.07060].

[156] D. Brout, D. Scolnic, R. Kessler, C. B. D'Andrea, T. M. Davis, R. R. Gupta et al., *First Cosmology Results Using SNe Ia from the Dark Energy Survey: Analysis, Systematic Uncertainties, and Validation*, *ApJ* **874** (2019) 150 [1811.02377].

[157] R. Hounsell et al., *Simulations of the WFIRST Supernova Survey and Forecasts of Cosmological Constraints*, 1702.01747.

[158] D. Spergel, N. Gehrels, C. Baltay, D. Bennett, J. Breckinridge, M. Donahue et al., *Wide-Field InfrarRed Survey Telescope-Astrophysics Focused Telescope Assets WFIRST-AFTA 2015 Report*, *arXiv e-prints* (2015) arXiv:1503.03757 [1503.03757].

[159] C.-E. Rydberg, D. J. Whalen, M. Maturi, T. Collett, M. Carrasco, M. Magg et al., *Detecting strongly lensed supernovae at z ~5-7 with LSST*, *arXiv e-prints* (2018) arXiv:1805.02662 [1805.02662].

[160] T. Hartwig, V. Bromm and A. Loeb, *Detection strategies for the first supernovae with JWST*, *MNRAS* **479** (2018) 2202 [1711.05742].

[161] B. P. Abbott, R. Abbott, T. D. Abbott, S. Abraham, F. Acernese, K. Ackley et al., *GWTC-1: A Gravitational-Wave Transient Catalog of Compact Binary Mergers Observed by LIGO and Virgo during the First and Second Observing Runs*, *Physical Review X* **9** (2019) 031040 [1811.12907].

[162] C. J. Moore, R. H. Cole and C. P. L. Berry, *Gravitational-wave sensitivity curves*, *Classical and Quantum Gravity* **32** (2015) 015014 [1408.0740].

[163] V. Baibhav, E. Berti, D. Gerosa, M. Mapelli, N. Giacobbo, Y. Bouffanais et al., *Gravitational-wave detection rates for compact binaries formed in isolation: LIGO/Virgo O3 and beyond*, *Phys. Rev. D* **100** (2019) 064060 [1906.04197].

[164] H. Luck, *The GEO-600 project*, *Class. Quant. Grav.* **14** (1997) 1471.

[165] H. Lück, C. Affeldt, J. Degallaix, A. Freise, H. Grote, M. Hewitson et al., *The upgrade of GEO 600*, in *Journal of Physics Conference Series*, vol. 228 of *Journal of Physics Conference Series*, p. 012012, May, 2010, 1004.0339, DOI.

[166] L. S. Finn and K. S. Thorne, *Gravitational waves from a compact star in a circular, inspiral orbit, in the equatorial plane of a massive, spinning black hole, as observed by LISA*, *Phys. Rev. D* **62** (2000) 124021 [gr-qc/0007074].

[167] C. D. Ott, *TOPICAL REVIEW: The gravitational-wave signature of core-collapse supernovae*, *Classical and Quantum Gravity* **26** (2009) 063001 [0809.0695].

[168] J. Abadie, B. P. Abbott, R. Abbott, T. D. Abbott, M. Abernathy, T. Accadia et al., *Search for Gravitational Waves Associated with Gamma-Ray Bursts during LIGO Science Run 6 and Virgo Science Runs 2 and 3*, *ApJ* **760** (2012) 12 [1205.2216].

[169] B. P. Abbott, R. Abbott, T. D. Abbott, M. R. Abernathy, F. Acernese, K. Ackley et al., *Prospects for Observing and Localizing Gravitational-Wave Transients with Advanced LIGO and Advanced Virgo*, *Living Reviews in Relativity* **19** (2016) 1.

[170] R. S. Foster and D. C. Backer, *Constructing a Pulsar Timing Array*, *ApJ* **361** (1990) 300.

[171] L. P. Grishchuk, *REVIEWS OF TOPICAL PROBLEMS: Relic gravitational waves and cosmology*, *Physics Uspekhi* **48** (2005) 1235 [gr-qc/0504018].

[172] P. Binétruy, A. Bohé, C. Caprini and J.-F. Dufaux, *Cosmological backgrounds of gravitational waves and eLISA/NGO: phase transitions, cosmic strings and other sources*, *JCAP* **2012** (2012) 027 [1201.0983].

[173] T. Damour and A. Vilenkin, *Gravitational radiation from cosmic (super)strings: Bursts, stochastic background, and observational windows*, *Phys. Rev. D* **71** (2005) 063510 [hep-th/0410222].

[174] N. Christensen, *Stochastic gravitational wave backgrounds*, *Reports on Progress in Physics* **82** (2019) 016903 [1811.08797].

[175] Planck collaboration, *Planck 2013 results. XVI. Cosmological parameters*, *Astron. Astrophys.* **571** (2014) A16 [1303.5076].

[176] Planck collaboration, *Planck 2015 results. XIII. Cosmological parameters*, *Astron. Astrophys.* **594** (2016) A13 [1502.01589].

[177] E. Belgacem, G. Calcagni, M. Crisostomi, C. Dalang, Y. Dirian, J. María Ezquiaga et al., *Testing modified gravity at cosmological distances with LISA standard sirens*, *JCAP* **2019** (2019) 024 [1906.01593].

[178] J. Baker, T. Baker, C. Carbone, G. Congedo, C. Contaldi, I. Dvorkin et al., *High angular resolution gravitational wave astronomy*, *arXiv e-prints* (2019) arXiv:1908.11410 [1908.11410].

[179] C. Brans and R. H. Dicke, *Mach's principle and a relativistic theory of gravitation*, *Phys. Rev.* **124** (1961) 925.

[180] P. Ruiz-Lapuente, *Dark energy, gravitation and supernovae*, *Class. Quant. Grav.* **24** (2007) R91 [0704.1058].

[181] M. Zumalacárregui and J. García-Bellido, *Transforming gravity: From derivative couplings to matter to second-order scalar-tensor theories beyond the Horndeski Lagrangian*, *Phys. Rev. D* **89** (2014) 064046 [1308.4685].

[182] J. Gleyzes, D. Langlois, F. Piazza and F. Vernizzi, *Healthy theories beyond Horndeski*, *Phys. Rev. Lett.* **114** (2015) 211101 [1404.6495].

[183] D. Langlois and K. Noui, *Degenerate higher derivative theories beyond Horndeski: evading the Ostrogradski instability*, *JCAP* **1602** (2016) 034 [1510.06930].

[184] J. Ben Achour, M. Crisostomi, K. Koyama, D. Langlois, K. Noui and G. Tasinato, *Degenerate higher order scalar-tensor theories beyond Horndeski up to cubic order*, *JHEP* **12** (2016) 100 [1608.08135].

[185] D. Duniya, T. Moloi, C. Clarkson, J. Larena, R. Maartens, B. Mongwane et al., *Probing beyond-Horndeski gravity on ultra-large scales*, 1902.09919.

[186] D. Traykova, E. Bellini and P. G. Ferreira, *The phenomenology of beyond Horndeski gravity*, *JCAP* **1908** (2019) 035 [1902.10687].

[187] S. Peirone, G. Benevento, N. Frusciante and S. Tsujikawa, *Cosmological constraints and phenomenology of a beyond-Horndeski model*, *Phys. Rev.* **D100** (2019) 063509 [1905.11364].

[188] M. Fierz and W. Pauli, *On relativistic wave equations for particles of arbitrary spin in an electromagnetic field*, *Proc. Roy. Soc. Lond.* **A173** (1939) 211.

[189] D. G. Boulware and S. Deser, *Can gravitation have a finite range?*, *Phys. Rev. D* **6** (1972) 3368.

[190] G. R. Dvali, G. Gabadadze and M. Porrati, *4-D gravity on a brane in 5-D Minkowski space*, *Phys. Lett.* **B485** (2000) 208 [hep-th/0005016].

[191] E. A. Bergshoeff, O. Hohm and P. K. Townsend, *Massive Gravity in Three Dimensions*, *Phys. Rev. Lett.* **102** (2009) 201301 [0901.1766].

[192] C. de Rham, G. Gabadadze and A. J. Tolley, *Resummation of Massive Gravity*, *Phys. Rev. Lett.* **106** (2011) 231101 [1011.1232].

[193] C. de Rham, *Massive Gravity*, *Living Rev. Rel.* **17** (2014) 7 [1401.4173].

[194] L. Heisenberg, *Generalization of the Proca Action*, *JCAP* **1405** (2014) 015 [1402.7026].

[195] G. Tasinato, *Cosmic Acceleration from Abelian Symmetry Breaking*, *JHEP* **04** (2014) 067 [1402.6450].

[196] E. Allys, P. Peter and Y. Rodriguez, *Generalized Proca action for an Abelian vector field*, *JCAP* **1602** (2016) 004 [1511.03101].

[197] J. Beltran Jimenez and L. Heisenberg, *Derivative self-interactions for a massive vector field*, *Phys. Lett.* **B757** (2016) 405 [1602.03410].

[198] L. Heisenberg, R. Kase and S. Tsujikawa, *Beyond generalized Proca theories*, *Phys. Lett.* **B760** (2016) 617 [1605.05565].

[199] R. Kimura, A. Naruko and D. Yoshida, *Extended vector-tensor theories*, *JCAP* **1701** (2017) 002 [1608.07066].

[200] C. Wetterich, *Effective nonlocal Euclidean gravity*, *Gen. Rel. Grav.* **30** (1998) 159 [gr-qc/9704052].

[201] M. Maggiore, *Phantom dark energy from nonlocal infrared modifications of general relativity*, *Phys. Rev.* **D89** (2014) 043008 [1307.3898].

[202] M. Maggiore and M. Mancarella, *Nonlocal gravity and dark energy*, *Phys. Rev.* **D90** (2014) 023005 [1402.0448].

[203] B. Withers, *Einstein-aether as a quantum effective field theory*, *Class. Quant. Grav.* **26** (2009) 225009 [0905.2446].

[204] E. Belgacem, Y. Dirian, A. Finke, S. Foffa and M. Maggiore, *Gravity in the infrared and effective nonlocal models*, 2001.07619.

[205] C. M. Will, *The Confrontation between General Relativity and Experiment*, *Living Reviews in Relativity* **17** (2014) 4 [1403.7377].

[206] E. Di Casola, S. Liberati and S. Sonego, *Nonequivalence of equivalence principles*, *American Journal of Physics* **83** (2015) 39 [1310.7426].

[207] P. Touboul, G. Métris, M. Rodrigues, Y. André, Q. Baghi, J. Bergé et al., *MICROSCOPE Mission: First Results of a Space Test of the Equivalence Principle*, *Phys. Rev. Lett.* **119** (2017) 231101 [1712.01176].

[208] A. Bauch and S. Weyers, *New experimental limit on the validity of local position invariance*, *Phys. Rev. D* **65** (2002) 081101.

[209] V. W. Hughes, H. G. Robinson and V. Beltran-Lopez, *Upper Limit for the Anisotropy of Inertial Mass from Nuclear Re sonance Experiments*, *Phys. Rev. Lett.* **4** (1960) 342.

[210] R. W. P. Drever, *A search for anisotropy of inertial mass using a free precession technique*, *Phil. Mag.* **6** (1961) 683.

[211] S. K. Lamoreaux, J. P. Jacobs, B. R. Heckel, F. J. Raab and E. N. Fortson, *New limits on spatial anisotropy from optically-pumped sup201hg and* ^{199}Hg, *Phys. Rev. Lett.* **57** (1986) 3125.

[212] T. E. Chupp, R. J. Hoare, R. A. Loveman, E. R. Oteiza, J. M. Richardson, M. E. Wagshul et al., *Results of a new test of local lorentz invariance: A search for mass anisotropy in* ^{21}Ne, *Phys. Rev. Lett.* **63** (1989) 1541.

[213] M. P. Haugan, *ENERGY CONSERVATION AND THE PRINCIPLE OF EQUIVALENCE*, *Annals Phys.* **118** (1979) 156.

[214] S. S. Shapiro, J. L. Davis, D. E. Lebach and J. S. Gregory, *Measurement of the Solar Gravitational Deflection of Radio Waves using Geodetic Very-Long-Baseline Interferometry Data, 1979-1999*, *Phys. Rev. Lett.* **92** (2004) 121101.

[215] S. S. Shapiro, J. L. Davis, D. E. Lebach and J. S. Gregory, *Measurement of the solar gravitational deflection of radio waves using geodetic very-long-baseline interferometry data, 1979–1999*, *Phys. Rev. Lett.* **92** (2004) 121101.

[216] B. Bertotti, L. Iess and P. Tortora, *A test of general relativity using radio links with the Cassini spacecraft*, *Nature* **425** (2003) 374.

[217] K. Nordtvedt, *Equivalence principle for massive bodies. i. phenomenology*, *Phys. Rev.* **169** (1968) 1014.

[218] H. Thirring, *Über die Wirkung rotierender ferner Massen in der Einsteinschen Gravitationstheorie.*, *Physikalische Zeitschrift* **19** (1918) 33.

[219] J. Lense and H. Thirring, *Über den Einfluß der Eigenrotation der Zentralkörper auf die Bewegung der Planeten und Monde nach der Einsteinschen Gravitationstheorie*, *Physikalische Zeitschrift* **19** (1918) 156.

[220] J. D. Anderson, M. A. Slade, R. F. Jurgens, E. L. Lau, X. X. Newhall and E. Myles, *Radar and spacecraft ranging to Mercury between 1966 and 1988*, *Proceedings of the Astronomical Society of Australia* **9** (1991) 324.

[221] G. A. Krasinskii, E. V. Pit'eva, M. L. Sveshnikov and L. I. Chuniaeva, *The motion of major planets from observations 1769 1988 and some astronomical constants*, *Celestial Mechanics and Dynamical Astronomy* **55** (1993) 1.

[222] E. V. Pitjeva, *Experimental testing of relativistic effects, variability of the gravitational constant and topography of Mercury surface from radar observations 1964 1989*, *Celestial Mechanics and Dynamical Astronomy* **55** (1993) 313.

[223] J. G. Williams, S. G. Turyshev and D. H. Boggs, *Progress in Lunar Laser Ranging Tests of Relativistic Gravity*, *Phys. Rev. Lett.* **93** (2004) 261101 [gr-qc/0411113].

[224] I. Ciufolini, A. Paolozzi, E. Pavlis, J. Ries, R. Koenig, R. Matzner et al., *The LARES Space Experiment: LARES Orbit, Error Analysis and Satellite Structure.*

[225] S. C. Cohen, R. W. King, R. Kolenkiewicz, R. D. Rosen and B. E. Schutz, *LAGEOS scientific results.*, *Journal of Geophysics Research* **90** (1985) 9215.

[226] I. Ciufolini, A. Paolozzi, E. C. Pavlis, G. Sindoni, J. Ries, R. Matzner et al., *An Improved Test of the General Relativistic Effect of Frame-Dragging Using the LARES and LAGEOS Satellites*, *Eur. Phys. J.* **C79** (2019) 872 [1910.09908].

[227] T. Clifton, *Parametrized post-Newtonian limit of fourth-order theories of gravity*, *Phys. Rev. D* **77** (2008) 024041 [0801.0983].

[228] Z. Berezhiani, F. Nesti, L. Pilo and N. Rossi, *Gravity modification with Yukawa-type potential: dark matter and mirror gravity*, *Journal of High Energy Physics* **2009** (2009) 083 [0902.0144].

[229] E. Fischbach and C. Talmadge, *Six years of the fifth force*, *Nature* **356** (1992) 207.

[230] E. G. Adelberger, B. R. Heckel and A. E. Nelson, *Tests of the Gravitational Inverse-Square Law*, *Annual Review of Nuclear and Particle Science* **53** (2003) 77 [hep-ph/0307284].

[231] J. M. Cline, S. Jeon and G. D. Moore, *The phantom menaced: Constraints on low-energy effective ghosts*, *Phys. Rev. D* **70** (2004) 043543 [hep-ph/0311312].

[232] N. A. Hamed, H. S. Cheng, M. A. Luty and S. Mukohyama, *Ghost Condensation and a Consistent IR Modification of Gravity*, *Journal of High Energy Physics* **2004** (2004) 074 [hep-th/0312099].

[233] A. I. Vainshtein, *To the problem of nonvanishing gravitation mass*, *Physics Letters B* **39** (1972) 393.

[234] C. Deffayet, G. Dvali, G. Gabadadze and A. Vainshtein, *Nonperturbative continuity in graviton mass versus perturbative discontinuity*, *Phys. Rev. D* **65** (2002) 044026 [hep-th/0106001].

[235] G. Dvali, *Predictive power of strong coupling in theories with large distance modified gravity*, *New Journal of Physics* **8** (2006) 326 [hep-th/0610013].

[236] J. Khoury and A. Weltman, *Chameleon cosmology*, *Phys. Rev. D* **69** (2004) 044026 [astro-ph/0309411].

[237] J. Khoury and A. Weltman, *Chameleon Fields: Awaiting Surprises for Tests of Gravity in Space*, *Phys. Rev. Lett.* **93** (2004) 171104 [astro-ph/0309300].

[238] K. Hinterbichler and J. Khoury, *Screening Long-Range Forces through Local Symmetry Restoration*, *Phys. Rev. Lett.* **104** (2010) 231301 [1001.4525].

[239] C. Deffayet, X. Gao, D. A. Steer and G. Zahariade, *From k-essence to generalised Galileons*, *Phys. Rev.* **D84** (2011) 064039 [1103.3260].

[240] T. Kobayashi, M. Yamaguchi and J. Yokoyama, *Generalized G-inflation: Inflation with the most general second-order field equations*, *Prog. Theor. Phys.* **126** (2011) 511 [1105.5723].

[241] E. Bellini and I. Sawicki, *Maximal freedom at minimum cost: linear large-scale structure in general modifications of gravity*, *JCAP* **2014** (2014) 050 [1404.3713].

[242] C. Wetterich, *Cosmology and the Fate of Dilatation Symmetry*, *Nucl. Phys.* **B302** (1988) 668 [1711.03844].

[243] B. Ratra and P. J. E. Peebles, *Cosmological Consequences of a Rolling Homogeneous Scalar Field*, *Phys. Rev.* **D37** (1988) 3406.

[244] C. Deffayet, O. Pujolas, I. Sawicki and A. Vikman, *Imperfect Dark Energy from Kinetic Gravity Braiding*, *JCAP* **1010** (2010) 026 [1008.0048].

[245] T. Kobayashi, M. Yamaguchi and J. Yokoyama, *G-inflation: Inflation driven by the Galileon field*, *Phys. Rev. Lett.* **105** (2010) 231302 [1008.0603].

[246] O. Pujolas, I. Sawicki and A. Vikman, *The Imperfect Fluid behind Kinetic Gravity Braiding*, *JHEP* **11** (2011) 156 [1103.5360].

[247] N. Chow and J. Khoury, *Galileon Cosmology*, *Phys. Rev.* **D80** (2009) 024037 [0905.1325].

[248] I. Sawicki, I. D. Saltas, L. Amendola and M. Kunz, *Consistent perturbations in an imperfect fluid*, *JCAP* **1301** (2013) 004 [1208.4855].

[249] S. M. Carroll, V. Duvvuri, M. Trodden and M. S. Turner, *Is cosmic speed - up due to new gravitational physics?*, *Phys. Rev.* **D70** (2004) 043528 [astro-ph/0306438].

[250] Y.-S. Song, W. Hu and I. Sawicki, *The Large Scale Structure of f(R) Gravity*, *Phys. Rev.* **D75** (2007) 044004 [astro-ph/0610532].

[251] S. M. Carroll, A. De Felice, V. Duvvuri, D. A. Easson, M. Trodden and M. S. Turner, *The Cosmology of generalized modified gravity models*, *Phys. Rev.* **D71** (2005) 063513 [astro-ph/0410031].

[252] A. De Felice, D. F. Mota and S. Tsujikawa, *Matter instabilities in general Gauss-Bonnet gravity*, *Phys. Rev.* **D81** (2010) 023532 [0911.1811].

[253] J. Noller and A. Nicola, *Radiative stability and observational constraints on dark energy and modified gravity*, 1811.03082.

[254] A. Adams, N. Arkani-Hamed, S. Dubovsky, A. Nicolis and R. Rattazzi, *Causality, analyticity and an IR obstruction to UV completion*, *JHEP* **10** (2006) 014 [hep-th/0602178].

[255] A. Nicolis, R. Rattazzi and E. Trincherini, *Energy's and amplitudes' positivity*, *JHEP* **05** (2010) 095 [0912.4258].

[256] B. Bellazzini, *Softness and amplitudes' positivity for spinning particles*, *JHEP* **02** (2017) 034 [1605.06111].

[257] C. de Rham, S. Melville, A. J. Tolley and S.-Y. Zhou, *Positivity bounds for scalar field theories*, *Phys. Rev.* **D96** (2017) 081702 [1702.06134].

[258] C. de Rham, S. Melville, A. J. Tolley and S.-Y. Zhou, *UV complete me: Positivity Bounds for Particles with Spin*, *JHEP* **03** (2018) 011 [1706.02712].

[259] S. Melville and J. Noller, *Positivity in the Sky: Constraining dark energy and modified gravity from the UV*, *Phys. Rev.* **D101** (2020) 021502 [1904.05874].

[260] S. M. Carroll, *Quintessence and the rest of the world: Suppressing long-range interactions*, *Phys. Rev. Lett.* **81** (1998) 3067.

[261] C. J. A. P. Martins, A. M. M. Pinho, P. Carreira, A. Gusart, J. López and C. I. S. A. Rocha, *Fine-structure constant constraints on dark energy: II. Extending the parameter space*, *Phys. Rev.* **D93** (2016) 023506 [1601.02950].

[262] J. M. A. V. Boas, D. M. N. Magano, C. J. A. P. Martins, A. Barbecho and C. Serrano, *Distinguishing freezing and thawing dark energy models through measurements of the fine-structure constant*, *Astron. Astrophys.* **635** (2020) A80 [2001.09129].

[263] J. K. Erickson, R. R. Caldwell, P. J. Steinhardt, C. Armendariz-Picon and V. F. Mukhanov, *Measuring the speed of sound of quintessence*, *Phys. Rev. Lett.* **88** (2002) 121301 [astro-ph/0112438].

[264] M. Chevallier and D. Polarski, *Accelerating universes with scaling dark matter*, *Int. J. Mod. Phys.* **D10** (2001) 213 [gr-qc/0009008].

[265] E. V. Linder, *Exploring the expansion history of the universe*, *Phys. Rev. Lett.* **90** (2003) 091301 [astro-ph/0208512].

[266] V. Barger, E. Guarnaccia and D. Marfatia, *Classification of dark energy models in the (w(0), w(a)) plane*, *Phys. Lett.* **B635** (2006) 61 [hep-ph/0512320].

[267] R. R. Caldwell and E. V. Linder, *The Limits of quintessence*, *Phys. Rev. Lett.* **95** (2005) 141301 [astro-ph/0505494].

[268] E. V. Linder, *Quintessence's last stand?*, *Phys. Rev.* **D91** (2015) 063006 [1501.01634].

[269] K. Aylor, M. Joy, L. Knox, M. Millea, S. Raghunathan and W. L. K. Wu, *Sounds Discordant: Classical Distance Ladder & ΛCDM -based Determinations of the Cosmological Sound Horizon*, *Astrophys. J.* **874** (2019) 4 [1811.00537].

[270] V. Poulin, T. L. Smith, T. Karwal and M. Kamionkowski, *Early Dark Energy Can Resolve The Hubble Tension*, *Phys. Rev. Lett.* **122** (2019) 221301 [1811.04083].

[271] J. Renk, M. Zumalacárregui, F. Montanari and A. Barreira, *Galileon gravity in light of ISW, CMB, BAO and H_0 data*, *JCAP* **1710** (2017) 020 [1707.02263].

[272] S. Peirone, G. Benevento, N. Frusciante and S. Tsujikawa, *Cosmological data favor Galileon ghost condensate over ΛCDM*, *Phys. Rev.* **D100** (2019) 063540 [1905.05166].

[273] LSST collaboration, *Tomographic Galaxy Clustering with the Subaru Hyper Suprime-Cam First Year Public Data Release*, 1912.08209.

[274] A. Albrecht et al., *Report of the Dark Energy Task Force*, astro-ph/0609591.

[275] A. Linde, *Inflationary Cosmology after Planck 2013*, in *Proceedings, 100th Les Houches Summer School: Post-Planck Cosmology: Les Houches, France, July 8 - August 2, 2013*, pp. 231–316, 2015, 1402.0526, DOI.

[276] DES collaboration, *First Cosmology Results using Type Ia Supernovae from the Dark Energy Survey: Constraints on Cosmological Parameters*, *Astrophys. J.* **872** (2019) L30 [1811.02374].

[277] E. V. Linder, *Dark Energy from α-Attractors*, *Phys. Rev.* **D91** (2015) 123012 [1505.00815].

[278] K. Dimopoulos and C. Owen, *Quintessential Inflation with α-attractors*, *JCAP* **1706** (2017) 027 [1703.00305].

[279] K. Dimopoulos and C. Owen, *Instant Preheating in Quintessential Inflation with α-Attractors*, 1712.01760.

[280] Y. Akrami, R. Kallosh, A. Linde and V. Vardanyan, *Dark energy, α-attractors, and large-scale structure surveys*, 1712.09693.

[281] S. Casas, M. Pauly and J. Rubio, *Higgs-dilaton cosmology: An inflation–dark-energy connection and forecasts for future galaxy surveys*, *Phys. Rev.* **D97** (2018) 043520 [1712.04956].

[282] K. Dimopoulos and T. Markkanen, *Dark energy as a remnant of inflation and electroweak symmetry breaking*, *JHEP* **01** (2019) 029 [1807.04359].

[283] S. Casas, G. K. Karananas, M. Pauly and J. Rubio, *Scale-invariant alternatives to general relativity. III. The inflation-dark energy connection*, *Phys. Rev.* **D99** (2019) 063512 [1811.05984].

[284] J. E. Camargo-Molina, T. Markkanen and P. Scott, *Dark energy without fine tuning*, 1905.00045.

[285] M. Shahalam, R. Myrzakulov, S. Myrzakul and A. Wang, *Observational constraints on the generalized α attractor model*, *Int. J. Mod. Phys.* **D27** (2018) 1850058 [1611.06315].

[286] S. Bag, S. S. Mishra and V. Sahni, *New tracker models of dark energy*, 1709.09193.

[287] F. X. L. Cedeño, A. Montiel, J. C. Hidalgo and G. Germán, *Bayesian evidence for α-attractor dark energy models*, 1905.00834.

[288] A. A. Starobinsky, *A New Type of Isotropic Cosmological Models Without Singularity*, *Phys. Lett.* **91B** (1980) 99.

[289] S. D. Odintsov and V. K. Oikonomou, *Inflationary α-attractors from $F(R)$ gravity*, *Phys. Rev.* **D94** (2016) 124026 [1612.01126].

[290] T. Miranda, J. C. Fabris and O. F. Piattella, *Reconstructing a $f(R)$ theory from the α-Attractors*, *JCAP* **1709** (2017) 041 [1707.06457].

[291] S. S. Mishra, V. Sahni and Y. Shtanov, *Sourcing Dark Matter and Dark Energy from α-attractors*, *JCAP* **1706** (2017) 045 [1703.03295].

[292] M. Galante, R. Kallosh, A. Linde and D. Roest, *Unity of Cosmological Inflation Attractors*, *Phys. Rev. Lett.* **114** (2015) 141302 [1412.3797].

[293] R. Kallosh and A. Linde, *Universality Class in Conformal Inflation*, *JCAP* **1307** (2013) 002 [1306.5220].

[294] Planck collaboration, *Planck 2015 results. XIV. Dark energy and modified gravity*, *Astron. Astrophys.* **594** (2016) A14 [1502.01590].

[295] B. Whitt, *Fourth Order Gravity as General Relativity Plus Matter*, *Phys. Lett.* **145B** (1984) 176.

[296] K.-i. Maeda, *Inflation as a Transient Attractor in R^2 Cosmology*, *Phys. Rev.* **D37** (1988) 858.

[297] J. D. Barrow, *The Premature Recollapse Problem in Closed Inflationary Universes*, *Nucl. Phys.* **B296** (1988) 697.

[298] R. N. Cahn, R. de Putter and E. V. Linder, *Field Flows of Dark Energy*, *JCAP* **0811** (2008) 015 [0807.1346].

[299] P. Peter and J.-P. Uzan, *Primordial Cosmology*, p. 708. Oxford Graduate Texts. Oxford University Press, first ed., 2009.

[300] BOSS collaboration, *Baryon acoustic oscillations in the Lyα forest of BOSS DR11 quasars*, *Astron. Astrophys.* **574** (2015) A59 [1404.1801].

[301] J. Evslin, *Isolating the Lyman Alpha Forest BAO Anomaly*, *JCAP* **1704** (2017) 024 [1604.02809].

[302] H. Akaike, *A new look at the statistical model identification*, *IEEE Transactions on Automatic Control* **19** (1974) 716.

[303] G. Schwarz, *Estimating the Dimension of a Model*, *Annals Statist.* **6** (1978) 461.

[304] K. N. Abazajian et al., *Inflation Physics from the Cosmic Microwave Background and Large Scale Structure*, *Astropart. Phys.* **63** (2015) 55 [1309.5381].

[305] U. Seljak, *Extracting primordial non-gaussianity without cosmic variance*, *Phys. Rev. Lett.* **102** (2009) 021302 [0807.1770].

[306] A. Lewis and A. Challinor, *Weak gravitational lensing of the CMB*, *Phys. Rept.* **429** (2006) 1 [astro-ph/0601594].

[307] W. Hu and T. Okamoto, *Mass reconstruction with cmb polarization*, *Astrophys. J.* **574** (2002) 566 [astro-ph/0111606].

[308] D. Alonso, P. Bull, P. G. Ferreira, R. Maartens and M. Santos, *Ultra large-scale cosmology in next-generation experiments with single tracers*, *Astrophys. J.* **814** (2015) 145 [1505.07596].

[309] SDSS collaboration, *Color separation of galaxy types in the Sloan Digital Sky Survey imaging data*, *Astron. J.* **122** (2001) 1861 [astro-ph/0107201].

[310] H. J. Mo and S. D. M. White, *An analytic model for the spatial clustering of dark matter haloes*, *Mon. Not. Roy. Astron. Soc.* **282** (1996) 347 [astro-ph/9512127].

[311] D. H. Weinberg, R. Dave, N. Katz and L. Hernquist, *Galaxy clustering and galaxy bias in a lambda-CDM universe*, *Astrophys. J.* **601** (2004) 1 [astro-ph/0212356].

[312] A. L. Coil et al., *The DEEP2 Galaxy Redshift Survey: Color and luminosity dependence of galaxy clustering at z similar to 1*, *Astrophys. J.* **672** (2008) 153 [0708.0004].

[313] I. Mohammed, U. Seljak and Z. Vlah, *Perturbative approach to covariance matrix of the matter power spectrum*, *Mon. Not. Roy. Astron. Soc.* **466** (2017) 780 [1607.00043].

[314] C. S. Lorenz, D. Alonso and P. G. Ferreira, *Impact of relativistic effects on cosmological parameter estimation*, *Phys. Rev.* **D97** (2018) 023537 [1710.02477].

[315] D. H. Rudd, A. R. Zentner and A. V. Kravtsov, *Effects of Baryons and Dissipation on the Matter Power Spectrum*, *Astrophys. J.* **672** (2008) 19 [astro-ph/0703741].

[316] M. P. van Daalen, J. Schaye, C. M. Booth and C. D. Vecchia, *The effects of galaxy formation on the matter power spectrum: A challenge for precision cosmology*, *Mon. Not. Roy. Astron. Soc.* **415** (2011) 3649 [1104.1174].

[317] M. P. van Daalen, J. Schaye, I. G. McCarthy, C. M. Booth and C. Dalla Vecchia, *The impact of baryonic processes on the two-point correlation functions of galaxies, subhaloes and matter*, *Mon. Not. Roy. Astron. Soc.* **440** (2014) 2997 [1310.7571].

[318] W. A. Hellwing, M. Schaller, C. S. Frenk, T. Theuns, J. Schaye, R. G. Bower et al., *The effect of baryons on redshift space distortions and cosmic density and velocity fields in the EAGLE simulation*, *Mon. Not. Roy. Astron. Soc.* **461** (2016) L11 [1603.03328].

[319] J. Harnois-Déraps, L. van Waerbeke, M. Viola and C. Heymans, *Baryons, Neutrinos, Feedback and Weak Gravitational Lensing*, *Mon. Not. Roy. Astron. Soc.* **450** (2015) 1212 [1407.4301].

[320] N. E. Chisari, M. L. A. Richardson, J. Devriendt, Y. Dubois, A. Schneider, M. C. Brun, Amandine Le et al., *The impact of baryons on the matter power spectrum from the Horizon-AGN cosmological hydrodynamical simulation*, 1801.08559.

[321] H.-J. Huang, T. Eifler, R. Mandelbaum and S. Dodelson, *Modeling baryonic physics in future weak lensing surveys*, 1809.01146.

[322] I. Sawicki and E. Bellini, *Limits of quasistatic approximation in modified-gravity cosmologies*, *Phys. Rev.* **D92** (2015) 084061 [1503.06831].

[323] D. N. Limber, *The Analysis of Counts of the Extragalactic Nebulae in Terms of a Fluctuating Density Field.*, *Astrophys. J.* **117** (1953) 134.

[324] R. R. Caldwell, R. Dave and P. J. Steinhardt, *Cosmological imprint of an energy component with general equation of state*, *Phys. Rev. Lett.* **80** (1998) 1582 [astro-ph/9708069].

[325] J. E. Lidsey, A. R. Liddle, E. W. Kolb, E. J. Copeland, T. Barreiro and M. Abney, *Reconstructing the inflation potential : An overview*, *Rev. Mod. Phys.* **69** (1997) 373 [astro-ph/9508078].

[326] P. G. Ferreira and M. Joyce, *Cosmology with a primordial scaling field*, *Phys. Rev.* **D58** (1998) 023503 [astro-ph/9711102].

[327] E. J. Copeland, M. Sami and S. Tsujikawa, *Dynamics of dark energy*, *Int. J. Mod. Phys.* **D15** (2006) 1753 [hep-th/0603057].

[328] S. Tsujikawa, *Quintessence: A Review*, *Class. Quant. Grav.* **30** (2013) 214003 [1304.1961].

[329] D. J. E. Marsh, P. Bull, P. G. Ferreira and A. Pontzen, *Quintessence in a quandary: Prior dependence in dark energy models*, *Phys. Rev.* **D90** (2014) 105023 [1406.2301].

[330] M. Raveri, P. Bull, A. Silvestri and L. Pogosian, *Priors on the effective Dark Energy equation of state in scalar-tensor theories*, *Phys. Rev.* **D96** (2017) 083509 [1703.05297].

[331] F. Gerardi, M. Martinelli and A. Silvestri, *Reconstruction of the Dark Energy equation of state from latest data: the impact of theoretical priors*, *JCAP* **1907** (2019) 042 [1902.09423].

[332] T. Sprenger, M. Archidiacono, T. Brinckmann, S. Clesse and J. Lesgourgues, *Cosmology in the era of Euclid and the Square Kilometre Array*, *JCAP* **1902** (2019) 047 [1801.08331].

[333] D. Huterer and H. V. Peiris, *Dynamical behavior of generic quintessence potentials: Constraints on key dark energy observables*, *Phys. Rev.* **D75** (2007) 083503 [astro-ph/0610427].

[334] S. Joudaki et al., *CFHTLenS revisited: assessing concordance with Planck including astrophysical systematics*, *Mon. Not. Roy. Astron. Soc.* **465** (2017) 2033 [1601.05786].

[335] E. J. Copeland, A. R. Liddle and D. Wands, *Exponential potentials and cosmological scaling solutions*, *Phys. Rev.* **D57** (1998) 4686 [gr-qc/9711068].

[336] T. Barreiro, E. J. Copeland and N. J. Nunes, *Quintessence arising from exponential potentials*, *Phys. Rev.* **D61** (2000) 127301 [astro-ph/9910214].

[337] S. C. C. Ng, N. J. Nunes and F. Rosati, *Applications of scalar attractor solutions to cosmology*, *Phys. Rev.* **D64** (2001) 083510 [astro-ph/0107321].

[338] A. de la Macorra and G. Piccinelli, *General scalar fields as quintessence*, *Phys. Rev.* **D61** (2000) 123503 [hep-ph/9909459].

[339] W. Fang, W. Hu and A. Lewis, *Crossing the Phantom Divide with Parameterized Post-Friedmann Dark Energy*, *Phys. Rev.* **D78** (2008) 087303 [0808.3125].

[340] A. Gelman and D. B. Rubin, *Inference from Iterative Simulation Using Multiple Sequences*, *Statist. Sci.* **7** (1992) 457.

[341] Planck collaboration, *Planck 2015 results. I. Overview of products and scientific results*, *Astron. Astrophys.* **594** (2016) A1 [1502.01582].

[342] Planck collaboration, *Planck 2015 results. XI. CMB power spectra, likelihoods, and robustness of parameters*, *Astron. Astrophys.* **594** (2016) A11 [1507.02704].

[343] F. Beutler, C. Blake, M. Colless, D. H. Jones, L. Staveley-Smith, L. Campbell et al., *The 6dF Galaxy Survey: Baryon Acoustic Oscillations and the Local Hubble Constant*, *Mon. Not. Roy. Astron. Soc.* **416** (2011) 3017 [1106.3366].

[344] A. J. Ross, L. Samushia, C. Howlett, W. J. Percival, A. Burden and M. Manera, *The clustering of the SDSS DR7 main Galaxy sample – I. A 4 per cent distance measure at* $z = 0.15$, *Mon. Not. Roy. Astron. Soc.* **449** (2015) 835 [1409.3242].

[345] F. Beutler, C. Blake, M. Colless, D. H. Jones, L. Staveley-Smith, G. B. Poole et al., *The 6dF Galaxy Survey:* $z \approx 0$ *measurement of the growth rate and* σ_8, *Mon. Not. Roy. Astron. Soc.* **423** (2012) 3430 [1204.4725].

[346] A. Lewis, *GetDist: a Python package for analysing Monte Carlo samples*, 1910.13970.

[347] K. M. Gorski, *On Determining the spectrum of primordial inhomogeneity from the Cobe DMR sky maps. 1. Method*, *Astrophys. J.* **430** (1994) L85 [astro-ph/9403066].

[348] K. M. Gorski, G. Hinshaw, a. Banday, C. L. Bennett, E. L. Wright, a. Kogut et al., *On determining the spectrum of primordial inhomogeneity from the COBE dmr sky maps. 2. Results of two year data analysis*, *Astrophys. J.* **430** (1994) L89 [astro-ph/9403067].

[349] J. R. Bond, *Signal-to-Noise Eigenmode Analysis of the Two-Year COBE Maps*, *Physical Review Letters* **74** (1995) 4369 [astro-ph/9407044].

[350] K. M. Gorski, A. J. Banday, C. L. Bennett, G. Hinshaw, A. Kogut, G. F. Smoot et al., *Power spectrum of primordial inhomogeneity determined from the four year COBE DMR sky maps*, *Astrophys. J.* **464** (1996) L11 [astro-ph/9601063].

[351] K. M. Górski, *Cosmic microwave background anisotropy in the COBE DMR 4-year sky maps*, in *Microwave background anisotropies. Proceedings, 31st Rencontres de Moriond, 16th Moriond Astrophysics Meeting, Les Arcs, France, March 16-23, 1996*, pp. 77–84, 1997, astro-ph/9701191.

[352] M. Tegmark, *How to measure CMB power spectra without losing information*, *Phys. Rev. D* **55** (1997) 5895 [astro-ph/9611174].

[353] J. R. Bond, A. H. Jaffe and L. Knox, *Estimating the power spectrum of the cosmic microwave background*, *Phys. Rev. D* **57** (1998) 2117 [astro-ph/9708203].

[354] B. D. Wandelt, E. Hivon and K. M. Gorski, *The pseudo-C_ℓ method: cosmic microwave background anisotropy power spectrum statistics for high precision cosmology*, *Phys. Rev.* **D64** (2001) 083003 [astro-ph/0008111].

[355] M. Tegmark and A. de Oliveira-Costa, *How to measure CMB polarization power spectra without losing information*, *Phys. Rev. D* **64** (2001) 063001 [astro-ph/0012120].

[356] E. Hivon, K. M. Górski, C. B. Netterfield, B. P. Crill, S. Prunet and F. Hansen, *MASTER of the Cosmic Microwave Background Anisotropy Power Spectrum: A Fast Method for Statistical Analysis of Large and Complex Cosmic Microwave Background Data Sets*, *ApJ* **567** (2002) 2 [astro-ph/0105302].

[357] B. D. Wandelt and F. K. Hansen, *Fast, exact CMB power spectrum estimation for a certain class of observational strategies*, *Phys. Rev. D* **67** (2003) 023001 [astro-ph/0106515].

[358] A. J. S. Hamilton, M. Tegmark and N. Padmanabhan, *Linear redshift distortions and power in the IRAS Point Source Catalog Redshift Survey*, *MNRAS* **317** (2000) L23 [astro-ph/0004334].

[359] D. Huterer, L. Knox and R. C. Nichol, *The Angular Power Spectrum of Edinburgh/Durham Southern Galaxy Catalogue Galaxies*, *ApJ* **555** (2001) 547 [astro-ph/0011069].

[360] G. Efstathiou and S. J. Moody, *Maximum likelihood estimates of the two- and three-dimensional power spectra of the APM Galaxy Survey*, *MNRAS* **325** (2001) 1603 [astro-ph/0010478].

[361] B. Hayes, R. Brunner and A. Ross, *The SDSS DR7 Galaxy Angular Power Spectrum*, *arXiv e-prints* (2011) arXiv:1112.5723 [1112.5723].

[362] F. Köhlinger, M. Viola, W. Valkenburg, B. Joachimi, H. Hoekstra and K. Kuijken, *A direct measurement of tomographic lensing power spectra from CFHTLenS*, *MNRAS* **456** (2016) 1508 [1509.04071].

[363] A. Balaguera-Antolínez, M. Bilicki, E. Branchini and A. Postiglione, *Extracting cosmological information from the angular power spectrum of the 2MASS Photometric Redshift catalogue*, *MNRAS* **476** (2018) 1050 [1711.04583].

[364] H. S. Xavier, M. V. Costa-Duarte, A. Balaguera-Antolínez and M. Bilicki, *All-sky angular power spectra from cleaned WISE×SuperCOSMOS galaxy number counts*, *arXiv e-prints* (2018) arXiv:1812.08182 [1812.08182].

[365] H. Camacho, N. Kokron, F. Andrade-Oliveira, R. Rosenfeld, M. Lima, F. Lacasa et al., *Dark Energy Survey Year 1 Results: Measurement of the Galaxy Angular Power Spectrum*, *MNRAS* (2019) 1446 [1807.10163].

[366] C. Hikage, M. Oguri, T. Hamana, S. More, R. Mandelbaum, M. Takada et al., *Cosmology from cosmic shear power spectra with Subaru Hyper Suprime-Cam first-year data*, *Publications of the ASJ* **71** (2019) 43 [1809.09148].

[367] S. Hamimeche and A. Lewis, *Likelihood analysis of CMB temperature and polarization power spectra*, *Phys. Rev. D* **77** (2008) 103013 [0801.0554].

[368] E. Sellentin, C. Heymans and J. Harnois-Déraps, *The skewed weak lensing likelihood: why biases arise, despite data and theory being sound*, *MNRAS* **477** (2018) 4879 [1712.04923].

[369] J. W. Tukey*Annals Math.Statist.* **29** (1958) 614.

[370] J. D. Barrow, S. P. Bhavsar and D. H. Sonoda, *A bootstrap resampling analysis of galaxy clustering.*, *MNRAS* **210** (1984) 19.

[371] A. J. S. Hamilton, *Omega from the Anisotropy of the Redshift Correlation Function in the IRAS 2 Jansky Survey*, *ApJ* **406** (1993) L47.

[372] I. Zehavi, M. R. Blanton, J. A. Frieman, D. H. Weinberg, H. J. Mo, M. A. Strauss et al., *Galaxy Clustering in Early Sloan Digital Sky Survey Redshift Data*, *ApJ* **571** (2002) 172 [astro-ph/0106476].

[373] S. Escoffier, M. C. Cousinou, A. Tilquin, A. Pisani, A. Aguichine, S. de la Torre et al., *Jackknife resampling technique on mocks: an alternative method for covariance matrix estimation*, *arXiv e-prints* (2016) arXiv:1606.00233 [1606.00233].

[374] M. Manera, R. Scoccimarro, W. J. Percival, L. Samushia, C. K. McBride, A. J. Ross et al., *The clustering of galaxies in the SDSS-III Baryon Oscillation Spectroscopic Survey: a large sample of mock galaxy catalogues*, *MNRAS* **428** (2013) 1036 [1203.6609].

[375] S. Avila, M. Crocce, A. J. Ross, J. García-Bellido, W. J. Percival, N. Banik et al., *Dark Energy Survey Year-1 results: galaxy mock catalogues for BAO*, *MNRAS* **479** (2018) 94 [1712.06232].

[376] L. Blot, M. Crocce, E. Sefusatti, M. Lippich, A. G. Sánchez, M. Colavincenzo et al., *Comparing approximate methods for mock catalogues and covariance matrices II: power spectrum multipoles*, *MNRAS* **485** (2019) 2806 [1806.09497].

[377] A. Cooray and W. Hu, *Power Spectrum Covariance of Weak Gravitational Lensing*, *ApJ* **554** (2001) 56 [astro-ph/0012087].

[378] M. Sato, T. Hamana, R. Takahashi, M. Takada, N. Yoshida, T. Matsubara et al., *Simulations of Wide-Field Weak Lensing Surveys. I. Basic Statistics and Non-Gaussian Effects*, *ApJ* **701** (2009) 945 [0906.2237].

[379] M. Takada and B. Jain, *The impact of non-Gaussian errors on weak lensing surveys*, *MNRAS* **395** (2009) 2065 [0810.4170].

[380] M. Takada and W. Hu, *Power spectrum super-sample covariance*, *Phys. Rev. D* **87** (2013) 123504 [1302.6994].

[381] M. Takada and D. N. Spergel, *Joint analysis of cluster number counts and weak lensing power spectrum to correct for the super-sample covariance*, *MNRAS* **441** (2014) 2456 [1307.4399].

[382] Y. Park, E. Krause, S. Dodelson, B. Jain, A. Amara, M. R. Becker et al., *Joint analysis of galaxy-galaxy lensing and galaxy clustering: Methodology and forecasts for Dark Energy Survey*, *Phys. Rev. D* **94** (2016) 063533 [1507.05353].

[383] A. Barreira, E. Krause and F. Schmidt, *Accurate cosmic shear errors: do we need ensembles of simulations?*, *Journal of Cosmology and Astro-Particle Physics* **2018** (2018) 053 [1807.04266].

[384] M. A. Troxel, E. Krause, C. Chang, T. F. Eifler, O. Friedrich, D. Gruen et al., *Survey geometry and the internal consistency of recent cosmic shear measurements*, *MNRAS* **479** (2018) 4998 [1804.10663].

[385] G. Efstathiou, *Myths and truths concerning estimation of power spectra: the case for a hybrid estimator*, *MNRAS* **349** (2004) 603 [astro-ph/0307515].

[386] M. L. Brown, P. G. Castro and A. N. Taylor, *Cosmic microwave background temperature and polarization pseudo-C_l estimators and covariances*, *MNRAS* **360** (2005) 1262 [astro-ph/0410394].

[387] A. Challinor and G. Chon, *Error analysis of quadratic power spectrum estimates for cosmic microwave background polarization: sampling covariance*, *MNRAS* **360** (2005) 509 [astro-ph/0410097].

[388] G. Efstathiou, *Hybrid estimation of cmb polarization power spectra*, *Mon. Not. Roy. Astron. Soc.* **370** (2006) 343 [astro-ph/0601107].

[389] Planck Collaboration, P. A. R. Ade, N. Aghanim, C. Armitage-Caplan, M. Arnaud, M. Ashdown et al., *Planck 2013 results. XV. CMB power spectra and likelihood*, *A&A* **571** (2014) A15 [1303.5075].

[390] F. Couchot, S. Henrot-Versillé, O. Perdereau, S. Plaszczynski, B. Rouillé d'Orfeuil, M. Spinelli et al., *Cosmology with the cosmic microwave background temperature-polarization correlation*, *A&A* **602** (2017) A41 [1609.09730].

[391] Planck Collaboration, N. Aghanim, Y. Akrami, M. Ashdown, J. Aumont, C. Baccigalupi et al., *Planck 2018 results. V. CMB power spectra and likelihoods*, *arXiv e-prints* (2019) arXiv:1907.12875 [1907.12875].

[392] Y. Li, S. Singh, B. Yu, Y. Feng and U. Seljak, *Disconnected covariance of 2-point functions in large-scale structure*, *Journal of Cosmology and Astro-Particle Physics* **2019** (2019) 016 [1811.05714].

[393] L. Knox, *Determination of inflationary observables by cosmic microwave background anisotropy experiments*, *Phys. Rev. D* **52** (1995) 4307 [astro-ph/9504054].

[394] W. Hu and B. Jain, *Joint galaxy-lensing observables and the dark energy*, *Phys. Rev. D* **70** (2004) 043009 [astro-ph/0312395].

[395] F. Delgado, A. Saha, S. Chandrasekharan, K. Cook, C. Petry and S. Ridgway, *The LSST operations simulator*, in *Modeling, Systems Engineering, and Project Management for Astronomy VI*, vol. 9150 of *Proceedings of the SPIE*, p. 915015, Aug., 2014, DOI.

[396] D. J. Schlegel, D. P. Finkbeiner and M. Davis, *Maps of Dust Infrared Emission for Use in Estimation of Reddening and Cosmic Microwave Background Radiation Foregrounds*, *ApJ* **500** (1998) 525 [astro-ph/9710327].

[397] G. B. Rybicki and W. H. Press, *Interpolation, realization, and reconstruction of noisy, irregularly sampled data*, *ApJ* **398** (1992) 169.

[398] A. Slosar, U. Seljak and A. Makarov, *Exact likelihood evaluations and foreground marginalization in low resolution WMAP data*, *Phys. Rev. D* **69** (2004) 123003 [astro-ph/0403073].

[399] F. Elsner, B. Leistedt and H. V. Peiris, *Unbiased pseudo-C_ℓ power spectrum estimation with mode projection*, *MNRAS* **465** (2017) 1847 [1609.03577].

[400] K. M. Gorski, E. Hivon, A. J. Banday, B. D. Wandelt, F. K. Hansen, M. Reinecke et al., *HEALPix - A Framework for high resolution discretization, and fast analysis of data distributed on the sphere*, *Astrophys. J.* **622** (2005) 759 [astro-ph/0409513].

[401] J. Hartlap, P. Simon and P. Schneider, *Why your model parameter confidences might be too optimistic. Unbiased estimation of the inverse covariance matrix*, *A&A* **464** (2007) 399 [astro-ph/0608064].

[402] S. Dodelson and M. D. Schneider, *The effect of covariance estimator error on cosmological parameter constraints*, *Phys. Rev. D* **88** (2013) 063537 [1304.2593].

[403] A. Taylor, B. Joachimi and T. Kitching, *Putting the precision in precision cosmology: How accurate should your data covariance matrix be?*, *MNRAS* **432** (2013) 1928 [1212.4359].

[404] E. Krause, T. F. Eifler, J. Zuntz, O. Friedrich, M. A. Troxel, S. Dodelson et al., *Dark Energy Survey Year 1 Results: Multi-Probe Methodology and Simulated Likelihood Analyses*, *arXiv e-prints* (2017) arXiv:1706.09359 [1706.09359].

[405] A. Lewis, A. Challinor and N. Turok, *Analysis of CMB polarization on an incomplete sky*, *Phys. Rev. D* **65** (2002) 023505 [astro-ph/0106536].

[406] E. F. Bunn, M. Zaldarriaga, M. Tegmark and A. de Oliveira-Costa, *E/B decomposition of finite pixelized CMB maps*, *Phys. Rev. D* **67** (2003) 023501 [astro-ph/0207338].

[407] K. M. Smith, *Pseudo-C_ℓ estimators which do not mix E and B modes*, *Phys. Rev. D* **74** (2006) 083002 [astro-ph/0511629].

[408] H. Aihara, N. Arimoto, R. Armstrong, S. Arnouts, N. A. Bahcall, S. Bickerton et al., *The Hyper Suprime-Cam SSP Survey: Overview and survey design*, *Publications of the ASJ* **70** (2018) S4 [1704.05858].

[409] SDSS collaboration, *Cosmological Constraints from the SDSS Luminous Red Galaxies*, *Phys. Rev.* **D74** (2006) 123507 [astro-ph/0608632].

[410] G. R. Blumenthal, S. M. Faber, J. R. Primack and M. J. Rees, *Formation of Galaxies and Large Scale Structure with Cold Dark Matter*, *Nature* **311** (1984) 517.

[411] S. J. Maddox, G. Efstathiou, W. J. Sutherland and J. Loveday, *The APM galaxy survey. I - APM measurements and star-galaxy separation*, *Mon. Not. Roy. Astron. Soc.* **243** (1990) 692.

[412] C. M. Baugh, *The real space correlation function measured from the apm galaxy survey*, *Mon. Not. Roy. Astron. Soc.* **280** (1996) 267 [astro-ph/9512011].

[413] S. J. Maddox, G. Efstathiou and W. J. Sutherland, *The apm galaxy survey. 3. An analysis of systematic errors in the angular correlation function and cosmological implications*, *Mon. Not. Roy. Astron. Soc.* **283** (1996) 1227 [astro-ph/9601103].

[414] D. J. Eisenstein and M. Zaldarriaga, *Correlations in the spatial power spectrum inferred from angular clustering: methods and application to apm*, *Astrophys. J.* **546** (2001) 2 [astro-ph/9912149].

[415] A. J. S. Hamilton and M. Tegmark, *The Real space power spectrum of the PSCz survey from 0.01 to 300 h Mpc**-1*, *Mon. Not. Roy. Astron. Soc.* **330** (2002) 506 [astro-ph/0008392].

[416] 2dFGRS collaboration, *The 2dF Galaxy Redshift Survey: Power-spectrum analysis of the final dataset and cosmological implications*, *Mon. Not. Roy. Astron. Soc.* **362** (2005) 505 [astro-ph/0501174].

[417] M. Jarvis, B. Jain, G. Bernstein and D. Dolney, *Dark energy constraints from the CTIO Lensing Survey*, *Astrophys. J.* **644** (2006) 71 [astro-ph/0502243].

[418] R. Massey et al., *COSMOS: 3D weak lensing and the growth of structure*, *Astrophys. J. Suppl.* **172** (2007) 239 [astro-ph/0701480].

[419] T. Schrabback, J. Hartlap, B. Joachimi, M. Kilbinger, P. Simon, K. Benabed et al., *Evidence of the accelerated expansion of the Universe from weak lensing tomography with COSMOS*, *A&A* **516** (2010) A63 [0911.0053].

[420] H. Lin, S. Dodelson, H.-J. Seo, M. Soares-Santos, J. Annis, J. Hao et al., *The SDSS Co-add: Cosmic Shear Measurement*, *ApJ* **761** (2012) 15 [1111.6622].

[421] C. Heymans et al., *CFHTLenS tomographic weak lensing cosmological parameter constraints: Mitigating the impact of intrinsic galaxy alignments*, *Mon. Not. Roy. Astron. Soc.* **432** (2013) 2433 [1303.1808].

[422] M. Kilbinger, L. Fu, C. Heymans, F. Simpson, J. Benjamin, T. Erben et al., *CFHTLenS: combined probe cosmological model comparison using 2D weak gravitational lensing*, *MNRAS* **430** (2013) 2200 [1212.3338].

[423] M. J. Jee, J. A. Tyson, S. Hilbert, M. D. Schneider, S. Schmidt and D. Wittman, *Cosmic Shear Results from the Deep Lens Survey - II: Full Cosmological Parameter Constraints from Tomography*, *Astrophys. J.* **824** (2016) 77 [1510.03962].

[424] DES collaboration, *Dark Energy Survey Year 1 results: Cosmological constraints from cosmic shear*, *Phys. Rev.* **D98** (2018) 043528 [1708.01538].

[425] M. Cacciato, F. C. v. d. Bosch, S. More, R. Li, H. J. Mo and X. Yang, *Galaxy Clustering & Galaxy-Galaxy Lensing: A Promising Union to Constrain Cosmological Parameters*, *Mon. Not. Roy. Astron. Soc.* **394** (2009) 929 [0807.4932].

[426] Planck collaboration, *Planck 2015 results. XV. Gravitational lensing*, *Astron. Astrophys.* **594** (2016) A15 [1502.01591].

[427] M. Zaldarriaga and U. Seljak, *Reconstructing projected matter density from cosmic microwave background*, *Phys. Rev.* **D59** (1999) 123507 [astro-ph/9810257].

[428] Y. Omori et al., *A 2500 deg^2 CMB Lensing Map from Combined South Pole Telescope and Planck Data*, *Astrophys. J.* **849** (2017) 124 [1705.00743].

[429] DES, NOAO Data Lab collaboration, *The Dark Energy Survey Data Release 1*, *Astrophys. J. Suppl.* **239** (2018) 18 [1801.03181].

[430] DES collaboration, *Dark Energy Survey Year 1 Results: Photometric Data Set for Cosmology*, *Astrophys. J. Suppl.* **235** (2018) 33 [1708.01531].

[431] B. Flaugher, H. T. Diehl, K. Honscheid, T. M. C. Abbott, O. Alvarez, R. Angstadt et al., *The dark energy camera*, *The Astronomical Journal* **150** (2015) 150.

[432] DES collaboration, *redMaGiC: Selecting Luminous Red Galaxies from the DES Science Verification Data*, *Mon. Not. Roy. Astron. Soc.* **461** (2016) 1431 [1507.05460].

[433] DES collaboration, *Dark Energy Survey year 1 results: Galaxy clustering for combined probes*, *Phys. Rev.* **D98** (2018) 042006 [1708.01536].

[434] DES collaboration, *Dark Energy Survey Year 1 Results: Weak Lensing Shape Catalogues*, *Mon. Not. Roy. Astron. Soc.* **481** (2018) 1149 [1708.01533].

[435] E. Huff and R. Mandelbaum, *Metacalibration: Direct Self-Calibration of Biases in Shear Measurement*, 1702.02600.

[436] E. S. Sheldon and E. M. Huff, *Practical Weak Lensing Shear Measurement with Metacalibration*, *Astrophys. J.* **841** (2017) 24 [1702.02601].

[437] DES collaboration, *Dark Energy Survey year 1 results: Galaxy-galaxy lensing*, *Phys. Rev.* **D98** (2018) 042005 [1708.01537].

[438] J. Zuntz, T. Kacprzak, L. Voigt, M. Hirsch, B. Rowe and S. Bridle, *IM3SHAPE: A maximum-likelihood galaxy shear measurement code for cosmic gravitational lensing*, *Mon. Not. Roy. Astron. Soc.* **434** (2013) 1604 [1302.0183].

[439] DES collaboration, *Dark Energy Survey Year 1 Results: The Impact of Galaxy Neighbours on Weak Lensing Cosmology with im3shape*, *Mon. Not. Roy. Astron. Soc.* **475** (2018) 4524 [1708.01534].

[440] D. Coe, N. Benitez, S. F. Sanchez, M. Jee, R. Bouwens and H. Ford, *Galaxies in the Hubble Ultra Deep Field. 1. Detection, Multiband Photometry, Photometric Redshifts, and Morphology*, *Astron. J.* **132** (2006) 926 [astro-ph/0605262].

[441] DES collaboration, *Dark Energy Survey Year 1 Results: Redshift distributions of the weak lensing source galaxies*, *Mon. Not. Roy. Astron. Soc.* **478** (2018) 592 [1708.01532].

[442] T. Okamoto and W. Hu, *CMB lensing reconstruction on the full sky*, *Phys. Rev.* **D67** (2003) 083002 [astro-ph/0301031].

[443] Planck collaboration, *Planck 2015 results. IX. Diffuse component separation: CMB maps*, *Astron. Astrophys.* **594** (2016) A9 [1502.05956].

[444] M. Bucher, C. S. Carvalho, K. Moodley and M. Remazeilles, *CMB lensing reconstruction in real space*, *Phys. Rev. D* **85** (2012) 043016 [1004.3285].